An Evaluation of Geomechanical Properties of Potential Shale Gas Reservoirs in the Lower Indus Basin, Pakistan

A Thesis Submitted to the College of
Graduate and Postdoctoral Studies
In Partial Fulfillment of the Requirements For the

Degree of Doctor of Philosophy

In the

Department of Civil, Geological and
Environmental Engineering University of
Saskatchewan
Saskatoon

By

Ghulam Mohyuddin Sohail

© Copyright Ghulam Mohyuddin Sohail, April, 2020. All rights reserved.

Permission to Use

In presenting this thesis in partial fulfillment of the requirements for a Postgraduate degree from the University of Saskatchewan, I agree that the Libraries of this University may make it freely available for inspection. I further agree that permission for copying of this thesis in any manner, in whole or in part, for scholarly purposes may be granted by Dr. Christopher D. Hawkes who supervised my thesis work or, in his absence, by the Head of the Civil, Geological and Environmental Engineering or the Dean of the College of Engineering. It is understood that any copying, publication, or use of this thesis or parts thereof for financial gain shall not be allowed without my written permission. It is also understood that due recognition shall be given to me and to the University of Saskatchewan in any scholarly use, which may be made of any material in my thesis.

Requests for permission to copy or to make other use of the material in this thesis in whole or part should be addressed to:

Head of the Department of Civil, Geological and Environmental Engineering
University of Saskatchewan
Saskatoon, Saskatchewan S7N 5A9 Canada
OR
Dean
College of Graduate and Postdoctoral Studies
University of Saskatchewan
116 Thorvaldson Building, 110 Science Place
Saskatoon, Saskatchewan S7N 5C9 Canada

Abstract

Pakistan has been facing a growing energy crisis for the last decade, and the government is seeking new horizons for enhancing oil and gas production to reduce the gap between supply and demand. Although several shales of the Indus Basin in Pakistan are known source rocks for conventional hydrocarbon reservoirs, data currently available to assess their potential as shale gas reservoirs are somewhat limited. The objective of this research was to investigate, assess and improve methods for geomechanical characterization of shales using standard datasets of the type available (in the public domain) for Indus Basin shales.

In this research, six shales which are known to be source rocks in the Indus Basin, Pakistan, were evaluated for their shale gas potential by comparison against several of the most active shale gas plays in North America. The comparison included available geological, geochemical, petrophysical and elastic properties, and concluded that all of the Pakistani shales investigated are promising regarding their shale gas potential. However, more petrophysical and geomechanical data are required before conclusions about these shales can be made with greater confidence. In light of this, the remainder of the research conducted in this project focused on applying (and improving) advanced interpretation techniques on two of the prospective Lower Indus shales deemed to have the best available (public domain) data.

The interpretation of geomechanical properties generally requires knowledge of sonic shear wave velocity (Vs). Given that Vs measurement is commonly omitted from routine geophysical logging suites, many investigators have developed empirical models and rock physics models of varying form and complexity for the estimation of Vs using available well log and/or core analysis data. This study evaluated various relationships in the literature for the estimation of shear wave velocity applied to sandy shale and shale intervals of the Lower Goru Formation, Lower Indus Basin, for which two wells with Vs data were available. The results reveal that some empirical models can be effective for estimating Vs, but only when the model coefficients are adjusted by calibrating to site-specific Vp and Vs data. A modification to rock physics modeling developed for this type of work demonstrated that the use of Biot's model (rather than Gassmann's model) for fluid substitution improved model performance for Vs estimation in gas-saturated sandy shale and shale of the Lower Goru Formation. The rock physics-based model offers the advantage of being useful in settings where only Vp data are

available for model calibration, and it is suggested that the rock physics model should be reliable when applied to a broader range of saturations and lithologies in the Lower Goru Formation.

The next phase this work involved characterization of a shale interval in the Early Cretaceous-age Sembar Formation, Lower Indus Basin of Pakistan, using only readily available data. A workflow was developed for the estimation and mapping of geomechanical properties using logs from multiple wells and relevant post-stack seismic reflection data. Mineralogy data from well cuttings, core testing results for elastic properties and hydraulic fracturing test data were utilized to constrain the values of the properties estimated from geophysical data. The following results obtained at the well-scale suggest that the Sembar Shale is favorable for development: high gas saturation, good porosity (up to 10%), moderate quantity of thermally mature organic matter (2% - 4% TOC), a number of brittle intervals separated by thicker intervals that fall slightly below the brittle-ductile threshold, and a strike-slip stress regime. At the scale of the study area, robust statistical techniques were used to invert seismic stacks and develop a 3D mechanical earth model. This model shows a trend of increasing shale brittleness towards the northeastern portion of the study area, hence suggesting that this area might be most prospective for initial shale gas development.

The final phase of this research involved the assessment and improvement of techniques for estimating mechanical properties using drill cuttings, which serve as the only available basis for laboratory testing when core samples are unavailable. Microindentation testing was selected for this work based on the literature review. Experimental techniques developed or improved in this work include: embedding multiple cuttings into an epoxy puck to facilitate sample preparation, mineralogical analysis, and testing of a large number of sampling points; progressive re-saturation to restore cuttings to in-situ moisture conditions; selection of optimal indentation force; assessment of sample anisotropy; brittleness assessment based on indentation morphology; (and a statistical / rock physics framework for estimating macroscopic properties from extensive testing of samples with variable mineralogy). Limitations of this testing method are discussed, as are recommendations for future research.

Acknowledgments

I first would like to express my earnest gratitude and appreciation to my respected supervisor, Dr. Christopher D. Hawkes, for his guidance and support throughout my work during the Ph.D. program. I thank Dr. Hawkes for allowing me time to studycomplicated ideas while keeping things simple at the end. His critical suggestions have been priceless at every stage of this research.

I want to extend my acknowledgment to advisory committee members Dr. Doug Milne, Dr. James Meriam, and Mrs. Donna Beneteau for their valuable suggestions and feedback. The time and support of the advisory committee chair, Dr. Haithem Soliman, is greatly acknowledged. The assistance of Rock Mechanics Laboratory staff (especially Mr. Zbigniew Szczepanik) for testing of rock samples, is highly appreciated. I take this opportunity to thank my industry and academic fellows, Dr. Nayyer Islam and Dr. Mohammad Asif, Dr. Qamar Yasin and Mr. Kashif, for their critical comments to improve the quality of work and their support to obtain different datasets used in this study.

Furthermore, I would like to thank the UET, Lahore, Pakistan for providing the scholarship to pursue Ph.D. studies abroad. I would like to thank my senior colleagues/teachers in the Department of Geological Engineering, to motivate me for Ph.D. studies abroad. Finally yet importantly, I am extremely grateful to my parents for their support and motivation throughout my Ph.D. program. I specially thankful to my wife, Rabia Sohail, and sons, Affan and Rohaan, for limitless support and happiness they brought to me.

Table of Contents

List of Tables

List of Figures

List of Abbreviations and Symbols

Abbreviations:

AI	Accoustic Impedance
API	American Petroleum Institute (unit for gamma-ray)
ASTM	American Society for Testing Material
Bcm	Billion cubic meter
BI	Brittleness index
$BI_{mineralogy}$	Mineralogy-based BI
BI_{YME} or BI_E	Young's modulus-based BI
BI_PR or BI_v	Poisson's ratio-based BI
BP	Backpropagation
BPNN	back-propagation neural network
BRIT_average or BRIT_avg	Average BI based on elastic properties
DSST	Dipole shear sonic imager tool
DST	Drill stem test
DT4P or DTP	Monopole compressional waves interval transit time
DT4S	Monopole shear waves interval transit time
DTP	Compressional sonic transit time
fc	Characteristics frequency
GI	Genetic Inversion
GP	Generation potential
GPa	Giga pascal
GR	Gamma-ray
GR_uranium	Gamma-ray value for uranium
GRFS	Gaussian random function simulation
GR_{log}	Computed gamma-ray log (HCGR)
GR_{max}	Maximum value of GR
GR_{min}	Minimum value of GR
HC	hydrocarbon
HI	Hydrogen index
HSGR	Hostile environment standard gamma-ray
HCGR	Hostile environment computed gamma-ray
I	Illite
IGR	Gamma-ray index

K	Kaolinite
kHz	Kilo hertz
KT	Kuster and Toksoz
KT-Gassmann	Combination of KT and Gassmann theories
$KTOC$	Weight fraction of carbon in kerogen
LGF	Lower Goru Formation
LIB	Lower Indus Basin
LLD	Lateral log deep
LOM	Level of maturity
M	Mica
MHz	Mega hertz
MIB	Middle Indus Basin
MLC	Multilayer linear calculator
MMSCFD	Million standard cubic feet per day
MPa	Mega pascal
ND	Neutron-density
NN	Neural network
NPHI	Neutron log porosity
OI	Oxygen index
PEF	Photoelectric effect
PHIE	Effective porosity (= connected pore volume / bulk volume)
PHIE_corrected	Corrected effective porosity
PHIT	Total porosity (= total pore volume / bulk volume)
PHIT_corrected	Corrected total porosity
PHIT_ND	Total porosity from combination of neutron and density logs
$PHIT\_Sonic\_Rymer$	Total porosity using Rymer et al.'s equation
PSO	Particle swarm optimization
Q	Quartz
QEMSCAN	Quantitative evaluation of minerals by scanning electron microscopy
Quanti_Elan	A module in Techlog software for mineralogy analysis
RC	Reflection coefficient
RH	Relative humidity
RHOB	Bulk density log
RMS	Root mean square
SL	Seismic line

SRC	Saskatchewan Research Council
STD	Standard deviation
T or TWT	Two-way travel time
TDR	Time-depth relation
TOC	Total organic carbon
TOC_DlogR	TOC using 'delta log R' technique
TRR	Technically recoverable reserve
UIB	Upper Indus Basin
USA	United States of America
VR	Vitrinite reflectance
XRD	X-ray diffraction

Symbols :

A_s	Surface area of indentation
a	Invasion factor
A and B	Constants
°C	Centigrade
$DT_{p-sonic\ baseline}$	Baseline value of $DT_{p-sonic}$
$DT_{p-sonic}$	Sonic transit time for compressional wave
1D, 2D & 3D	One, two & three dimension
d_1 & d_2	Diagonal lengths
d_v	Mean Vickers indentation diagonal
E	Static Young's modulus
E_{dyn}	Dynamic Young's modulus
e	Constant
F_{gf}	Force in grams-force
g	Gravitational acceleration
Hv	Vickers Hardness
K_d	Dry bulk modulus
K_m	Bulk modulus of matrix
K_m	Matrix bulk modulus
$K_{m\_average}^{HS}$	Average of bulk modulus of matrix (Kmat_HS), HS for Hashin and Shtrikman
K^{HS-}	Lower bound of bulk modulus using Hashin and Shtrikman's equation

K^{HS+}	Upper bound of bulk modulus using Hashin and Shtrikman's equation
K_{sand} & K_{clay}	Bulk moduli of sand and clay
K'	Bulk modulus of inclusion
K	Slope of trend line
K	Permeability
K_{fl}	Bulk modulus of fluid
K_{gas}, K_{brine}	Bulk moduli of gas and brine
m	Cementation exponent
n	Saturation exponent
n_k	Gassmann-Krief exponent
n_{μ}	Gassmann-Krief exponent in Vs_BGK
OH^-	Hydroxyl ions
P_p	Pore pressure
R^2	Coefficient of determination or r-square
R_{LLD}	Resisitivity from LLD
$R_{LLD_{baseline}}$	Baseline value of R_{LLD}
R_{mf}	Mudfilterate resistivity
Ro	Vitrinite reflectance
R_{sh}	Average resisitivity in shale zone
R_t	Deep resistivity from lateral log
R_w	Water resistivity
R_{xo}	Flushed zone resistivity
S1	Indication of free hydrocarbons
S2	Indication of hydrocarbons produced from the cracking of kerogen
S3	Indication of the amount of oxygen in the kerogen
S_{gas}	Gas saturation
S_{Hmax} & S_{Hmin}	Maximum and minimum horizontal stresses
S_v	Vertical stress
S_w	Water saturation
S_{XO}	Flushed zone water saturation
Tmax	Pyrolysis temperature
T_{ijij}	Scalar in KT theory
$T_{ijij} - \frac{1}{3T_{iijj}}$	Scalar in KT theory

T_n	TWT for nth layer
V_{avg_i}	Average velocity at the top of ith layer
Vcl	Volume of clay
V'_{cl}	Volume of solid clay matrix (Normalized)
V_i	Interval Velocity
$V_{int.P}$	Interval velocity of primary waves
V_{ker}	Volume fraction of kerogen (unitless)
V_o	Primary or compressional wave velocity at zero effective stress in pore pressure equation, or Velocity at the seismic horizon top in velocity-time equation
V_{st}	Stacking Velocity
Vol	Component volumes in cm^3 (cc)
$Vol\%$	Volume percent
Vp	Compression wave velocity
Vp_log	Vp from compressional wave sonic log
Vp_RP	Rock physics-based Vp
Vs	Shear wave velocity
Vs_BGK	Biot-Gassmann-Krief ‘s equation for Vs estimation
Vs_log	Vs from shear wave sonic log
Vs_LV	Vernik (2016)’s equation for Vs estimation
Vs_RP	Rock physics-based Vs
Vs1 to Vs7	Equations for Vs estimations from serial number 1 to 7
V_{sh}	Volume of shale
$W_{dry}\%$	Dry weight in percent
W_{ker}	Mass fraction of kerogen (unitless)
W_{TOC}	TOC weight fraction
α	Tortuosity parameter in Biot’s equation
α_c	Aspect ratio for clay related pores
α_s	Aspect ratio for sand related pores
ΔT_{0i}	Difference between zero-offset travel times at the top and bottom of the i^{th} layer
Δt_g^p	Primary sonic interval transit time for the sand grains
Δt_g^s	Shear sonic interval transit time for the sand grains
$\Delta t_m^s, \Delta t_m^p$	Shear, primary (compressional) sonic interval transit time for a matrix

Δt_{sh}^{p}	Primary sonic time for clay minerals
Δt_{sh}^{s}	Shear sonic interval transit time for clay minerals
$\Delta t_{fluid_{corr}}$	Interval transit time corrected for fluid
Δt_{fluid}	Interval transit time of fluid
Δt_{matrix}	Interval transit time of matrix
Δt_{p}	Interval transit time (μs/ft) from compressional sonic log
Δt_{p_ker}	Compressional wave interval transit time for kerogen
ε_{Hmax}	Maximum horizontal strain
μ_{d}	Dry shear modulus
μ_{fl}	Fluid shear modulus
μ_{fr}	Shear modulus of dry rock frame
μ_{m}	Shear modulus of matrix
μ_{sand} & μ_{clay}	Shear moduli of sand and clay
μ_{s}	Shear modulus of matrix in Vs_BGK
μ_{sat}	Shear modulus of saturated rock
μ^{HS^+} & μ^{HS^+}	Upper and lower bounds of shear modulus using Hashin and Shtrikman's equation
$\mu_{m\_average}^{HS}$	Average shear modulus of matrix (μmat_HS)
μ'	Shear modulus of inclusion
ν	Static Poisson's ratio
ν_{dyn}	Dynamic Poisson's ratio
ρ_{b}	Bulk density
ρ_brine	Brine density
ρ_{fl}	Fluid density
ρ_gas	Gas density
ρ_{g} & ρ_{cl}	Density of sand and clay grains
ρ_{ker}	Kerogen density
ρ_{matrix} *or* ρ_{m}	Matrix density
ρ_{min}	Mineral grain density
σ_{μ}	Gassmann's coefficient in Vs_BGK
$\Phi_{n_{clay}}$	Clay porosity from neutron log
$\Phi_{n_{clay}}$	Neutron porosity at a high volume of clay interval (unitless)
$\Phi_{s_{clay}}$	Clay porosity from sonic log

$\Phi_{s_{clay}}$	Sonic log porosity at a high volume of clay interval (unitless)
Φ_e	Effective porosity or PHI_effective = connected pore volume / bulk volume
Φ_n	Neutron log porosity (unitless) or PHIT_neutron
Φ_{n_ker}	Neutron porosity for kerogen
Φ_{nc} , Φ_{sc}	Corrected porosities from neutron and sonic logs
Φ_s	Sonic log porosity (unitless) or PHIT_sonic
Φ_{s_ker}	Sonic porosity for kerogen
Φ_t	Total porosity or PHIT = total pore volume / bulk volume
Φ or Φ_t	Total Porosity

Chapter 1 - Introduction

1.1 Background

Pakistan has been facing a growing energy crisis for the last decade, and the government is seeking new horizons for enhancing oil and gas production to reduce the gap between supply and demand. Significant volumes of natural gas are contained within shale formations in Pakistan. The initial estimate of technically recoverable shale gas resources is around 3000 bcm (billion cubic meter) (US EIA, 2015). Shale gas development could considerably reduce the gap between supply and demand of natural gas in Pakistan. This scenario not only motivates exploration companies to seek shale gas development opportunities, but also attracts researchers to come up with an initial assessment of shale gas potential based on limited available technical data from previously drilled wells.

1.2 Overview

The United States is the largest holder of recoverable shale gas resources, and the hydrocarbon production from shales has increased dramatically over the past few years (US EIA, 2015). Currently, shales of the Barnett, Haynesville, Marcellus, Fayetteville and Eagle Ford formations are the primary gas producers in the United States. On the other hand, most production of oil and gas in Pakistan occurs in conventional reservoirs of the Indus Basin (Kazmi and Abbasi, 2008), which is subdivided into three parts; i.e., the Upper, Middle and Lower Indus Basins (UIB, MIB and LIB, respectively). Most of the marine shales of the Indus Basin have been demonstrated to be source rocks for conventional reservoirs in the basin (Kadri, 1995). Although these shales have supplied the hydrocarbons that migrated into conventional reservoirs, the present-day abundance of thermally mature and hydrogen-rich organic matter within the shales supports the possibility that they presently contain hydrocarbons. As such, it seems reasonable to assess their potential for shale gas production.

Shales are generally fine-grained, organically rich with very low porosity and permeability, and mostly require horizontal drilling and hydraulic fracturing for economical

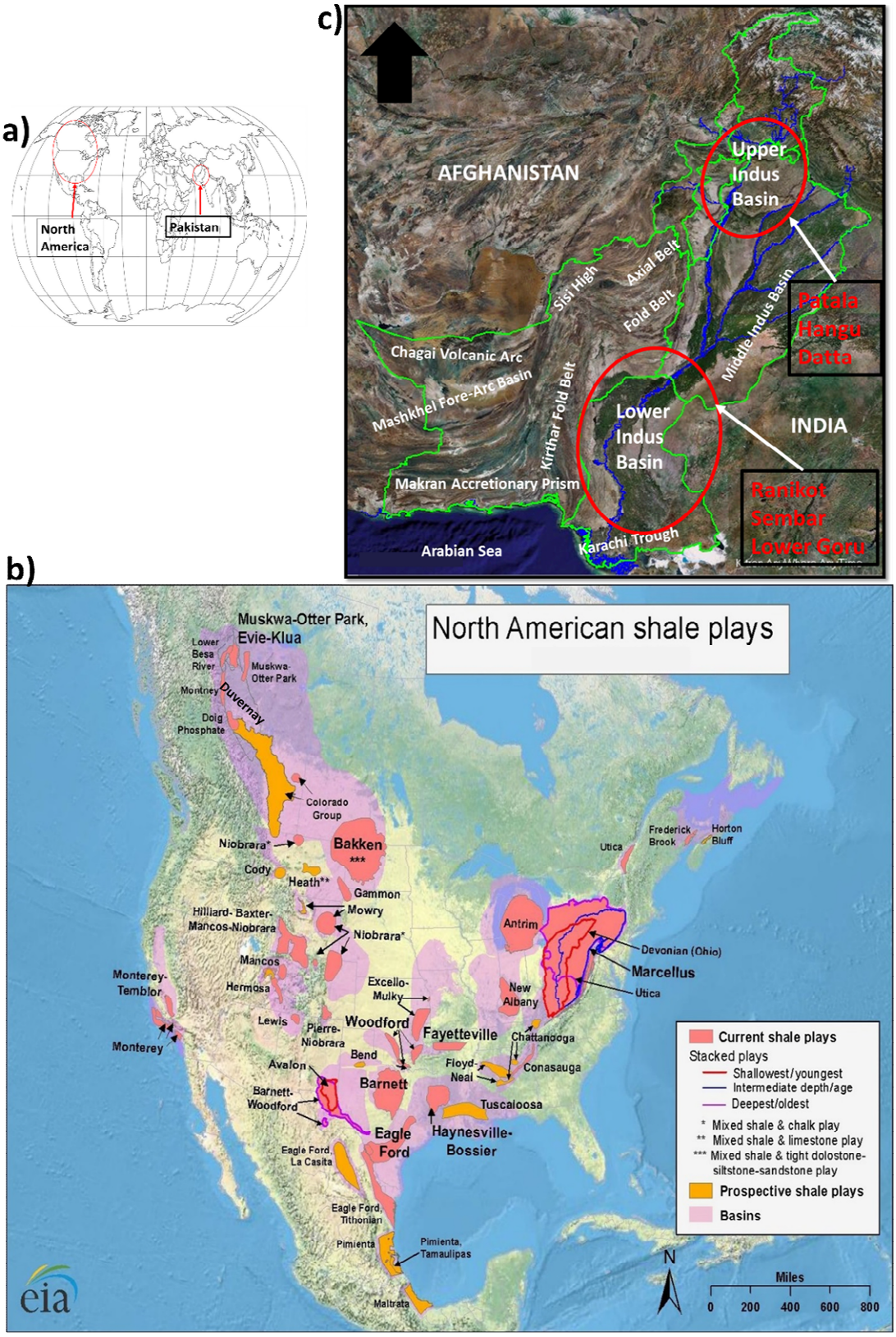

Figure 1.1 (a) World map showing the general location of shale plays investigated in this work. (b) Map showing North American shale plays (modified after US EIA, 2011). (b) Map showing Pakistani shale plays (modified after King and Cole, 2008). See Figure 1.2 for a generalized stratigraphic chart which includes the relevant shale formations in Pakistan.

production. Shale can act both as a source and reservoir for natural gas. Thermogenic or biogenic natural gas may be stored in shale in free, adsorbed and/or dissolved states (Curtis, 2002). The location of stored gas and the pathways that allow the gas to flow from the matrix to a wellbore (e.g., through induced artificial fractures) are factors that play a crucial role in the success of shale gas development. Multistage hydraulic fracturing via horizontal wells in shale gas reservoirs has proven effective for the economic recovery of gas in numerous cases throughout the world. Given the complexity of shale gas reservoirs, comprehensive evaluation, exploration, and development programs are required for successful shale gas exploitation.

The main goals can be divided into two parts: first, to evaluate the geological and geochemical properties of different Pakistani shales using analogs selected from various gas-producing North American shales to selectpotential shale gas reservoirs, and second, to conduct a focused study of petrophysical and geomechanical properties of a potential Pakistani shale gas reservoir using available data.

1.3 Research Objectives

The hypothesis underlying this research is the following: several shale formations in Indus Basin of Pakistan have significant potential for shale gas development, and it should be possible to conduct an assessment of shale gas potential if current datasets (e.g., geological, geochemical, well logs and drill cuttings, and post-stack seismic data) are appropriately studied and linked. The following are the specific objectives of each study conducted on Pakistani shales to assess their suitability as a shale gas reservoir.

1. To evaluate six Pakistani shales, as encircled in Figure 1.2, for shale gas potential, through comparison of geological, geochemical, petrophysical and geomechanical properties to those of the most active shale gas plays in North America.

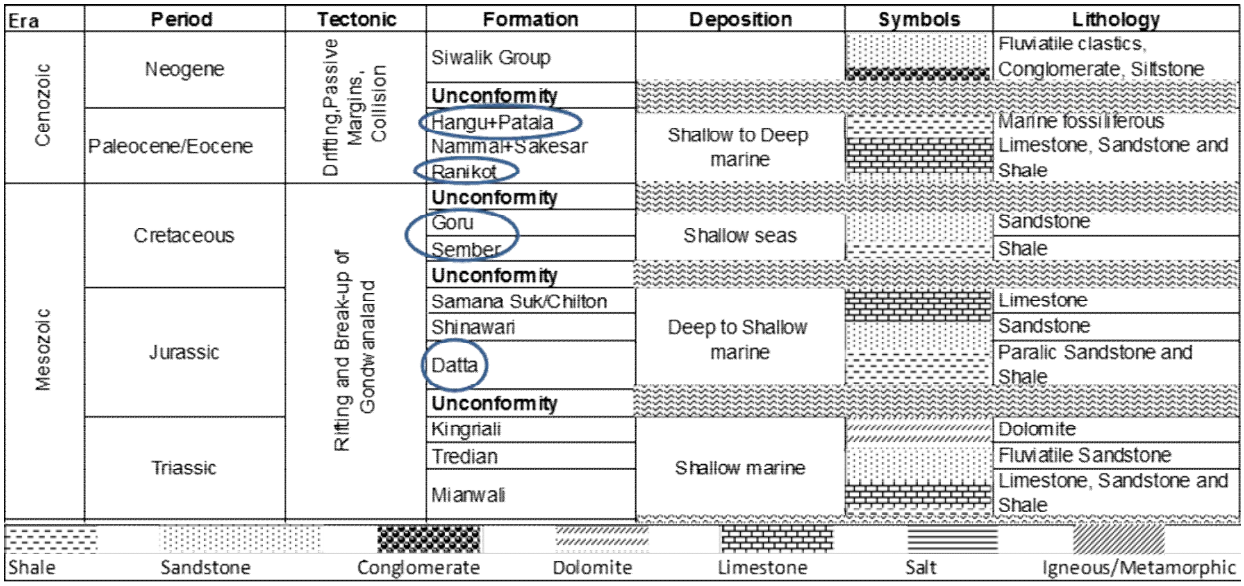

Figure 1.2 Generalized stratigraphy of Pakistani shales (modified after Kadri, 1995).

2. To evaluate various published relationships for the estimation of shear wave velocity (Vs) applied to sandy shale and shale intervals of the Lower Goru Formation, Lower Indus Basin, through the following steps: statistical analysis of the difference between estimated and measured Vs, and test a modification to the conventional rock-physics model to make it better for a potential shale gas reservoir.

3. To characterize the shale of the Sembar formation, Lower Indus Basin, through a workflow for the estimation and mapping of geomechanical properties using logs from multiple wells and post-stack seismic data.

4. To assess and improve the techniques for estimating mechanical properties using drill cuttings, through a comprehensive literature review, and running of multiple pilot experiments for defining the acquisition parameters, expose the cuttings to moisture to achieve in-situ moisture conditions for testing, interpret the morphology of indent for brittleness.

1.4 Structure of the Dissertation

This document is a manuscript-based thesis, in which Chapters 2 through 5 are based on technical papers that have been accepted (Chapters 2 and 3) or submitted (Chapters 4 and 5) at the time of the thesis defense. The following is a summary of the contents of each chapter.

Chapter 1 presents the background, motivation and objectives for this research, and a high-level summary of the research methods used.

Chapter 2 presents a study in which source rocks of Pakistan were evaluated for their shale gas potential based on analogs selected from various North American shales for which data had been published. Published data for Pakistani shales were compiled, then assessed, and supplemented through consultation with industry professionals. Pakistani formations reviewed were the Datta (shaly sandstone), Hangu (sandy shale), Patala (sandy shale), Ranikot (shaly sandstone), Sembar (sandy shale) and Lower Goru (shaly sandstone) formations, all of which are known source rocks in the Indus Basin. For this study, geological (e.g., depositional environment, depth, thickness, mineralogy), geochemical (e.g., quantity and thermal maturity of organic carbon), petrophysical (e.g., porosity, permeability) and elastic parameters (e.g., Young's modulus, Poisson's ratio) were investigated and explicitly correlated with the eight most active shale gas plays of the North America, while data for other North American shale gas plays were used for general discussion on prospective Pakistani shales.

Chapter 3 presents a study in which several empirical and rock-physics based relationships in the literature for the estimation of shear wave velocity (Vs) were applied to sandy shale and shale intervals of the Lower Goru Formation (LGF), Lower Indus Basin, Pakistan. The input parameters (e.g., petrophysical and elastic properties) were estimated using available logs and optimized through correlation of recorded and calculated compressional wave velocity (Vp) values. Some modifications were suggested for a rock-physics model of Xu and White (1995), to make it better for the estimation of Vs in a potential shale gas reservoir. Statistical analysis was used to quantify the difference between measured and predicted Vs. The prediction of Vs in LGF resulted in the validation of petrophysical properties (e.g., mineralogy, porosity, and saturation) which are helpful for assessing the shale gas potential of LGF. Further, the methodology developed in this chapter was useful for the Sembar Shale investigations presented in Chapter 4.

Chapter 4 presents a study in which petrophysical and geomechanical properties were integrated to construct a mechanical earth model using geophysical logs and post-stack seismic reflection data. Where available, mineralogy data from well cuttings, core testing results for elastic properties, and hydraulic fracturing test data were utilized to improve the accuracy of the properties estimated from geophysical data. This study first focused on one key well (with best data availability) to characterize the Sembar Formation ("Sembar Shale")

and to understand the inter-dependence of petrophysical and mechanical properties at the local scale. Additional research using seismic reflection survey data and available logs from other vertical wells extended the extent of the study area towards the northeast and southwest.

Chapter 5 presents a study in which the assessment and improvement of techniques for estimating mechanical properties using drill cuttings of Sembar Shale were undertaken. The techniques developed/improved include: embedding multiple cuttings into an epoxy puck to facilitate sample preparation, mineralogical analysis, and testing of a large number of sampling points; progressive re-saturation to restore cuttings to in-situ moisture conditions; selection of optimal indentation force; brittleness assessment based on indentation morphology. A couple of pilot experiments were conducted to define the acquisition parameters for micro indentation testing on shale cuttings.

Chapter 6 is a summary of the results of each study conducted in this thesis. The research contributions and recommendations for future research are also described.

1.5 Contributions to Engineering

Engineers must have access to shale reservoir properties before designing drilling and completion operations in these reservoirs. As such, the main contributions of this research to engineering are the following:

- Evaluation of different models, and suggestion of a modifiedrock physics model for shear wave velocity (Vs) estimation in a potential shale gas reservoir. This significantly improves the shale gas reservoir characterization in wells where Vs was not recorded.
- Construction of a mechanical earth model to assist engineers in drilling and completing shale gas wells in the study area.
- Introduction, and recommended improvements, of a technology (e.g., microindentation) for testing of drill cuttings, which can yield estimates of mechanical properties in the absence of core samples.

References

Curtis, J. B. (2002). Fractured shale-gas systems. *AAPG Bulletin, 86*. doi: 10.1306/61eeddbe-173e-11d7-8645000102c1865d.

Kadri, I. B. (1995). *Petroleum geology of Pakistan*. Karachi, Pakistan Petroleum Ltd.

Kazmi, A. H., and Abbasi, I. A. (2008). *Stratigraphy and historical geology of Pakistan*, Department & NCE in Geology, University of Peshawar.

King, A., and Cole B. (2008). Pakistan Satellite Image. Retrieved 2020, from https://geology.com/world/pakistan-satellite-image.shtml

US EIA., (2015). Technically Recoverable Shale Oil and Shale Gas Resources: India and Pakistan, A Report, Energy Information Administration (EIA), 42. (Retrieved 2016, from https://www.eia.gov/analysis/studies/worldshalegas/pdf/India_Pakistan_2013-15.pdf/

US EIA., (2011). Review of Emerging Resources: U.S. Shale Gas and Shale Oil Plays, A Report, Energy Information Administration, 105.

Xu, S., and White, R. E. (1995). A new velocity model for clays and mixtures*: Geophysical Prospecting, 43*, 91-118.

Chapter 2 - Literature Review: An Overview of Pakistani Shales for Shale Gas Exploration and Comparison to North American Shale Plays

The expanded abstract of this chapter has been accepted for an international conference, as follows:

Cited as: Sohail, G. M, Hawkes, C. D. (2019). *An Overview of Pakistani Shales for Shale Gas Exploration and Comparison to North American Shale Plays*. International Conference on Economic Geology and Mining, World Academy of Science, Engineering and Technology, Dubai, United Arab Emirates, 9-10 Novembar 2020.

Contribution of the Ph.D. candidate

Ghulam Mohyuddin Sohail carried out the evaluation presented in this chapter, with technical review feedback provided by Dr. Christopher Hawkes during weekly meetings. Mr. Sohail wrote the manuscript, with review feedback provided by Dr. Hawkes.

Contribution of this chapter to the overall study

Several shale formations are well-known to be hydrocarbon source rocks in the Indus Basin of Pakistan. A comprehensive literature-based study of these shales was undertaken in this chapter in order to select a couple of these shales that have strong potential to serve as shale gas reservoirs. Also, this study highlighted a couple of technical issues with the available dataset for Pakistani shales, which motivated the work reported in the following chapters.

2.1 Abstract

Pakistan has been facing a growing energy crisis for the last decade, and the government is seeking new horizons for enhancing oil and gas production to reduce the gap between supply and demand. Recent developments in technologies to produce natural gas from shales at economic rates has unlocked new horizons for hydrocarbon exploration and development. Operating companies in the USA and Canada have been particularly successful at producing shale gas, so comparing against the properties of shale gas reservoirs in these countries is used for an initial assessment of prospective shale gas reservoirs in other parts of the world. In this study, selected source rocks from Pakistan are evaluated for their shale gas potential using analogs selected from various North American shales, for which data have been published. Published data for Pakistani shales were compiled, then assessed and supplemented through consultation with industry professionals. Pakistani formations reviewed are the Datta (shaly sandstone), Hangu (sandy shale), Patala (sandy shale), Ranikot (shaly sandstone), Sembar (sandy shale) and Lower Goru (shaly sandstone) formations, all of which are known source rocks in the Indus Basin. For this study, available geological, geochemical, petrophysical and elastic parameters have been investigated and are explicitly correlated with the eight most active shale gas plays of the USA, while data for other North American shale gas plays are used for general discussion on prospective Pakistani shales. The results of this study show that the geological and geochemical parameters of all the Pakistani shales reviewed in this work are promising regarding their shale gas potential. However, more geochemical, petrophysical and geomechanical data are required before conclusions about these shales can be made with confidence.

2.2 Introduction

The energy crisis in Pakistan needs a long-term solution to reduce the gap between supply and demand because production from conventional reservoirs is not sufficient to fulfill the country's growing demand for energy (Abbasi et al., 2014). According to initial studies of the United States Energy Information Administration, Pakistan contains approximately 3000 bcm (billion cubic meters) of shale gas reserves (US EIA, 2015); moreover, Abbasi et al. (2014) suggest that the total resource potential for shale gas is even higher than this.

The following sedimentary basins exist within Pakistan: the Indus Basin, the Balochistan Basin, and the Pishin Basin. Most production of conventional oil and gas occurs in the Indus Basin (Kazmi and Abbasi, 2008), which is subdivided into three parts; i.e., the Upper, Middle and Lower Indus Basins (UIB, MIB and LIB, respectively) – see Figure 2.1. Though the Lower Indus Basin (LIB) is likely more prospective for hydrocarbon production, most of the marine shales of the Indus Basin have been demonstrated to be source rocks for conventional reservoirs in the basin (Kadri, 1995). As such, it seems reasonable to assess their potential for shale gas production.

Shales have been deposited over a broad range of geological time (from Precambrian through Cenozoic) and are common throughout the world's sedimentary basins. However, not all shales are organic-rich; hence not all shales are deemed prospective as shale gas reservoirs. Paleoenvironmental and geological factors (tectonism, sedimentation rates) affecting the development of self-sourced, organic-rich shales have been discussed by Eoff (2013). Organic-rich shales most commonly formed in anoxic deep marine environments; however, anoxic environments, which foster the development of organic-rich deposits, can also occur in shallow marine settings (Rine and Ginsburg, 1985; Loucks and Ruppel, 2007). In terms of quantifying and characterizing organic content, total organic carbon (TOC) content and vitrinite reflectance (Ro) are useful parameters. TOC (notably kerogen and bitumen) defines the capacity to produce and store hydrocarbons within a shale formation (TOC < 1% suggests a poor quality shale reservoir; TOC > 1% suggests a good shale reservoir) (Bratovich and Walls, 2016). Ro is used to assess the thermal maturity of shale reservoirs; Ro > 1.1% suggests dry gas and kerogen of Type II/III (Bratovich and Walls, 2016). The TOC and maturity are critical factors to recognize the oil & gas-bearing potential of source rock. It is necessary to study the source types and environment of deposition of organic matter, which are linked to the hydrocarbons potential in shales. Types II kerogen and I are unstructured, and derived from algae and soft plant parts like leaf cuticles. Types III and IV are structured and derived from woody plant material. Types II and I are oil-prone and also generate gas. Type III is incapable of generating oil and only produces gas. Type IV is inert. Type I is generally lacustrine, Types II and III are commonly found in marine sediments.

Shale mineralogies can vary considerably (e.g., variable amounts of clays, fine-grained quartz, and carbonates), hence resulting in a wide range of mechanical properties

and varying degrees of brittleness (Slatt, 2011). Given the relatively ductile nature of many clays under in-situ conditions, the presence of silica or other hard minerals improves the ability of shale to fracture more easily (Johnson, 2009). The mineralogy of the shale also plays a central role in understanding the link between fracture complexity and fracture conductivity, thereby determining the potential for gas recovery from the reservoir (Sunjay, 2011). Ideally, it is best to measure shale mechanical properties directly. However, when this is not possible, mineralogy can provide valuable insights as to mechanical behavior (e.g., brittleness).

The shale gas potential of an organic-rich shale is affected by its permeability (which is a function of its porosity and pore structure). The permeability affects gas flow rates and mechanical properties (e.g., elastic properties, which affect in-situ stresses, and brittleness), and these impact the hydraulic fracturing operations that are typically required to achieve economic production rates. Different types of porosity systems exist within organic-rich shales (e.g., kerogen pores, inter-particle, intra-particle, and fracture type pores). As such, it is helpful to recognize the dominant porosity systems when evaluating a shale gas reservoir for its potential productivity (Bratovich and Walls, 2016); though ultimately, it is best to have direct measurements of permeability.

Shale gas development in the USA and Canada has been active for nearly two decades, and the characterization of several important shales has reached a mature state. Though there are no single, well-defined standard values for various properties that enable quantification of shale gas potential (Wang and Wang, 2016), a comparison of unproven prospects against various properties measured on known shale gas producers serves as a useful basis for screening shale gas candidates. Thus, an integrated comparison has been undertaken in this work, to assess the shale gas potential of various Pakistani shales and identify critical data gaps that must be addressed to achieve a more positive assessment in the future. This comparison included the thickness, burial depth, mineralogy, TOC, Ro, and porosity, all of which have been published for both North American shale gas reservoirs and Pakistani shale gas candidates. Further, the data compilation included permeability and selected mechanical properties (Young's modulus and Poisson's ratio) for the North American shales, though data for these properties were found to be unavailable for the Pakistani shales. The work presented here expands upon previous comparative studies of Pakistani and North American shales undertaken by Ayaz et al. (2012) and Haider et al. (2012), in that additional shales with actual thickness of shales in shale formation are

considered, and more emphasis is placed on identifying data gaps (e.g., regarding mechanical properties) which should be addressed in future research.

2.3 Methodology

Relevant data for Pakistani and North American shales were collected from published literature, and the Pakistani data were further assessed and supplemented using well logs and geochemical (Rock-Eval Pyrolysis, vitrinite reflectance, and maceral analysis) data. The depths and thicknesses of different Pakistani shales were established from available well data. Shale intervals were identified using gamma-ray (GR) logs and the interval thicknesses were summed to get the total thickness of shale in each shale formation, as summarized in Appendix 2-A (Figure 2.1 shows well locations and Figure 2.2 (a,b,c) and 2.3 (a,b,c) give total thickness of shaly formations encountered in the studied wells). A ternary plot of mineralogy was developed and used to classify the shales based on their siliceous, argillaceous and calcareous contents. Bar charts of Depth, Thickness, TOC, Ro, and Porosity for six Pakistani and eight USA shales were developed for comparison. The type, quality and maturity of kerogen in Pakistani shales was assessed through different standard plots (Hydrogen index versus Oxygen index, TOC versus S2, Temperature versus Hydrogen index), for which data are given in Appendix 2-B. A polar chart of all the parameters was constructed to compare and highlight the data gaps of Pakistani shales. The characteristics of Pakistani shales were studied and discussed concerning other North American shales as given in Appendix 2-C.

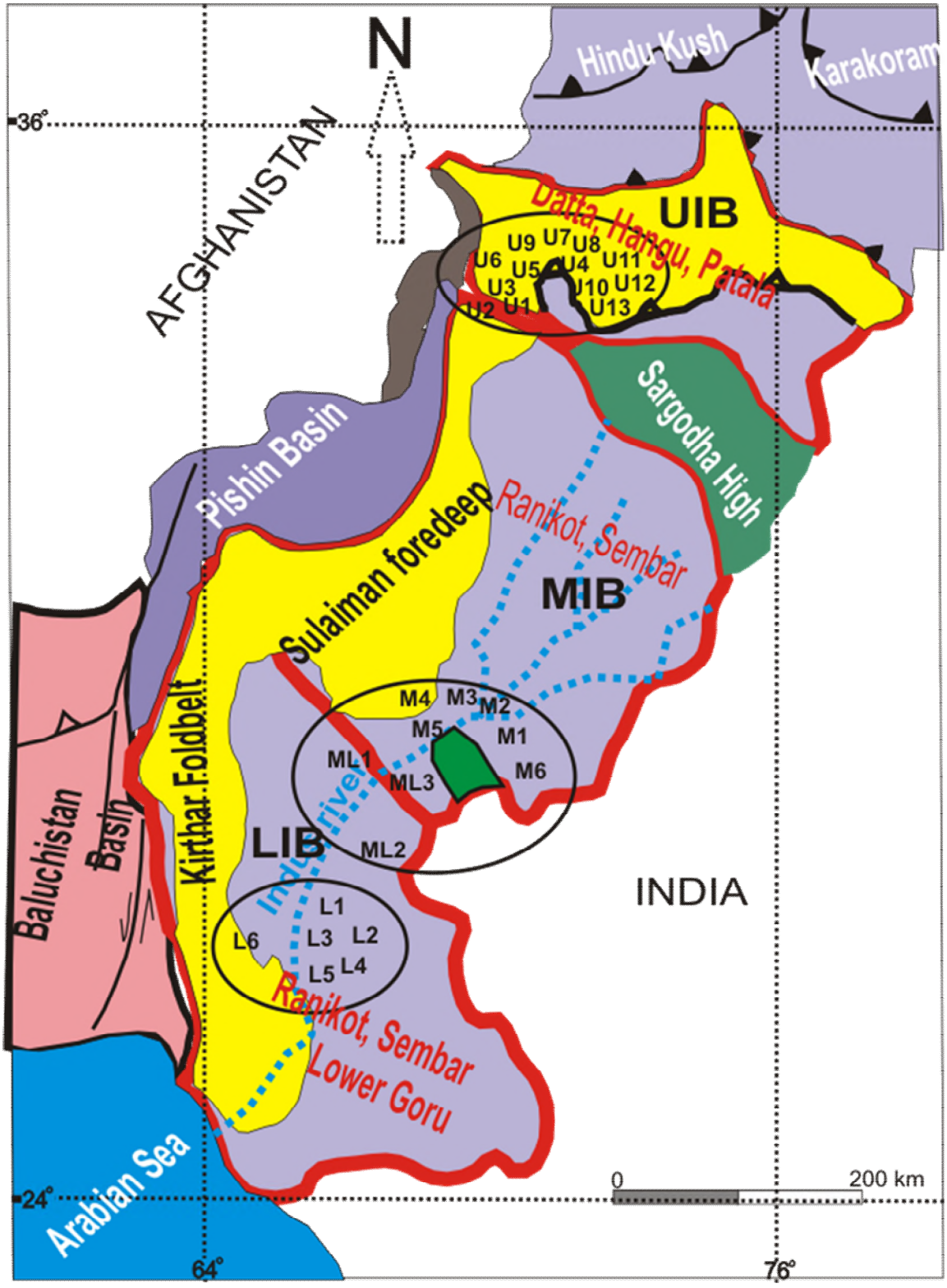

Figure 2.1 Map of Pakistan showing sedimentary basins, including the Upper, Middle and Lower Indus Basins (UIB, MIB and LIB, respectively). Potential shale gas formations of the UIB, MIB, and LIB are also shown, as well as the locations of wells analyzed in this study (circled in black).

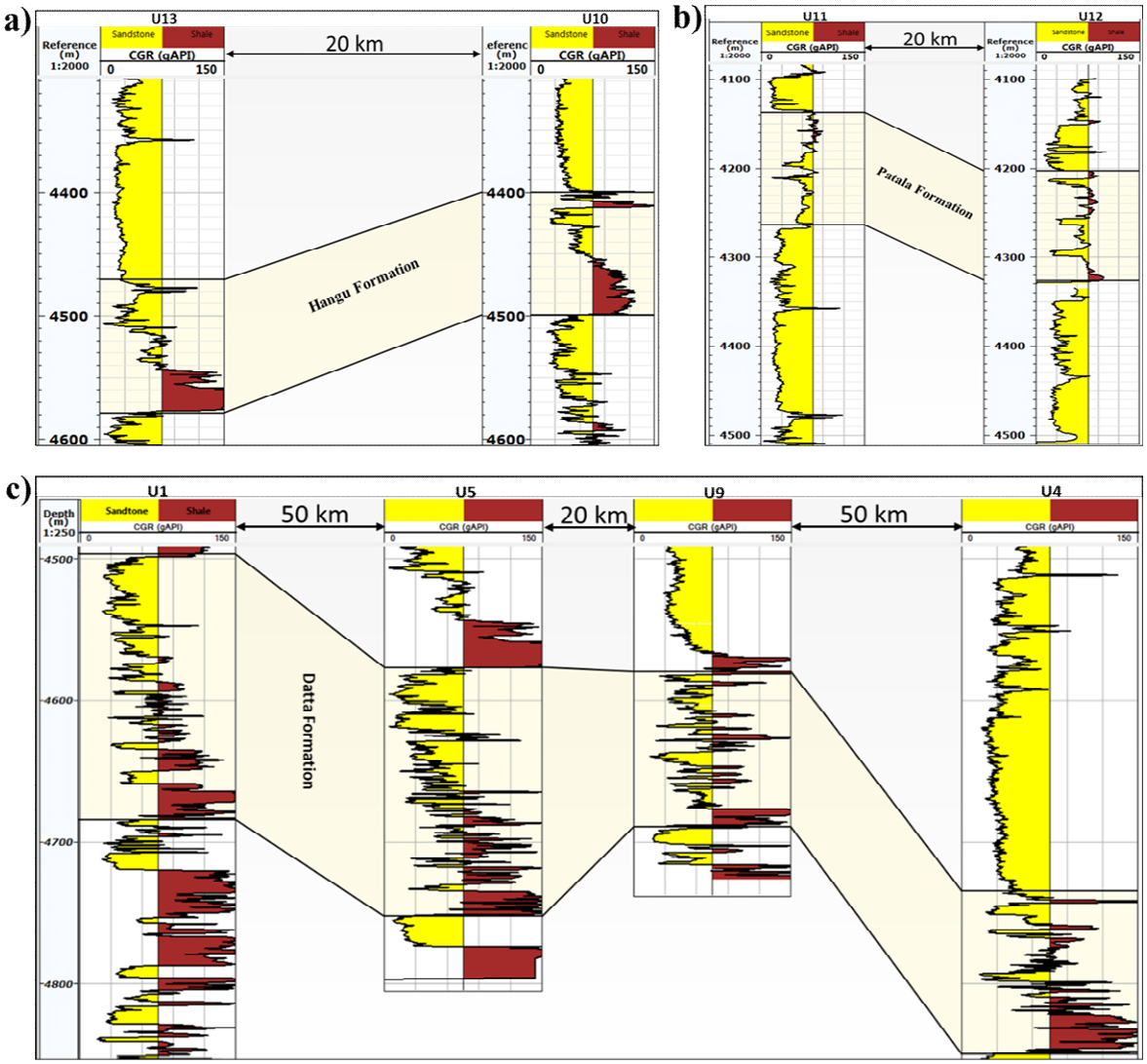

Figure 2.2 Geological well correlation for (a) Hangu, (b) Patala and (c) Datta Formations.

2.4 Prospective Shale Gas Formations in Pakistan

The six prospective shale gas formations used in this study are listed in Table 2.1. Where available, technically recoverable reserves are also listed. A brief description of these formations, along with their shale intervals in the studied wells, is discussed in the subsections 2.4.1 to 2.4.6 based on data given in appendices 2-A and 2-B.

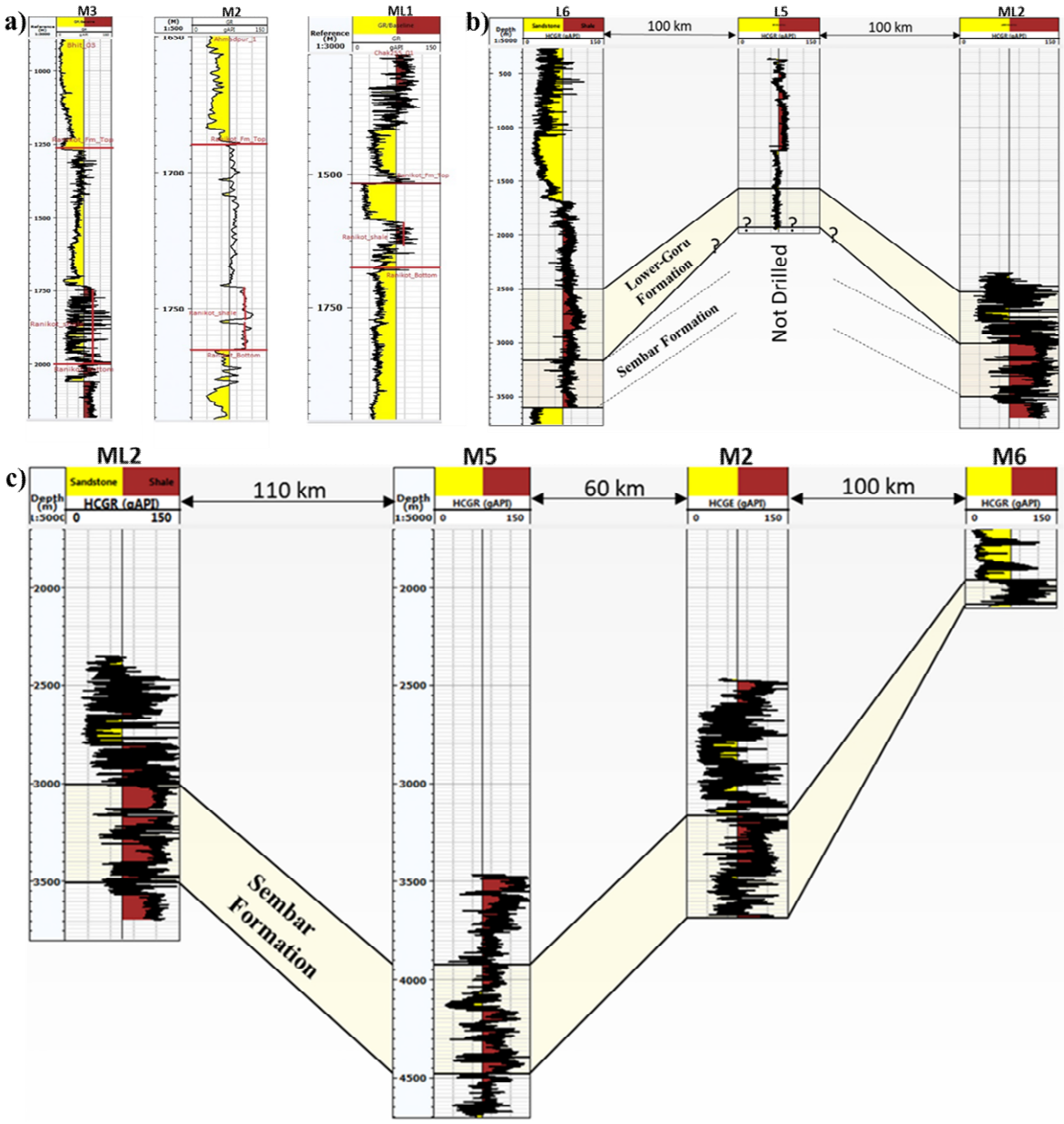

Figure 2.3 Wells correlation for (a) Ranikot, (b) Sembar and (c) Lower Goru Formations.

2.4.1 Hangu Formation

The Hangu Formation is of early Paleocene age and was deposited in a marginal marine environment. It is comprised of sandstone with minor mudstone, claystone, carbonaceous shale, and intercalations of limestone (Warwick et al., 1995). The depth and thickness of the shale intervals vary from 2700 m to 4500 m and, 3 m to 32 m, respectively, as shown in appendices A and C. TOC (2-10%) and Ro (0.81-1.3%) values are relatively high in this shale, which has high quartz (60-70%) and low clay (<20%) contents (Haider et al., 2012; Shah et al., 2013).

Table 2.1 Prospective shale gas formations of Pakistan

Shale Gas Formation	TRR (bcm)
Hangu	N.A.
Patala	N.A.
Datta	N.A.
Sembar	2860 (EIA 2015)
Ranikot	125 (EIA 2015)
Lower Goru	N.A.
TRR: Technically recoverable reserves, bcm: billion cubic meter N.A.: Not available	

The petrographic analysis of outcrop samples in the study area, as given in Appendix 2-B, shows the kerogen is of Type-II and III with poor hydrocarbon generation potential (Shahzad, 2007). Hangu Formation cutting samples from U3 well (see location in Figure 2.1) are organic-rich (TOC = 2.3 %), and S1 and S2 values (7.78 and 5.78 mg/g rock, respectively) suggest very good hydrocarbons potential regarding generated and residual hydrocarbons, respectively. The hydrogen index as shown in Figure 2.4 (257 mg/g TOC), indicates organic matter derived from Type-II and Type-III kerogen (Asif, 2015). The S2-TOC plot (as shown in Figure 2.5) also shows Type-III, but in the HI-Tmax plot (as shown in Figure 2.6) suggests that the kerogen is immature. The kerogen may be mature away from wells used in this study, as reported by Haider et al. (2012) and Shah et al. (2013).

2.4.2 Patala Formation

This formation of late Paleocene age was deposited in an intertidal lagoonal environment. Its lithology is highly variable throughout the Indus Basin; it contains a high volume of organic-rich shale along with limestone (Jalees, 2014). The depth and thickness of shale intervals in the Patala Formation varies from 2600 m to 4200 m and 7 m to 33 m, respectively (Haider et al., 2012). It contains quartz (30-40%), clay (25-30%) and calcite (0-20%), although in some wells the quartz contents are much higher (70-80%) than clay and calcite (Jalees, 2014). The values of S1 range between 0.5 to 3 mg HC/g rock (mg of hydrocarbon per gram of rock) and values of S2 lie in the range between 6.5-19 mg HC/g

rock, indicating fair to very good and good to very good quality, respectively, in the studied wells (see Appendix 2-B). The Van Krevlen diagram and S2 vs.TOC plot (Figures 2.4 and 2.5), show that the shales of Patala Formation contain Type-III kerogen and have the potential to produce gas. Published studies based on wells data show excellent TOC (~5-10%) with thermally mature kerogen of Type II/III (Jalees, 2014).

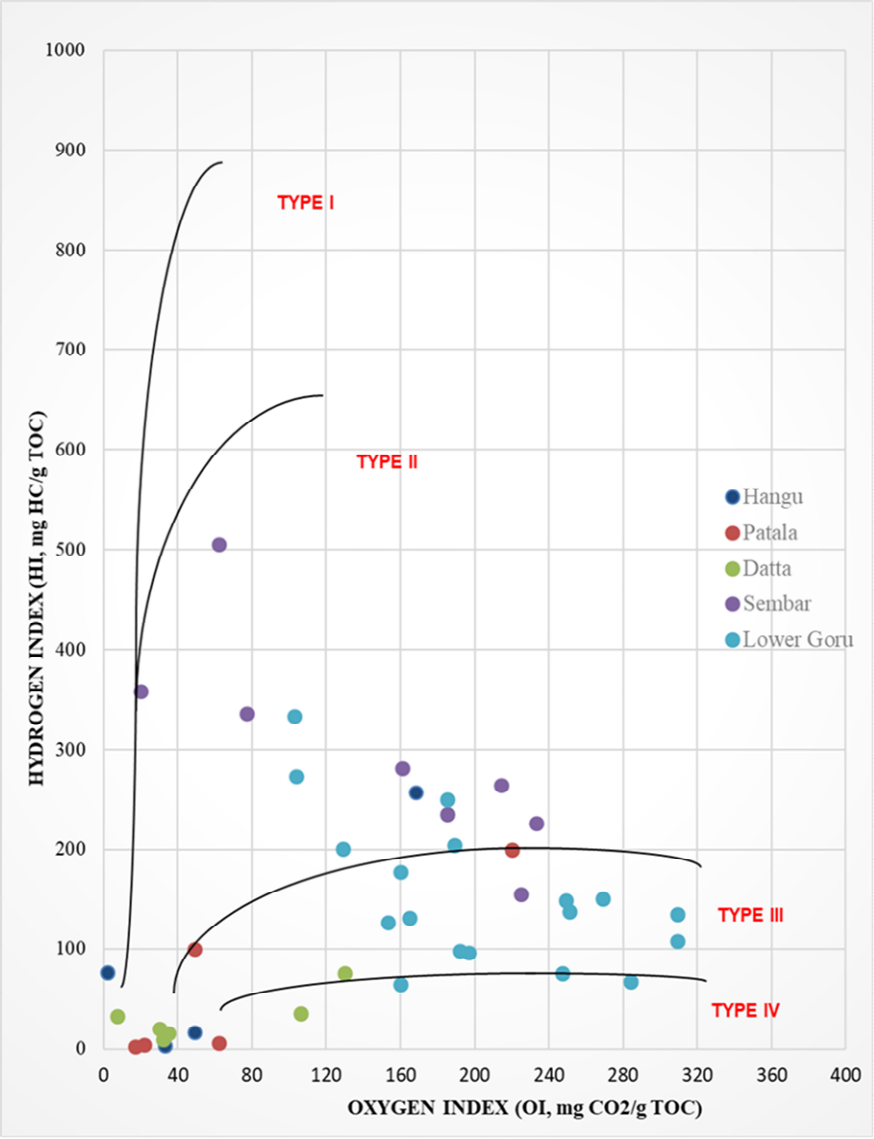

Figure 2.4 Kerogen types for selected shale formation of the Indus Basin, based on OI-HI cross plot (Van Krevlen diagram) (Data source: Ahmed et al., 2012; Robinson et al., 1999).

Although the maximum historical temperature of the Patala Formation was in the early to main stage the oil maturity window (Figure 2.6), the formation may act as a minor source of gas in Well U13 (Jalees, 2014).

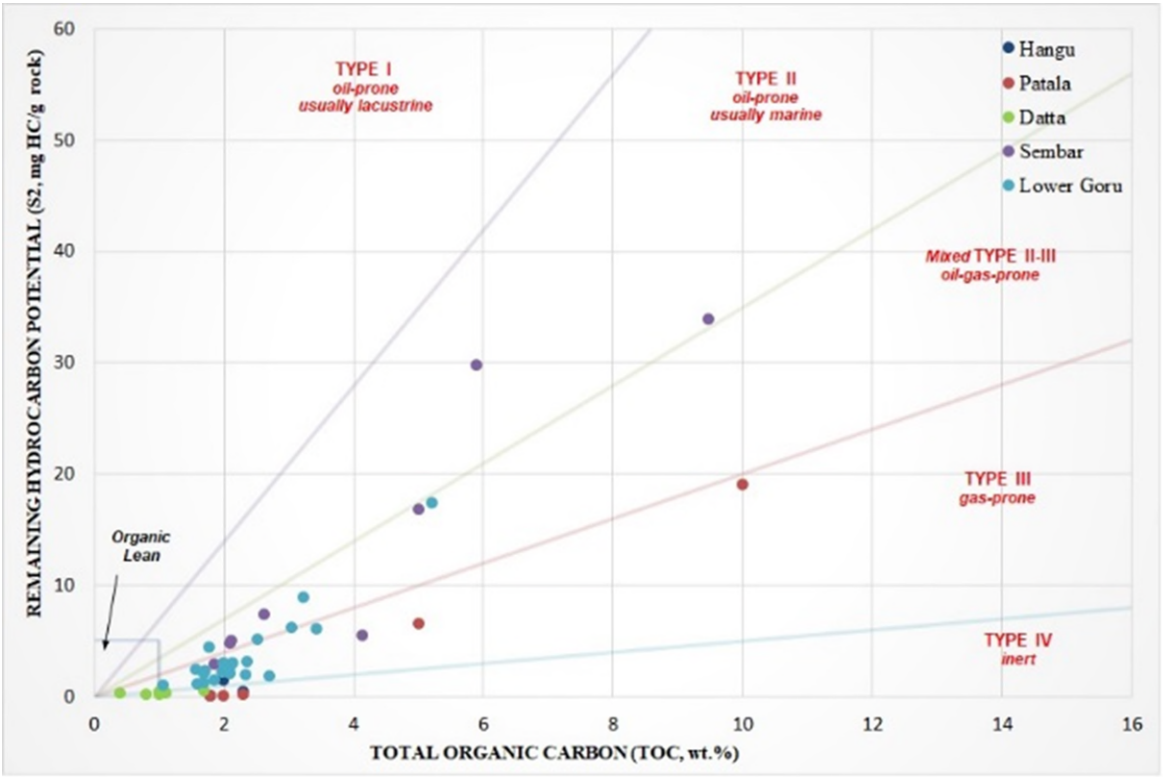

Figure 2.5 Kerogen types and quality based on a TOC-S2 cross plot for Pakistani shales (Data source: Ahmed et al., 2012; Robinson et al., 1999).

2.4.3 Datta Formation

The Lower Jurassic Datta Formation was deposited in a delta plain setting of a fluvial-dominated delta, and facies variations reflect that marine conditions prevailed in some parts of the UIB (Kazmi and Abbasi, 2008). It is comprised of sandstone interbedded with siltstone, shale, carbonaceous clays and coal stringers (Kazmi and Abbasi, 2008). The shale interval depths are in the range of 4650 m to 4700 m with thicknesses in the 6 m to 54 m range. These shale intervals contain high quartz (>50%) and low (10-20%) clay contents (Gul et al., 2016). The shale of the Datta formation (in the entire Upper Indus Basin) has fair-to-good source rock potential based on its total organic carbon content (TOC = 0.5-2%), and contains the entire oil window maturity based on vitrinite reflectance (Ro = 0.5-0.55%) (Khalid et al., 2015). The TOC values range from 1.73% to 3.73% in the studied wells, indicating good to very good quality. The S1 (0.05-0.18 mg HC/g rock) and S2 (0.30-0.56 mg HC/g rock) values are poor (see Appendix 2-B). The Van Krevlen diagram and S2-TOC plot show that the Datta Shale contains Type-III kerogen and has the potential to produce

gas. Kerogen is generally of Type-III, though Type-II is also present. The Tmax-HI plot shows the kerogen is immature in studied wells.

2.4.4 Sembar Formation

The Early Cretaceous Sembar Formation is exposed at the boundary of the Middle Indus Basin (MIB) and Lower Indus Basin (LIB) and is composed of shale with minor siltstones and sandstones (Kazmi and Abbasi, 2008; Ahmad et al., 2012). The Sembar Formation was deposited on the western shelf of the Indian Plate (passive margin setting) during the early Cretaceous period, as it drifted northward and entered warmer latitudes (Iqbal and Shah, 1980; Ahmad et al., 2012). The Sembar Formation has been encountered in some wells of the Indus Basin at depths ranging from 750 m to 3500 m, with thickness varying from 50 m to more than 600 m (Iqbal and Shah, 1980; Kadri, 1995; Ahmad et al., 2012). In the studied wells, the thickness of shale varies from 17 m to 550 m and contains quartz (40-50%), clay (30-40%) and calcite (10-15%) minerals (Ahmad et al., 2012). The shale of the Sembar Formation is the source rock for most of the conventional producing reservoirs in the MIB and LIB, and has high values of TOC (2-10%) and Ro (0.85-1.50%) (Haider et al., 2012). The geochemical data acquired using well cuttings samples of the studied wells (as given in Appendix 2-B) shows the S1 range 1.79 to 10.16 mg HC/g rock and S2 lie in the range 2.65 to 33.91 mg HC/g rock, which indicates good to very good and fair to very good quality source rock, respectively. The Van Krevlen diagram and S2-TOC plot (Figures 2.4 and 2.5) show that the Sembar Shale contains type II and III kerogen (mixed type) and has the potential to produce oil and gas. On the Tmax-HI plot (Figure 2.6), some data points are in the dry gas window, which still needs to be confirmed through more samples from other wells.

2.4.5 Ranikot Formation

The Paleocene-age Ranikot Formation was deposited in a shallow marine environment and is comprised of sandstone with minor shales and siltstones (Hakro and Baig, 2014). The depth and thickness of shale intervals vary from 270 m to 2135 m and

64 m to 214 m, respectively, in studied wells of the MIB and LIB. The values of TOC (2-3%) and Ro (0.85-1%) from outcrop samples indicate that shales of the Ranikot Formation are organic-rich and thermally mature with Type III kerogen (Hakro and Baig, 2014). The

shale intervals contain quartz (60-70%), clay (10-30%) and calcite (5-10%) in outcrop samples (Hakro and Baig, 2014). There are no published geochemical data for this formation, so the shales of Ranikot Formation cannot be interpreted based on outcrop data only, although high shale gas reserves have been declared by the US EIA (United States Energy Information Administration) (2015) based on unpublished geochemical data.

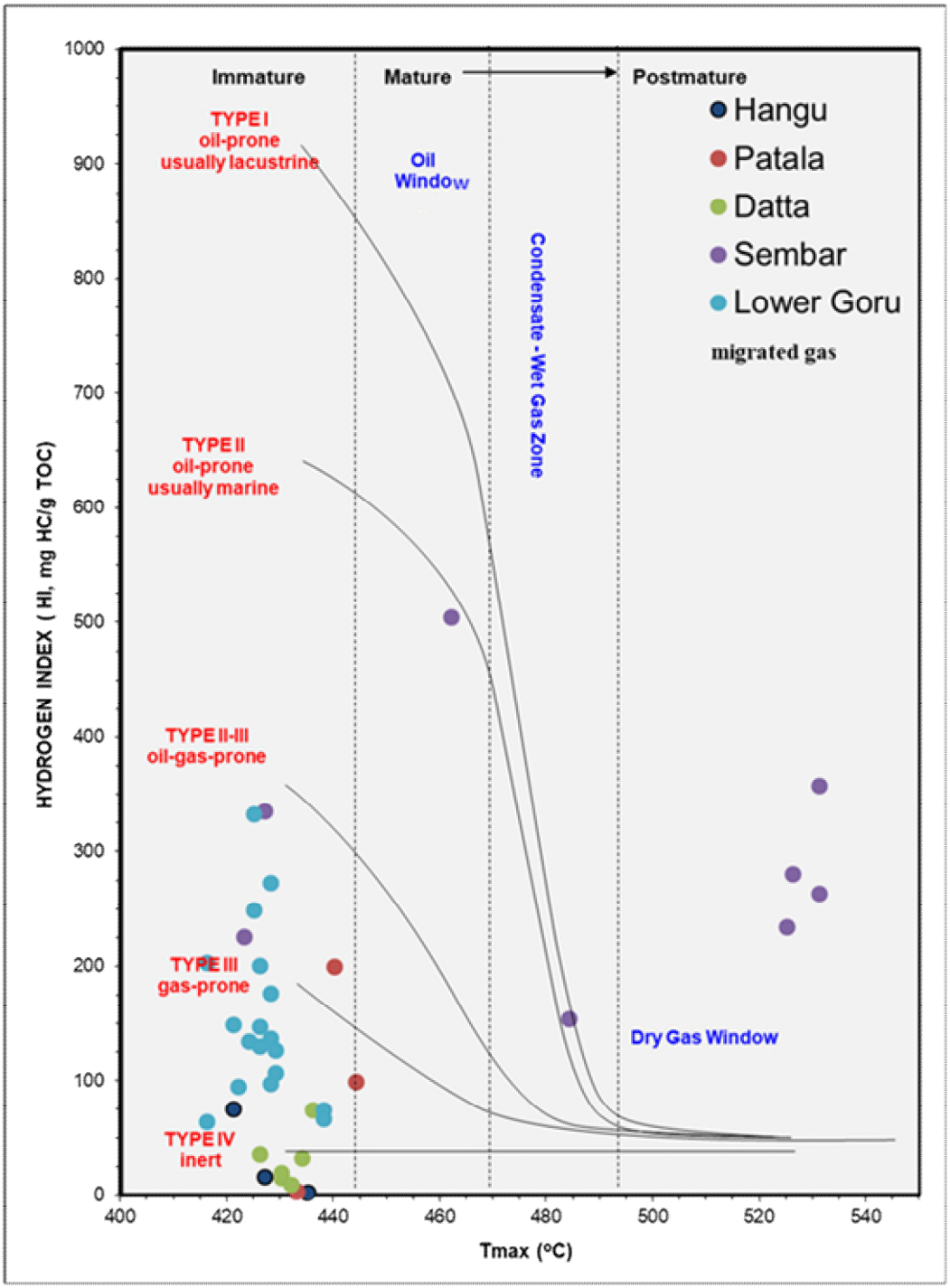

Figure 2.6 Kerogen types and maturity plot for Pakistani shales (Data sources are given in Appendix 2-B).

2.4.6 Lower Goru Formation

The Lower Goru Formation is of early Cretaceous age and was deposited in a marine environment. Its depth varies from 2250 m to 3650 m, and the total thickness of shales in this formation range from 198 m to 795 m in the LIB (based on Sidique et al., 2014, and work conducted by the author during this research). The shales of the Lower Goru Formation haave favorable values of TOC (1-1.5%) and Ro (2-3%) and contain quartz (40-50%), clay (40-45%) and calcite (5-10%) (Sidique et al., 2014; Haider et al., 2012). The values of S1 (0.57 to 5.64 mg HC/g rock) and S2 (1.02-17.37 mg HC/g rock) indicate fair to good and poor to very good quality kerogen, respectively. The Van Krevlen diagram and S2 -TOC plot show that the Lower Goru Shale contains Type-II and III kerogen and has the potential to produce both oil and gas. The Lower Goru is typically Type-II kerogen with some terrigenous input. The Tmax-HI plot shows that kerogen is thermally immature.

2.5 Comparison between selected North American and Pakistani Shales

The eight most active shale gas plays in North America, as shown in Table 2.2, were selected for analog plots with Pakistani shales. Other shale gas plays in North America, as listed in Appendix 2-C, are also used as a basis for comparison later in this paper (discussion section). In this section, various geological and petrophysical parameters of Pakistani shales are plotted and compared against those of North American shales, as a means of putting the shale gas potential of Pakistani shales in context.

Table 2.2 Production rates for selected shale gas plays in North America (Data source: Kennedy et al., 2016)

Shale Gas Play	Production (bcm/day)	Average thickness (m)	Production normalized by average thickness (bcm/day/m)
Haynesville	0.59-0.70	75	0.007-0.009
Barnett	0.28-0.36	108	0.002-0.003
New Albany	0.00019-0.0002	22	0.000008-0.000009
Antrim	0.03-0.05	12	0.0025-0.0041
Eagle Ford	0.45-0.59	88	0.005-0.006
Fayetteville	0.36-0.45	33	0.011-0.014
Montney	0.01-0.06	175	0.00005-0.0003
Duvernay	0.00005-0.0001	45	0.0000011-0.0000022
bcm: billion cubic meters			

2.5.1 Tectonics and Depositional Environment

Tectonic events of the Mesozoic and Cenozoic eras played important roles in the deposition of Pakistani shales. In contrast, most of the North American shale gas reservoirs, as given in Table 2.2, (except the Haynesville, Eagle Ford and Montney Shale of the Mesozoic era) were deposited in the Paleozoic era. The Indus Basin was located on the passive continental margin of the Indian Plate during the Mesozoic era, and Pakistani shales were deposited under significant sea-level changes (Khan, 2012; Kadri, 1995). The separation of Eastern Gondwanaland (India-Antarctica-Australia) from Western Gondwanaland (Africa-South America) in the Mesozoic created shallow seas where Pakistani shales of Cretaceous age were deposited (Kadri, 1995). In the Tertiary period, movement of the Indian plate accelerated (16 cm/year), and it collided with the Eurasian plate in the north; shales were deposited in different phases of transgression and regression cycles (Kadri, 1995). North American shales were deposited in flooded foreland basins along collisional margins during the Paleozoic era and semi-restricted basins along an overall ramp-type setting of a rifted margin during the Mesozoic era (Eoff, 2013; Goldhammer, 1998).

2.5.2 Depth and Thickness

Present-day depths of the Pakistani shales are generally comparable to or slightly greater than the North American shales, as shown in Figure 2.7a. At 270 m, the minimum depth of the Ranikot shale is significantly shallower than the other Pakistani shales, which range from 750 to 3600 m minimum depth. The minimum depth of the Ranikot Shale is greater than two of the North American shales (Antrim and New Albany), but lower than the rest (which range from 305 to 3200 m). The maximum depths of the Pakistani shales range from 3500 to 4500 m, compared to North American shales which range from 610 to 4268 m. With the exception of the Sembar Shale (minimum and maximum thicknesses of 17 and 550 m, respectively), the thicknesses of the Pakistani and North American shales fall in similar ranges as shown in Figure 2.7b (4 to 60 m minimum thickness for North American shales compared to 3 to 198 m for Pakistani shales; 21 to 305 m maximum thickness for North American shales compared to 30 to 305 m for Pakistani shales).

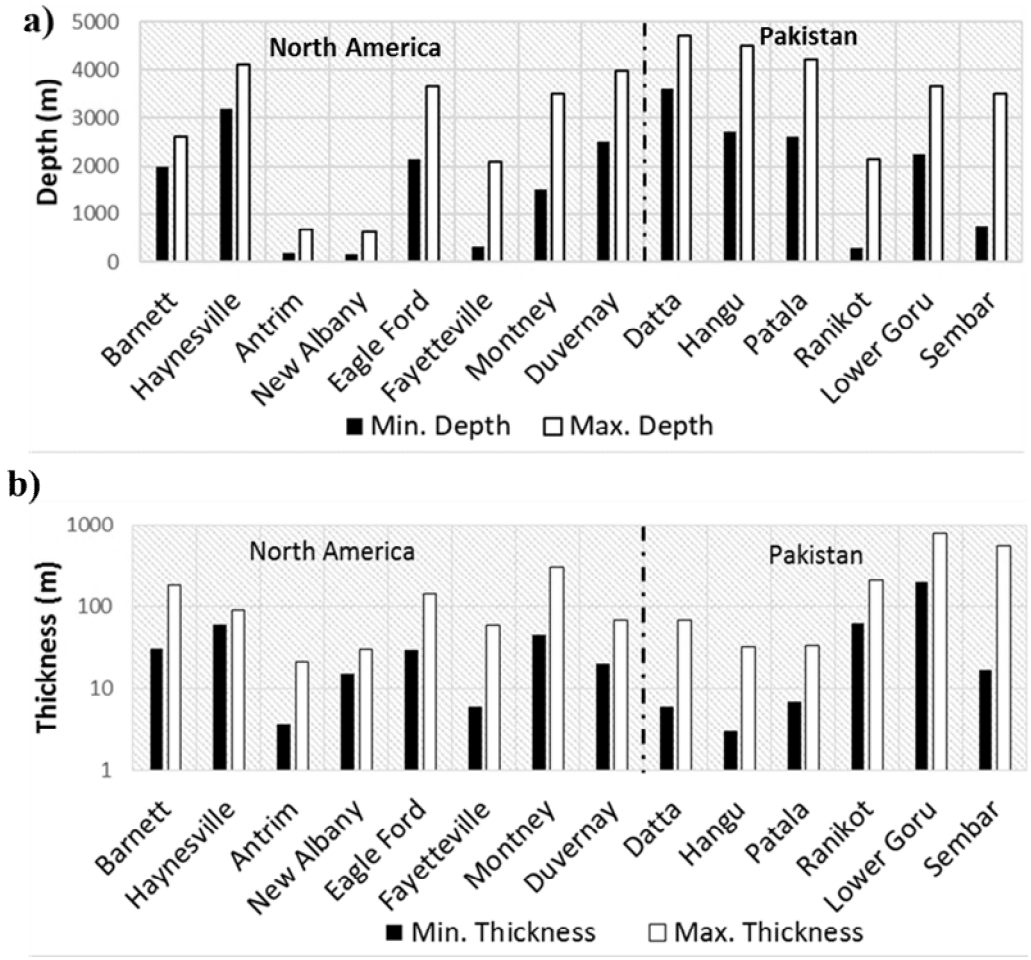

Figure 2.7 (a) Depths and (b) Thicknesses of selected North American and Pakistani shales (Data sources are given in Appendix 2-C). (See Figure 1.1 for the locations of these shale gas reservoirs.)

2.5.3 Mineralogy and Brittleness

Different researchers (Cui et al., 2017; Sone and Zoback, 2013; Rickman et al., 2008; Wang & Gale, 2009) have linked mineralogy to the brittleness index (BI) of shale gas reservoirs and found positive correlations between brittle mineral content (e.g., quartz) and BI. It is further suggested that pyrite and calcite are also critical in the calculation of BI, and separate studies should be conducted to reveal the impact of these minerals on BI (Zhang et al., 2017). Zoback and Kohli (2019) suggest it is not grain mineralogy that impacts hydraulic fracturing of shale gas reservoirs but rather the types of cement between the mineral grains. A detail discussion is beyond the scope of this chapter but is included in chapter-4 of this thesis.

According to the ternary plots shown in Figure 2.8, all of the Pakistani shales except the Ranikot and Hangu shales have quartz contents in the 40% to 50% range (approximately), which is similar to most of the North American shales. North American shales falling below this range are the Haynesville, Duvernay, New Albany (partially) and Eagle Ford. Of these, the latter (Eagle Ford) stands apart from all of the shales studied based on its high calcite content (63% to 73%). The Ranikot and Hangu shales have the highest quartz contents (62% to 75%) of all the shales studied (Hakro et al., 2014; Shah et al., 2013). Pakistani shales that are closest to multiple North American shales in terms of mineralogy are the Sembar (similar to Antrim, New Albany and Barnett) and the Datta (similar to Montney, Fayetteville and Antrim).

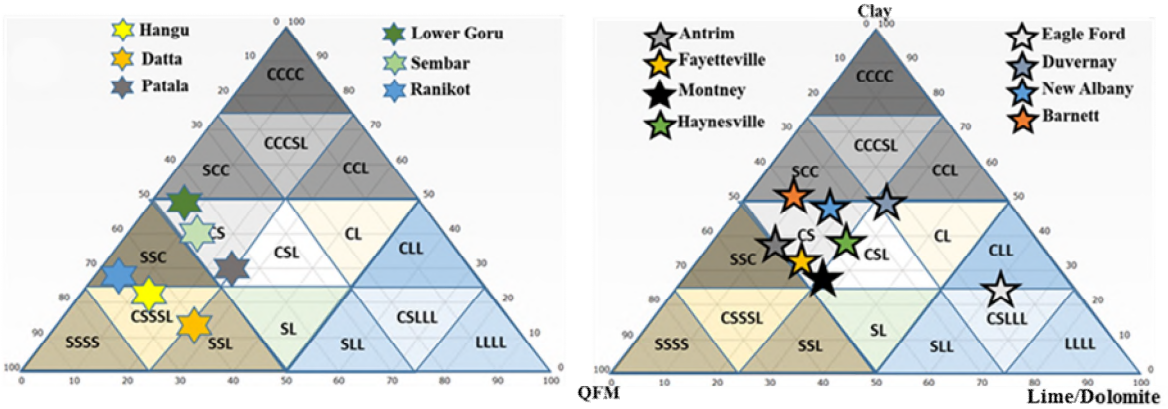

Note: CCCC: claystone, CCCSL: calcareous and siliceous claystone, SCC: siliceous claystone, CS: mixed claystone and sandstone, SSC: clayey sandstone, CSSSL: clayey and calcareous sandstone, SSSS: sandstone, CCL: calcareous claystone, CL: mixed claystone and limestone/dolostone, CSL: (tri-mineral) mixed mudstone, SL: mixed sandstone/limestone/dolostone, SSL: calcareous sandstone, CLL: clayey limestone/dolostone, CSLLL: clayey and siliceous limestone/dolostone, SLL: siliceous limestone/dolostone, LLLL: limestone/dolostone/anhydrite. **QFM: quartz feldspar mica**

Figure 2.8 Ternary plot showing mineralogy of selected North American and Pakistani shales (Data sources are given in Appendix 2-C).

2.5.4 TOC, Ro, Kerogen Type and Quality

The range of TOC values for the Pakistani shales has considerable overlap with the North American shales, though overall, they are somewhat lower. As shown in Figure 2.9a, the minimum TOC for North American shales is 0.4% to 4% compared to 0.5% to 2% for Pakistani shales; the maximum TOC for North American shales is 4% to 25% compared to 2% to 10% for Pakistani shales. The high maximum TOC of the Hangu and Sembar shales (10%) is comparable to the New Albany, Antrim and Duvernay shales. The maximum TOC values for the Ranikot (3%), Lower Goru (1.5%) and Datta (2%) shales are lower than all North American shales (Kennedy et al., 2016; Haider et al., 2012; Arthur et al., 2008).

As shown in Figure 2.9b, the minimum Ro for North American shales is 0.35% to 1.29% compared to 0.5% to 2% for Pakistani shales; the maximum Ro for North American shales is 1.2% to 4% compared to 1% to 3% for Pakistani shales. Although only one of the top four maximum Ro values (Fayetteville, Lower Goru, Duvernay and Montney) is associated with a Pakistani shale, overall there is little that differentiates the North American and Pakistani shales regarding Ro values (Gul et al., 2016; Kennedy et al., 2016; East et al., 2012; Haider et al., 2012).

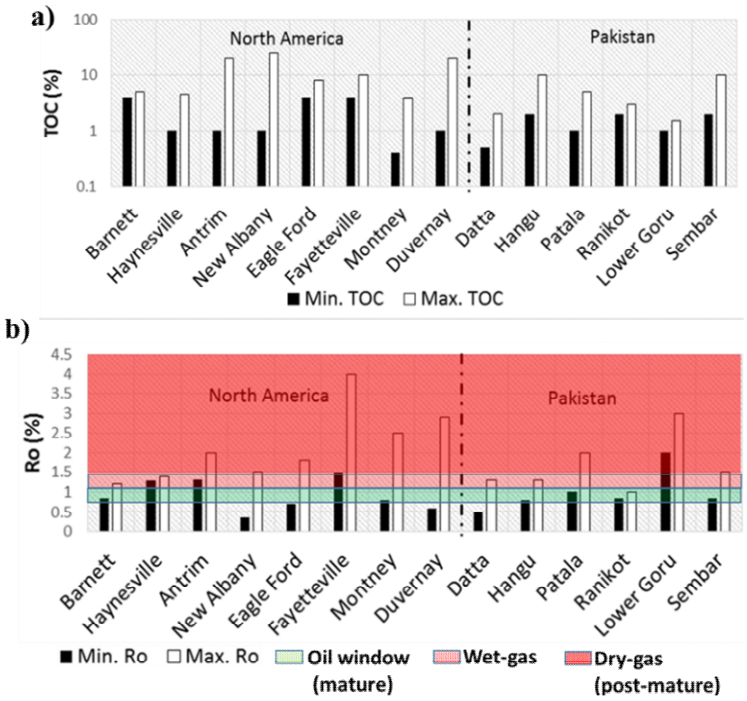

Figure 2.9 (a) Total Organic Carbon (TOC) contents and (b) Vitrinite Reflectance (Ro) of selected North American and Pakistani shales (Data sources are given in Appendix 2-C).

Most of gas-bearing North American shales are predominated by organic matter of Type-II (marine), while the Pakistani shales are dominated by mixed-type of marine kerogen (Type II and III) as shown in Figures 2.5 to 2.6. However, a few data points for the Sembar and Lower Goru shales fall in the Type-III kerogen type, which supports the potential for gas production from these shales. Some researchers (Ahmed et al., 2012; Sheikh and Giao, 2017; US EIA, 2015) have estimated that the retained gas in the Sembar Shale is 0.002 bcm/m^3, which also suggests it is a strong candidate for shale gas exploitation. Due to a lack of sufficient data, gas volume calculations may not be possible for other Pakistani shales at this stage; any assessment made must be based upon the limited available data.

2.5.5 Porosity

As shown in Figure 2.10, minimum porosity for North American shales is 2% to 10% compared to 5% to 10% for Pakistani shales; maximum porosity for North American shales is 5% to 14% compared to 10% to 20% for Pakistani shales. Overall, the North American and Pakistani shales are similar in terms of porosity; as compiled in this study, some Pakistani shales (notably Patala and Ranikot) have higher porosities than the North American shales, though it also appears that porosities of Pakistani shales are known with a lesser degree of precision.

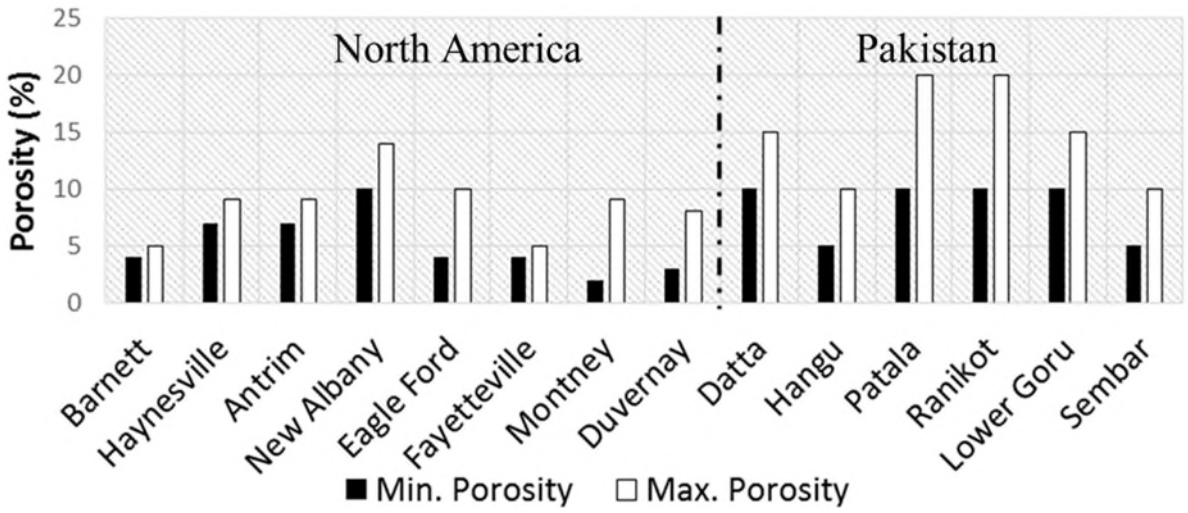

Figure 2.10 Porosities of selected North American and Pakistani shales (Data sources are given in Appendix 2-C).

2.6 Discussion

The data for North American shales suggest that geological age, depositional environment, depth nor thickness of shale serve as unique indicators of shale gas potential; both old (Devonian) and young (Miocene), deep marine and deltaic, deep (4268 m) and shallow (152 m), thick (915 m) and thin (4 m) shales are successful gas producers (see Appendix 2-C for details). As such, it is necessary to compare multiple factors. The six Pakistani shales studied here were deposited in shallow marine environments under anoxic conditions (Kazmi and Abbasi, 2008). This depositional environment is comparable with the Haynesville, Duverney, and Montney shales.

Moreover, due to the anoxic conditions, there is a good possibility of organic matter preservation that would support the occurrence of TOC values exceeding the 1% threshold for suitable shale gas reservoirs. Thermal maturity (desired Ro in the 1% to 3% range, or higher) and the amount of recoverable gas are directly proportional to burial depth and thickness of shale, respectively (Crain, 2016). Pakistani shales are generally deep and thick, which is favorable for thermal maturity and may or may not be better for a good recovery ratio. The Antrim Shale gas reservoir, which occurs at a relatively shallow depth compared to the Barnett Shale, has a recovery ratio (26%) higher than the Barnett (13.5%; expected to increase to 25% after improvement in horizontal drilling and hydraulic fracturing) (Editorial Board of "Series of Shale Gas Geology and Exploration and Development, 2009), although the other factors (e.g., adsorbed gas contents and formation pressure), are also linked with burial depth. Pakistani shales are already known to serve as source rocks for conventional gas reservoirs, which suggest the likely presence of gas in these shales.

There are no well-defined threshold values for porosity and permeability of a shale gas play. However, some researchers (e.g., Bratovich and Walls, 2016; Crain, 2016) recommend the study of porosity systems along with mineralogy within organic-rich shales to help in reserve estimation and stimulation design. In a continental shelf and shallow marine environment, the relatively high quartz content makes the shales more porous compared to shales from deep marine settings (Kennedy et al., 2016), so the Pakistani shales are expected to match - and in some cases exceed - the porosity of the North America shales. Comparisons of Ranikot and Montney shales (of shallow marine) reveal that intragranular pores are dominant in both shales, as shown in Figure 2.11, though other types of pores also need to be identified for better estimation of porosity.

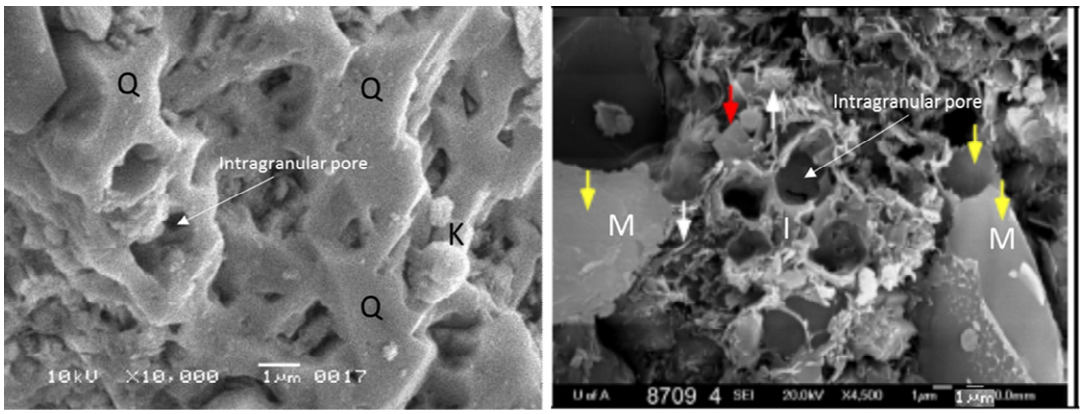

Figure 2.11 A thin section of Ranikot (left, Hakro et al., 2014) and Montney Shale (right, Anderson et al., 2010), Where Q=quartz, K=kaolinite, M=mica, I=illite, yellow arrows show micas, the red arrow shows dolomite, and the white arrows on Montney Shale show illite clusters.

Compared to the North American shales (porosities generally in the 5% to 10% range), the Pakistani shales have similar or higher values of porosity (up to 15%); this is favorable, but not sufficient to determine shale gas potential without studying other parameters such as permeability, Young's modulus and Poisson's ratio. Unfortunately, data for these parameters lack for Pakistani shales, hence indicating a need for future research.

Relatively high quartz contents (i.e., higher than approximately 50%) are favorable for hydraulic fracturing, as mentioned by Kennedy et al. (2016) when discussing the Barnett, New Albany and Antrim shales.

Figure 2.12 shows a graphical compilation of data assembled during this study. For the North American shales, the range for each property is shown separately for each shale. For the Pakistani shales, the overall range determined for all shales is shown as a dotted line for each property. The Pakistani shales compare favorably in terms of depth, thickness, TOC, Ro and porosity. Notable is the fact that permeability, Poisson's ratio and Young's modulus are available for the North America shales (as tabulated in Appendix 2-C), but not for the Pakistani shales. These missing parameters are critical to deciding the economic feasibility of a shale gas reservoir even if the shale formation is deep, thick, thermally mature, organically rich and porous. Once these properties have been measured and compiled, the North American data can be used as a basis for comparison.

2.8 Conclusion

- Pakistani shales are of shallow marine origins, so they should be compared with shallow marine shales of North America if such data can be accessed.

- There is some uncertainty in the characterization of Pakistani shales presented in this work due to the lack of certain types of data (e.g., elastic properties, permeability), so the preliminary assessments presented here should be revisited as the data gaps are filled.
- It is suggested that an integrated petrophysical and geomechanical characterization of Pakistani shales could lead to the successful exploration/exploitation of shale gas reservoirs in Pakistan.

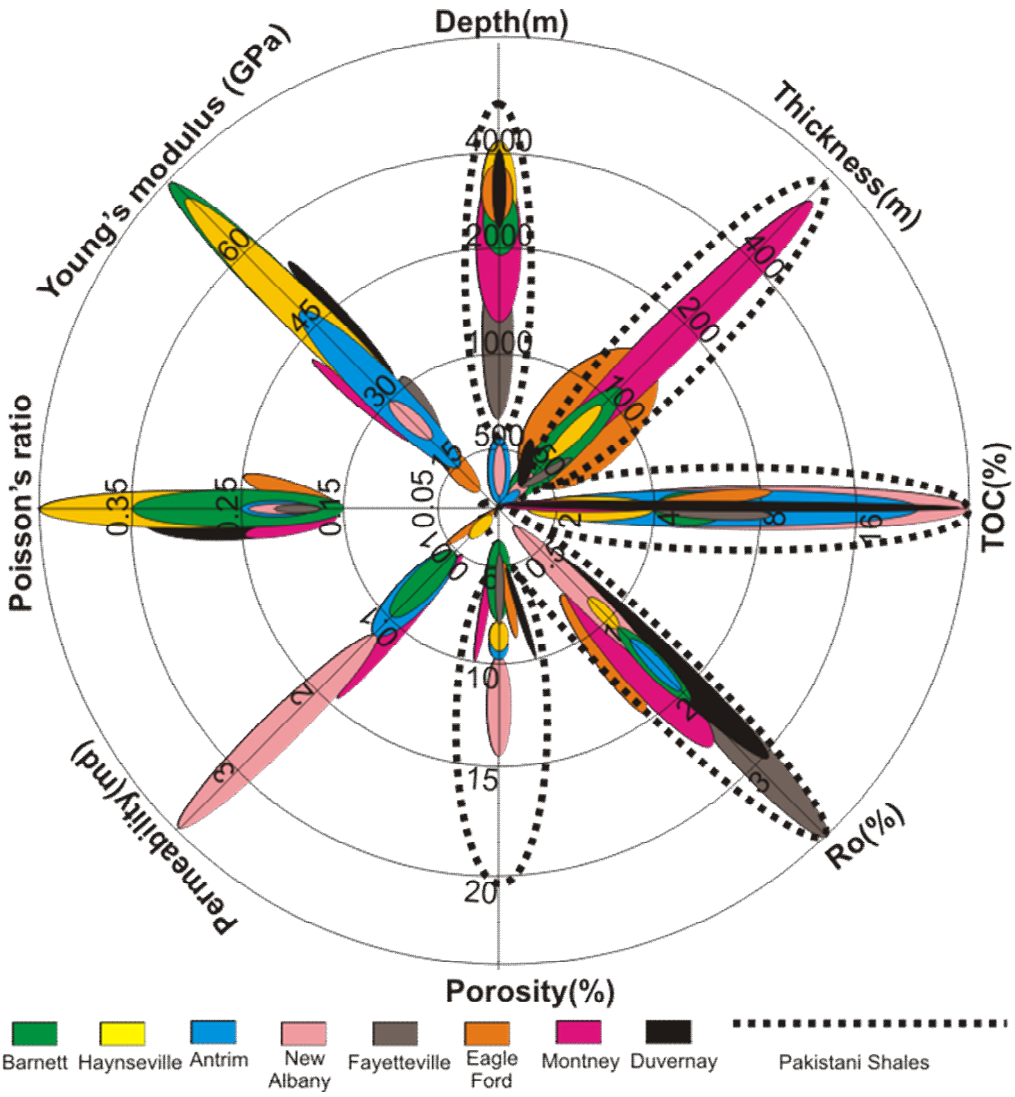

Figure 2.12 Composite plot comparing various attributes of selected North American shales (separately) and all Pakistani shales (combined) (Data sources are given in Appendix 2-C).

Acknowledgment

The authors acknowledge DGPC (Directorate General of Petroleum Concession) and HDIP (Hydrocarbon Development Institute of Pakistan) for giving wells data and the University of Saskatchewan, Canada, and University of Engineering & Technology, Lahore, Pakistan for facilitating this research. We are also thankful to Dr. Muhammad Asif (Petroleum Geochemist, Exxon Mobil, Texas) for giving suggestions to improve this study.

References

Abbasi, I. A., Haneef, M., Obaid, S., Daud, F., & Qureshi, A. W. (2011). Mesozoic deltaic system along the western margin of the Indian plate: lithofacies and depositional setting of Datta Formation, North Pakistan. *Arabian Journal of Geosciences, 5(3),* 471– 480. doi:10.1007/s12517-010-0276-1

Abbasi, A. H., Mehmood, F., Kamal, M., & Naqvi, S. (2014). Shale oil and gas: lifeline for Pakistan. A Report, Islamabad: Sustainable Development Policy Institute, Pakistan, 136 p.

Ahmad, N., Javed, M., Kashif, S., Mehmood, N., & Arif, F. (2012). *Shale gas potential of Lower Cretaceous Sembar Formation in Middle and Lower Indus sub-basins, Pakistan.* Search and Discovery, Retrieved May 7, 2018, from http://www.searchanddiscovery.com/abstracts/pdf/2012/90138papg/abstracts/ndx_ahmad04.pdf

Ahmadov, R. S., (2011). *Microtextural elastic and transport properties of source rocks* Ph.D. Thesis, Stanford University, (Retrieved 2016, from http://purl.stanford.edu/bt842hc0861)

Alexandre, T.J., (2015). Organic Matter-Rich Shale Depositional Environments, In: Rezaee, R. (1st edition), *Fundamentals of Gas Shale Reservoirs,* John Wiley & Sons, Inc.

Anderson, S.D.A., Rokosh, C.D., Pawlowicz, J.G., Berhane, H., and Beaton, A.P. (2010). Mineralogy, permeametry, mercury porosimetry, pycnometry and scanning electron microscope imaging of the Montney Formation in Alberta: shale gas data release; Energy Resources Conservation Board, ERCB/AGS Open File Report 2010-03.

Apotria, T., Kaiser, C. J., & Cain, B. A., (1994, January). *Fracturing and Stress History of the Devonian Antrim Shale, Michigan Basin, in Nelson,* P.P., and Lanbach, S.E., eds., Proceedings of 1st North American Rock Mechanics Symposium, 8, 809–816.

Arthur, D. J., Langhus B., and Alleman D., (2008). An Overview of Modern Shale Gas Development in the United States, A Report All Consulting Engineers, USA

Asif, M., (2010). *Geochemical Applications of Polycyclic Aromatic Hydrocarbons in Crude Oils and Sediments from Pakistan,* PhD Thesis, retrieved November 26, 2018, from http://prr.hec.gov.pk/jspui/bitstream/123456789/303/1/271S.pdf

Ayaz, A.S., Haider, A.B., Ismail, K., and Smith, M.P., (2012, March). *Unconventional Hydrocarbon Resource Plays in Pakistan: An Overview Awakening a South East Asian Sleeping Giant-Technological Solutions to Unlock the Vast Unconventional Reserves of Pakistan,* Proceedings of Geoscience Technology Workshop (GTW) on Unconventional Hydrocarbons, Singapore, 20–45.

Barrett, R., (2008, July). *The Depositional Setting of The Marcellus Black Shale*. Seminar conducted by Independent Oil and Gas Association of West Virginia,1–4.

Bracket, W., (2015). *How Marcellus and Utica Production Compares to Other Shale Basins (Natural Gas)*. A Webinar, Pennsylvania State University. (Retrieved March 30, 2016, from http://extension.psu.edu/natural-resources/natural-gas/webinars/how-marcellus-and-utica-production-compares-to-other-shale-basins)

Bratovich, W. M. and Walls, F., (2016). The Unconventional Basins and Plays-North America, the Rest of the World and Emerging Basins, In: Ahmed U. and Nathan M, D., (eds.), *Unconventional Oil and Gas Resources: Exploitation and Development,* Baker Hughes, Canada, p. 8–60.

Carr, R.T., Wang G., and McClain T., (2013, March). *Petrophysical Analysis and Sequence Stratigraphy of Utica Shale and Marcellus Shale, Appalachian Basin, USA,* International Petroleum Technology Conference, China, 2–12.

Corapcioglu, H., (2014). Fracturing Fluid Effects on Young's Modulus and Embedment in the Niobrara Formation, M.Sc. Thesis, Colorado School of Mines, USA

Crain, E. R., (2016). *Crain's Petrophysical Handbook* - Special Cases -- Gas Shales. 1p. (Retrieved March 30, 2016, from https://spec2000.net/17-specshgas.htm)

Dobson, P., (2014). *Prospective Application of Well Stimulation Technologies in California*, Report, California Council on Science and Technology. (Retrieved from https://ccst.us/publications/2014/2014wst4.pdf)

Dunn, L., Schmidt, G., Hammermaster, K., Brown, M., Bernard, R., Wen, E., Befus, R., and Gardiner, S., (2012, March). *The Duvernay Formation (Devonian): Sedimentology and Reservoir Characterization of a Shale Gas/Liquids play in Alberta, Canada*, Geo-Convention: Vision, Canada. 1–5.

East, A. J., Swezey, S. C., Repetski, E. J., and Hayba, O. D., (2012). Thermal Maturity Map of Devonian Shale in the Illinois, Michigan, and Appalachian Basins of North America, *U.S Geological Survey Bulletin*.1–25.

Editorial Board of "Series of Shale Gas Geology and Exploration and Development, (2009). New development of the shale gas exploration and development in North America. *Petroleum Industry Press*, Beijing.

Edwin, I. E., (2013). *Tight Gas Reservoir Characterization in Montney Formation, Northeastern British Columbia, Western Canada,* Ph.D. Thesis, Department of Earth and Atmospheric Sciences, University of Alberta, Canada.

Emadi, H., Soleiman, M., Samuel, R., Harville, D., and Gamadi, T., (2014, March). *Effect of Temperature on the Compressive Strength of Eagle Ford Oil Shale Rock: An Experimental Study*, IADC/SPE Drilling Conference and Exhibition, Texas, USA 1–9.

Eoff, D. J., (2013). Shale Hydrocarbon Reservoirs: Some Influences of Tectonics and Paleogeography during Deposition. In Geology of the Haynesville Gas Shale in East Texas and West Louisiana, *AAPG Memoir* 105, 5–27. (Retrieved 2016, from http://archives.datapages.com/data/specpubs/memoir105/data/5_aapgsp1950005.htm?doi=10.1306%2F13441842M1053597#aff1)

Eshkalak, O. M., Mohaghegh, D. S., and Esmaili, S., 2014, Geomechanical Properties of Unconventional Shale Reservoirs, *Journal of Petroleum Engineering*, 2, 10–12.

Ewing, T. E., (2001). Review of Late Jurassic Depositional Systems and Potential Hydrocarbon Plays of the Northern Gulf of Mexico Basin. *AAPG Bulletin*, 85, 85–96.

Franseen, K. E., Goldstein, H. R., and Doveton, J., (2014, June). *Depositional Controls on Distribution and Reservoir Character of Deep Water Deposits in the Permian Wolfcamp, Bone Spring, and Wolfbone Plays of the Delaware Basin,* Kansas Interdisciplinary Carbonates Consortium Prospectus, 1–25.

Goldhammer, R.K., (1998, April). *Second-order Accommodation cycles and points of Stratigraphic turnaround: Implications for high-resolution Sequence Stratigraphy and Facies Architecture of the Haynesville and Cotton Valley Lime pinnacle reefs of the East Texas Salt Basin*: Houston Geological Society Bulletin North American Explorationists Meeting, Houston, Texas, April, 27, 1–2.

Gul, A. M., Khan, S. M., and Sohail M. G., (2016). Evaluation of Shale Gas Prospect in Datta Formation, Upper Indus Basin, Pakistan, *Journal of Pakistan Institute of Chemical Engineers*, 44(1), 1–8.

Gupta, N., Rai, S. C., and Sondergeld H. C., 2013, Petrophysical Characterization of the Woodford Shale, *Petrophysics,* 54 (4), 368–382.

Haider, A. B., Aizad, T., Ayaz, A. S., and Shoukry, A., (2012, December). *A Comprehensive Shale Gas Exploitation Sequence for Pakistan and other Emerging Shale Plays,* Society of Petroleum Engineers (SPE) Annual Technical Conference, Islamabad, Pakistan, 1–21.

Hall, D. C., Jennings, D., and Miller, R., (2011). Comparison of the Reservoir Properties of the Muskwa (Horn River Formation) with Other North American Gas Shales, A Report, Core Laboratories, Houston, Texas, USA, 1-3.

Hakro, A. A., Baig, A. M., Baqri, R. S., and Khokhar, Q., (2014). Clay mineralogy of the Bara Formation exposed at Ranikot, Lakhra and in the subsurface of Thar coalfield, Sindh, Pakistan, *International Journal of Economic and Environmental Geology*, 5(2), 32–38.

Hakro, D. A. and Baig, A. M., (2013). Depositional Environment of the Bara Formation, Fort Ranikot Area, Sindh, *Sindh University Research Journal* (Science Series), 45 (1), 83–94.

Harris, B. N. and Dong T., (2013). *Characterizing porosity in the Horn River shale, Northeastern British Columbia,* in Geoscience Reports, British Columbia Ministry of Natural Gas Development, 40.

Hentz, T. F. and Ruppel, S. C., (2010, October). *Regional lithostratigraphy of the Eagle Ford Shale: Maverick Basin to East Texas Basin*: Transactions of the Gulf Coast Association of Geological Societies, Society of Economic Paleontologists and Mineralogists, Annual Meeting. 225–337.

Hovey, R. (2011).The Niobrara Shale. A Report, U.S.A: Energy Strategy Partners, 37.

Iqbal, M.W. A., and Shah, S.M.I., (1980). *A guide to the Stratigraphy of Pakistan, Geological Survey of Pakistan Records*. Geological Survey of Pakistan, Quetta, 53, 340-350.

Jalees, I. M., (2014). *Geochemical Segregation of Petroleum Systems of Potwar Basin using GC-MS and Pyrolysis Techniques,* Ph.D. Thesis, Department of Chemistry, University of Engineering & Technology, Lahore, Pakistan, 140.

Jansen, A. T., (2014). *The Effect of Rock Properties on Hydraulic Fracture Conductivity in the Eagle Ford and Fayetteville Shales,* M.Sc. Thesis, Texas A&M University, USA, 45.

Johnson, M. D., (2009). *A Perspective on Canadian Shale Gas,* National Energy Board: A Premier for Understanding Canadian Shale Gas. Canada. Retrieved from https://www.cer-rec.gc.ca/nrg/sttstc/ntrlgs/rprt/archive/prmrndrstndngshlgs2009/prmrndrstndngshlgs2009-eng.pdf.

Kadri, I. B., (1995). *Petroleum geology of Pakistan*. Karachi, Pakistan Petroleum Ltd.

Kazmi, A. H. and Abbasi, I. A., (2008). *Stratigraphy and historical geology of Pakistan*. Department & NCE in Geology, University of Peshawar, Pakistan.

Kennedy, R., Luo X. L., and Kussakra, V., (2016). The Unconventional Basins and Plays-North America, the Rest of the World and Emerging Basins, In: Ahmed U. and Nathan M, D.,(eds.), *Unconventional Oil and Gas Resources: Exploitation and Development,* Baker Hughes, Canada. 2–33.

Khalid, P., Yasin, Q., Sohail, M. G., Kashif, M., (2015). Integrating Core and Wireline Log Data to Evaluate Porosity of Jurassic Formations of Injra-1 and Nuryal-2 Wells, Western Potowar, *Journal of the Geological Society of India*, 86, 553–562.

Khan, S., (2012). *Biostratigraphy and Microfacies of the Cretaceous Sediments in the Indus Basin, Pakistan*, Ph.D. Thesis, The University of Edinburg, UK..

Kluessendorf, J. J., Mikulic, G. D., and Carman, R. M., (1988). *Distribution and Depositional Environments of the Westernmost Devonian Rocks in the Michigan Basin*, *Devonian of the World*: Proceedings of the 2nd International Symposium on the Devonian System — Memoir 14, Volume I: Regional Syntheses. 251–263.

LeFever, J. A., (1991). History of oil production from the Bakken Formation, North Dakota, in Hansen, W.B. (ed.), *Guidebook to Geology and horizontal drilling of the Bakken Formation*: Montana Geological Society. 9–17.

Lineback, J. A., (1968). Subdivisions and Depositional Environments of New Albany Shale (Devonian-Mississippian) in Indiana, *AAPG Bulletin*, 7, 1290–1302.

Loucks, R. G. and Ruppel, S. C., (2007). Missipian Barnett Shale: lithofacies and depositional setting of a deep-water shale-gas succession in the Fort Worth Basin, Texas. *AAPG Bulletin*, 92, 579–601.

Mastalerz, M., Drobniak, A., and Rupp, J., (2014). *Evaluation of Geological characteristics of the New Albany Shale as a potential liquids from shale play in Illinois Basin*, Eastern Unconventional Oil and Gas Symposium, Kentucky, USA, Nov. 5–7, 1–50.

McDonald, B. and Wright, T. H., (2016). *Completion Optimization in Fayetteville Shale Utilizing Rate Transient Analysis for Candidate Selection*, SPE Hydraulic Fracturing Technology Conference, Texas, USA, Feb. 9–11, 1–7.

Murphy, E., Warner, M., and Sarmah, B., (2013, August). *A workflow to Evaluate Porosity, Mineralogy and TOC in the Utica-Point Pleasant Shale Play*, SPE Eastern Regional Meeting, Pennsylvania, USA, Aug. 20–22, 1–20.

Nadaraju, G. and Elliott, D., (2010). Understanding Montney reservoir heterogeneity: A geoengineering approach, A Report, Encana Corporation, Calgary, Canada, 85-87.

Osamn, M. T, and Bilgesu I. H., (2015, October). *Impact of Geomechanical Properties on the Fracture Treatment of Utica Shale,* Society of Petroleum Engineers, Eastern Regional Meeting, West Virginia, USA 1–11.

Parker, M., Buller, D., Petre, E., and Dreher D., (2009, April). *Haynesville Shale Petrophysical Evaluation*, Rocky Mountains Petroleum Technology Conference, Colorado, USA 1–11.

Perry, F. V., Kelley, R. E., Dobson, P. F., & Houseworth, J. E. (2014). *Regional Geology: GIS Database for Alternative Host Rocks and Potential Siting Guidelines.* Report # FCRD-UFD-2014-000068. 168-170. (Retrieved July 10, 2016, from https://energy.gov/ne/downloads/regional-geology-gis-database-alternative-host-rocks-and-potential-siting-guidelines)

Reeves, R. S., Hill, D. G., and Cox, O. D., (1993). *Production Optimization in the Antrim Shale,* Production Operations Symposium, Oklahoma, USA 1–11.

Rickman, R., (2008, September). *A practical use of shale petrophysics for stimulation design optimization: All shale plays are not clones of the Barnett shale,* SPE Annual Technical Conference and Exhibition, Denver, Colorado, USA, SPE 115258-ms.

Rine, J. M. and Ginsburg, R. N., (1985). Depositional facies of a mud shore face in Suriname, South America: a mud analog to Sandy shallow-marine deposits. *Journal of Sedimentary Petrology*, 55, 633–652.

Rivera, S., Saidian, M., Godinez, J. L., and Prasad M., (2014, August). *Effect of Mineralogy on NMR, Sonic, and Resistivity: A Case Study of Monterey Formation,* Unconventional Resources Technology Conference (URTEC) Colorado, USA, 1–20.

Roberts, D. F., (2013). *Identifying and Mapping Clay-Rich Intervals in the Fayetteville Shale: Influence of Clay on Natural Gas Production Intervals,* M.Sc. Thesis, The University of Texas, Austin, 53.

Robison, C., Smith, M., & Royle, R. (1999). Organic facies in Cretaceous and Jurassic hydrocarbon source rocks, Southern Indus basin, Pakistan. *International Journal of Coal Geology, 39(1-3),* 205–225. doi: 10.1016/s0166-5162(98)00046-9

Rokosh, D. C., Beaton, A., Pawlowicz, J., Anderson, S., and Berhane, M., (2010). Mineralogy of Duvernay, Muskwa, and Montney Formations for Shale Gas Resource Evaluation, Report Summary, Geo-Canada /Alberta Geological Survey, 2.

Ruotsala, A. (1980). Mineralogy of Antrim Shale, Michigan. Report # FE-2346-79, Dow Chemical Co., Midland, MI, USA, 2. (Retrieved April 10, 2016, from http://www.osti.gov/scitech/biblio/5201912)

Saddique, B., Ali, N., Irfan, U., Hanif, M., Shah, A. S., Saleem, I., Faizi, M. M., and Yasir, M. A., (2016). Petrophysical analysis of the reservoir intervals in Kahi-01 well, Kohat Sub-Basin, Pakistan, *Journal of Himalayan Earth Sciences,* 49(1), 30–40.

Salehi, A. I., (2009). New Albany Shale Gas Project, A Joint Research Project, Annual Progress Report, Gas Technology Institute USA, 40.

Sarg, F. J., (2012). The Bakken – An Unconventional Petroleum and Reservoir System, Final Scientific/Technical Report, Colorado School of Mines, USA, 65.

Shah, M. S., Ahmad N., Ahmad N., and Ahsan N., (2013). The Mineralogical and Petrographical Studies of the Lithofacies of the Hangu Formation in the Salt Range, Punjab, Pakistan, *Pakistan Journal of Science,* 65(1), 142–149.

Shahzad, A., (2007). *Identification of Potential Hydrocarbon Source Rocks using Biological Markers in Kohat Plateau, North Pakistan,* M.Sc. Thesis, National Center of Excellence in Geology, University of Peshawar, Pakistan.

Sheikh, N., & Giao, P. H. (2017). Evaluation of shale gas potential in the Lower Cretaceous Sembar Formation, the Southern Indus Basin, Pakistan. *Journal of Natural Gas Science and Engineering,* 44, 162–176. Doi: 10.1016/j.jngse.2017.04.014.

Siddiqui, I. F., Adhami, A., Asghar, A., Hussain, A., and Khan, W. M., (2013). *Shale Gas Potential of the Lower Goru Formation over the Lakhra High in Lower Indus Basin, Pakistan,* AAPG Annual Convention and Exhibition, Pittsburgh, Pennsylvania, USA, 1–28.

Slatt, M. R., (2011). Important geological properties of unconventional resource shales. *Central European Journal of Geosciences,* 3 (4), 435–448.

Soeder, J. D., (2011). *Petrophysical Characterization of the Marcellus & Other Gas Shales*, AAPG Eastern Section Meeting, Arlington, Virginia, USA, 1–35.

Soltanzadeh, M., Fox A., and Rahim A., (2015, May). *Application of an Integrated Approach for the Characterization of Mechanical Rock Properties in the Duvernay Formation*, Geo-Convention, Calgary, Canada., 1–4.

Sone, H. and Zoback, D. M., (2013). Mechanical Properties of Shale-Gas Reservoir Rocks — Part 1:Static and Dynamic Elastic Properties and Anisotropy, *Geophysics, 78 (5),* 381–392.

Sunjay. (2011). *Shale Gas Exploration and Production*. In 12th International Congress of the Brazilian Geophysical Society & EXPOGEF, Rio de Janeiro. doi: https://doi.org/10.1190/sbgf2011-296

Ucok, H., (1988, October). *A Sensitivity Study on the Geological Factors Influencing the Oil Recovery from the Monterey Formation*, 63rd Annual Technical Conference and Exhibition of the Society of Petroleum Engineers, Houston, Texas, USA, 1–8.

US EIA., (2015). Technically Recoverable Shale Oil and Shale Gas Resources: Canada, India and Pakistan, A Report, Energy Information Administration (EIA), 42. (Retrieved 2016, from https://www.eia.gov/analysis/studies/worldshalegas/pdf/India_Pakistan_2013-15.pdf/

US EIA., (2011). Review of Emerging Resources: U.S. Shale Gas and Shale Oil Plays, A Report, Energy Information Administration, 105.

Walls, D. J. and Morcote, A., (2015). *Quantifying Variability of Reservoir Properties From a Wolfcamp Formation Core,* Unconventional Resource Technology Conference, San Antonio, Texas, USA, 1–10.

Walls, D. J. and Morcote, A., Dvorkin, J., (2016, July). *Describe the Elastic Rock Properties revealed by whole Core-CT Scanning of Samples from the Wolfcamp Formation*, Understanding Rock Properties, Oilfield Technology, USA, 60–64.

Walter, S., Beavis, K., Whibbs, C., Stricker, S., Preston, A., Jenkins, J., and Hein, F., (2016). *Recognizing Duvernay B-Carbonate Distribution and Its Potential Implications on Resource and Reserve Estimations,* AAPG Conference & Exhibition, Calgary, Canada, 1–2.

Wandrey, C. J., Law, B. E., and Shah, H. A., (2004). Sembar Goru/Ghazij Composite Total Petroleum System, Indus and Sulaiman-Kirthar Geologic Provinces, Pakistan and India, *U.S. Geological Survey Bulletin,* 2208-C, USA, 29.

Wang, Q. and Wang, L., (2016). Comparative Study and Analysis of the Development of Shale Gas between China and the USA, *International Journal of Geosciences, 7,* 200–209.

Wang, F.P., and Gale, J. F. W., (2009). Screening criteria for shale-gas systems: *Gulf Coast Association of Geological Societies Transactions, 59,* 779-793

Warwick, D. P., Javed, S., Tahir, A. S., Shakoor T., Khan, M. A., and Khan, L. A., (1995). Lithofacies and Palynostratigraphy of Some Cretaceous and Paleocene Rocks, Surghar and Salt Range Coal Fields, Northern Pakistan, *US Geological Bulletin* , 2096, 29.

Zhang, C., Dong, D., Wang, Y., & Guan, Q. (2017). Brittleness evaluation of the Upper Ordovician Wufeng–Lower Silurian Longmaxi shale in Southern Sichuan Basin, China. *Energy Exploration & Exploitation, 35(4),* 430–443. doi: 10.1177/0144598716687929.

Zoback, M., & Kohli, A. (2019). *Unconventional Reservoir Geomechanics: Shale Gas, Tight Oil, and Induced Seismicity*. Cambridge: Cambridge University Press. doi:10.1017/9781316091869.

Appendix 2-A: Thickness of shale intervals in studied formations of Pakistan, interpreted using GR log of each well

Basin	Formation	Well	Latitude (degrees)	Longitude (degrees)	Formation Top	Formation bottom	Formation Thickness	Shale Thickness	Shale Thickness in Literature
					Meter (m)	(m)	(m)	(m)	(m)
UIB	Datta	U1	33.23	71.51	4751	4795	44	6	6 to 70
		U4	33.20	72.08	4730	4894	164	44	
		U5	33.14	71.98	4572	4726	154	54	
	Hangu	U8	32.96	73.01	2747	2752	5	5	Not available
		U9	33.22	71.49	4424	4449	25	3	
		U10	32.97	72.66	2712	2729	17	10	
		U1	33.23	71.51	4475	4570	95	32	
		U3	32.87	71.94	2700	2750	50	5	
	Patala	U9	33.22	71.49	4203	4350	147	7	Not available
		U11	32.94	72.66	2603	2625	22	10	
		U12	32.95	72.66	2620	2647	22	27	
		U13	33.12	72.99	3052	3120	68	26	
		U1	33.23	71.51	4134	4268	134	33	
MIB/LIB	Sembar	M1	29.11	71.39	2324	2346	22	17	Not available
		M2	28.60	71.74	1040	1201	161	157	
		M3	30.40	70.46	1410	2167	757	550	
		M4	30.25	67.58	796	833	37	37	
		M5	28.14	69.96	3480	3530	50	50	
		M6	28.03	70.85	1641	1664	23	23	
		L6	27.46	69.34	3411	3550	139	80	
	Ranikot	M1	29.11	71.39	1683	1765	81	64	Not available
		ML1	25.27	68.17	270	1095	825	214	
		ML2	26.28	67.46	1250	2000	750	165	
		ML3	28.15	70.23	1520	1680	160	33	
		M2	31.19	71.52	1916	2135	219	85	
	Lower Goru	L1	26.98	69.20	2615	3639	1024	639	200 to 400
		L2	27.00	68.76	2500	3550	1050	795	
		L3	27.18	69.24	3084	3485	401	389	
		L4	27.02	68.93	2696	3440	744	640	
		L5	25.57	68.39	2598	2800	202	198	
		L6	27.46	69.34	2260	3410	1150	768	

Appendix 2-B: Geochemical Data for Pakistani shales (data source of relevant shale is mentioned in reference column)

Pakistani Shale	Location			Rock-Eval Pyrolysis							Vitrinite Reflectance (Ro) and Maceral Analysis			
			TOC	**S1**	**S2**	**S3**	**Tmax**	**GP =** S1+S2	**PI =** S1/S1+S2	**OI**	**HI**	**Ro**	**Petrographic Analysis**	**Kerogen Type**	**Reference**
			%	mg HC/g rock	mg HC/g rock	mg HC/g rock	^{0}C	mg HC/g rock	unitless	mg CO2/g TOC	mg HC/g TOC	%			
Hangu	Outcrop		2.3	0.14	0.39	1.1	427	0.5	0.26	49	17	0.5	Vitrinite (≥50%), Inertinite (<20%)	Marginally mature	Shahzad (2007)
			1.8	0.08	0.05	0.6	432	0.1	0.62	33	3	0.9	Vitrinite (≥50%), Inertinite (<20%)	III and IV	
			2	0.07	1.48	0	421	1.6	0.05	2	76	0.5	Vitrinite (≥50%), Inertinite (<20%) Liptinite (<5%)	Marginally mature	
	Well	**Depth**													
	U3	4692-94	2.3	7.78	5.78	-	-	13.56	0.57	-	257	-	-	II and III	Asif (2010)
Patala	Outcrop		2	0.04	0.08	0.4	433	0.12	0.33	22	4	-	-	-	Shahzad (2007)
			1.8	0.09	0.04	0.3	380	0.13	0.69	17	2	-	-	-	
			2.3	0.15	0.13	1.4	380	0.3	0.54	62	6	0.5	Vitrinite (≥50%) Inertinite (<20%)	II and III, marginally mature	
	Well	**Depth**													
	U12	2630	10	3	19	0.7	444	21	0.42	49	100		-	III, gas prone	Jalees (2014)
	U13	3062	5	0.5	6.5	0.7	440	11.5	0.3	220	200		-	III, minor oil and gas potential	
Datta	Outcrop		0.8	0.05	0.13	0.3	430	0.2	0.28	35	16	0.5	Vitrinite (≥50%) Inertinite (<5%)	Marginally mature	Shahzad (2007)
			1.1	0.24	0.31	0.3	430	0.5	0.53	30	20	-	Inertinite (≥50%) Liptinite (<5%) Vitrinite absent	II, oil window	
			1	0.04	0.1	0.3	432	0.1	0.29	32	10	0.7	Vitrinite (≥50%) Inertinite (<20%)	III, peak maturation	

													Liptinite (<20%)		
			TOC	**S1**	**S2**	**S3**	**Tmax**	**GP**	**PI**	**OI**	**HI**	**Ro**	**Petrographic**	**Kerogen Type**	**Ref.**
Datta	**Well**	**Depth**													
	U1	4605-07	1	0.05	0.36	1.06	426	0.41	0.12	106	36	0.5	-	II/III	Jalees (2014) and Author's work
	U5	4704-06	0.4	0.05	0.30	0.52	436	0.35	0.14	130	75	0.7	-		
	U4	4830-32	1.7	0.18	0.56	0.13	434	0.74	0.24	7.6	33	0.6	-		
Sembar	M5	3482	5.0	5.03	16.83	3.84	427	21.86	0.23	77	336	1	Vitrinite 5%, Inertinite 5%	II, Gas prone 25%, Oil prone 70%	Robinson et al., (1999) and Ahmed et al., (2012)
	L6	3509	2.62	2.85	7.37	4.21	426	5.47	0.52	161	281			II/III, wet gas window	
		3518	5.89	10.16	29.75	3.68	422	16.05	0.63	62	505				
		3520	9.48	6.57	33.91	1.93	431	16.05	0.41	20	358				
		3531	2.11	2.37	4.96	3.90	425	7.33	0.32	185	235	1.09	Vitrinite 25%		
		3559	2.09	1.66	4.72	4.88	423	6.38	0.26	233	226	1	-		
		3598	1.86	1.79	2.88	4.19	424	3.65	0.49	225	155				
	ML2	3477	1.92	-	4.52	-	-	-	-	-	-				
		3487	1.87	-	2.65	-	-		-	-	-				
Lower Goru	L6	2603	1.58	1.12	2.37	4.25	421	3.49	0.32	269	150	-	Vitrinite 10%	III, Gas prone	
		2618	1.77	1.24	4.41	3.28	425	5.65	0.22	185	249				
		2638	1.06	0.57	1.02	2.09	422	1.59	0.36	197	96				
		2653	1.69	0.69	1.26	4.18	438	2.38	0.29	247	75				
		2668	1.60	0.43	1.07	4.55	438	2.03	0.21	284	67				
		2738	1.72	1.36	2.33	5.31	424	3.69	0.37	309	135				
		2758	2.14	1.02	2.95	5.37	428	3.97	0.26	251	138				
		2798	2.00	1.73	2.96	4.97	426	4.69	0.37	249	148				
		2868	2.53	1.65	5.15	4.78	416	6.80	0.24	189	204				
		2898	1.98	0.91	2.13	6.12	429	3.04	0.30	309	108				
		2918	2.10	0.94	2.66	3.22	429	3.60	0.26	153	127				
		2958	2.36	1.47	3.09	3.90	426	4.56	0.32	165	131				
		2983	3.05	2.48	6.14	3.94	426	8.62	0.29	129	201				
		2990	3.24	2.34	8.83	3.36	428	11.17	0.21	104	273				
		3377	2.10	0.96	2.05	4.04	428	3.01	0.31	192	98	-	Vitrinite 5%		

		3399	2.71	1.55	1.76	4.34	416	3.31	0.47	160	65				
		3419	5.22	5.64	17.37	5.38	425	23.01	0.24	103	333				
		3452	3.43	3.32	6.07	5.48	428	9.39	0.35	160	177	-	Vitrinite 5%		

Depth is in meter (m)

S1 (milligrams of hydrocarbon per gram of rock) is an indication of free hydrocarbons (gas and oil) in the sample. S1 > 1 mg HC/g rock may be indicative of an oil show.

S2 (milligrams of hydrocarbon per gram of rock) shows the hydrocarbons result from the cracking of kerogen and high molecular weight free hydrocarbons that do not vaporize in the S1 peak.

S3 is an indication of the amount of oxygen in the kerogen and is used to calculate the oxygen index. Generally, S3 values >200 mg CO2/g rock are anomalously high, possibly due to high concentrations of carbonates that break down at temperatures <390°C and may or may not be valid.

GP generation potential

PI (production index) is indicative of the conversion of kerogen into free hydrocarbons or, in a general sense, the transformation ratio (Espitalié et al., 1977).
PI < 0.2: immature rocks, PI = 0.3–0.4: typical for samples in the petroleum window, PI > 0.5: may indicate the proximity of migrated hydrocarbons or trapped petroleum

HI (hydrogen index _mg generated HC/g of organic carbon) is normalized hydrocarbon content of a rock sample. Kerogen type information is derived from this value as Type I kerogens are hydrogen-rich, Type III kerogens are hydrogen poor, Type II kerogens are intermediate between Type I and Type III

OI (oxygen index _mg CO2/g of organic carbon) is the normalized oxygen content of a rock sample. Type III kerogens generally have higher OI than either Type I or II kerogens. However, the hydrogen content is the principal discriminating factor for oil or gas potential. OI may be increased by weathering or mineral matrix interactions, which elevate the S3 value. If TOC is <0.50 wt%, OI may be meaningless (Espitalié, 1982). OI correlates with the ratio of O to C, which is high for polysaccharide-rich

remains of land plants and inert organic material encountered as background in marine sediments. OI values range from near 0 to ~150. High OI values (>100) are an indicator of continental organic matter or immature organic matter from all sources.

Tmax pyrolysis temperature at which a maximum yield of generated hydrocarbons occurs _Tmax increases with increasing maturation. Tmax is the temperature of the maximum rate of evolution of S2 hydrocarbons (top of S2 peak). Tmax indicates the stage of maturation of the organic matter. Tmax values are affected by low organic matter content, where low S2 peaks are encountered. When the S2 value is <0.5 mg HC/g rock and the S2 peak does not have a definitive peak (i.e., is broad and flat), Tmax values may not be reliable. Also, organic-lean clayey sediments with S2 values as high as 2.00mg HC/g rock may have unreliable Tmax values (Espitalié et al., 1985). Tmax may be affected by the presence of heavy free hydrocarbons in the S2 peak, which may cause Tmax to be anomalously low (<400°C). Also, Tmax may be affected by reworked organic matter or salt ionization, which may cause Tmax to be anomalously high (>550°C). Tmax values and true Tmax temperatures vary with the temperature programming rate (Claypool and Reed, 1976) and are useful for approximating kinetic values. Tmax is a calibrated temperature and does not represent the true (absolute) temperature.

Appendix 2-C: Data for North American and Pakistani shales

Region	Formation	Age	Depositional Environment	Depth	Shale Thickness	TOC	Ro	Mineralogy			Φ	K	Poisson's ratio	Young's modulus	Remarks
				(m)	(m)	%	%	Quartz	Clay	Calcite	%	millidarcy	fraction	GPa	
USA	Barnett	Late Mississippian[1]	Deep marine[2,3] (Intrabasinal)	1980-2590[1]	30-185[1]	4-5[1]	1.3-2.1[1]	35-50[1]	20-40[1]	10-15[1]	4-8[1]	0.01-0.10 [2]	0.15-0.35[4]	20-80[4]	Brittle[1]
	Haynesville	Upper Jurrasic[1]	shallow marine[6]	3200-4100[1]	60-90[1]	1-4.5[1]	1.29-1.39[1]	25-45[1]	30-45[1]	15-40[1]	8-9[1]	0.0056[5]	0.12-0.40[4]	20-80[4]	Ductile[1]
	Antrim	Upper Devonian[8]	Deep marine[18]	180-670[7]	4-21[7]	1-20[7]	1.3-2.0[8]	50-60[9]	20-35[9] (illite) 5-10[9] (Kaol.)	-----	9[10]	0.011-0.22[11]	0.20-0.25[12]	15-53[12]	Brittle[9]
	New Albany	U.Devonian/L. Mississippian[8]	Deep Marine[17] (anoxic)	152-610[7]	15-30[7]	1-25[7]	0.35-1.50[8]	25-50[14]	30-55[14] (illite)	Variable [41]	10-14[7]	0.017-4[15]	0.20-0.25[16]	25-30[16]	Brittle[16]
	Marcellous	Devonian[1]	Shallow marine, Intrabasinal[21]	1200-2600[1]	15-60[1]	2-8[1]	1.3-2.4[1]	10-60[1]	10-35[1]	3-50[1]	4-8[1]	0.02-0.06[19]	0.10-0.26[20]	13-28[20]	Brittle[1]
	Fayetteville	Late Mississippian[1]	Marine shelf[13]	305-2100[1]	6-60[1]	4-9.8[1]	1.5-4.0[1]	20-60[1]	30-35[13]	1-8[13]	4-5[1]	0.0000857-0.00018[22]	0.209-0.227[22]	28-30[22]	Brittle[22]
	Woodford	U. Devonian/L. Mississippian[1]	Marine, Intrabasinal[24]	1525-2900[1]	5-76[1]	4-8[1]	1.2-2.8[1]	50-65[1]	30-35[1]	5-10[1]	5-6[1]	0.000045[23]	<0.16[24]	>28[24]	Brittle[24]
	Eagle Ford (mixed oil &	Lower Cretaceous[1]	Marine, Intrabasinal[28]	2134-3660[1]	30-145[1]	4-8[1]	0.7-1.8[1]	20-30[27]	0-4[27]	65-75[27]	4-10[1]	0.0001-0.01[26]	0.15-0.25[25]	14-17[25]	-------
	Niobrara (mixed Oil & gas)	Upper Cretaceous[1]	Transgressive marine[29]	915-4268[1]	15-91[1]	3[1]	0.5-1.4[1]	-------	5-10[29]	80-90[29]	7-12[1]	0.01-3[30]	0.18-0.27[29]	42-62[29]	Brittle[29]
	Utica (oil and gas)	Middle Ordovician[1]	Transgressive marine[31]	610-4268[1]	21-229[1]	0.3-2.5[1]	1.1-4.0[1]	10-20[32]	10-20[32]	45-50[32]	6-12[1]	0.000001[33]	0.2-0.25[32]	17-31[32]	-------
	Wolf camp (oil)	Permian[1]	Deep marine[34]	1676-3354[1]	457-793[1]	2-6[1]	0.8[1]	45-60[35]	30-40[35]	0-10[35]	2-10[1]	0.00002-0.008[35]	0.15-0.30[36]	30-50[36]	Brittle[1]
	Monterey (oil)	Miocene[1]	Deep marine[40]	2439-4268[1]	305-915[1]	5[1]	0.6-1[1]	50-80[39]	5-15[39]	0-10[39]	13-29[1]	0.001-1[38]	0.09[37]Dyn.	10-15[37] Dyn.	Ductile[38]
	Bakken (oil)	Late Devonian/Early Mississipian[1]	Shallow to deep marine[41]	2927-3170[1]	12-23[1]	9+[1]	0.6-1[1]	5-85[42]	25-95[42]	10-15[42]	8-12[1]	0.001-0.01[42]	0.07-0.45[43] Dyn.	5.9-7.3[43] Dyn.	Brittle[42]

Region	Formation	Age	Depositional Environment	Depth	Shale Thickness	TOC	Ro	Mineralogy (%)			Φ	K	Poisson's ratio	Young's modulus	Remarks
				(m)	(m)	%	%	Quartz	Clay	Calcite	%	millidarc			
Canada	Horn River	Middle Devonian[1]	Deep marine[44,45]	1982-2744[1]	38-137[1]	1-6[1]	2.2-2.8[1]	55-85[45]	20-30[45]	20-30[45]	4-8[1]	$1.04x10^{-10}$ -$1.99x10^{-7}$ (46)	0.18-0.24[46]	11-14[46]	Brittle[46]
	Montney (dry and wet gas)	Early Triassic[1]	Deltaic , shallow marine[47]	1494-3506[1]	45-305[1]	0.4-4[1]	0.8-2.5[1]	20-45[48]	0-5[48]	0-5[48]	2-9[1]	0.01-0.5[48]	0.15-0.25[49]	27-41[49]	Brittle[49]
	Duvernay (mixed oil & gas)	Upper Devonian[1]	Deep marine[50]	2500-3994[1]	20-70[1]	1-20[1]	0.6-2.9[1]	50-70[1]	15-30[1]	10-30[1]	3-8[1]	$3.9x10^{-4}$ (51)	0.20-0.30[52]	35-50[52]	Brittle[51]
Pakistan	Datta	Jurassic[53]	Shallow marine[53]	3600-4750[55]*	6-70[55]*	0.5-2[55]*	0.5-1.3[55]*	>50*	10-20*	-----	10-15[54]*	0.1-1.15*	------	------	Brittle[55]*
	Hangu	Early Paleocene[55]	Shallow marine[55]	2700- 4500*	3-32*	2-10[58]	0.81-1.3[58]	60-70[59]	<20[59]	-----	5-10[57]	1-4*	------	------	------
	Patala	Late Paleocene[62]	Shallow marine[62]	2600-4200*	7-33*	1-5.0[58]	1-2[58]	30-40[62]	25-30[62]	0-20[62]	10-20*	------	------	------	------
	Sembar	Lower Cretaceous[60]	Pro-deltaic, shallow marine[60]	750-3500*	17-550*	2-10[58]	0.85-1.5[58]	40-50[61]	30-40[61]	10-15[61]	5-10[61]	------	------	------	------
	Ranikot	Paleocene[63]	Fluviatile, shallow marine[63]	270-2135*	64-214*	2-3[58]	0.85-1[58]	60-70[63]	10-30[63]	0-5[63]	10-20*	------	------	------	------
	Lower Goru	Early Cretaceous[64]	Pro-deltaic , shallow marine[64]	2250-3650[64]	198-795* 200-400[64]	1-1.5[58]	2-3[58]	40-50[64]	40-45[64]	5-10[64]	10-15*	------	------	------	------

* calculated using wireline logs

1. Kennedy et al. 2016
2. Bruner and Smosna 2011
3. Loucks and Ruppel 2007
4. Sone and Zoback 2013
5. Parker et al. 2009
6. Ewing 2001
7. Arthur et al. 2008
8. East et al. 2012
9. Ruotsala 1980
10. US, EIA 2011
11. Reeves et al. 1993
12. Apotria et al. 1994
13. Roberts 2013
14. Mastalerz et al. 2014
15. Zuber et al. 2002
16. Salehi 2009
17. Lineback 1968
18. Kluessendorf et al. 1988
19. Soeder 2011
20. Eshkalak et al. 2014
21. Barrett 2008
22. McDonald and Wright 2016
23. Younane et al. 2007
24. Gupta et al. 2013
25. Emadi et al. 2014
26. Walls and Sinclair, 2011
27. Jansen 2014
28. Hentz and Ruppel, 2010
29. Corapcioglu 2014
30. Hovey 2011
31. Carr et al. 2013
32. Murphy et al. 2013
33. Osamn and Bilgesu 2015
34. Franseen et al. 2014
35. Walls and Morcote 2015
36. Walls et al. 2016
37. Perry et al. 2014
38. Ucok 1988
39. Rivera et al. 2014
40. Dobson 2014
41. LeFever 1991
42. Sarg, 2012
43. Ahmadov 2011
44. US, EIA (Canada) 2015
45. Harris et al. 2013
46. Hall et al. 2011
47. Edwin 2013
48. Rokosh et al. 2010
49. Nadaraju and Elliott 2010
50. Walter et al. 2016
51. Dunn et al. 2012
52. Soltanzadeh et al. 2015
53. Abbasi et al. 2012
54. Khalid et al. 2015
55. Gul et al. 2016
56. Warwicket al. 1995
57. Saddique et al. 2016
58. Haider et al. 2012
59. Shah et al. 2013
60. Wandrey et al. 2004
61. Ahmad et al. 2013
62. Jalees 2014
63. Hakro et al. 2014
64. Siddiqui et al. 2013

Chapter 3 - An Evaluation of Empirical and Rock Physics Models to Estimate Shear Wave Velocity in a Potential Shale Gas Reservoir Using Wireline Logs

This chapter has been copyrighted and published as a research paper in the Journal of Petroleum Science and Engineering.

Citation: Sohail, G. M., & Hawkes, C. D. (2020). An evaluation of empirical and rock physics models to estimate shear wave velocity in a potential shale gas reservoir using wireline logs. *Journal of Petroleum Science and Engineering*, https://doi.org/10.1016/j.petrol.2020.106666.

Contribution of the Ph.D. candidate

Ghulam Mohyuddin Sohail carried out the evaluation presented in this chapter, with technical review feedback provided by Dr. Christopher Hawkes during weekly meetings. Mr. Sohail wrote the manuscript, with review feedback provided by Dr. Hawkes.

Contribution of this chapter to the overall study

Shear wave velocity (Vs) data, which are essential in estimating elastic properties, were found to be lacking in the available dataset of a Pakistani shale, which was screened out in the previous chapter. Therefore, comprehensive research has been completed to determine methods for estimates of Vs.

3.1 Abstract

Shear wave velocity (Vs) is essential for determining the elastic properties of rocks, which are useful for shale gas reservoir characterization. Many investigators have developed empirical models of varying form and complexity, and simplified rock physics models for the estimation of Vs using conventional well logs and/or laboratory measurements on core samples. Other investigators have developed rock physics models and used them to estimate velocities based on fundamental rock properties such as mineralogy, pore geometry and fluid saturations. The selection of a suitable model based on well logs is challenging, especially in cases where cores are not available. This study evaluates various relationships in the literature for the estimation of shear wave velocity applied to sandy shale and shale intervals of the Lower Goru Formation, Lower Indus Basin, Pakistan. Some inputs (e.g., compressional wave velocity) are directly taken from conventional log measurements, while others (e.g., petrophysical and elastic properties) are estimated using available log and literature data. A statistical analysis has been used to quantify the difference between measured and predicted Vs. The results reveal that some empirical models can produce a coefficient of determination (R^2) of roughly 0.8 when cross plotted against measured Vs values, and R^2 values can be further increased by 10% to 20% if the coefficients are adjusted based on available Vs data. However, these models do not explicitly account for the mechanisms of velocity variations in sandy shale and shale due to pore geometry (aspect ratio), consolidation and fluid saturations in the manner that rock physics models do. The rock physics modeling conducted for this work demonstrated that the use of Biot's model (rather than Gassmann's model) for fluid substitution improved model performance for Vs estimation in gas-saturated sandy shale and shale of the Lower Goru Formation. Although statistical analysis showed this model to be slightly less accurate than the best empirical models (R^2 of approximately 0.77), it is suggested that the rock physics model should be reliable when applied to a broader range of saturations and lithologies in the Lower Goru Formation. Also, using the rock physics approach, model input parameters can be optimized using Vp (compressional wave velocity) data, which represents a significant advantage over the empirical models which require Vs data for optimization. The modified rock physics model is thus deemed to be the best option available at present for the study area, and it is suggested that it should be appropriate for use in other settings – assuming that Vp data are available and sufficient knowledge regarding rock lithology is available.

3.2 Introduction

3.2.1 Background

Shear wave velocities (Vs) (in addition to compressional wave velocities and bulk density) are required to calculate dynamic elastic properties which are used directly and/or via correlation to static properties for designing various operations (e.g., drilling, fracture stimulation; and enhanced oil recovery). However, shear wave velocities are not routinely logged. Several relationships, with varying degrees of complexity, have been developed for the estimation of shear wave velocities during the past few decades. Most of these relationships have been established using the field and/or laboratory data for a specific lithology from a given area. A few researchers have tried to include data from all over the world to establish a global relation for the estimation of Vs. Regardless of their origins, most relationships have shown a better fit (between estimated Vs and measured Vs) for conventional reservoirs compared to unconventional shale gas reservoirs. The lower degree of accuracy for Vs relationships in unconventional reservoirs is attributed to the complex effects of lithology, porosity, pore geometry, clay volume, reservoir consolidation, water saturation and organic carbon content on velocities in shale gas reservoirs; effects which have differing degrees of influence on the various log properties that are used as input parameters, hence hindering the effectiveness of relationships that depend on a limited number of inputs. The objective of this study is to evaluate empirical and rock-physics-based models (e.g., Xu and White, 1995) in a potential shale gas reservoir (sandy shale and shale intervals of Lower Goru Formation) using the full suite of logs for two wells from the Lower Indus Basin, Pakistan. No core samples were available to support this investigation.

3.2.2 Literature Review

Shear wave velocities are not routinely measured, hence they must often be estimated from available logs such as gamma-ray (GR), neutron porosity, bulk density, resistivity and compressional wave velocity (Vp). A few researchers (Picket, 1963; Tosaya, 1982; Castagna et al., 1985; Han et al., 1986; William, 1990; Greenburg & Castagna, 1992; Liu and Chen, 2012) have introduced linear relationships to estimate Vs using Vp, the volume of shale (Vsh) and porosity in clean and shaly sandstone. Marion et al. (1992) concluded that there

is an initial increase in Vp with Vcl (volume of clay) up to at about 30% in sandstone because clay particles reduce the porosity by filling the inter-grain pores (often observed with pore-filling clay). For higher clay contents (>40%, i.e., sandy shale and shale) the Vp decreases with increasing Vcl due to the loss of grain-to-grain contact and the development of a predominantly clay matrix. This increment of clay content in sandy shale introduces pores with a low aspect ratio and significantly affects both Vp and Vs (Eastwood and Castagna, 1983). The randomly distributed pore geometries (hence variable aspect ratios) of sandy shale reduce the velocities of shear and compressional waves, due to the abundance of soft (platy, micro-fracture) pores as compared to stiff (spherical) pores (Ruiz and Dvorkin, 2010).

The aspect ratio of pores is affected by many factors (lithology, deposition and diagenesis, pore pressure, fracture density, consolidation) (Nur and Simmons, 1969), and it is difficult to study all these parameters to quantify aspect ratios. Aspect ratios have been linked with porosity and volume of clay by using a back-propagation neural network (BPNN) to estimate velocities (Vp and Vs) (Yan et al., 2002). Although this technique was validated using field data for a shaly sandstone reservoir in the North Sea, the presence of organic matter and low porosity sandy shale/shale intervals in shale gas reservoirs may restrict its global applications.

Kuster and Toksoz (KT) (1974) established a relationship between elastic moduli of the rock matrix and aspect ratios and provided an opportunity to link Vcl and porosity to aspect ratio in an iterative fashion, to obtain a better match between recorded and estimated velocities. The KT model is valid for rocks with very low aspect ratios such as sandy shale and shale (Keys and Xu, 2002). It can also be integrated with fluid substitution techniques (Gassmann, 1951 and Biot, 1956), to study the fluid effect on elastic moduli and velocities, which are inherently affected by aspect ratios.

Sonic waves behave differently in clay-dominated sandy shale as compared to quartz-dominated shaly sandstone, so it is essential to accurately calculate the volume of clay and porosity from available logs to estimate Vs in a shale gas reservoir. Vernik (2016) observed that the most commonly used gamma-ray (GR)-based linear model ($Vsh = (GR_{log} - GR_{min})/(GR_{max} - GR_{min})$) with traditional GR thresholds (GRmin = 10 API and GRmax = 100 API) for the volume of shale (Vsh) overestimates the clay volume because clays in shale (e.g., illite) have higher GR values (GRmax = 230 API) as compared to shale matrix (a mixture of clays, silt and other minerals). An increment in the upper limit of GR

in the GR-based equation (230 API instead of 100 API) can give Vcl instead of Vsh for shales, particularly rich in illite. Similarly, porosity logs (neutron, density or sonic) may provide inaccurate estimates of porosity in the presence of clays and organic matter (Holmes, 2014 ; Crain, 2016). Crain and Holgate (2014) and Holmes (2014) suggest subtracting clay and kerogen-related porosity from log-based porosity in shale gas reservoirs to get actual porosity (effective porosity) of the shale fraction.

Xu and White (1995) combined the Gassmann and KT models and used a fixed aspect ratio for sand (0.12) and clay (0.03) to estimate Vs in shaly sandstone and sandy shale intervals of two wells (one with >2000m depth and a second with <1500m depth) drilled in the North Sea. The deeper of these wells contained well-consolidated formations and the shallower contained poor to well-consolidated formations. They obtained a good fit between predicted and estimated Vs using these fixed aspect ratios. However, this may not work for other areas or wells. Several researchers (Mavko et al., 2003; Yan et al., 2002; Ruiz and Azizov, 2011) have identified two issues with the Xu and White (1995) model: First, the use of the fixed values of aspect ratios, and second the Gassmann equation for fluid substitution. The pore geometry will generally not be constant over broad depth intervals (~100m), so the aspect ratios should be varied with depth. Ideally, these would be known, and it would be possible to confirm known values by direct observation. In practice, initial values of aspect ratios are assigned based on Vcl and these values are adjusted by iteration to obtain a match between recorded and estimated Vp (Yan et al., 2002).

Gassmann's theory assumes that the wave-induced pore pressures are equilibrated through the pore space, which may not be true for high-frequency sonic waves (Ruiz and Azizov, 2011; Chopra and Castagna, 2014), especially in low permeability rocks (e.g., sandy shale and shale). Biot (1956) suggested that there is not enough time for the pore pressures to equilibrate when high-frequency waves (ultrasonic laboratory-based) travel through the saturated rock, and this scenario may be especially true in the low-permeability flaky pores of a shale gas reservoir (Mavko et al., 2003). Two types of flow mechanism occur during the propagation of sonic waves (high and low frequency) through fluid-filled pores: Biot (global or average flow) and squirt (local, at the grain scale) flow. According to these mechanisms, the relative motion of fluid and solid leads to dispersion and attenuation of sonic velocities. Biot (1956) suggested that global flow is dominant at high frequencies (MHz range), while Mavko and Jizba (1991) suggested that squirt flow is dominant at transition frequency (kHz range). Sarker and Batzle (2010) conducted experiments on dry and n-decane (a liquid, and

a component of gasoline and kerosene) saturated shales in the laboratory and found there is a negligible impact of frequency in the range of 2 kHz to 800 kHz on the dispersion of anisotropic elastic moduli. Siggins and Dewhurst (2010) suggested that the mechanism of velocity dispersion and attenuation in shales is enigmatic, and it is not clear yet that the squirt model applies to clay-rich shale.

Biot also includes a tortuosity parameter (α, similar to aspect ratio) that defines the geometry of pores. Stoll (1977) recommended a fixed value ($\alpha = 3$) for randomly distributed pores of any shape, although Mavko et al. (2003) recommend revisiting this fixed value for sonic waves recorded at transitional frequencies.

It is suggested here that the replacement of Gassmann with the Biot's equation (high-frequency solution) for fluid substitution, and relating the aspect ratios in KT theory with Vcl and porosity may give a better estimate of shear wave velocity in shale gas reservoirs. Although the application of Biot's equations (at ultrasonic frequency in MHz) for the prediction of sonic velocities (with kHz frequency) is still under debate, partly because the sonic frequency is well below the characteristic frequency (fc) of Biot's theory in shale gas reservoirs and also because, the Biot or squirt flow mechanism in clay-rich shale or sandy shale remains enigmatic (Mavko et al., 2003; Avseth et al., 2005). The authors feel it is worth considering, and thus it (Biot's high-frequency equations) has been tested for Vs estimation as an alternate of Gassmann in this work.

3.2.3 Geology of the Study Area

The study area chosen for this work is shown in Figure 3.1a. It is of interest because of the potential for shale gas development in this area (US EIA, 2015; Abbasi et al., 2014). It is located in the Lower Indus Basin of Pakistan, several hundred kilometers south of the tectonically active zone, where the Indian and Eurasian plates have collided. The area is bounded by two local Highs (Mari Kandkot in the North and Jacobabad in the South) that were developed due to western rifting of the Indian Plate, and which have played important roles in developing subsurface structural traps and high-temperature gradients (5 °C/100 m) (Ahmad and Chaudhry, 2002). The Cretaceous-age Goru Formation was deposited in a shallow marine environment, and its lower part (Lower Goru Formation or LGF) contains sandstone and shale strata (Kazmi and Jan, 1997). The sandstones were deposited in lower to inner and middle to inner shoreface settings, and the shales were deposited in pro-deltaic

to outer shelf environments (Siddiqui et al., 2013; Baig et al., 2016). The thickness of the LGF varies from roughly 250 m to 400 m in the study area, as shown in Figure 3.1b. The LGF has conformable contacts with the overlying Upper Goru Formation and underlying Sembar Formation, as shown in Figure 3.1c (Kadri, 1995; Kazmi and Abbasi, 2008). The presence of shales within the LGF provides seal and source rocks for sandstone reservoirs within this formation. The Early-Cretaceous Sembar Formation is also known to be a source rock in this area (Siddiqui et al., 2013). The LGF has been divided into several members listed (youngest to oldest) as follows; Upper Sands, Upper Shale, Middle Sands, Lower Shale, Upper Basal Sands, Talhar Shale and Lower Basal Sands. The Middle and Basal Sands are known gas reservoirs and are composed of medium to coarse-grained sandstones with minor siltstone (Kazmi and Abbasi, 2008).

The sandstone intervals of the LGF in the Lower Indus Basin are composed of quartz, feldspar, calcite, chlorite, illite, glauconite and volcanic rock fragments (Berger et al., 2009). The shales of the LGF in surrounding wells of the study area are composed of 40-50% clay, 40-45% quartz and 8-10% carbonates. Total organic carbon (TOC) content is typically 0.5% to 2%, consisting of Type II and III kerogen with vitrinite reflectance (Ro) of 0.5% to 0.55% (can produce both oil and gas) (Ehsan et al., 2016; Siddiqui et al., 2013). The thickness and average porosity of shale intervals of the LGF vary from 80 to 100 m and 10% to 12%, respectively, and in the south of the study area these shales contain montmorillonite which has a high capacity for gas absorption (Ehsan et al., 2016; Smith et al., 1992). The sand intervals of the LGF in the study area (Upper and lower Basal sands) contain chlorite and illite minerals. The illite may be formed by conversion of kaolinite or from precipitated components of k-feldspar dissolution during deep burial and elevated temperatures (Baig et al., 2016). The shale and sandy shale intervals between the Upper and Lower Basal Sands also contain chlorite and authigenic illite.

3.3 Methodology

3.3.1 Data Description

Two wells (labeled X and Y in Figure 3.1a) were studied in this work. Gas has been discovered in well X in a conventional sandstone reservoir (Basal Sands of the LGF), and gas shows in the LGF were observed during drilling of well Y. Both wells were drilled using water-based mud. These wells were chosen for this work based on log data availability in

the LGF, and because of their potential as shale gas reservoirs. The sonic logs used in this study were acquired using the dipole shear sonic imager tool (DSST) in both studied wells which operate in the frequency range of 8 kHz to 30 kHz. The specific outputs used were the monopole P (DT4P) and monopole S (DT4S) interval transit times. It is generally believed that a properly processed, full-waveform monopole log from this type of tool gives reliable estimates in fast formations such as "sandy shale" and "silty shale" if the borehole conditions are good. However, where the shear wave velocity drops to near 1500m/s (the speed of sound in drilling mud (water-based)), the shear wave arrivals become difficult to detect and the interpreted Vs is considered unreliable (Schlumberger, 2011). There was a small interval at the top of well-Y (3530-3560) where Vs falls near to 1500 m/s, and the data for this interval was discarded. The Vs logs in the shaly intervals of both wells seem reliable, and invasion corrections were deemed unnecessary.

Unfortunately, no cores were available for the sandy shale and shale intervals in these wells, so the petrophysical parameters required for this work (Vcl, TOC/volume of kerogen, effective porosity, and fluid saturation) were determined exclusively from log data, using the equations given in Table 3.2. More discussion of this process is given in the sections that follow. The approach adopted here was to extract core-based petrophysical parameters (acquired in nearby wells) of the LGF from literature and to fine-tune the estimated values based on a match between estimated and measured velocities (Vp and Vs) in the studied wells.

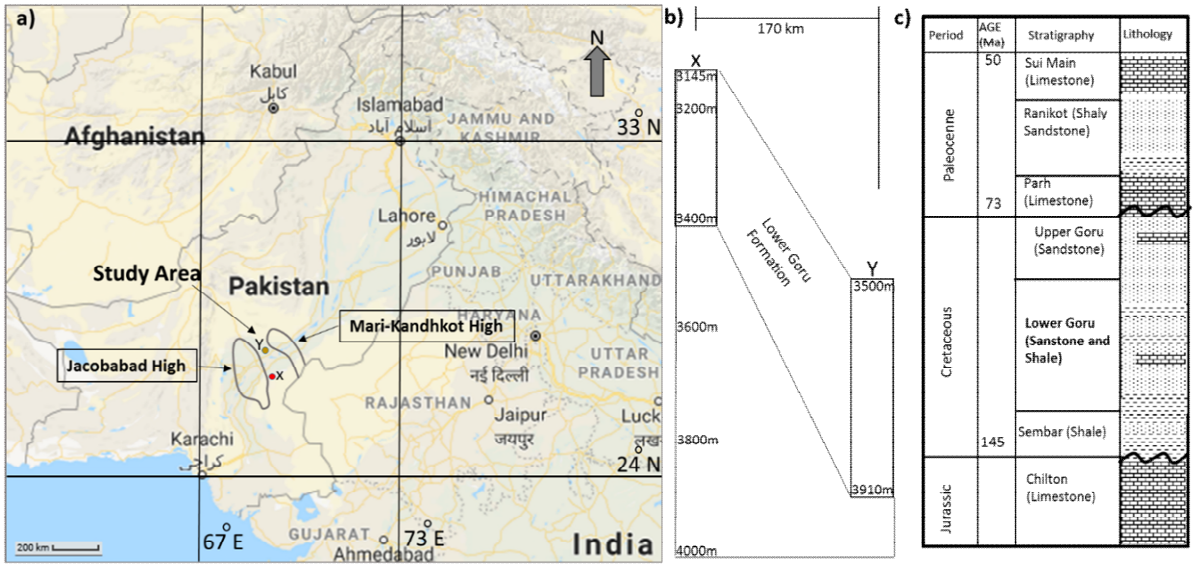

Figure 3.1 a) Location of study area (after Google Maps) ; including the locations of wells X and Y, b) top and bottom depths of the Lower Goru Formation in wells (X and Y) ; and c) generalized stratigraphy of study area (modified after Azeem et al., 2017).

3.3.2 Assessment of Lithology and Depositional Environment of the Lower Goru Formation

Berger et al. (2009) conducted a detailed mineralogical analysis of a sandstone interval in well-X (3260-3340 m). This interval is dominated by quartz and clay, with minor quantities of other minerals (dolomite, k-feldspar, micas and glauconite) and pore-filling cement comprised of chlorite and illite (Berger et al., 2009). An XRD (X-ray diffraction) analysis of drill cuttings over the lower interval of LGF in well-Y (3908-3910 m) showed higher quartz and illite contents with minor k-feldspar, dolomite and micas, which is in agreement with published data on LGF mineralogy.

In the absence of core and thin section data, the lithologies and depositional environments have been assessed using wireline and mud log data. The cross plot of density and neutron logs shows the presence of shale contents in studied intervals of both wells (Figure 3.2). The high density and gamma-ray values (~2.77 g/cc and >150 API respectively) on Figure 3.2 also gives some support to the presence of significant illite content in the shale and sandy shale intervals of the LGF. The cross plot between total porosities from density and neutron logs (as illustrated in Figure 3.3) shows most of the data points are fall near the left corner of the plot, which is the zone for dispersed shale. Some points above the dispersed shale zone are interpreted to be due to the presence of gas in the sandstone interval of well-X.

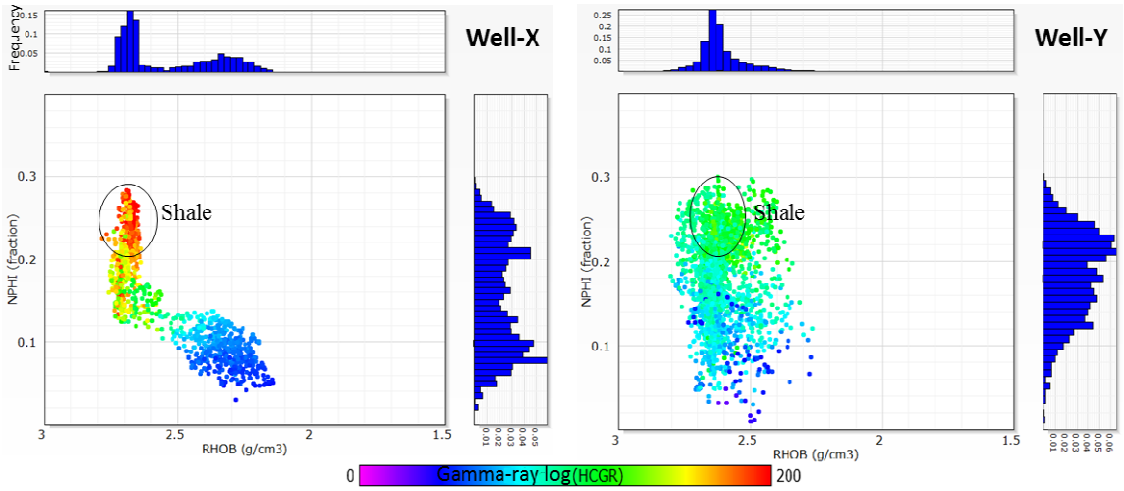

Figure 3.2 A cross plot between NPHI (neutron log porosity) and RHOB (bulk density log) color-coded with gamma-ray log to assess the lithology of the Lower Goru Formation in wells X and Y. Frequency histograms show data distribution. Note the presence of a significant number of data points in the cross plot zone typically interpreted as shale.

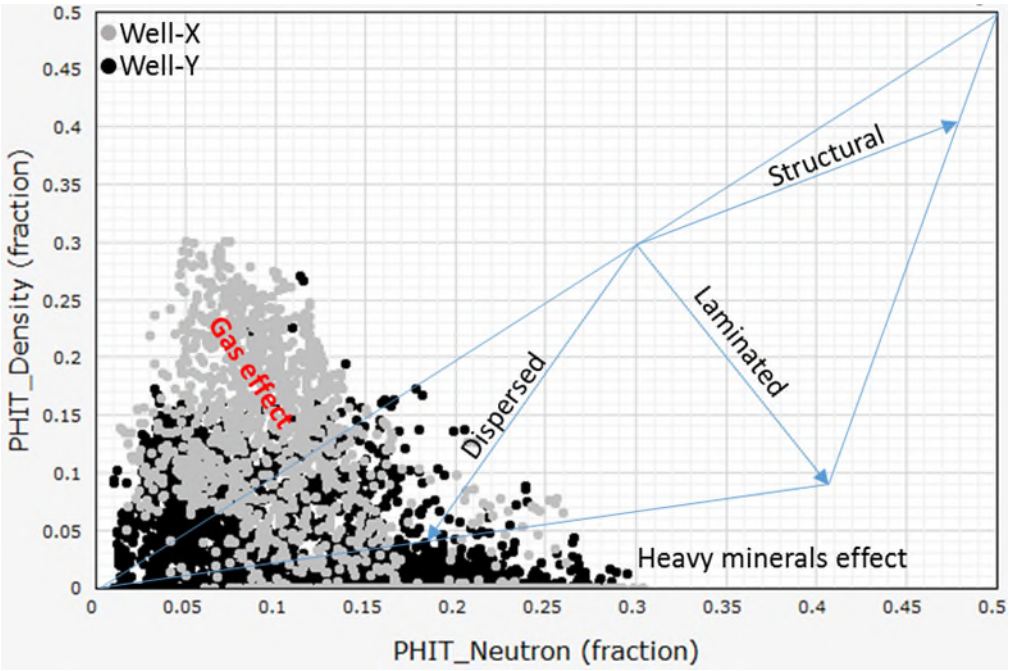

Figure 3.3 Neutron porosity (PHIT_Neutron=NPHI) vs. Density porosity (PHIT_Density = (matrix_density-RHOB)/(matrix_density-fluid_density)) cross plots showing distribution of shale in the Lower Goru Formation. Note that a significant number of the data points fall in the dispersed shale zone.

The gamma-ray and sonic logs based on the standard rock-physics templates of Avseth et al. (2005), adapted to the LGF of Lower Indus Basin by Nazeer et al. (2016), were used to assess depositional environment and lithologies. These are summarized in Table 3.1. Based on these templates, the Lower Goru Formation encountered in Well-X (3150-3400m) and Well-Y (3500m to 3910m) is classified as sandstone/shaly sandstone, sandy shale and shale. The results compare favorably to the core-based interpretation of lithologies and depositional environment of the LGF published by Nazeer et al. (2016) in the study area.

3.3.3 Assessment of Shale and Clay Volumes

The volume of clay (Vcl) affects the porosity of sandy shale and shale, and it affects the estimation of the velocity of shear and primary waves (Vernik, 2016). In petrophysics, the volume of shale (Vsh) is the fraction of bulk rock matrix which consists of a mixture of clay and silt. The volume of shale can reach 100%, but the volume of clay will generally be less than 100% due to the presence of silt particles (Vernik, 2016).

Table 3.1 Lithology prediction based on the GR log motif and recorded Vp (shown in the results and discussion section) (modified after Nazeer et al., 2016)

Recorded Attributes	Well-X Depth Range (m)	Well-Y Depth Range (m)	Lithology/Facies	Depositional Environment
• GR_log Funnel shape, low GR values (<75API), low Vp values • Serrated intermediate GR (75-100 API), high Vp values	3270-3340	3850-3910	Sandstone with coarse grain shaly sandstone	Upper to Lower Shoreface
Serrated high GR (100-120 API), low Vp	3200-3240	3660-3850	Sandy shale	Inner Shelf to Outer Shelf
Serrated very high GR (>150 API), low to high Vp values	3150-3200, 3240-3270, 3360-3370	3560-3660	Shale/Silty shale	Outer Shelf

The GR log can generally be used effectively for volume of shale interpretation in organically lean shales, but it is less effective in organically-rich shales because the presence of radioactive organic matter distorts the results (e.g., uranium salts associated with kerogen cause the higher values of GR) (Katahara, 1995; Passey et al., 2010). The TOC values interpreted from logs (TOC_DlogR, see Table 3.2 and Appendix 3-A) for the LGF shales are in the range of 2% to 4%, which compare favorably to laboratory-based TOC values of 1% to 3% published by Siddique et al. (2014). This range of TOC seems to have a negligible influence on the GR log (Wang and Carr, 2012). According to Vernik (2016), clay minerals (specifically illite) have high values of GR so the threshold limits of GR for the calculation of clay volume (Vcl) in illite-rich shale should also be increased (GR_max = 230 API rather than 100 API). The increase in the lower limit (GRmin = 30 API rather than 10 API) improves the data normalization, which also confirms the presence of a minor quantity of glauconite (mica group). As such, the Vernik's approach was tested in this work using multiple models (Clavier et al., 1971; Stieber, 1970; Larionov, 1969) for the estimation of Vcl (see Table 3.2 for equations). The results are shown in Figure 3.4. In the first case (GRmin = 10 API and GRmax = 100 API) the volume of clay becomes 100% for GR values of 100 API or greater in both wells. This scenario is not consistent with published mineralogies for the LGF. In the second case (GRmin = 30 API, GRmax = 230 API), Vcl ranges from 30% to 80% in well X and 10% to 65% in well Y. These Vcl ranges are

consistent with published data of Vcl. The use of the linear model along with Vernik's (2016) GR thresholds for Vcl yielded the best comparison between measured and estimated Vcl.

A complex mineralogy analysis using a software package (Schlumberger Techlog Quanti_Elan module) was conducted based on sonic, density, neutron, gamma-ray, photoelectric effect (PEF), and resistivity logs. The input minerals were decided based on published mineralogy of LGF (dominant minerals are illite, kaolinite, dolomite, and quartz) in the study area. The same input logs were predicted based on input mineralogy and fluid (clay bound water, free water and gas), and the best match between the input and predicted logs were obtained through a few iterations of fixed log values for input minerals. These iterations are attributed to varying minerals endpoints (specific value of log reading for each mineral), maximum volume based on published data, uncertainties factors, different types of sonic and neutron porosity models. The conversion of the weight percentage of minerals to volume percentage was performed within the software using values of grain density and porosity available within the software, although it is more appropriate to extract these values from XRD analysis of core samples. The results are shown in Figure 3.5, which confirms the dominance of clay (particularly illite) and quartz minerals in both wells.

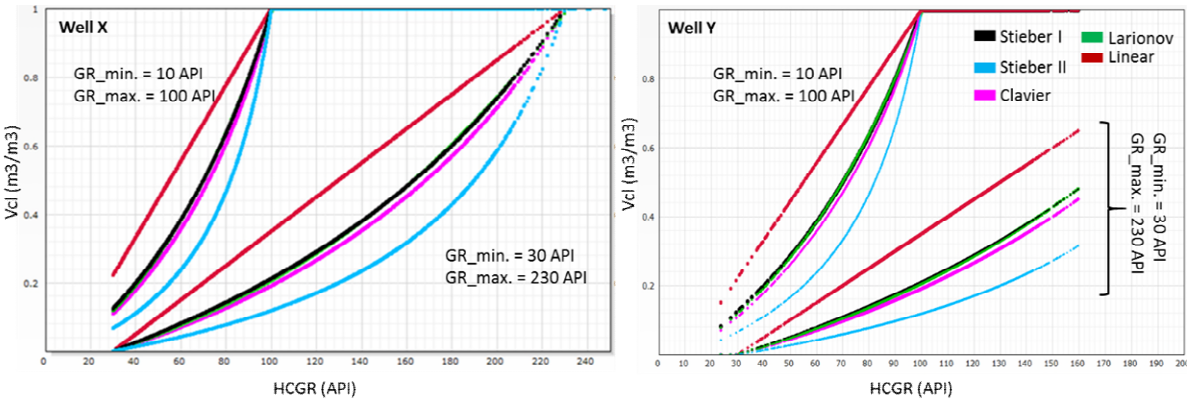

Figure 3.4 Cross plot between the estimated volume of clay (Vcl) and gamma-ray log for well X and Y, based on various models which are described in Table 3.2. (HCGR: computed gamma-ray corrected for Uranium (= HSGR - GR_uranium), where HSGR stands for Hostile Environment Standard Gamma Ray).

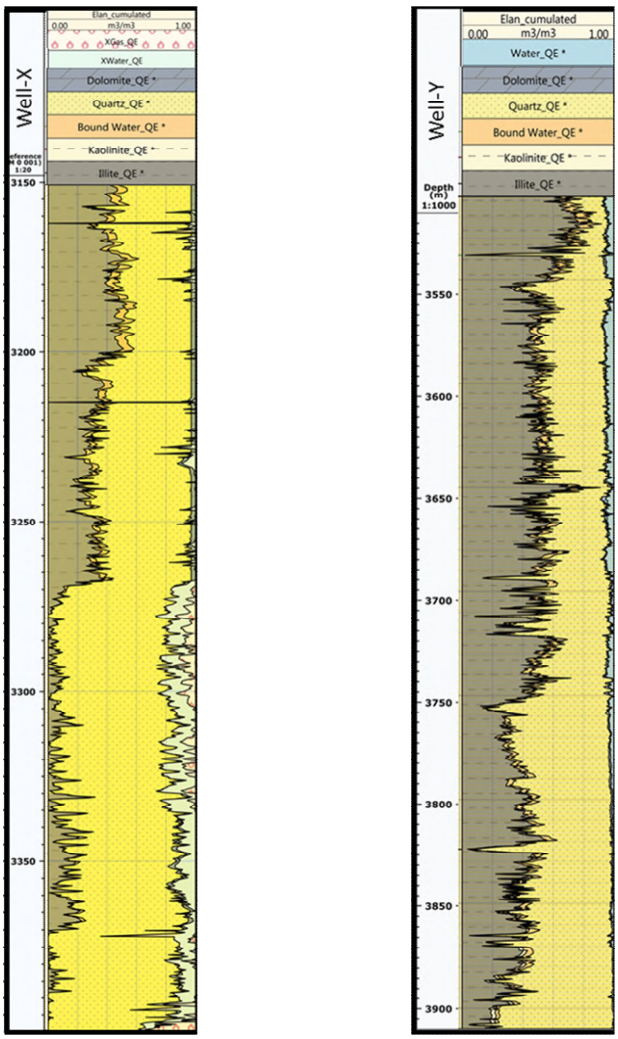

Figure 3.5 Shows the results of complex mineralogy analysis using Quanti_Elan.

3.3.4 Assessment of Porosity

Porosity also has a significant impact on velocities. When measured by logs, porosity is affected by various factors; e.g., volumes of clay and kerogen, fluid saturations and mineralogy. The best practice is to select logs that are least sensitive to these factors and to use interpretation techniques that correct for them. The low hydrogen index (HI) of gas reduces the neutron porosity and increases the density porosity, while the hydroxyl ions (OH^-) in clay minerals tend to increase the neutron porosity. As such, the combined use of these logs (e.g., interpreted porosity = average of neutron and density porosities) is often used (e.g., Passey et al., 2010) with the expectation that errors will largely offset one another. As such, the combined use of neutron and density logs has been implemented in some North American shale gas plays for porosity estimation. However, the complex lithologies, organic richness (high TOC) and clay bound water have proven to have negative impacts on the accuracy of porosity estimation (Glorioso and Rattia, 2012; Crain and Holgate, 2014).

Moreover, in the presence of gas, the density and the neutron tools may not read the same saturation due to different depths of investigation (Crain, 2016).

Another approach to porosity estimation from logs is the combined use of density and resistivity logs. Porosity interpretation in such cases requires accurate knowledge of formation mineralogy (e.g., glauconite affects both logs), water saturation, high-density mineral content (e.g., pyrite), low-density kerogen content and shale heterogeneity (Sondergeld et al., 2010; Wu and Aguilera, 2013). As such density-resistivity porosity may also be ineffective for the LGF due to poor control on mineralogy (unavailability of measured mineralogy data at multiple points in the studied wells) in its shale intervals.

The sonic log is also affected by multiple factors. Specifically, an increase in organic matter content increases the transit time of a sonic log because the organic matter is relatively soft, though an increase in thermal maturity of organic matter decreases the sonic transit time due to the expulsion of hydrocarbons. As such, sonic porosity also needs a correction based on the organic matter before use in shale gas reservoirs (Sondergeld et al., 2010; Glorioso and Rattia, 2012). The commonly used model of Wyllie et al. (1950) for the calculation of sonic porosity assumes the layered distribution of matrix and pores with layers oriented normal to the direction of wave propagation, whereas Raymer et al. (1980) account for the more evenly distributed nature of these phases (Dvorkin, 2008). A detailed discussion of these models is beyond the scope of this paper. Both methods were used, as shown in the porosity section of Table 3.2, and the results were compared.

It seems that log-based techniques of porosity estimation, which were initially designed for conventional sandstone reservoirs, may not work well for shale gas reservoirs. Some researchers suggest the use of these conventional relationships for shale gas reservoirs after applying corrections for clays and kerogen (Holmes et al., 2014; Crain, 2016). The neutron-sonic corrected porosity (effective porosity) as described in Table 3.2, is moderately insensitive to mineralogy and compensates for kerogen, and may work best as input for fluid substitution in gas-saturated sandy shales or shales (Crain and Holgate, 2014). The aforementioned models for total porosity estimation (sonic, density, neutron-density and neutron-sonic) were also tested for the fluid substitution model in this work, and the results are discussed later in this paper.

3.3.5 Assessment of Fluid Saturation

The fluids present in the LGF in wells X and Y are interpreted to be water and gas, according to drilling data (gas-cut drilling mud) for both wells and production data for well X. There are various log-based models (Indonesian, Dual Water, Simandaux, Waxman-Smits, Juhasz) for determining water saturation (Sw) in conventional sandstone reservoirs. These models tend to overestimate Sw due to high conductive clay contents in sandy shales and shales (Kadkhodaie and Rezaee, 2016). In conventional reservoirs, the current flows through formation water only while in shale gas reservoirs the current can also flow through interconnected clay particles (Rezaee, 2015). The modified Simandaux-model (Entyre, 1993) was selected in this work because it gives a reasonable Sw (40%-60%) in the sandy shale and shale intervals of the LGF as compared to other models which predict 100% water saturation in the shale intervals.

Table 3.2: Equations and workflow for log-based petrophysical interpretation

Volume of Shale from GR Log:

V_{sh} = volume of shale (Using the GR thresholds of Vernik (2016) this volume of shale considered equivalent to V_{cl} (volume of clay)).

$IGR = (GR_{log} - GR_{min})/(GR_{max} - GR_{min})$

$V_{sh} = 0.33 * (2^{2*IGR} - 1)$ .....(Larionov, 1969)

$V_{sh} = \frac{IGR}{2-IGR}$ .....Stieber I (Stieber, 1970)

$V_{sh} = \frac{IGR}{4-3*IGR}$.....Stieber II (Stieber, 1970)

$V_{sh} = 1.7 - \sqrt{3.38 - (IGR + 0.7)^2}$ .....(Clavier et al., 1971)

$V_{sh} = IGR$.....Linear Model (Katahara, 1995; Vernik, 2016)

Where:

GR_{log} = computed gamma − ray log (HCGR)

GR_{min}, GR_{max} = minimum and maximum values of GR (See text for discussion and values used)

IGR = gamma − ray index

Volume of Kerogen (Crain and Holgate, 2014):

$W_{TOC} = TOC_{DLogR}$, $W_{ker} = \frac{W_{TOC}}{KTOC}$, $Vol_{ker} = \frac{W_{ker}}{\rho_{ker}}$, $Vol_{matrix} = \frac{1-W_{ker}}{\rho_{matrix}}$,

$Vol_{rock} = Vol_{ker} + Vol_{matrix}$, $V_{ker} = \frac{Vol_{ker}}{Vol_{rock}}$

Where:

$TOC\_DLogR =$ total organic carbon, computed using DeltaLogR technique

(See Appendix 3-A, equation A)

$W_{TOC} =$ TOC weight fraction

$KTOC =$ weight fraction of carbon in kerogen

(0.80 is a common value which was assumed in this work)

$W_{ker} =$ mass fraction of kerogen (unitless)

$Vol =$ component volumes in cm^3(cc)

$\rho_{ker} =$ kerogen density $= 1.3\,\frac{g}{cc}$ (assumed for type III kerogen in the LGF)

$\rho_{matrix} =$ matrix density $= 2.68\ g/cc$ (assumed for sandy shale)

$V_{ker} =$ volume fraction of kerogen (unitless)

Porosity:

Total Porosity (PHIT) for the estimation of dry moduli:

Method-1:

$\Phi_t = \frac{\Delta t_p - \Delta t_{matrix}}{\Delta t_{fluid} - \Delta t_{matrix}}$ (Wyllie et al., 1956) ……..1

Where:

$\Delta t_{matrix} =$ interval transit time of matrix $= 65\ \mu s/ft$, for clay $-$ sand mixture (from recorded sonic_log)

$\Delta t_{fluid} =$ interval transit time of pore fluid $= 200\ \mu s/ft$, for freshwater drilling mud

$\Delta t_p =$ interval transit time $(\mu s/ft)$ from compressional sonic log

Fluid Correction ($\Delta t_{fluid_{corr}}$):

$\Delta t_{fluid_{corr}} = \boldsymbol{S_{xo}}\,\Delta t_{fluid} + (1 - \boldsymbol{S_{xo}}) * \Delta t_{hc}$

$S_{xo} = \left(a\,\frac{R_{mf}}{R_{xo}\Phi_t^m}\right)^{\frac{1}{n}}$ ……Archie equation

After fluid correction the equation 1 can be written as:

$$PHIT\_Sonic\_Wyllie = \Phi_t(fluid\ corrected) = \frac{\Delta t_p - \Delta t_{matrix}}{\Delta t_{fluid\_corr} - \Delta t_{matrix}}$$

Where**:**

$S_{XO} =$ flushed zone water saturation (From Archie equation)

Φ_t
$=$ total porosity from sonic log (using equation 1) and put in Archie equation for S_{XO}

R_{mf} = mudfilterate resistivity, R_{xo} = flushed zone resistivity, a = invasion factor = 1,

m = cementation exponent = 2, n = saturation exponent = 2

Method-2:

For 0-37% porosity:

$$PHIT\_Sonic\_Rymer = \Phi_t = 1 - C - \sqrt{(C)^2 + \frac{\Delta t_{matrix}}{\Delta t_{fluid_{corr}}} + \frac{\Delta t_{matrix}}{\Delta t_p}} \quad \text{.....2}$$

(Raymer et al. 1980)

Where: $C = \frac{\Delta t_{matrix}}{2\,\Delta t_{fluid}}$

Below is the comparison of PHIT results using both methods in well-X and Y:

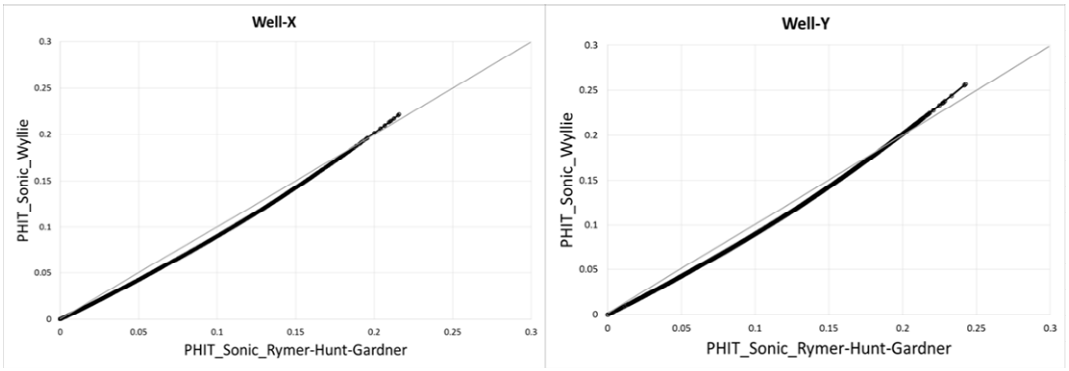

Effective Porosity for fluid substitution **(Crain and Holgate, 2014; Crain, 2016)**:

$$\Phi_{s\_ker} = \frac{\Delta t_{p\_ker} - 182}{474},$$

$$\Phi_{sc} = \Phi_s - \left(V_{cl} * \Phi_{s_{clay}}\right) - \left(V_{ker} * \Phi_{s\_ker}\right)$$

$$\Phi_{nc} = \Phi_n - \left(V_{cl} * \Phi_{n_{clay}}\right) - \left(V_{ker} * \Phi_{n_{ker}}\right)$$

$$\Phi_e = (\Phi_{sc} + \Phi_{nc})/2$$

Where:

Φ_{s_ker} = sonic porosity for kerogen

Δt_{p_ker} = compressional wave interval transit time for kerogen = 435 µs/m

Φ_s = sonic log porosity (unitless) = PHIT (as calculated using Wyllie and Raymer models)

$\Phi_{s_{clay}}$ = sonic log porosity at a high volume of clay interval (unitless)

Φ_n = neutron log porosity (unitless)

$\Phi_{n_{clay}}$ = neutron porosity at a high volume of clay interval (unitless)

Φ_{n_ker} = neutron porosity for kerogen = 0.65 (Zhang et al., 2018)

Φ_{nc} , Φ_{sc} = corrected porosities from neutron and sonic logs

Φ_e = effective porosity

Water Saturation (Modified Simandaux Model for shale gas reservoir (Entyre, 1993)):

$$\frac{1}{R_t} = \left(\frac{\Phi_e^m S_w^n}{aR_w(1 - V_{cl})}\right) + \left(\frac{V_{cl} S_w}{R_{sh}}\right)$$

Where:

R_t = deep resistivity in ohm. m (from LLD)

Φ_e = effective porosity

S_w = water saturation (%)

R_w = 0.03 ohm. m (extracted from well reports and also confirmed using SP log)

R_{sh} = average deep resistivity determined from log measurements in a shale zone

= 5 ohm. m

m & n = cementation & saturation exponents

= varies between 1.7 to 2 for getting saturation reported in literature and well reports

a = Tortuosity factor = 1

3.3.6 Vp Estimation

Vp is generally measured. For some empirical models for estimating Vs, Vp is simply used as an input parameter. When estimating Vs using rock physics models, calculation of Vp using the chosen rock physics model (and comparison against the measured values) can be a useful method of evaluating (and perhaps improving) the effectiveness of the selected model. In turn, this enhances confidence in the use of the chosen model for Vs estimation. At the fluid substitution stage, the difference between Vp and Vs estimation using rock physics models is the inclusion of fluid bulk modulus for determining effective bulk modulus for Vp estimation, while the shear modulus of the fluid (used for Vs estimation) is zero. The relevant equations for the required parameters to estimate Vp are given in Table 3.3.

The KT model accounts for the elastic properties (bulk and shear moduli) of the dry rock considering the pores as disconnected features. This, in turn, accounts for the effects of consolidation, porosity and pore geometry (Xu and White, 1995). The pores are assumed to be randomly distributed and randomly oriented, as illustrated in Figure 3.6. In this work, relatively high aspect ratios (α_s = 0.2, α_c = 0.09) were initially assigned to intervals with low clay content (Vcl≤40%) and low aspect ratios (α_s = 0.1, α_c = 0.01) to intervals of high clay

content (Vcl>40%). These limits were selected based on standard rock physics templates and published literature of shaly sandstone and sandy shale (Avseth et al., 2005; Nazeer et al., 2016; Azeem et al., 2017).

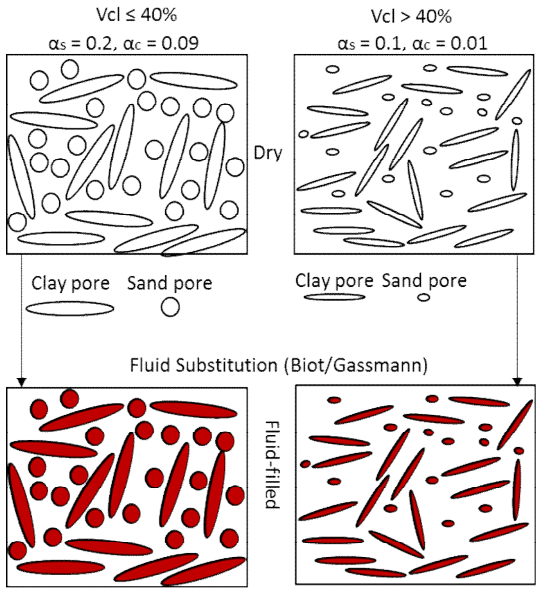

Figure 3.6 Randomly distributed pores in the clay-sand mixture (above), and mixed fluid (water and gas) substitution in pores.

The matrix moduli were determined using two approaches, as illustrated in Table 3.3 in the matrix moduli section: (1) following Xu and White (1995), based on Wyllie's equations; and (2) based on Hashin-Shtrikman's equations (as given by Berryman, 1995). The normalized matrix moduli calculated using both approaches for well-Y are plotted against the volume of clay, as shown in Figure 3.7. These results suggest only minor differences between matrix moduli calculated using both methods. Similar results were observed for well-X. Dry bulk and dry shear moduli were determined using the KT model, as given in Table 3.3.

The reservoir parameters for sandy shale and shale intervals of the LGF were assessed after studying published temperature and pressure gradients in the study area, and production data for well-X. The bulk moduli of individual fluids (K_{gas} and K_{brine}) were obtained from relations published by Batzle and Wang (1992) for a temperature of 175 ^{o}C, the pressure of 37.5 MPa, brine concentration of 20,000 ppm, brine density of 0.93 g/cc, and gas density of 0.17 g/cc. The effective bulk modulus (K_{fl}) and density (ρ_{fl}) for fluid were obtained after mixing the fluids using the equations of Brie et al. (1995) and Domenico (1976), respectively, as given in Table 3.3. The equation of Brie et al. (1995) yields the stiffest possible mixture, and its lower bound, as shown in Figure 3.8 (for e = 3) represents

a patchy fluid saturation scenario. In shale gas reservoirs, it is deemed reasonable to consider saturations as patchy because wave-induced pore pressures in this scenario will not equilibrate during the propagation of high-frequency sonic waves (Smith et al., 2003; Mavko et al., 2003; Avseth et al., 2005).

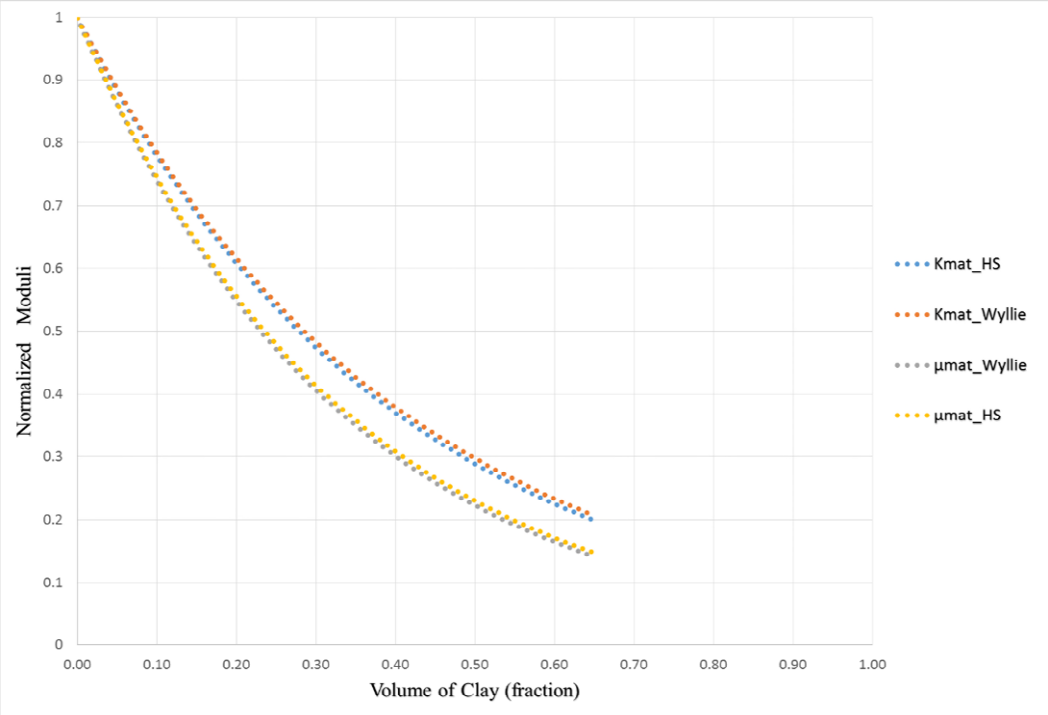

Figure 3.7 Normalized matrix moduli versus volume of clay (Vcl) for well-Y. The normalization factor used was the modulus value of the quartz at a Vcl of zero.

The fluid substitution was done using both the Gassmann and Biot models, as given in Table 3.3. Later, after introducing mixed fluid (water and gas) into the model, as illustrated in Figure 3.8, aspect ratios were iteratively adjusted to improve the match between measured and calculated Vp. All moduli (matrix, fluid and dry) and densities (matrix and fluid) were input separately into the equations for both the Gassmann and Biot models to obtain a rock physics-based Vp (denoted as Vp_RP).

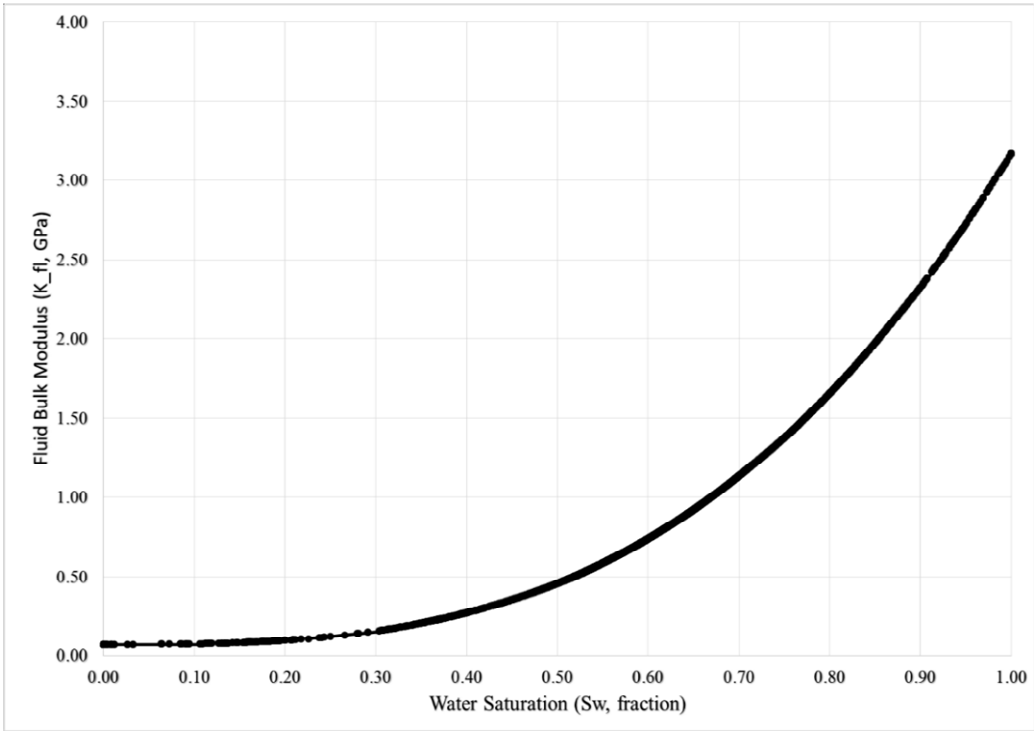

Figure 3.8 Plot between effective fluid (gas and water mixture) modulus and water saturation.

Table 3.3: Elastic properties and Velocities (Vp and Vs) estimation

Matrix Moduli (Wyllie et al., 1956; Hashin and Shtrikman, 1963; Xu and White, 1995):

Method-1 (based on Wyllie's Time Average Equations):

$\mu_m = \rho_m \left(\frac{1}{\Delta t_m^s}\right)^2, \ \Delta t_m^s = (1 - V'_{cl})\Delta t_g^s + V'_{cl}\Delta t_{sh}^s,$

$K_m = \rho_m \left(\frac{1}{\Delta t_m^p}\right)^2 - \frac{4}{3}\mu_m, \ \Delta t_m^p = (1 - V'_{cl})\Delta t_g^p + V'_{cl}\Delta t_{sh}^p$

$\rho_m = (1 - V'_{cl})\rho_g + V'_{cl} * \rho_{cl},$

$V'_{cl} = V_{cl}/(1 - \Phi_t),$

Where:

$\mu_m =$ matrix shear modulus

$K_m =$ matrix bulk modulus

$\Delta t_m^s, \Delta t_m^p =$ shear, primary (compressional) sonic interval transit time for a matrix

$\Delta t_g^s =$ shear sonic interval transit time for the sand grains $= 256$ μs/m

$\Delta t_g^p =$ primary sonic interval transit time for the sand grains $= 171$ μs/m

$\Delta t_{sh}^s =$ shear sonic interval transit time for clay minerals $= 584$ μs/m

$\Delta t_{sh}^p =$ primary sonic time for clay minerals $= 341$ μs/m

$V'_{cl} =$ volume of solid clay matrix (Normalized)

ρ_g & ρ_{cl} = density of sand and clay (illite dominant) grain respectively (2.65 & 2.75 g/cc respectively)

V_{cl} = volume of clay (See Table − 3.2 for details)

V_{sand} = volume of sand = $1 - \Phi_t - V_{cl}$

ρ_m = matrix (clay and sand)density = $V_{cl}\rho_{cl} + (1 - V_{cl})\,\rho_g$

Method-2 (Hashin and Shtrikman's Equations after Berryman (1995)):

For two phases (sand and clay):

Bulk modulus (upper bound) = K^{HS^+}

$$= K_{sand} + \frac{V_{cl}}{\left(K_{clay} - K_{sand}\right)^{-1} + V_{sand}\left(K_{sand} + \left(\frac{4}{3}\right)\mu_{sand}\right)^{-1}}$$

Bulk modulus (lower bound) = K^{HS^-}

$$= K_{clay} + \frac{V_{sand}}{\left(K_{sand} - K_{clay}\right)^{-1} + V_{clay}\left(K_{clay} + \left(\frac{4}{3}\right)\mu_{clay}\right)^{-1}}$$

$Shear\ modulus\ (upper\ bound) = \mu^{HS^+}$

$$= \mu_{sand} + \frac{V_{cl}}{\left(\mu_{clay} - \mu_{sand}\right)^{-1} + \frac{2V_{sand}(K_{sand} + 2\mu_{sand})}{5\mu_{sand}\left(K_{sand} + \left(\frac{4}{3}\right)\mu_{sand}\right)}}$$

$Shear\ modulus\ (lower\ bound) = \mu^{HS^-}$

$$= \mu_{clay} + \frac{V_{sand}}{\left(\mu_{sand} - \mu_{clay}\right)^{-1} + \frac{2V_{clay}(K_{clay} + 2\mu_{clay})}{5\mu_{clay}\left(K_{clay} + \left(\frac{4}{3}\right)\mu_{clay}\right)}}$$

$K_{m\_average}^{HS} = \frac{K^{HS^+} + K^{HS^-}}{2}$ (Plotted as Kmat_HS)

$\mu_{m\_average}^{HS} = \frac{\mu^{HS^+} + \mu^{HS^-}}{2}$ (Plotted as µmat_HS)

Where:

K_{sand} (37 GPa) & K_{clay}(21 GPa) are bulk moduli of sand and clay respectively

μ_{sand} (44 GPa) & μ_{clay}(6 GPa) are shear moduli for sand and clay respectively

The fixed values of moduli were selected from literature (Mavko et al., 2003; Saxena et al., 2018), and shear modulus of clay was varied between 6 and 12 GPa.

Dry bulk modulus (K_d) (Kuster and Toksoz Theory (after Yan et al., 2002)):

$$K_d = \frac{K_m + 4A\mu_m}{1 - 3A}$$

Where:

$$A = \frac{1}{3}\frac{K_{fl} - K_m}{\mu_m(3K_m + 4\mu_m)}\sum_{l=s,c}^{2} \Phi_l \left(T_{ijij}(\alpha_l)\right)$$

$T_{ijij} =$ (Equation B1 in Appendix 3-B)

$K_{fl} = 0$ for dry bulk modulus

Dry Shear modulus (Kuster and Toksoz, 1974):

$$\mu_d = \left[\frac{\mu_{fl} - \mu_m}{5}\frac{6\mu_d\,(K_m + 2\mu_m) + \mu_m(9K_m + 8\mu_m)}{5\mu_m(3K_m + 4\mu_m)}\sum_{l=s,c} \Phi_l F(\alpha_l)\right] + \mu_m$$

Where:

$\mu_d = dry$ shear modulus

$\mu_{fl} =$ fluid shear modulus

$l = s,$ for sand

$l = c,$ for clay

$\Phi_c = \Phi_{clay} = (\Phi_{n_{clay}} + \Phi_{s_{clay}})/2$

$\Phi_{s_{clay}}$ *and* $\Phi_{n_{clay}}$ are clay porosity from sonic and neutron logs respectively

$\Phi_s = \Phi_{sand} =$ (1- V_{cl}) $(\Phi_t/(1 - \Phi_t)$

$$F(\alpha_l) = T_{ijij}(\alpha_l) - \frac{T_{iijj}(\alpha_l)}{3}$$

$\alpha_s =$ aspect ratio for sand $related\ pores, \alpha_c =$ aspect ratio for clay related pores

$T_{ijij}(\alpha_l) - \frac{T_{iijj}(\alpha_l)}{3} =$ Equation B2 in Appendix 3-B

After Yan et al. (2002), KT's equation can be written as follow,

$$\mu_d = \mu_m \frac{1 + B(9K_m + 8\mu_m)}{1 - 6B(K_m + 2\mu_m)}$$

Where:

$$B = \frac{1}{25}\frac{\mu_{fl} - \mu_m}{\mu_m(3K_m + 4\mu_m)}\sum_{l=s,c}^{2} \Phi_l \left(T_{ijij}(\alpha_l) - \frac{T_{iijj}(\alpha_l)}{3}\right)$$

$\mu_{fl} = 0$ (For dry shear modulus)**Fluid Density and Modulus:**

Effective fluid density $= \rho_{fl} = S_w\rho_{brine} + S_{gas}\rho_{gas}$ (Domenico, 1976)
$K_{fl} = (K_{brine} - K_{gas})S_w^e + K_{gas}$ (Brie et al., 1995) (A plot between K_{fl} & S_w is shown in Figure 3.8)

Where:

$\rho\_brine = 0.928\ g/cc$

$\rho\_gas = 0.17\ g/cc$
$K_{gas} = 0.07\ GPa$
$K_{brine} = 3.17\ GPa$
$S_{gas} = 1 - S_w$
$K_{fl} =$ effective fluid modulus for patchy saturation

e = constant = 1 to ∞. For the LGF, e = 3 was used (as suggested by Avseth et al. (2005) to simulate patchy behavior in a shale gas reservoir)

Biot Equations for Velocities (Vp_RP and Vs_RP) (Mavko et al., 2003):

$$V_p = \sqrt{\frac{\Delta + \left[\Delta^2 - 4\left(\rho_{11}\rho_{22} - \rho_{12}^2\right)(PR - Q^2)\right]^{\frac{1}{2}}}{2\left(\rho_{11}\rho_{22} - \rho_{12}^2\right)}}$$

$$\Delta = P\rho_{22} + R\rho_{11} - 2Q\rho_{12}$$

$$P = \frac{\left[(1-\Phi_e)\left(1-\Phi_e-\frac{K_d}{K_m}\right)K_m + \frac{\Phi_e K_m K_d}{K_{fl}}\right]}{1-\Phi_e-\frac{K_d}{K_m}+\frac{\Phi_e K_m}{K_{fl}}} + \frac{4}{3}\mu_d$$

$$Q = \frac{\left(1 - \Phi_e - \frac{K_d}{K_m}\right)\Phi_e K_m}{1 - \Phi_e - \frac{K_d}{K_m} + \frac{\Phi_e K_m}{K_{fl}}}$$

$$R = \frac{\Phi_e^2 K_m}{1 - \Phi_e - \frac{K_d}{K_m} + \frac{\Phi_e K_m}{K_{fl}}}$$

$\rho_{11} = (1 - \Phi_e)\rho_m - (1 - \alpha)\Phi_e\rho_{fl}$
$\rho_{22} = \alpha\Phi_e\rho_{fl}$
$\rho_{12} = (1 - \alpha)\Phi_e\rho_{fl}$

Where:
$\alpha =$ Tortuosity coefficient $= 3$ (Stoll, 1977)

Shear wave velocity = Vs_RP = see Table 3.4b

Gassmann Equations for saturated Bulk Modulus and Velocities (Vp_RP_Gassmann and Vs_RP_Gassmann) (Mavko et al., 2003)

$$K_{sat} = \frac{\left(\frac{1-K_d}{K_m}\right)^2}{\frac{\Phi_e}{K_{fl}}+\frac{1-\Phi_e}{K_m}-\frac{K_d}{K_m^2}} + K_d \quad V_p = \sqrt{\frac{K_{sat}+\frac{4}{3}\mu_d}{\rho_b}}, \quad V_s = \sqrt{\frac{\mu_d}{\rho_b}}$$

Where:
$\mu_d = \mu_{sat}$, $\mu_{sat} =$ shear modulus of saturated rock for low − viscosity fluids
$\rho_b =$ effective bulk density $= \rho_m(1 - \Phi_e) + \rho_{fl}\Phi_e$
$\Phi_e =$ effective porosity

3.3.7 Vs Estimation

Equations for empirical correlations (Vs1 to Vs7 and Vs_LV) and rock physics-based models (Vs_RP and Vs_BGK) that were selected to estimate Vs in the LGF are given in Tables 3.4a and 3.4b, respectively. Log measured values were used as direct input for the Vp-based equations (Vs1, Vs3, Vs5, Vs6, Vs7, Vs_LV). The methods used to obtain the input parameters for Vs2 and Vs4 are given in Table 3.2. The workflow for calculating shear waves velocity based on rock physics modeling (Vs_RP) is summarized in Figure 3.9, and relevant equations for moduli are given in Table 3.3. This workflow is similar to the Xu and White (1995) model, except for modifications to porosity determination, Vcl and aspect ratios, and the use of the Biot model for fluid substitution rather than Gassmann. The dry shear modulus used for Vp_RP and corrected after comparison of Vp_RP with Vp_measured, was used for Vs_RP.

Although prior work investigating correrelations between resistivity log measurements and sonic velocities has been reported, such correlations were not included in this study due to the lack of a well-defined relationship between resistivity and Vs logs in shale gas reservoirs (Hacikoylu et al., 2006).

Assessment of the accuracy of estimated Vs values was conducted in several ways. The first step in this process was to overlay log plots of estimated Vs on plots of measured Vs and compare the curves visually. Further, the measured and calculated shear velocities were cross plotted, and the regression coefficient (r-square or R^2) for a fit-line passing through origin was calculated. If both variables have a linear relationship, the value of R^2 should be close to +1 (Draper and Smith, 1998). Further to R^2, the slope of the trendline is also important ; more specifically, a 1:1 slope indicates that the estimated values match the magnitudes of the measured values. Therefore, an identity line (1:1 line) was plotted, so the proximity of the data points to this line could be assessed visually. The error (the difference between Vs_log and Vs_calc.) was also assessed visually using histograms, and quantitatively by calculating the standard deviation (STD) of the error in the logged LGF intervals. Low and high values of STD show the closeness and farness of plotted data from the mean value of error, respectively (Bland and Altman, 1996). As discussed later, these statistical parameters were used to evaluate the effectiveness of each model for Vs estimation.

Table 3.4a: Compilation of empirical correlations (Vs1-Vs7, and Vs_LV; velocities are in km/s) used to estimate shear wave velocity.

ID	Relationship	Lithology	Sources	Comments
$Vs1$	$V_s = V_p/1.6$	Clean sandstone, dolomite, limestone	Pickett (1963)	• 1.6 is the limiting lower value of the Vp/Vs ratio for clean sandstone
$Vs2$	$V_s = 3.7 - 6.3\Phi_t - 2.1V_{cl}$	Shaly sandstone	Tosaya (1982)	• A regression is only applicable to a given set of conditions such as lithology, pressure, temperature and stress • An accurate estimation of Vcl is required
$Vs3$	$V_s = \frac{V_p - 1.360}{1.16}$	Mudrocks	Castagna et al. (1985)	• Area-specific; not recommended for different areas (Andrew and Sander, 2001)
$Vs4$	$V_s = 3.89 - 7.07\Phi_t - 2.04V_{cl}$	Shaly sandstone		
$Vs5$	$V_s = 0.79V_p - 0.79$	Water saturated sandstone	Han et al. (1986)	As above for Vs3 and Vs4 (William,1990)
$Vs6$	$V_s = 0.846V_p - 1.088$	Saturated sandstone	Williams (1990)	Area specific
$Vs7$	$V_s = 0.000158V_p^2 - 0.632162V_p + 2153.32$	Water saturated sandstone	Liu and Chen (2012)	Area-specific and particularly not recommended for gas reservoirs
Vs_LV	$V_s = \sqrt{aV_p^4 + bV_p^2 - c}$ Where: $a = 2.84e^{-3}\ \ b = 0.287\ \ c = 0.79$	Shaly sandstone	Vernik (2016)	• Applicable for predicting nonlinear drop in Vs as the sediment porosity approaches 40% in non-organic shale • Different coefficients for organic rich sandy shale and shale

Table 3.4b: Compilation of rock physics models used to estimate shear wave velocity.

ID	Relationship	Lithology	Sources	Comments
Vs_BGK	$V_s = \sqrt{\mu_s\,(1-\sigma_\mu)/\rho_b}$ Where: $1-\sigma_\mu = (1-\phi)^{\frac{n_\mu}{1-\phi}}$ $\sigma_\mu = Gassmann's\ coefficient$ n_μ $= Gassmann$ $- Krief\ exponent$ $(values\ for\ n_\mu\ are\ 1,2,3,5,10,and\ 100)$ μ_s $= shear\ modulus\ of\ matrix$ $\phi =\ porosity$ $\rho_b = bulk\ density$	Clean sandstones, shales, marls, and mudstones	Saxena et al. (2018)	• Extended BGK Model • n_μ needs to be fixed based on local conditions
Vs_RP	$V_s = \sqrt{\frac{\mu_{fr}}{\rho_m(1-\Phi_e)+\Phi_e\rho_{fl}(1-\alpha^{-1})}}$ $\mu_{fr} = shear\ modulus\ of\ dry\ rock\ frame\ from\ KT\ model$ $\rho_b =\ \rho_m(1-\Phi_e)+\Phi_e\rho_{fl}(1-\alpha^{-1})$ (See Table 3.3 for all input parameters)	Shaly sandstone, Sandy shale	Biot (1956), Kuster & Toksoz (1974), Mavko et al. (2003)	• A combination of Biot and KT and models • Applicable for gas saturated sandy shale and shale

3.4. Results and Discussion

3.4.1 Petrophysical Properties

The porosities (density, sonic, and neutron-density based total porosity) without corrections and traditional GR threshold limits over-estimate porosity and Vcl, based on comparison against core-based published values of porosity and Vcl measurements in sandy shale and shale intervals of LGF which indicates that values should be in the 0.01 to 0.15 (average 0.08) and 0.4 to 0.8 (average 0.6) ranges, respectively. The log-based porosities (unconnected total porosity) also produce a poor match between measured and estimated

velocities when used as inputs for fluid substitution (see supplementary plots in Appendix 3-D). The neutron-sonic based corrected porosity (effective porosity) and GR-based Vcl (IGR = Vcl, with GR_min = 30 API, GR_max = 230 API) as shown in tracks 4 & 6 of figures 3.10 and 3.11 respectively, are deemed most suitable for the sandy shale and shale intervals of the LGF in the studied wells because this approach ultimately produced the best match between Vp_log and Vp_RP as shown in track 8 of same figures.

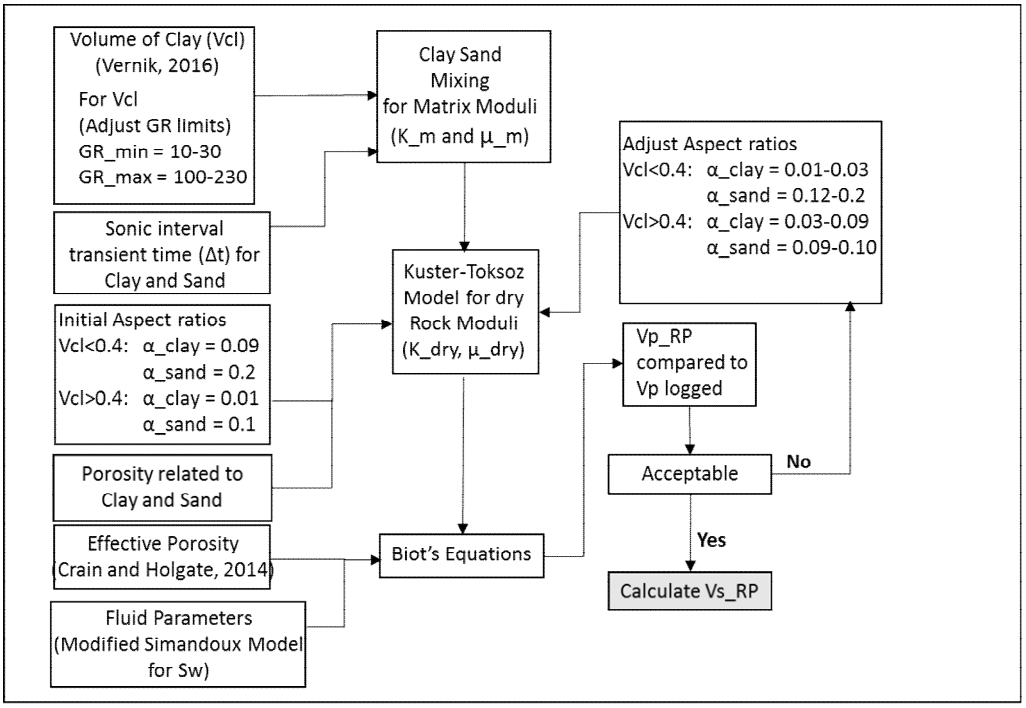

Figure 3.9 Flowchart for modified Xu & White (1995) rock physics model for shear waves velocity estimation (Vs_RP) (after Simm and Bacon, 2014)**.**

The neutron-sonic-based effective porosity (described in Table 3.2), accounts for the combined effect of TOC and Vcl on porosity. This effective porosity and Vcl also seem appropriate for getting a reasonable fluid saturations (Sw 40%-60% based on published data and well reports of LGF) in sandy shale and shale intervals using the Modified Simandoux model which is also useful when using fluid substitution models to estimate Vp though less so for Vs, which is insensitive to fluid properties. This enhanced confidence in the petrophysical input parameters (porosity, Vcl, fluid saturations) and helped in getting a better fit between estimated and recorded velocities (for both Vp and Vs) based on the rock physics model. A good match between recorded and estimated Vp is also a useful quality check on estimated porosities (total and effective) and volume of clay.

3.4.2 Vs From Empirical Models

Shear wave velocities estimated using empirical correlations (Vs1 to Vs7, and Vs_LV) are shown in tracks 9, 10 and 11 of Figures 3.10 and 3.11. Enlarged views of these tracks, for the intervals of greatest interest, are shown in Figures 3.12 and 3.13. Based on the visual comparison, the shear velocities estimated using the linear correlations Vs3,Vs5 and Vs6 compare more favorably to measured Vs than the other linear correlations (Vs1, Vs2 and Vs4). The statistical analysis of the former correlations (Vs3, Vs5 and Vs6), showed relatively high R^2 (0.78 for Vs3, 0.80 for Vs5, 0.78 for Vs6 in well-X, and 0.89, 0.82, 0.89 in well-Y) and low STD (169, 148, 164 m/s in well-X and 100, 97, 105 m/s in well-Y), as illustrated in Figures 3.14 and 3.15. Most of the estimated data points for Vs1,Vs3, Vs5 and Vs6 are close to the identity line (i.e., 1:1 slope), whereas many of the data points for Vs2 and Vs4 lie significantly above or below the identity line. Although the results for Vs1 show favourable R^2 values (0.80 in well-X and 0.77 in well-Y) and low STD (115 m/s in well-X and 99 m/s in well_Y), most of the data points lie above the identity line, which means this correlation consistently over-estimates Vs. For further analysis, the linear Vp-based equations (Vs1, Vs3, Vs5, Vs6) were overlayed on the cross plot between recorded velocities, as shown in Figure 3.16. Apparently, by coincidence, Vs5 (red color in Figure 3.16) is closest to the trendline fit to this dataset and may be suitable for this dataset.

The second-order polynomial correlations based on Vp (Vs7 and Vs_LV) show trends that track closely with the Vs_log as shown in track-11 of Figures 3.10 & 3.11 and track 6 on Figures 3.12 and 3.13. The statistical analysis of Vs7 and Vs_LV showed relatively low r-square for well-X and high for well-Y (0.79 for Vs7, 0.77 for Vs_LV in well-X and 0.82 for Vs7, 0.88 for Vs_LV in well-Y), and low and high STD (130, 193m/s in well-X and 109, 168 m/s in well-Y), as illustrated in Figures 3.14 and 3.15. The data of Vs7 seems to be underestimated (as falling below the identity line), and both over and underestimated values are commonly observed for Vs_LV. Vs7 was derived for water-saturated sandstones and Vs_LV for non-organic shale. For the sandy shale and shale intervals of the LGF, the coefficients of both equations were modified to enhance the R^2 values, as illustrated in Figure 3.17a and 3.17b. The new R^2 values, obtained after comparison of Vs_log and estimated Vs (Vs7 and Vs_LV), increased by approximately 10% to 20% for both wells. In particular, Figure 3.17a illustrates how further improvements in accuracy can be obtained if the correlation is selectively developed and used in intervals

possessing specific lithologies of interest (i.e., in this case, by excluding shaly sandstone intervals from the analysis).

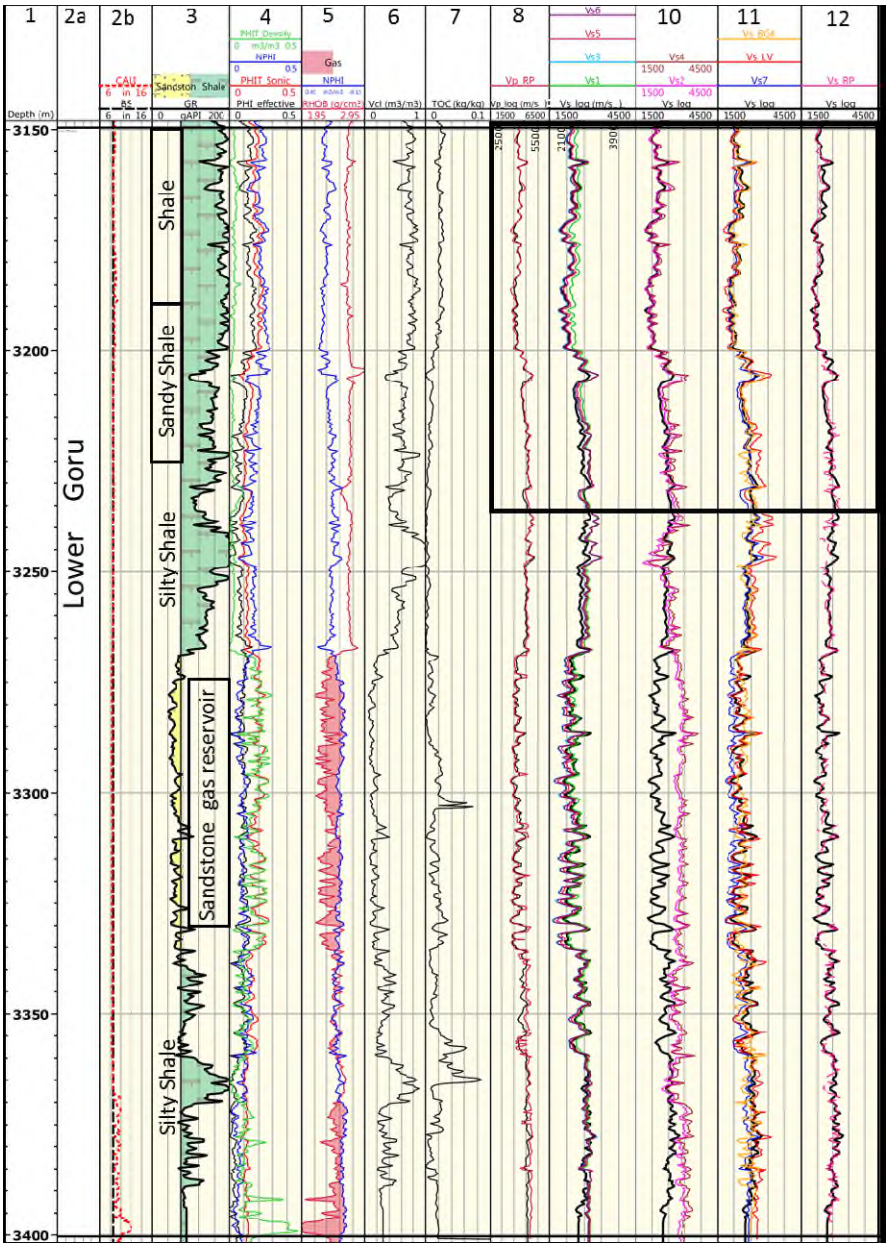

Figure 3.10 Well X**,** Track 1 shows depth in metres (m); Track 2a shows a formation name; Track 2b shows caliper log (CALI in inch) and Bit size (BS in inch); Track 3 shows gamma ray (GR) log with shading based on a cut-off of 75 API units to differentiate shale (green) and sandstone (yellow); Track 4 shows uncorrected total porosity from individual density (PHIT_D), neutron (PHIT_Neutron), sonic (PHIT_sonic) logs, and effective porosity (PHI_effective) from a combination of neutron and sonic; Track 5 shows bulk density (RHOB) and neutron (NPHI) logs, the cross-over between these two curves is filled with light red color to denote gas-bearing zones; Track 6 shows volume of clay (Vcl); Track 7 shows total organic carbon content (TOC); Track 8 shows recorded (black) and estimated Vp in m/s (Vp_log and Vp_RP); Track 9 shows recorded (black) and estimated Vs in m/s (Vs1,Vs3,Vs5,Vs6); Track 10 shows recorded (black) and estimated Vs (Vs2,Vs4); Track 11 shows recorded (black) and estimated Vs (Vs_LV, Vs7, Vs_BGK); Track 12 shows recorded (black) and estimated Vs (Vs_RP). The zone bounded by the rectangle is shown in Figure 3.12 with greater detail.

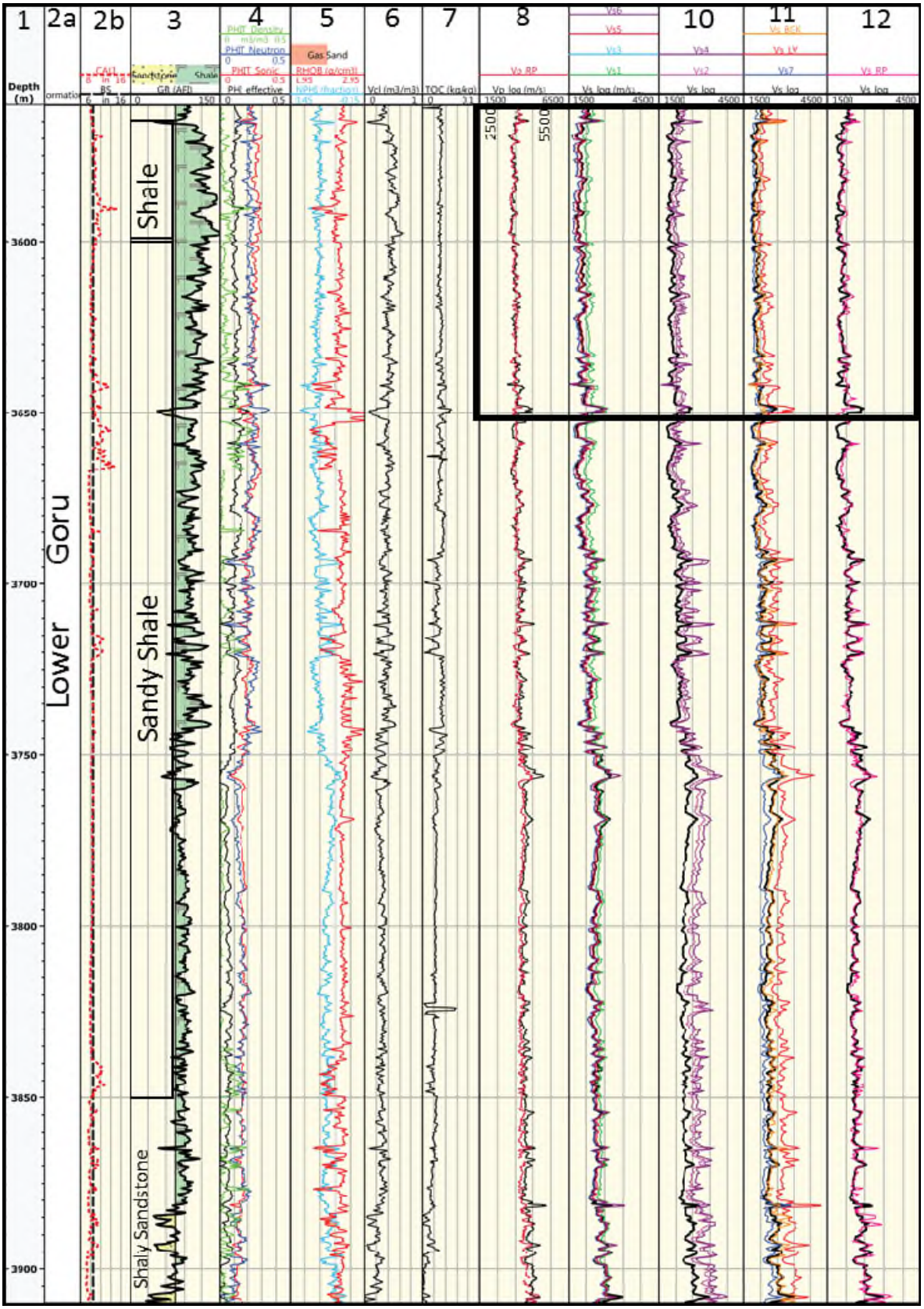

Figure 3.11 Log data for Well Y.The sequence and description of tracks is the same as Figure 3.10. The zone bounded by the rectangle is shown in greater detail in Figure 3.13.

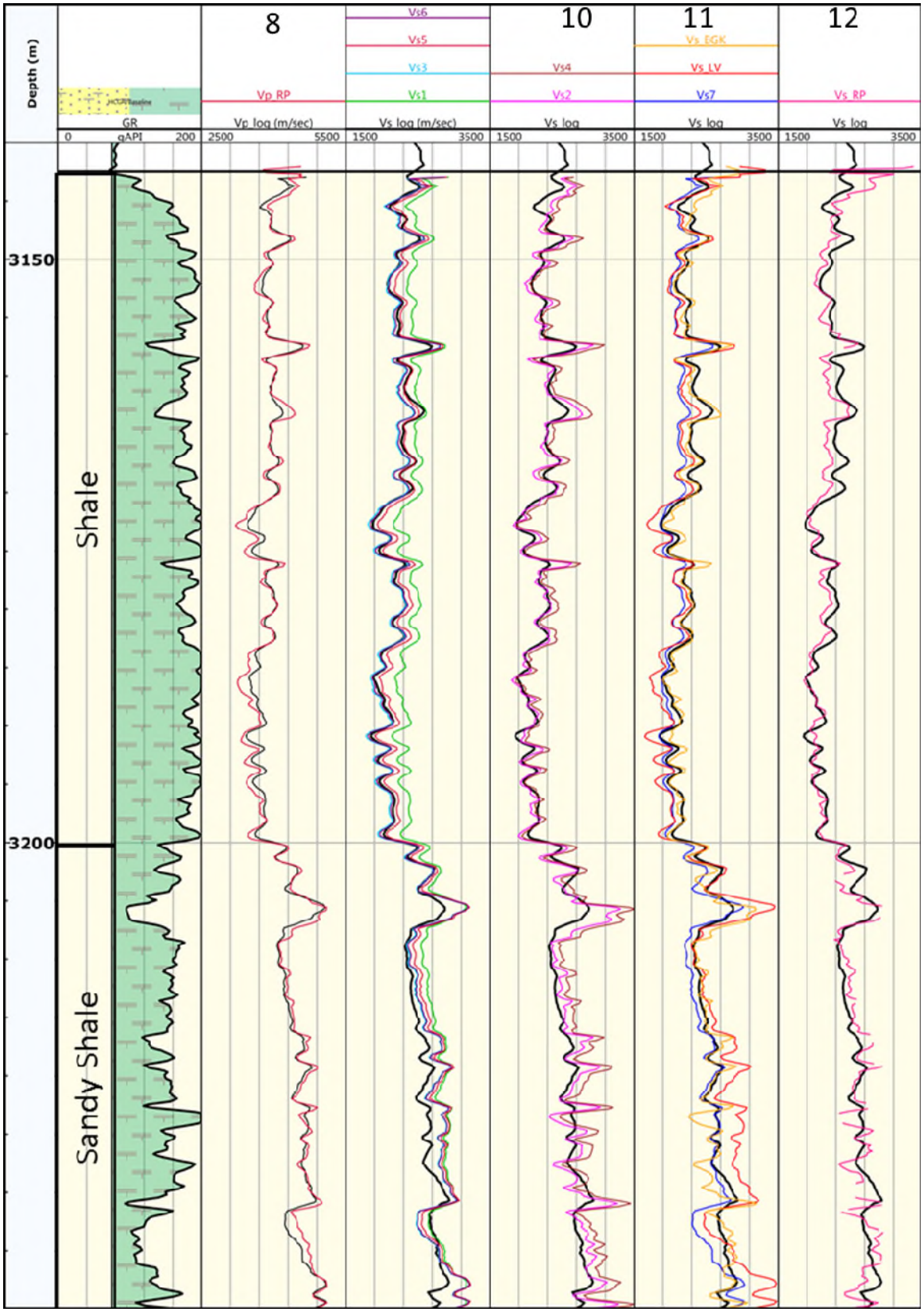

Figure 3.12 A comparison of velocities in Shale and Sandy Shale intervals of Well-X, extracted from the interval denoted in Figure 3.10 and re-plotted with an expanded scale.

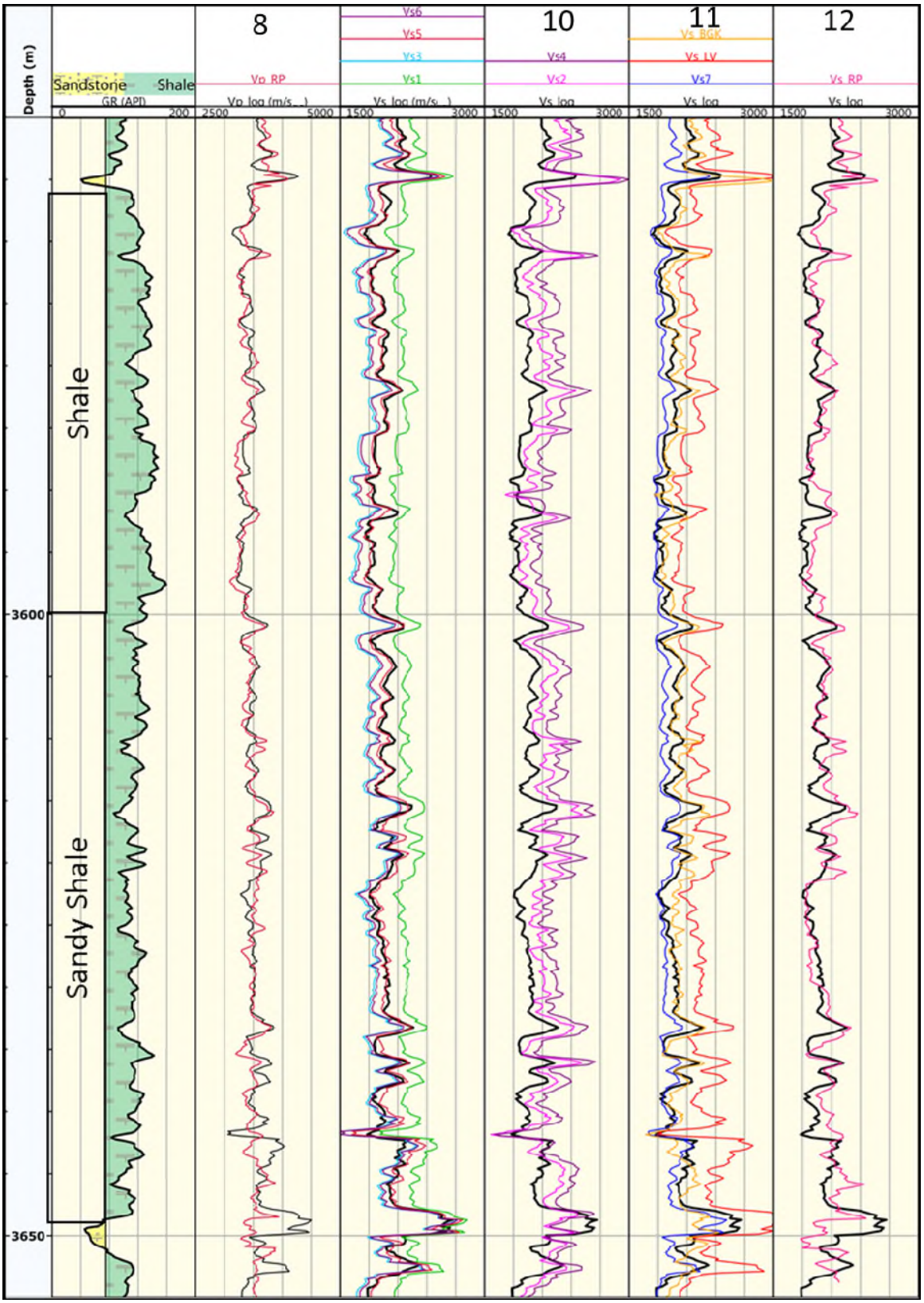

Figure 3.13 A comparison of velocities in Shale and Sandy Shale intervals of Well-Y, extracted from the interval denoted in Figure 3.11 and re-plotted with an expanded scale.

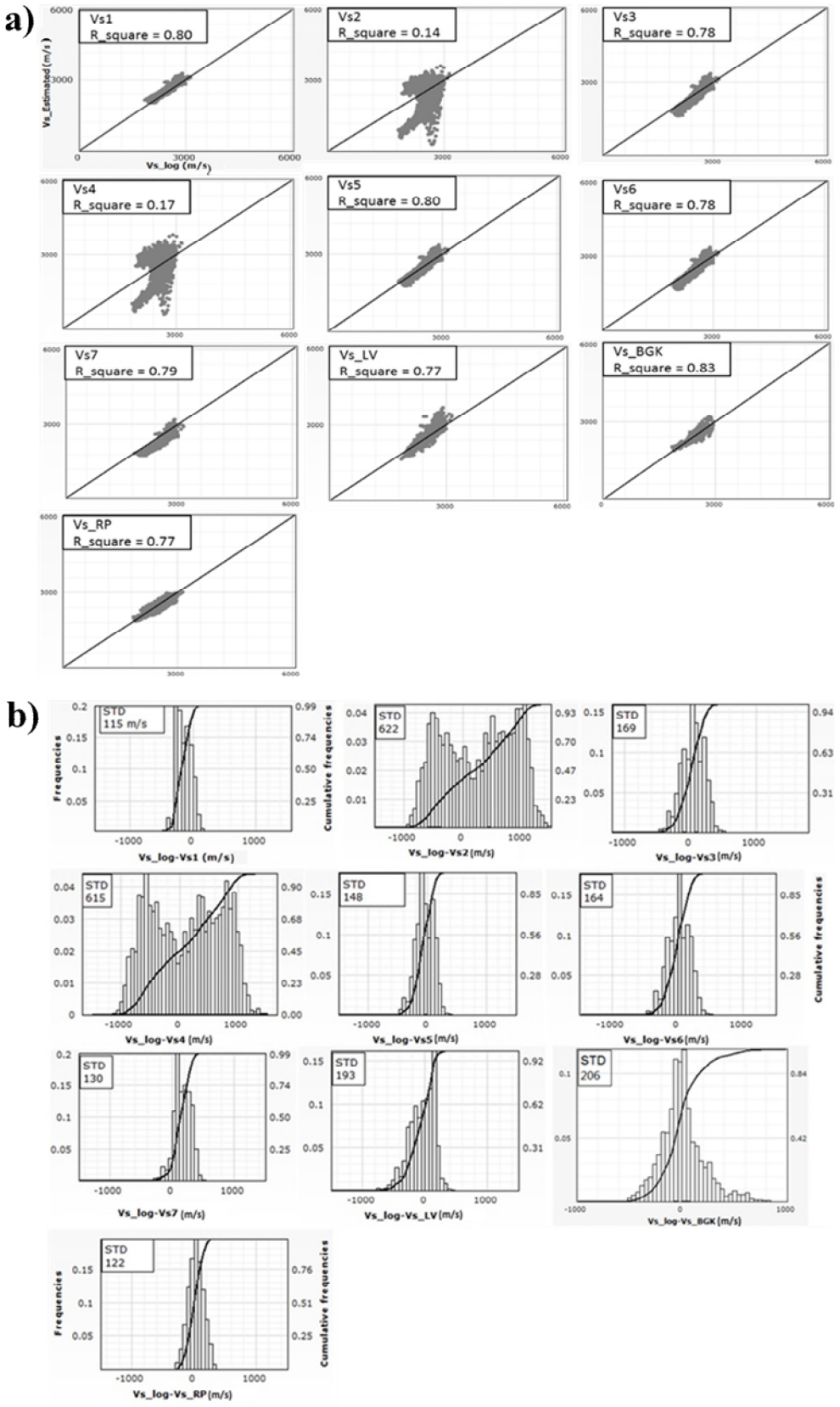

Figure 3.14 (a) Cross plots between measured and estimated Vs for Well X. **(b)** Frequency histograms and Cumulative curve for the difference between measured and estimated Vs for Well X.

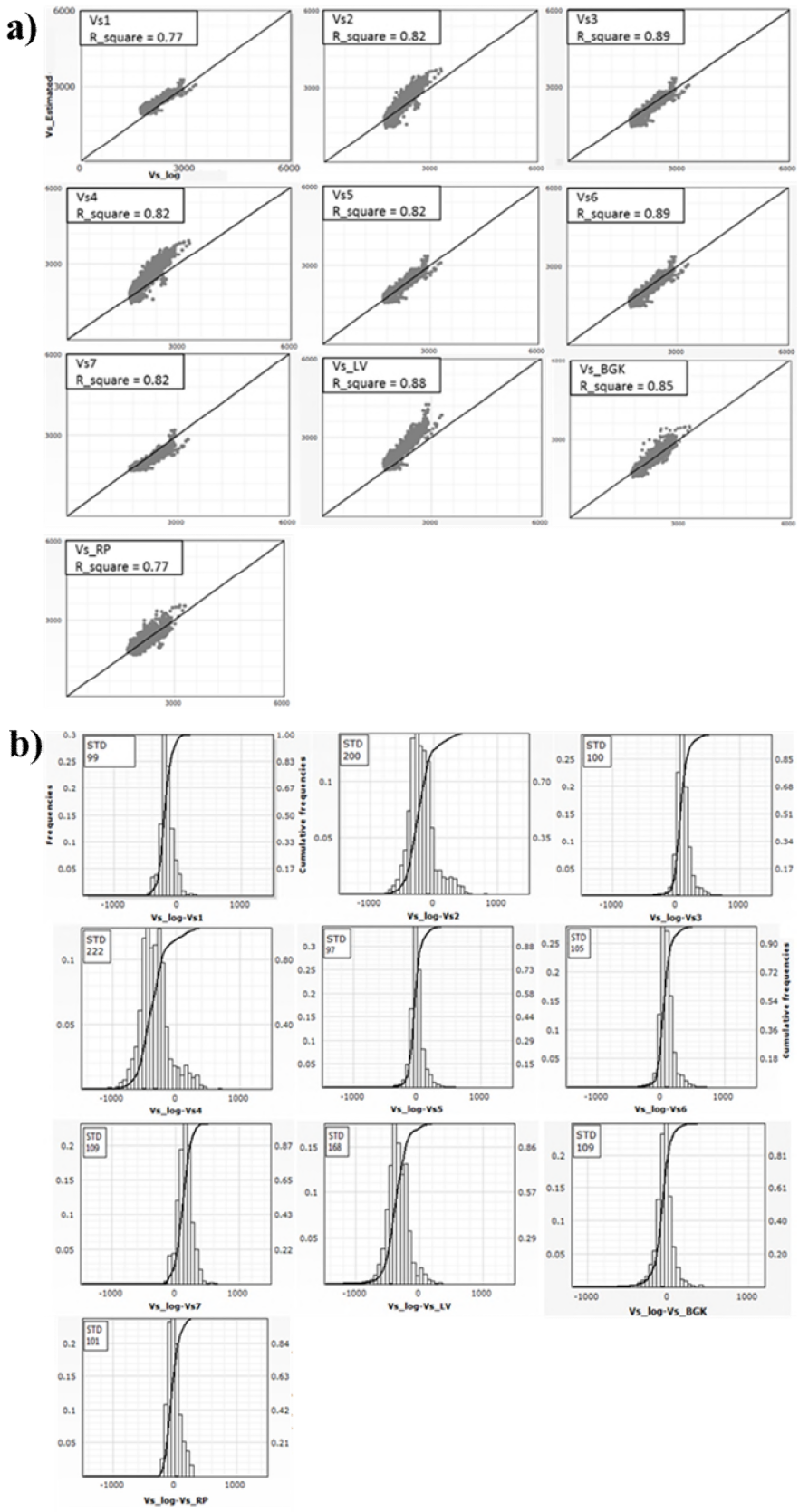

Figure 3.15 (a) Cross plots between measured and estimated Vs for Well Y. **(b)** Frequency histograms and the Cumulative curve for the difference between measured and estimated Vs for Well Y.

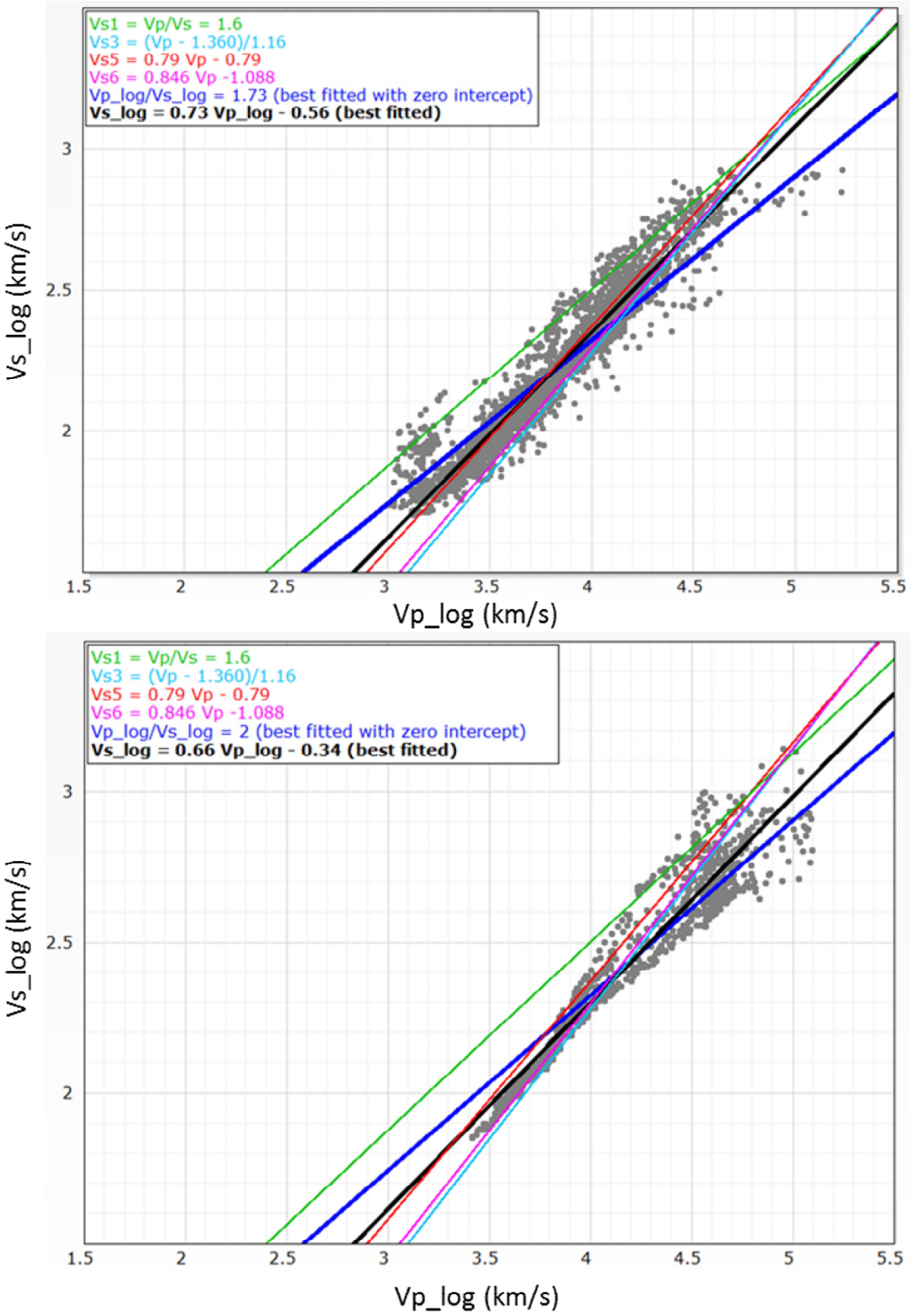

Figure 3.16 Cross plot between recorded velocities in well-X (a) (excluding the sandstone interval, 3270-3340m) and well-Y (b). Different colored lines represent different original empirical equations (as given in Table 3.4a) and given at top left corner of each graph.

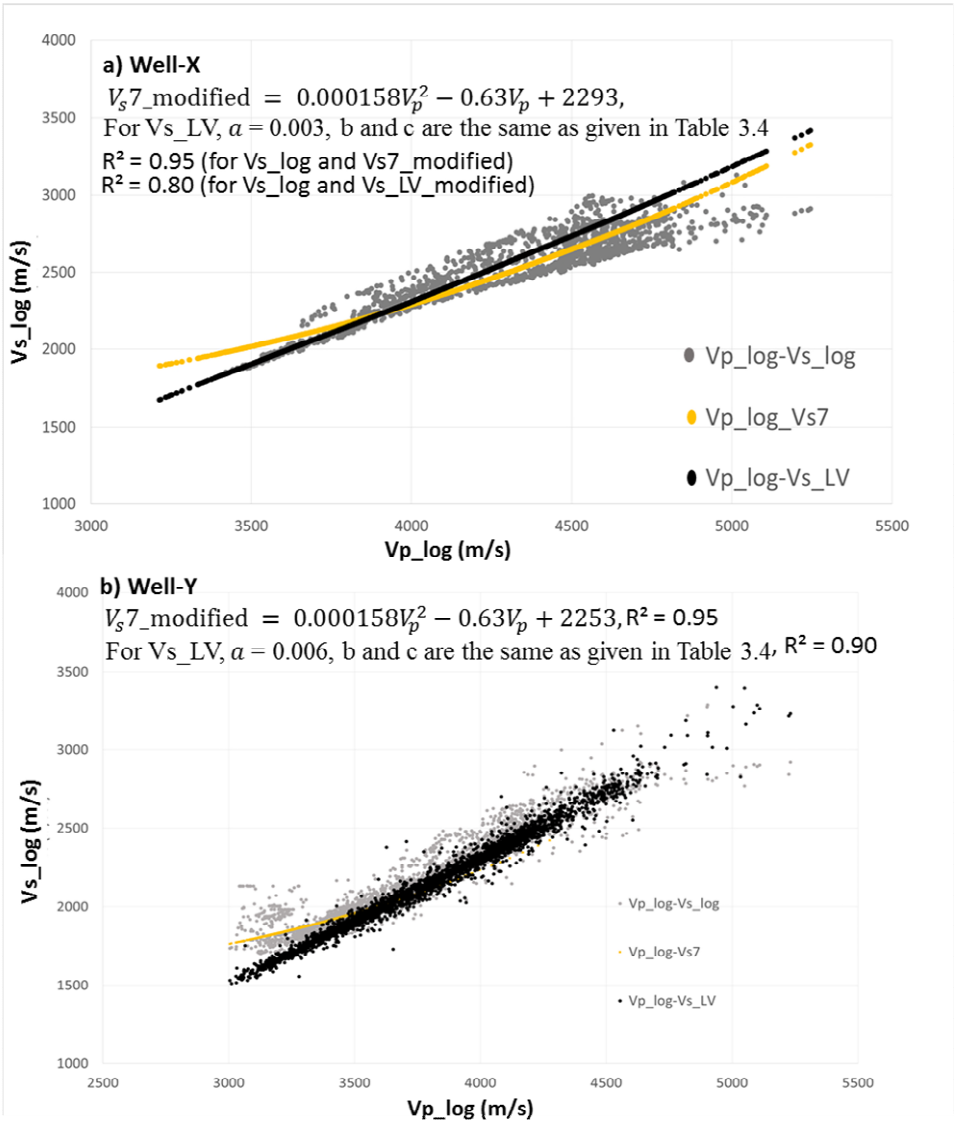

Figure 3.17 Cross plot between Vs_log and Vp_log, overlayed by estimated Vs (Vs7 and Vs_LV as given in Table 3.4a) with modified coefficients for well-X (**a**) and well-Y (**b**). The improved R^2 values obtained after the correlation between estimated and measured Vs.

It is observed that the nature of the empirical Vp-based model (linear or polynomial) has limited impact on the accuracy of the estimated Vs for this specific dataset; the statistical results presented in Figures 3.14 & 3.15 (before modification to coefficients) and in 3.16 & 3.17 (after modification) are favourable for both. It is suggested that the polynomial equations might be better in general because they allow more flexibility in the correlation of Vp and Vs, though they offer no clear benefit for the dataset studied in this work. The statistical results favor the use of Vp-based empirical models after modification to coefficients based on comparison to measured Vs, assuming of course, that the quality of the Vp data has been assessed and deemed to be good.

It makes sense that Vp-based correlations should work well because Vp values are affected by many of the same factors that also affect Vs, such as the porosity, mineralogy and clay content. Hence the Vp-based correlations for Vs implicitly account for these factors (Vernik et al., 2017). Vp generally decreases with increasing Vcl due to an increase of soft clay-bound pores, and a similar trend can be observed in Figure 3.18. Measured Vp values show a negative correlation with effective porosity and Vcl in both wells, though for porosities below 5% there is no well-defined trend compared to higher porosities (>5%). The velocities are more scattered against Vcl and effective porosity in well-Y compared to well-X, it is due to large interval of sandy shale (green color in Figure 3.18c and 3.18d) in well-Y where effective porosity varies between 0% to 15% and Vcl from 20% to 50%. The data trends in sandy shale may not be possible to capture using empirical Vp-based correlations even after the modification to coefficients because these are deemed to be linked complex pore structures developed due to the mixing of sand and clays.

Rock physics models explicitly account for variations in several factors including mineral grain elastic moduli, pore geometries, and fluid properties and saturation. Empirical models, on the other hand, are not explicitly linked to these fundamental factors, and hence might be ineffective when they vary outside the range that exists in the dataset used as the foundation for these correlations. For example, the empirical models presented in this work were derived in brine-saturated rocks, and hence are likely to show decreasing accuracy with increasing gas saturation.

The extended BGK model for Vs estimation shows a good match in clay-rich shales (sandy shale and shale) of well-X and well-Y as shown in track 11 of Figures 3.10 and 3.11, and track 6 of Figures 3.12 and 3.13. The R2 and STD values are good (Figures 3.14 and 3.15). The data points fall close to the identity line. Figure 3.19 shows the variability of compressional sonic transit time (DTP) with effective porosity at different values of n_k (Biot-Krief exponent), and at n_k = 3 and n_μ = 2, the BGK model produces matchable results to recorded DTP data in sandy shale intervals of well-X. The exponents (n_k, n_μ) in the BGK model seem to have sensitivity in sandy shale, and their values need to be selected by studying the available data in the interval(s) of interest. In both wells studied here, after overlaying the recorded DTP data on a standard DTP-porosity cross plot of the BGK model, values of exponents (between 1 and 10) were chosen. The matrix moduli in the BGK model are found to be more compatible with the Hashin-Shtrikman model (as given in Table 3.3) so a reasonable control on mineralogy may also be required to implement this

model with reasonable accuracy. In the absence of recorded Vp, it may be difficult to assess the exponents for the BGK model, but in the sense of its simplicity (relative to a rock physics model), it may be preferred over a complex rock physics model.

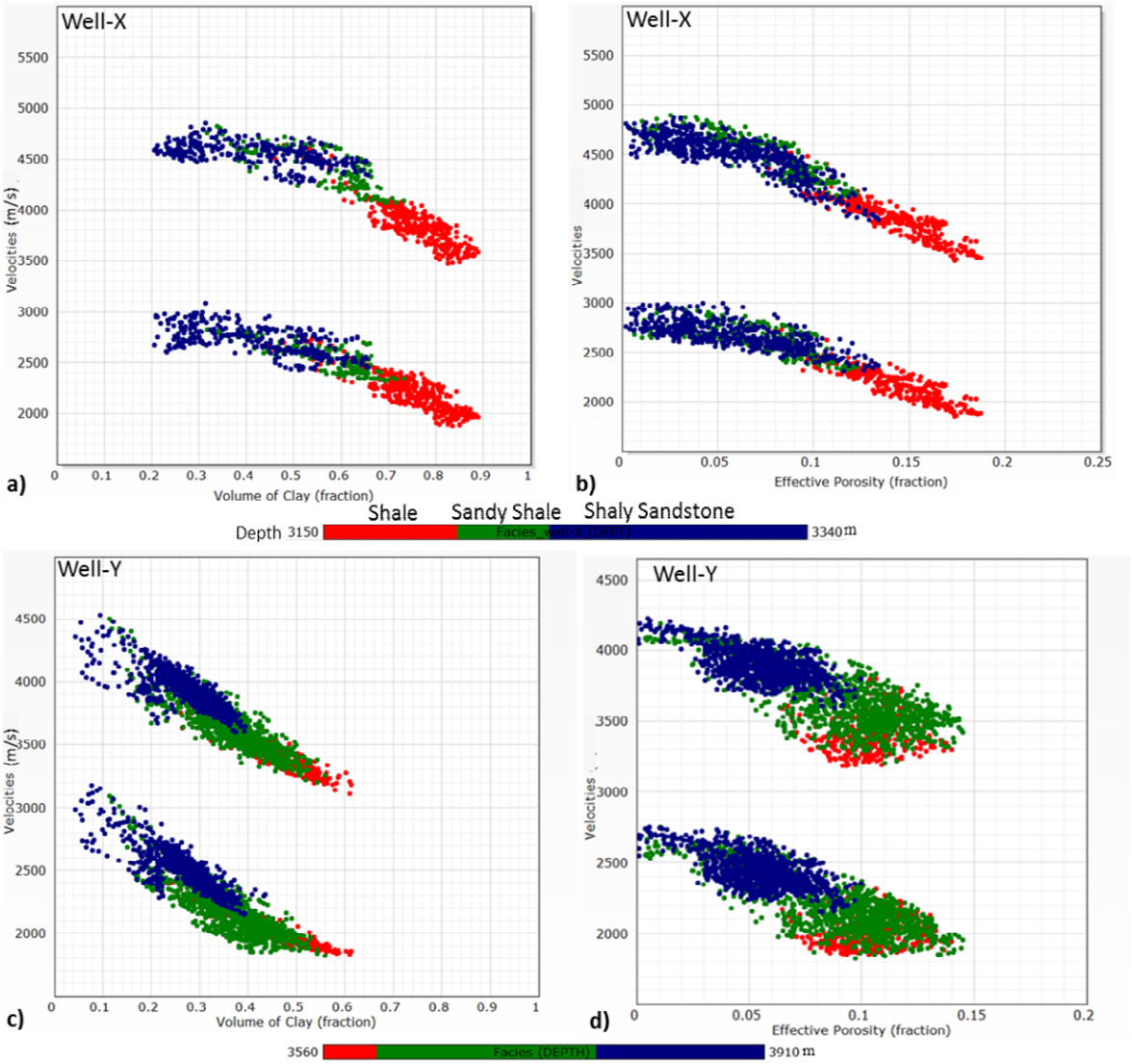

Figure 3.18 Cross plots (**a and c**) between the volume of clay (Vcl) and recorded velocities (Vp at top and Vs at the bottom of each plot), and (**b and d**) between effective porosity and velocities for wells X (exclude the silty shale intervals) and Y. The colors represent the depth interval of three facies identified in both wells.

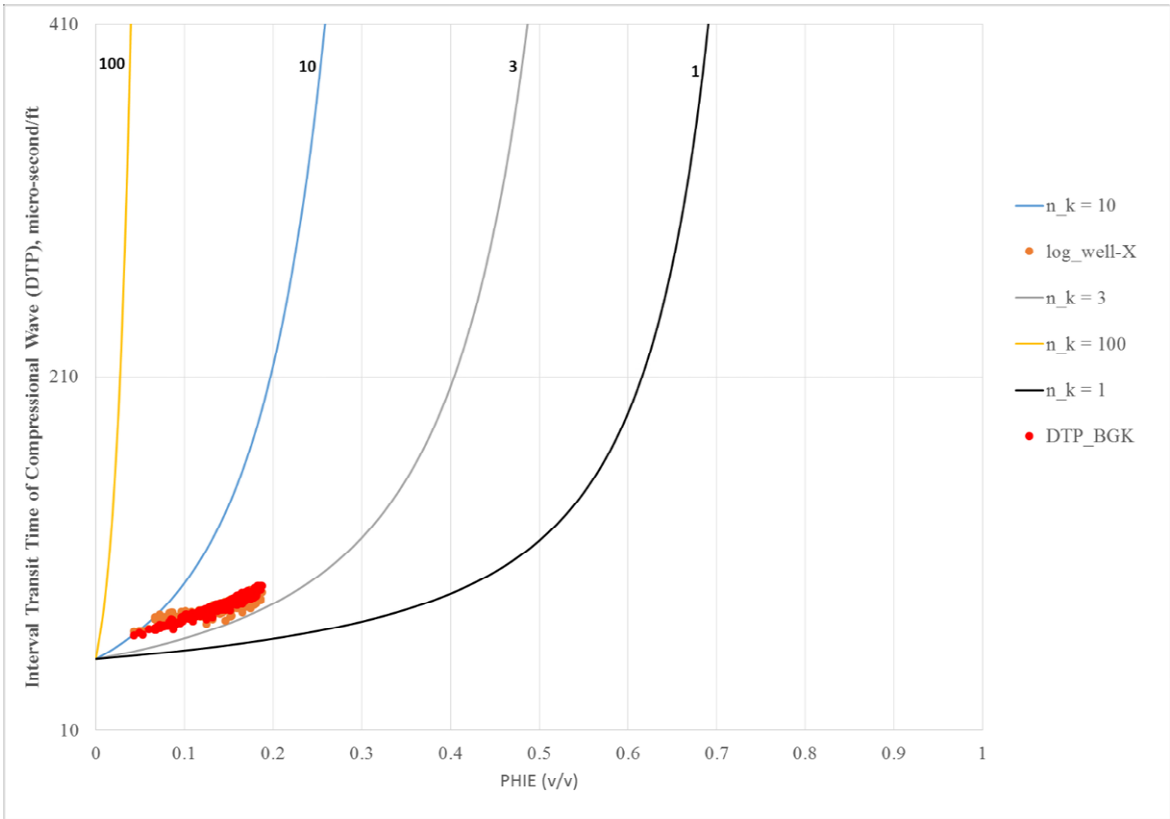

Figure 3.19 Analysis of BGK model after plotting the logged (orange color) and estimated (red color) compressional sonic against effective porosity of sandy shale and shale intervals of well-X.

3.4.3 Vs From Rock Physics-based Models (Vs_RP)

The rock physics model yielded scattered estimates of Vp and Vs when using uncorrected GR-based volume of clay estimates, and neutron-density (ND) or individual logs (neutron, density, sonic) for porosity over the intervals of sandy shale and shale in the studied wells as illustrated in supplementary plots (Appendix 3-D). This scatter was deemed to be due to the exclusion of other factors; e.g., corrected volume of clay, corrected porosity (effective), TOC, variable pore aspect ratios and effective bulk density (Xu and White, 1995; Andrew and Sandor, 2001; Mathew et al., 2002; Avseth et al., 2005; Vernik, 2016). This demonstrates the fact that the effective use of a rock physics model for Vs estimation requires corrections to log-derived input parameters. The selected models for the volume of clay and porosity were tuned based on making adjustments as needed to obtain a good match between recorded and rock physics-based Vp (Vp_RP). Ideally, of course, these log-based parameters would have been adjusted based on a comparison against core-measured, but this was not possible because no cores were available for studied intervals of wells X and Y and published

measured values in surrounding wells of the study area were used. Each well required a separate calibration to recorded Vp to get appropriate values of aspect ratios through iteration, the optimized curves of aspect ratios are given in supplementary material. Also, for both wells, allowing depth-wise variation of aspect ratio was found to be most effective. The sensitivity of input parameters to estimated velocity was studied separately and is given in Appendix 3-C.

The Xu and White model, which combines KT (for dry moduli) and the Gassmann (for fluid substitution) models, produces a scenario where low porosity does not influence low-frequency sonic waves (<100Hz generated in seismic surveys) through saturated sandy shale because excess fluid pressures due to wave propagation are dissipated (partially drained condition). Higher-frequency sonic waves for borehole sonic logging (8 kHz to 30 kHz) can create an undrained condition in the pores where incremental pressures due to sonic waves are not dissipated. The KT-Gassmann approach (Xu and White model) overestimates and gives comparatively scattered values of Vp in both wells as shown in Figure 3.20a. The data scatter observed when using the Gassmann model may be due to multiple factors, and poor connectivity of pores (very low effective porosity <5%) and undrained-condition seem to be dominant. The KT-Gassmann model seems unable to handle the lowest porosities (~0.01-0.05) in the sandy shale intervals of both wells. Due to the improved estimation of Vp using Biot's model (high frequency) compared to Gassmann, the use of Biot's model for Vp estimation seems appropriate for this work.

Both the Biot and Gassmann models produce similar results of Vs estimation, as shown in Figure 3.20b. The effective bulk density in the Biot and Gassmann equations seems to dominantly control the saturation effect on estimated Vs (Vs_RP). Fluid saturations are linearly related to effective bulk density, and saturation obtained from the Modified Simandaux model seems to have a minor impact on Vs estimation. So the accuracy of Vs_RP is dependent on the shear modulus, which was obtained from KT theory and corrected after calibration of recorded and estimated Vp. The shear modulus is least affected by fluid properties and most affected by other factors; e.g., aspect ratios, matrix moduli, Vcl and porosity. By optimizing the aspect ratios within given ranges (in Figure 3.9) and using the corrected Vcl and porosity, a good match between recorded and calculated velocities (Vp and Vs) was achieved in sandy shale and shale intervals of both wells. Calibration of estimated Vp is highly recommended in cases where Vp is available.

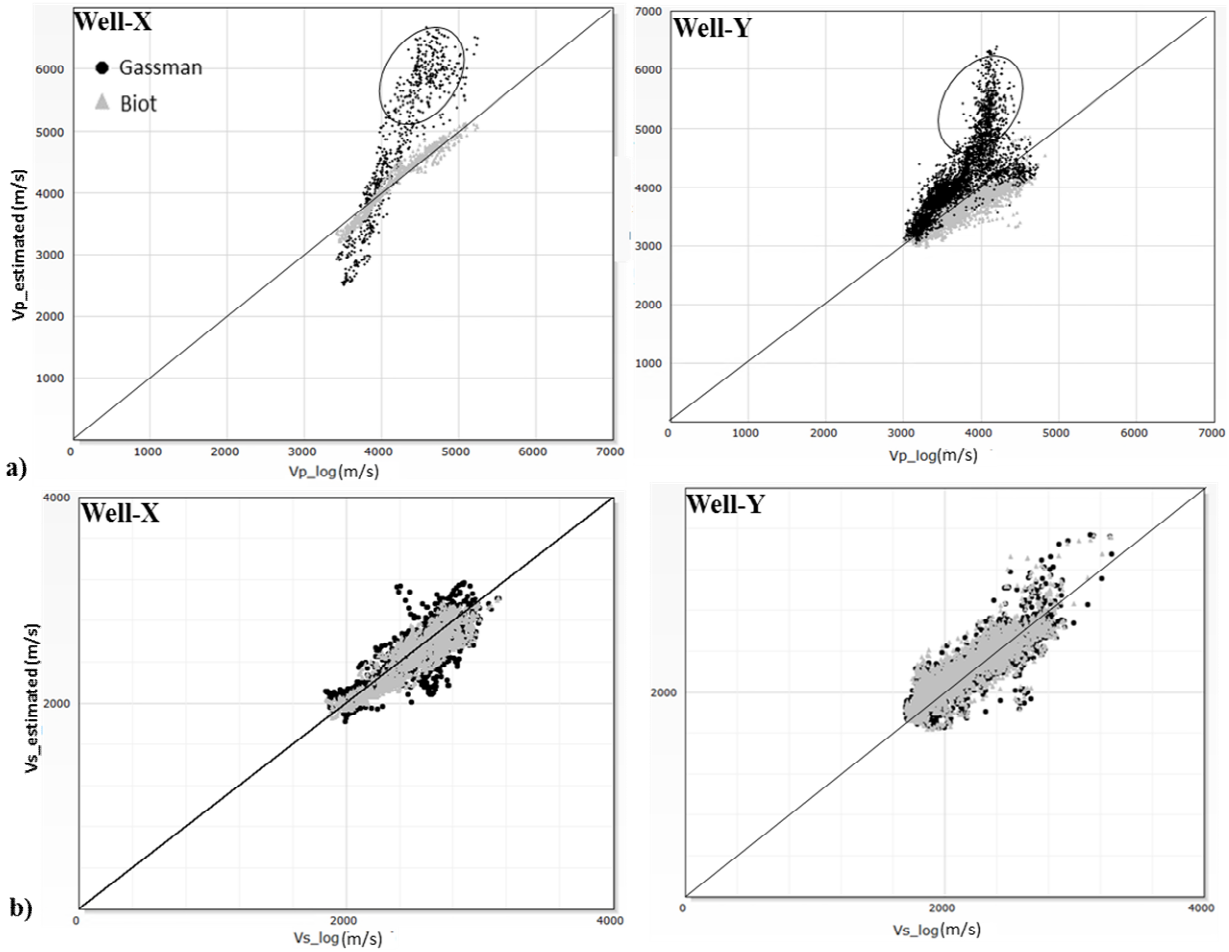

Figure 3.20 Crossplots between recorded and estimated velocities, (**a**) Vp and (**b**) Vs, to compare the Gassmann and Biot fluid substitution equations in the rock physics model adopted in this work. The encircled zones on the Vp-plots represent sandy shale intervals encountered in both wells.

The statistical analysis of Vs_RP (R^2= 0.77, and STD = 122-201) in both wells as shown in Figures 3.14 and 3.15, also enhances the authenticity regarding the modified Xu and White model, although the R^2 values are somewhat lower (0.77) than empirical models, the data points are closer to identity line compared to the empirical models. For the sandy shale intervals in both wells, it is difficult to find aspect ratios and matrix modulus, providing a 100% match between estimated and recorded velocities (Vp and Vs). This mismatch in some intervals may also be due to heterogeneity in lithology and micro-fracturing, which can be explored in future research.

3.5 Conclusion

Vp-based empirical correlations and the extended BGK model for estimating Vs produce promising results in both wells studied in this work, so these can be utilized for Vs estimation after optimization of coefficients. Among all these empirical models, the BGK model, which may be viewed as a simplified form of a rock physics model, looks effective in the estimation of Vs. The disadvantage of the empirical correlations, when considered for general use, is their inability to explain the combined impact of moduli, Vcl, porosity, TOC and fluid saturations on Vs. On the other hand, the modified Xu and White (1995) rock physics model provides a solid base for quantifying the variability of Vs and creates an opportunity to gain insight into the mechanisms of shear wave propagation through shale gas reservoirs. Although this approach requires a significant number of input parameters, these can be extracted from available log data to get stable and robust results. The input parameters for each well should be adjusted according to lithology for a rock-physics-based model, which may be the hurdle in defining a particular range of these parameters for Vs_RP in shale gas reservoirs globally. Although the use of Biot's high-frequency equation in this study may seem unconventional for intermediate frequencies used by sonic-logs, in this particular dataset, this approach yielded improved results. One significant contribution of this work is to demonstrate that the use of Biot's fluid substitution model improved the performance of Xu and White's model in gas-saturated sandy shale. Also, using this approach the equations for estimating Vs can be optimized using Vp data, meaning that optimization is possible in cases where Vs data are not available; this represents a significant advantage over the empirical models, which require Vs data for optimization. The modified Xu and White model is thus deemed to be the best option available at present, and can be further evaluated by future researchers once cores are obtained. The accurate estimation of Vs using commonly available well log data will enhance our confidence in dynamic elastic properties, which have a variety of uses in drilling, completion and production operations.

3.5.1 Recommendation

This study relies on available logs and published data of porosity, TOC and mineralogy because the study area is under exploration phase to assess shale gas prospects. Cores samples are not available yet for sandy shales and shales in the LGF for conducting the laboratory tests required to determine ultrasonic velocities, porosity, TOC and mineralogy. Further, the impact of squirt flow mechanism should be evaluated once cores

are available. The impact of TOC on velocities can also be explored at the laboratory scale, and some modifications to Kuster and Toksoz model (1974) can be suggested. Therefore, it is recommended that the results should be confirmed after getting cores from relevant wells. The use of resistivity logs for the estimation of Vs in shale gas reservoir is also needed to be explored.

Acknowledgment

The authors acknowledge the DGPC (Directorate-General for Petroleum Concession) of Pakistan for providing the data, the Department of Civil, Geological and Environmental Engineering, University of Saskatchewan, Saskatoon, Canada, for providing computing facilities and technical support, and the Department of Geological Engineering, University of Engineering & Technology Lahore, Pakistan, for funding the Ph.D. studies. We are thankful to Dr. Wayne D Pennington and Mr. Michel Krief for a fruitful discussion on different issues relevant to shear wave velocity estimation.

References

Abbasi, A. H., Mehmood, F., Kamal, M., & Naqvi, S. (2014). Shale oil and gas: lifeline for Pakistan. A Report, Islamabad: Sustainable Development Policy Institute, Pakistan, 136.

Andrew, R, and Sandor B., (2001). *Shear wave velocity estimation techniques: a comparison*: Canadian Society of Exploration Geophysicist (CSEG) Convention, 1-6.

Ahmad, N., & Chaudhry, S. (2002). Kadanwari Gas Field, Pakistan: A disappointment turns into an attractive development opportunity. *Petroleum Geoscience,8*(4), 307-316. doi:10.1144/petgeo.8.4.307

Avseth, P., Mukerji, T., & Mavko, G. (2005). *Quantitative seismic interpretation: Applying rock physics tools to reduce interpretation risk.* Cambridge: Cambridge University Press.

Azeem, T., Chun, W. Y., M., Khalid, P., Qing, L. X., Ehsan, M. I., Wei, X. (2017). An integrated petrophysical and rock physics analysis to improve reservoir characterization of

Cretaceous sand intervals in Middle Indus Basin, Pakistan. *Journal of Geophysics and Engineering, 14(2),* 212-225. doi:10.1088/1742-2140/14/2/212

Baig, M. O., Harris, N. B., Ahmed, H., & Baig, M. O. (2016). Controls On Reservoir Diagenesis In The Lower Goru Sandstone Formation, Lower Indus Basin, Pakistan. *Journal of Petroleum Geology,39(1),* 29-47. doi:10.1111/jpg.12626

Batzle, M., & Wang, Z. (1992). Seismic properties of pore fluids. *Geophysics,57(11),* 1396-1408. doi:10.1190/1.1443207.

Berger, A., Gier, S., & Krois, P. (2009). Porosity-preserving chlorite cements in shallow-marine volcaniclastic sandstones: Evidence from Cretaceous sandstones of the Sawan gas field, Pakistan: *AAPG Bulletin,93(5),* 595-615. doi:10.1306/01300908096

Berryman, J.G., (1995). Mixture theories for rock properties, in *A Handbook of Physical Constants,* T.J. Ahrens, ed. American Geophysical Union, Washington, D.C., 205-228.

Biot, M. A. (1956). Theory of Propagation of Elastic Waves in a Fluid-Saturated Porous Solid. II. Higher Frequency Range. *The Journal of the Acoustical Society of America*, *28*(2), 179–191. doi: 10.1121/1.1908241

Bland, J. M., and Altman, D. G., (1996). "Statistics notes: measurement error". *BMJ, 312* (7047), 1654. https://doi.org/10.1136/bmj.312.7047.1654

Brie, A., Pampuri, F., Marsala, A., & Meazza, O. (1995). *Shear Sonic Interpretation in Gas-Bearing Sands*. Proceedings of SPE Annual Technical Conference and Exhibition. doi:10.2523/30595-ms

Castagna, J. P., Batzle, M. L., & Eastwood, R. L. (1985). Relationships between compressional-wave and shear-wave velocities in clastic silicate rocks. *Geophysics*, *50*(4), 571–581. doi: 10.1190/1.1441933

Chopra, S., & Castagna, J. P. (2014). *AVO*. Tulsa, Okl.: Soc. of Exploration Geophysicists.

Clavier, C., Hoyle, W., & Meunier, D. (1971). Quantitative Interpretation of Thermal Neutron Decay Time Logs: Part II. Interpretation Example, Interpretation Accuracy, and Time-Lapse Technique. *Journal of Petroleum Technology*, *23*(6). doi: 10.2118/2658-pa

Crain, R. E., (2016). Porosity from Sonic Logs: *Crain's Petrophysical Handbook*, https://www.spec2000.net/12-phidt.htm accessed on 29th February 2016.

Crain, R. E, and Holgate, D., (2014). *A 12-step program to reduce uncertainty in kerogen-rich reservoirs:* FOCUS, GeoConvention, 1-11.

Domenico, S.N., 1976. Effect of Brine-Gas Mixture on Velocity in an Unconsolidated Sand Reservoir. *Geophysics 41 (5),* 882–894. doi:10.1190/1.1440670.

Draper, N. R. and Smith H., (1998). *Applied Regression Analysis*, Willey-Interscience, 471, http://onlinelibrary.wiley.com/doi/10.1002/9781118625590.ch1/pdf

Dvorkin, J. P. (2008). Yet another Vs equation. *Geophysics,73*(2). doi:10.1190/1.2820604

Eastwood, R. L, and Castagna, J. P., (1983). *Basis for interpretation of Vp/Vs, ratios in complex lithologies:* Society of Professional Well Log Analysts, 24th Annual Logging Symposium Proceedings.

Ehsan, M., Gu, H., Akhtar, M. M., Abbasi, S. S., & Ullah, Z. (2017). Identification of Hydrocarbon Potential of Talhar Shale: Member of Lower Goru Formation Using Well Logs Derived Parameters, Southern Lower Indus Basin, Pakistan. *Journal of Earth Science*, *29*(3), 587–593. doi: 10.1007/s12583-016-0910-2

Entyre, L. M. (1993, January 1). *Comparative Performance Of A Dual Water Model Equation In Laminar Shaly Sands.* Society of Petrophysicists and Well-Log Analysts.

Gassmann, F., 1951,. Ijber Die Elastizitat poroser Medien. Eel: der Natul: Gesellschaft in Zurich, 96, 1-23.

Glorioso, J. C., & Rattia, A. J. (2012, January). *Unconventional Reservoirs: Basic Petrophysical Concepts for Shale Gas.* Society of Petroleum Engineers. doi:10.2118/153004-MS

Greenberg, M. L., & Castagna, J. P. (1992). Shear-Wave Velocity Estimation In Porous Rocks: Theoretical Formulation, Preliminary Verification And Applications1. *Geophysical Prospecting, 40(2),* 195–209. doi: 10.1111/j.1365-2478.1992.tb00371.x

Han, D. H., Nur, A., & Morgan, D. (1986). Effects of porosity and clay content on wave velocities in sandstones. *Geophysics, 51(11),* 2093–2107. doi: 10.1190/1.1442062

Hashin, Z., & Shtrikman, S. (1963). A variational approach to the theory of the elastic behaviour of multiphase materials. *Journal of the Mechanics and Physics of Solids, 11(2),* 127-140. doi:10.1016/0022-5096(63)90060-7

Hacikoylu, P., Dvorkin, J., & Mavko, G. (2006). Resistivity-velocity transforms revisited. *The Leading Edge, 25(8),* 1006–1009. doi: 10.1190/1.2335159

Holmes, M., Holmes, A., & Holmes, D. (2014, July). *A Comprehensive Deterministic Petrophysical Analysis Procedure, For Reservoir Characterization: Conventional and Unconventional Reservoirs.* Search and Discovery Article #90193 © 2014 Rocky Mountain Section AAPG Annual Meeting, Denver, Colorado, July 20-22, 2014.

Katahara, K. W. (1995, July). *Gamma Ray Log Response In Shaly Sands.* Society of Petrophysicists and Well-Log Analysts

Kadkhodaie, A., & Rezaee, R. (2016). A new correlation for water saturation calculation in gas shale reservoirs based on compensation of kerogen-clay conductivity. *Journal of Petroleum Science and Engineering,146,* 932-939. doi:10.1016/j.petrol.2016.08.004

Kadri, I. B. (1995). *Petroleum geology of Pakistan*. Karachi: Pakistan Petroleum Ltd.

Kazmi, A. H., & Abbasi, I. A. (2008). *Stratigraphy & historical geology of Pakistan*. Peshawar: Dept. & National Centre of Excellence in Geology.

Keys, R. G., & Xu, S. (2002). An approximation for the Xu-White velocity model. *Geophysics*, *67*(5), 1406–1414. doi: 10.1190/1.1512786

Kazmi, A. H. and Jan, M. Q. (1997). *Geology and Tectonics of Pakistan*. Karachi, Pakistan: Graphic Publishers.

Kuster, G. T., & Toksöz, M. N. (1974). Velocity And Attenuation Of Seismic Waves In Two-Phase Media: Part I. Theoretical Formulations. *Geophysics*, *39*(5), 587–606. doi: 10.1190/1.1440450

Larionov, V. V., (1969). Radiometry of boreholes (in Russian): *NEDRA*, Moscow, U.S.S.R.

Liu, Y. and Chen, Z., (2012). *Shear velocity prediction and its rock mechanic Implications*: Geological Survey of Canada, Geo-Convention,1-5

Marion, D., Nur, A., Yin, H., & Han, D. (1992). Compressional velocity and porosity in sand-clay mixtures. *Geophysics*, *57*(4), 554–563. doi: 10.1190/1.1443269

Matthew B, Carr, L. H, and Jack D., (2002, May*). Shear velocity prediction in the Norwegian Sea*: Proceedings of EAGE 64th Conference & Exhibition, Italy, 1-4, http://www.qipetrophysics.com/Files/2002_eage_vs_prediction_carr_etal.pdf

Mavko, G, Mukerji, T, and Dvorkin, J., (2003). *The Rock Physics Handbook*: *Tools for Seismic Analysis of Porous Media.* Cambridge University Press, New York, 162-192.

Mavko, G., & Jizba, D. (1991). Estimating grain-scale fluid effects on velocity dispersion in rocks. *Geophysics,56(12),* 1940-1949. doi:10.1190/1.1443005

Nazeer, A., Abbasi, S. A., & Solangi, S. H. (2016). Sedimentary facies interpretation of Gamma Ray (GR) log as basic well logs in Central and Lower Indus Basin of Pakistan. *Geodesy and Geodynamics,7(6),* 432-443. doi:10.1016/j.geog.2016.06.006

Nur, A., & Simmons, G. (1969). The effect of saturation on velocity in low porosity rocks. *Earth and Planetary Science Letters,7*(2), 183-193. doi:10.1016/0012-821x(69)90035-1.

Passey Q. R., S. Creaney, J. B. Kulla, F. J. Moretti and J. D. Stroud, (1990). A Practical Model for Organic-Richness from Porosity and Resistivity Logs: *AAPG Bulletin, 74 (12),* 1777-1794.

Passey, Q. R., Bohacs, K., Esch, W. L., Klimentidis, R., & Sinha, S. (2010, January*). From Oil-Prone Source Rock to Gas-Producing Shale Reservoir* - Geologic and Petrophysical Characterization of Unconventional Shale Gas Reservoirs. Society of Petroleum Engineers. doi:10.2118/131350-MS

Pickett, G.R., (1963). Acoustic character logs and their application in formation evaluation: *Journal of Petroleum Technology, 15,* 659-667.

Rezaee, R. (2015). *Fundamentals of gas shale reservoirs*. Hoboken (New Jersey): Wiley.

Ruiz, F, and Azizov, I., (2011, September) *Fluid substitution in tight shale using the soft-porosity model,* Annual International Meeting, SEG San Antonio, Expanded Abstracts.

Raymer, L. L., Hunt, E. R., and Gardner, J. S., (1980). *An improved sonic transit time-to-porosity transform,* SPWLA 21 Annual Logging Symposium. 1-12.

Ruiz, F., Dvorkin, J., (2010). Predicting elasticity in nonclastic rocks with a differential effective medium model. *Geophysics 75 (1).* doi:10.1190/1.3267854.

Sarker, R., & Batzle, M. (2010, January). *Anisotropic Elastic Moduli of the Mancos B Shale-An Experimental Study.* Society of Exploration Geophysicists.

Saxena, V., Krief, M., & Adam, L. (2018). *Handbook of borehole acoustics and rock physics for reservoir characterization.* Amsterdam: Elsevier.

Schlumberger, (2011). Logging Quality Control Reference Manual, Retrieved at https://www.slb.com/resources/publications/books/lqcrm.aspx

Siddiqui, F. I., Adhami, A., Asghar, A., Hussain, A., & Khan, M. (2013). *Shale Gas Potential of the Lower Goru Formation over the Lakhra High in Lower Indus Basin, Pakistan*. Search

and Discovery, Retrieved from: http://www.searchanddiscovery.com/abstracts/html/2013/90163ace/abstracts/huss.htm

Siggins, A., & Dewhurst, D. (2010, April). *Elastic Wave Attenuation in a Clay Rich Shale*. EAGE Shale Workshop. doi:10.3997/2214-4609.20145374

Simm, R., & Bacon, M. (2014). *Seismic amplitude: An interpreter's handbook.* Cambridge: Cambridge University Press.

Smith, M. A., Karl W., and Schwab, K. K. B., (1992). Organic Facies Analysis of Cretaceous Petroleum Source Rocks, Southern Indus Basin, Pakistan. *AAPG Bulletin, 76(7),* 1126-1127

Smith, T. M., Sondergeld, C. H., & Rai, C. S. (2003). Gassmann fluid substitutions: A tutorial. *Geophysics*,*68*(2), 430-440. doi:10.1190/1.1567211

Sondergeld, C. H., Newsham, K. E., Comisky, J. T., Rice, M. C., & Rai, C. S. (2010, January). *Petrophysical Considerations in Evaluating and Producing Shale Gas Resources*. Society of Petroleum Engineers. doi:10.2118/131768-MS

Stieber, S. J., 1970, *Pulsed neutron capture log evaluation - Louisiana Gulf Coast*: Society of Petroleum Engineers, 45th Annual Fall Meeting.

Stoll, R. D. (1977). Acoustic Waves In Ocean Sediments. *Geophysics, 42*(4), 715–725. doi: 10.1190/1.1440741

Tosaya, C.A., (1982). Acoustical properties of clay-bearing rocks: Ph.D. thesis, Stanford University. Retrieved at https://pangea.stanford.edu/departments/geophysics/dropbox/SRB/public/docs/theses/SRB_015_JUN82_Tosaya.pdf

US, EIA. (2015). Technically Recoverable Shale Oil and Shale Gas Resources: India and Pakistan, A Report, Energy Information Administration (EIA), 42-50. (Retrieved 2016, from https://www.eia.gov/analysis/studies/worldshalegas/pdf/India_Pakistan_2013-15.pdf/)

Vernik, L. (2016). *Seismic petrophysics in quantitative interpretation.* Tulsa, OK: SEG, Society of Exploration Geophysicists.

Vernik, L., Castagna, J., & Omovie, S. J. (2017). S-wave velocity prediction in unconventional shale reservoirs. *Geophysics, 83(1).* doi:10.1190/geo2017-0349.1

Wang, G, and T R. Carr. (2012). Marcellus Shale Lithofacies Prediction by Multiclass Neural Network Classification in the Appalachian Basin. *Mathematical Geosciences, 44 (8),* 975–1004., doi:10.1007/s11004-012-9421-6.

Williams, D. M., (1990). *The acoustic log hydrocarbon indicator:* Society of Petrophysicists and Well Log Analysts, 31st Logging Symposium, W 1-22.

Wyllie, M. R., Gregory, A. R., & Gardner, L. W. (1956). Elastic Wave Velocities In Heterogeneous And Porous Media. *Geophysics,21(1),* 41-70. doi:10.1190/1.1438217

Wu, P., & Aguilera, R. (2013, November). *Uncertainty Analysis of Shale Gas Simulation: Consideration of Basic Petrophysical Properties*. Society of Petroleum Engineers. doi:10.2118/167236-MS

Xu, S, and White, R. E., (1995). A new velocity model for clays and mixtures: *Geophysical Prospecting, 43,* 91-118.

Yan, J., Li, X.Y, and Liu, E., (2002). Effects of pore aspect ratios on velocity prediction from well-log data: *Geophysical Prospecting, 50,* 289–300.

Zhang, C., Shan, W. and Wang, X. (2018). Quantitative Evaluation of Organic Porosity and Inorganic Porosity in Shale Gas Reservoirs Using Logging Data. *Energy Sources, Part A: Recovery, Utilization, and Environmental Effects, 41,* 811–828., doi:10.1080/15567036.2018.1520361.

Appendix 3-A: DeltaLogR Technique for TOC Estimation

The Delta Log R technique was developed by Passey et al. (1990). It involves using an overlay between a porosity log and a resistivity log to capture the deviation from expected formation log response values due to the presence of organic matter.

$$\mathrm{TOC} = \mathrm{DeltaLogR_{Sonic}} * 10^{(2.297-(0.169*\mathrm{LOM}))} \quad \text{..... A}$$

Below are the equations for input parameters of equation A.

$$\mathrm{DeltaLogR_{Sonic}} = \log\left(\frac{\mathrm{R_{LLD}}}{\mathrm{R_{LLD_{baseline}}}}\right) + 0.02 * \left(\mathrm{DT_{p-sonic}} - \mathrm{DT_{p-sonic\ baseline}}\right)$$

$$\mathrm{R_{LLD_{baseline}}}\ (\text{for both wells}) = 5\ \text{ohm. m}$$

$$\mathrm{DT_{p-sonic\ baseline}}(\text{for both wells}) = 295\,\frac{\mu\text{sec}}{\text{m}}$$

$$\mathrm{LOM} = 0.099 * \mathrm{x}^5 - 2.159 * \mathrm{x}^4 + 12.392 * \mathrm{x}^3 - 29.032 * \mathrm{x}^2 + 32.53 * \mathrm{x} - 3.034$$

Where:

LOM = Level of maturity

x = VR = Vitrinite reflectance value = 0.90 (from laboratory testing for both wells)

TOC = total organic carbon in weight fraction

Appendix 3-B: Scalars in the Kuster and Toksoz theory

$$T_{ijij} = \frac{3F_1}{F_2} \quad \text{.....B1}$$

$$T_{ijij} - \frac{1}{3T_{iijj}} = \frac{2}{F_3} + \frac{1}{F_4} + (F_4F_5 + F_6F_7 - F_8F_9)/F_2F_4 \quad \text{.....B2}$$

Where:

$$\boldsymbol{F_1} = 1 + \left(\frac{\mu'}{\mu_m} - 1\right)\left[\frac{3}{2}(g+\theta) - R\left(\frac{3}{2}g + \frac{5}{2}\theta - \frac{4}{3}\right)\right]$$

$$\boldsymbol{F_2} = 1 + \left(\frac{\mu'}{\mu_m} - 1\right)\left[1 + \frac{3}{2}(g+\theta) - \left(\frac{R}{2}\right)(3g+5\theta)\right] + \frac{1}{3}\left(\frac{K'}{K_m} - \frac{\mu'}{\mu_m}\right)(3-4R)$$
$$+ \frac{\frac{\mu'}{\mu_m}-1}{2}\left(\left(\left(\frac{\mu'}{\mu_m} - 1\right) + \frac{1}{3}\left(\frac{K'}{K_m} - \frac{\mu'}{\mu_m}\right)\right)(3-4R)\right)[g + \theta - R(g - \Phi + 2\theta^2)])$$

$$\boldsymbol{F_3} = 1 + \frac{\frac{\mu'}{\mu_m} - 1}{2}\left[R(2-\theta)+)\frac{1+\alpha^2}{\alpha^2}g(R-1)\right]$$

$$\boldsymbol{F_4} = 1 + \frac{\frac{\mu'}{\mu_m} - 1}{4}[3\theta + g - R(g-\theta)]$$

$$\boldsymbol{F_5} = \left(\frac{\mu'}{\mu_m} - 1\right)\left[R\left(g + \theta - \frac{4}{3}\right) - g\right] + \frac{1}{3}\left(\frac{K'}{K_m} - \frac{\mu'}{\mu_m}\right)\theta(3-4R)$$

$$\boldsymbol{F_6} = 1 + \left(\frac{\mu'}{\mu_m} - 1\right)[1 + g - R(g+\theta)] + \frac{1}{3}\left(\frac{K'}{K_m} - \frac{\mu'}{\mu_m}\right)(1-\theta)(3-4R)$$

$$\boldsymbol{F_7} = 2 + \frac{\left(\frac{\mu'}{\mu_m} - 1\right)}{4}[9\theta + 3g - R(5\theta + 3g)] + \frac{1}{3}\left(\frac{K'}{K_m} - \frac{\mu'}{\mu_m}\right)\theta(3-4R)$$

$$\boldsymbol{F_8} = \left(\frac{\mu'}{\mu_m} - 1\right)\left[1 - 2R + \frac{g}{2}(R-1) + \frac{\theta}{2}(5R-3)\right] + \frac{1}{3}\left(\frac{K'}{K_m} - \frac{\mu'}{\mu_m}\right)(1-\theta)(3-4R)$$

$$\boldsymbol{F_9} = \left(\frac{\mu'}{\mu_m} - 1\right)[g(R-1) - R\theta] + \frac{1}{3}\left(\frac{K'}{K_m} - \frac{\mu'}{\mu_m}\right)\theta(3-4R)$$

Where: $R = \frac{3\mu}{3K+4\mu}, g = \frac{\alpha^2}{1-\alpha^2}(3\theta - 2), \theta = \alpha/(1-\alpha^2)^{3/2}\left[\cos^{-1}\alpha - \alpha(1-\alpha^{1/2})\right]$

$\mu', K' = shear\ and\ bulk\ modulus\ of\ inclusion,$

$\mu_m, K_m = shear\ and\ bulk\ modulus\ of\ matrix$

Appendix 3-C: Sensitivity of Estimated Velocities against Different Input Parameters

The base-case parameters (Vcl=0.12 and 0.65, effective porosity = 0.08 and 0.2) chosen correspondence to two depths (3680m and 3590m, respectively) in well-Y. The plots (as shown in Figure C) show the variability of velocities obtained from the proposed rock physics model to the following parameters: a) volume of clay (Vcl); b) effective porosity; c) total organic carbon (TOC); and d) pore aspect ratios. All of the plots were generated at fixed fluid saturation (Sw=60% and Sg=40%). It is observed the Vp is decreasing with the increase of Vcl and Vp does not vary significantly with the increase of effective porosity. The TOC seems to have a negligible impact on Vp in the proposed model and it is consistent with TOC-velocity (at low TOC of 1% to 4%) relationship in Lower Goru Formation, although at higher TOC (>4%) it will be appropriate to evaluate TOC (consider maturity and type of

kerogen) in detail. The Vp seems to more sensitive to aspect ratios of sand pores compared to clay pores, as illustrated in plot-d, which is consistent with the findings of Xu and White (1995). Aspect ratio controls the porosity-velocity relationship because, at constant aspect ratio, the Vp does not vary significantly with porosity. The velocities, using Gassmann instead of Biot as shown in plot-b, are much higher at low porosities (<0.08) and constant Vcl (black dotted line for Vcl = 0.65, and grey dotted line for Vcl=0.12).

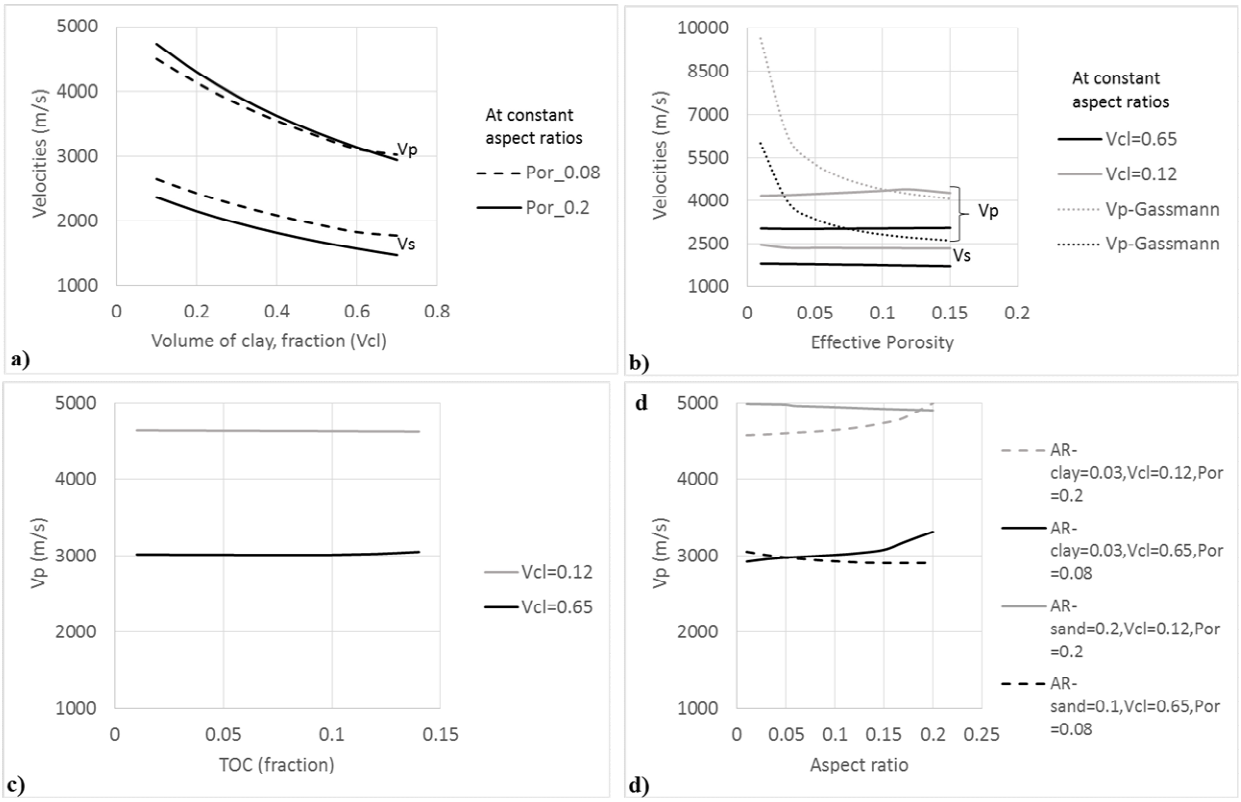

Figure 3-C Shows cross plots of (a) Vcl, (b) effective porosities, (c) TOC, and (d) aspect ratios versus estimated velocities. The dotted curves in the plot (b) are the velocities estimated using Gassmann fluid substitution equations at Vcl=0.65 (black dotted line) and Vcl=0.12 (grey dotted line).

Appendix 3-D: Supplementary Plots

3-D.1 Sensitivity of Velocities to Input Parameters

Figures 3-D.1 and 3-D.2 show plots for well-X and well-Y, respectively, between estimated (using modified Xu and White model for three plots (a, b and c) and KT-Gassmann for plt d) and measured velocities in sandy shale intervals. Following is the detail description of each plot.

Well X:

a) For the uncorrected volume of clay (from GR log using maximum and minimum observed values) and total porosity from density log ($\phi_t = \frac{\rho_m - \rho_b}{\rho_m - \rho_{fl}}$). It can be observed that estimated values are underestimated, which is due to overestimation of the volume of shale and porosity in sandy shale and shale intervals of well-X.

b and c) Even after using other techniques of porosity estimation (a combination of density and neutron logs (plot b) or sonic log (plot c)) do not improve the results.

d) The volume of clay was corrected (using Lev Vernik technique), and total porosity was determined using a combination of neutron-density logs. This time the fluid substitution was done through the use of Gassmann instead of Biot. It can be observed that the use of total porosity (PHIT_ND) and corrected-Vcl in KT-Gassmann produce scattered underestimated results.

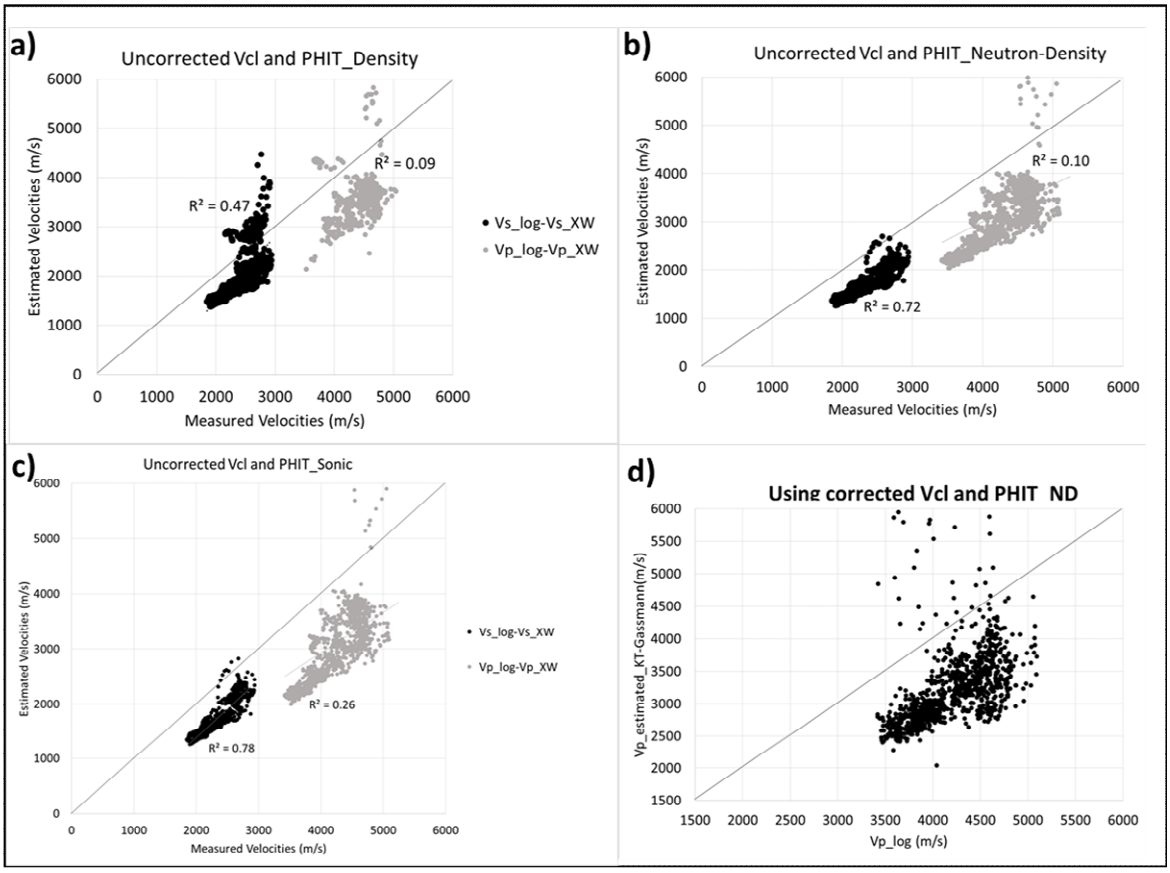

Figure 3-D.1 Cross plots between estimated and measured velocities under different scenario for well-X.

Well Y:

The results are a little better than well-X, but still are poor as shown in Figure 3-D.2.

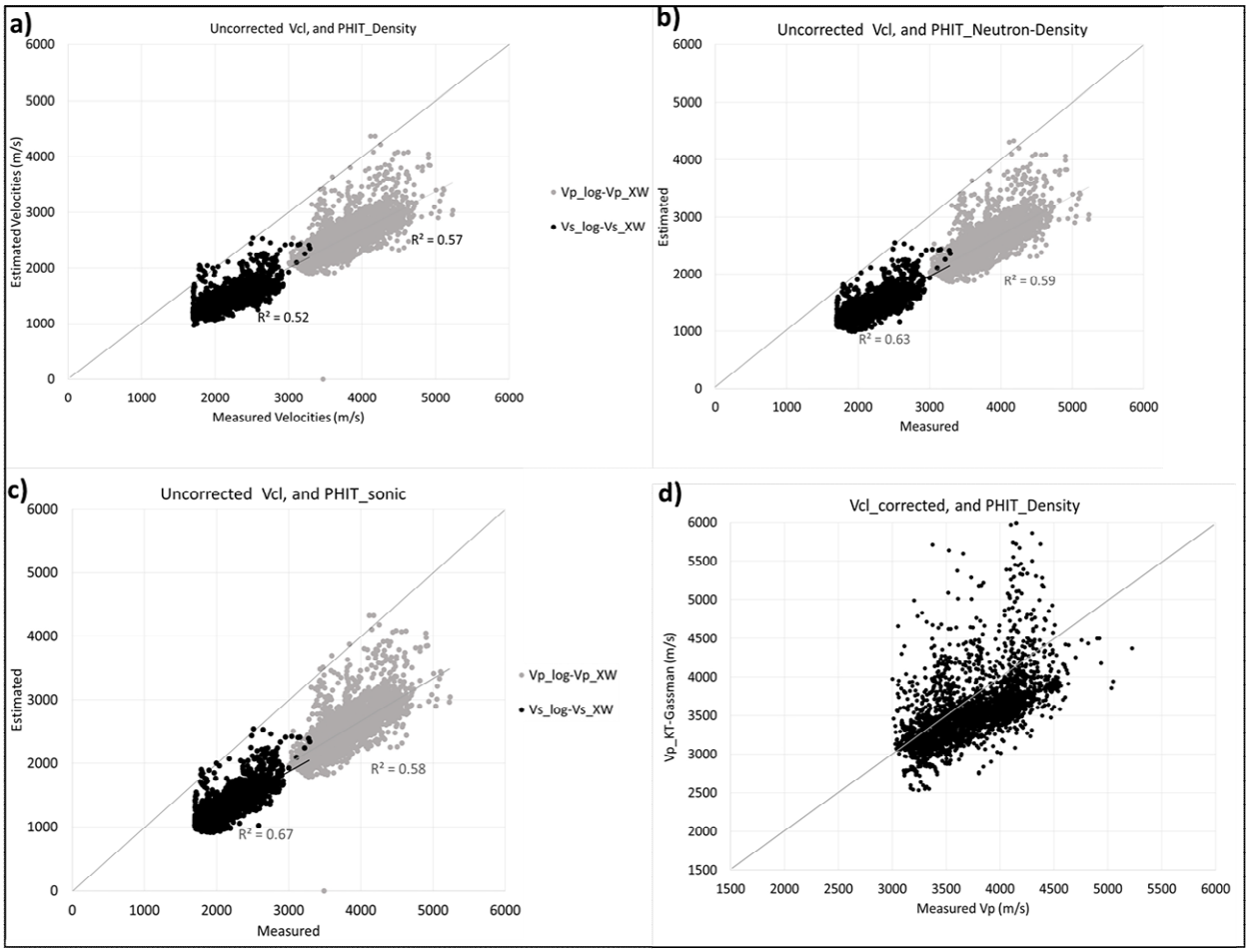

Figure 3-D.2 Cross plots between estimated and measured velocities under different scenario for well-Y.

3-D.2 Vcl, Porosity_corrected (effective porosity), TOC and optimized Aspect_ratios

Figure.3-D.3 shows the plot of different input parameters against depth in both wells. The aspect ratios were optimized along the depth to get a better match between estimated and measured Vp. It is observed that the Vcl is the major controlling factor compared to other input parameters for the estimation of Vp.

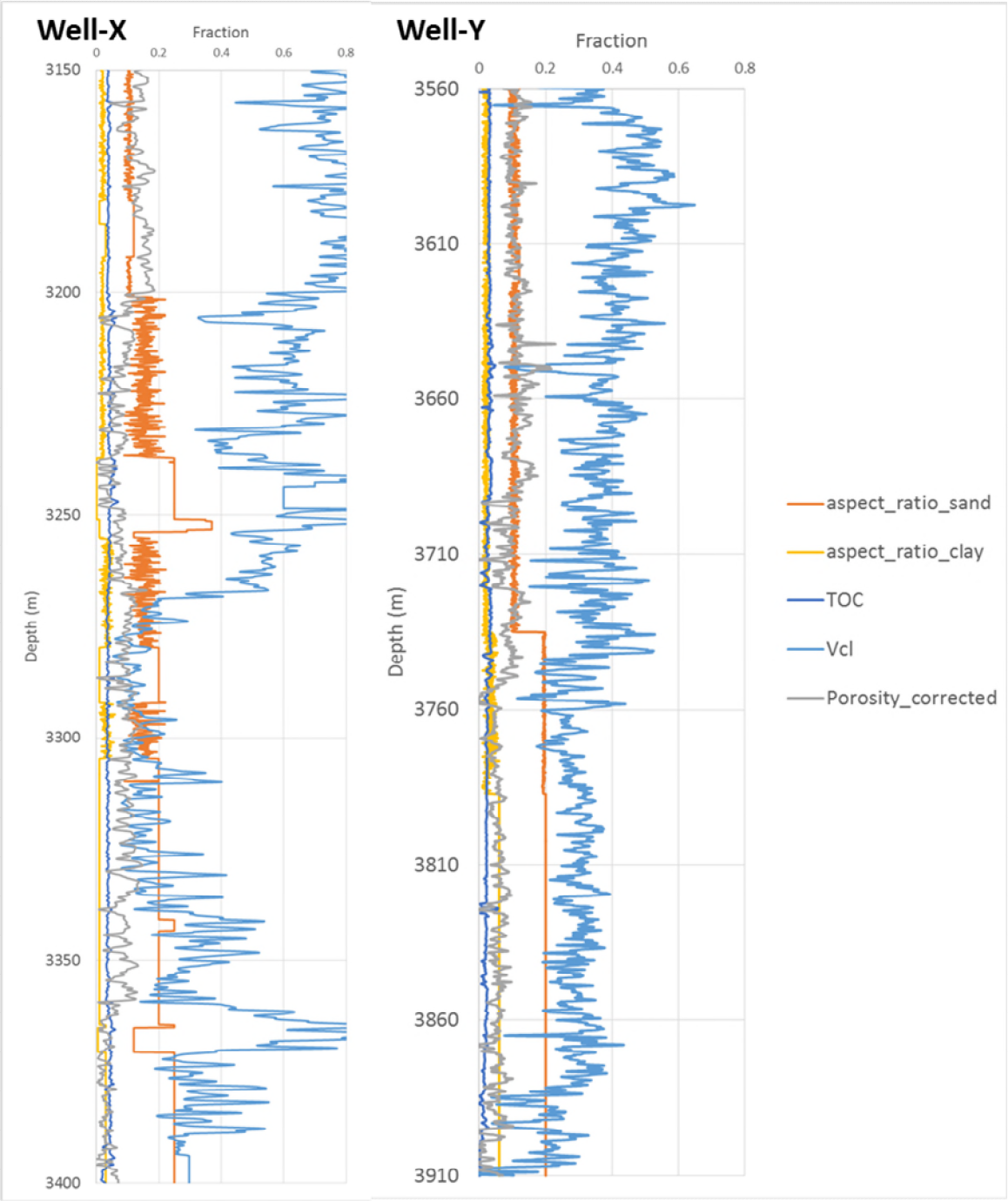

Figure 3-D.3 Plots of different input parameters used for rock-physics model.

3-D.3 Vs2 and Vs4 Model

Vs2 and Vs4 models were tested for effective porosity (PHIT_corrected) and Vcl to check the improvements in results. Figure 3-D.4 shows the cross plots of estimated Vs2 (a) and Vs4 velocities (b) and measured Vs. The original equations and estimated data points are shown in black color, and modified equations and data points are plotted in grey color.

After modification to coefficients (equations in grey color), the r-square value (0.11 for Vs2 and 0.13 for Vs4) does not improve significantly compared to r-square (0.14 for Vs2 and 0.17 for Vs4) of original equations. Even after excluding the clean sandstone interval of 3270m to 3340m, and estimated the velocities using modified equations (data points in green color) the r-square (0.17) is still weak. In all cases, the estimated data is falling below (underestimated) and above (overestimated) the identity line. These results show the inability of these equations to handle the effects of variability in porosity and Vcl on velocities for this dataset.

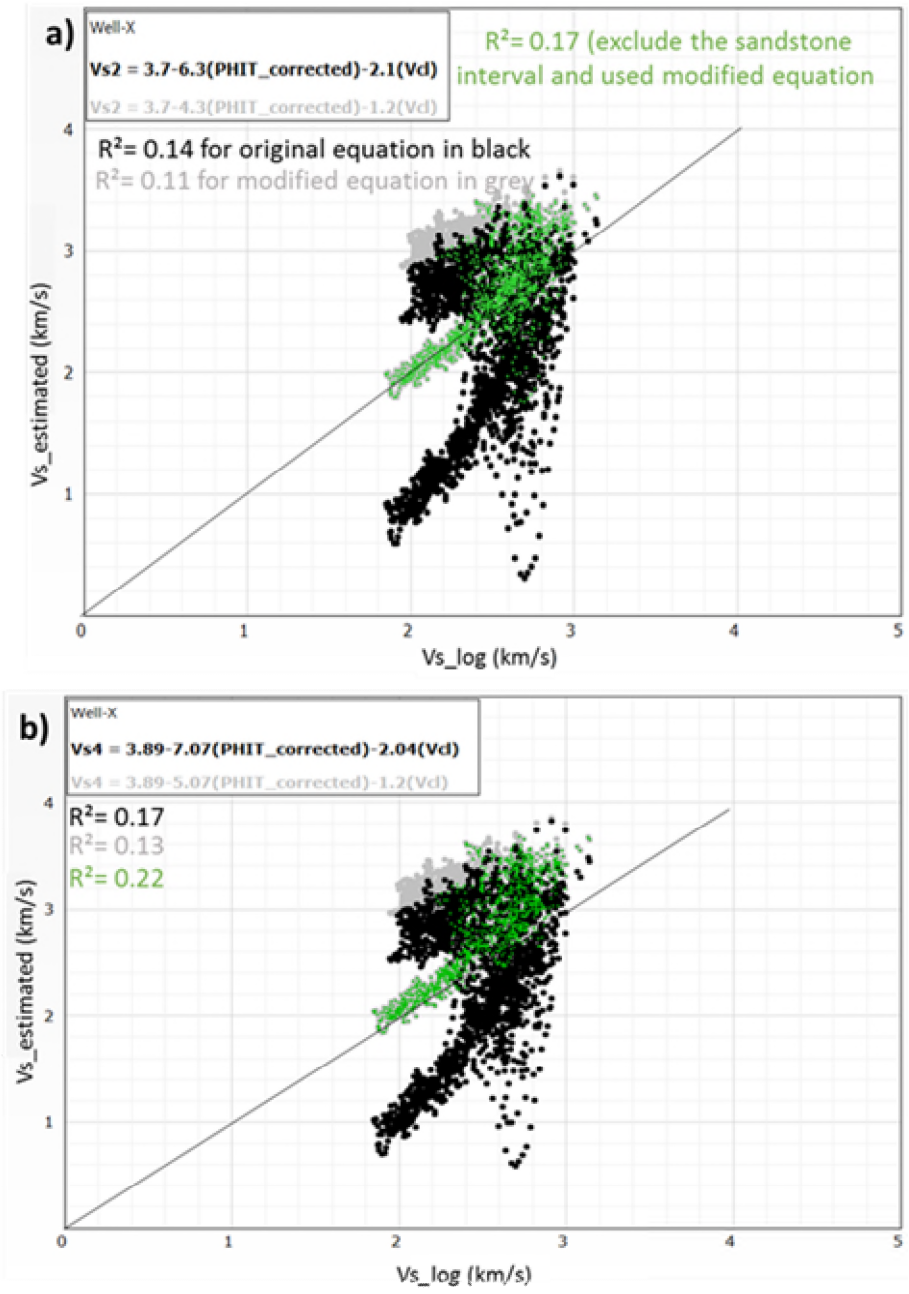

Figure 3-D.4 Cross plot between estimated (Vs2 (a), Vs4 (b)) and measured Vs. The grey (with modified coefficients) and black colors represent the original equation.

Chapter 4 - An Integrated Petrophysical and Geomechanical Characterization of Sembar Shale in the Lower Indus Basin of Pakistan, Using Well logs and Seismic Data

This chapter has been copyrighted and published as a research paper in the Journal of Natural Gas Science and Engineering.

Submitted as: Sohail, G. M., Hawkes, C. D., and Yasin, Q. (2020). An Integrated Petrophysical and Geomechanical Characterization of Sembar Shale in the Lower Indus Basin of Pakistan, Using Well logs and Seismic Data. *Journal of Natural Gas Science and Engineering*, https://doi.org/10.1016/j.jngse.2020.103327

Contribution of the Ph.D. candidate

Ghulam Mohyuddin Sohail carried out computation and interpretation presented in this chapter, with technical review feedback provided by Dr. Christopher Hawkes during weekly meetings. Mr. Sohail wrote the manuscript, with review feedback provided by Dr. Hawkes. Dr. Qamar Yasin (Geophysicist) performed seismic inversion using commercial software, and Sohail and Yasin interpreted the inverted seismic stacks with review feedback provided by Dr. Hawkes.

Contribution of this chapter to the overall study

Mechanical and petrophysical properties are interlinked as pointed out by a number of researchers, so an integrated study was carried out to enhance the credibility of the Sembar Shale evaluation as a shale gas reservoir. The inclusion of 2D and 3D seismic data further increases the resolution of mechanical properties at the regional scale. This chapter is also linked to chapter-3 through the estimation of shear wave velocity in Sembar Shale, which was a key parameter to investigate elastic properties.

4.1 Abstract

Shale gas reservoirs are generally exploited through horizontal drilling and hydraulic fracturing. Petrophysical and geomechanical parameters help to determine horizontal well orientation, to select drilling mud densities for stable drilling operations, to assess the suitability of specific zones in a formation for hydraulic fracturing, and to assess required hydraulic fracturing pressures. The primary objective of this work was to characterize a shale interval in the Early Cretaceous-age Sembar Formation in the Lower Indus Basin of Pakistan, using only readily available data. A workflow was developed for the estimation and mapping of geomechanical properties using logs from multiple wells and relevant post-stack seismic reflection data. Mineralogy data from well cuttings, core testing results for elastic properties and hydraulic fracturing test data (mostly obtained from one key well) were utilized to constrain the values of the properties estimated from geophysical data. The following results obtained at the well-scale suggest that the Sembar Shale is favorable for development: high gas saturation, good porosity (up to 10%), moderate quantity of thermally mature organic matter (2% - 4% TOC), a number of brittle intervals separated by thicker intervals that fall slightly below the brittle-ductile threshold, and a strike-slip stress regime. At the scale of the study area, robust statistical techniques were used to invert seismic stacks and develop a 3D mechanical earth model. This model shows a trend of increasing shale brittleness towards the northeastern portion of the study area, hence suggesting that this area might be most prospective for initial shale gas development. The results of sensitivity analyses are presented, which illustrate the potential errors in the estimated geomechanical properties. Future work to improve confidence in the shale gas potential of the Sembar Formation is given, including extensive coring and laboratory testing, in-situ stress and natural fracture characterization, and better delineation of shale thickness.

4.2 Introduction

4.2.1 Background

Petrophysical and geomechanical characterization of shale is essential to achieve effective production from shale gas reservoirs through horizontal drilling and subsequent hydraulic fracturing. Shale characterization is challenging due to the presence of compliant organic matter and platy clay minerals, low porosity and permeability, and the stress

sensitivity and anisotropy of shale properties (Passey et al., 2010; Eshkalak et al., 2014). The mechanical properties of shale (e.g., Young's modulus, Poisson's ratio, in-situ stresses, and brittleness) are affected by petrophysical properties (e.g., volume and type of clays, mineralogy, porosity, pore pressure, total organic carbon (TOC), fluid saturation). An integrated study of petrophysical and mechanical properties to produce 1D and 3D mechanical earth models is an important step in the design of stimulation treatments that result in the production of hydrocarbons at economical rates from shale gas reservoir (Sone and Zoback, 2013; Al-kharraa et al., 2015; Altowairqi et al., 2015; Crain, 2016). Shale characterization requires laboratory-based elastic properties (Young's modulus and Poisson's ratio measured on cores), shear sonic log data and prestack seismic gathers. These datasets are usually unavailable in shale formations of the Indus Basin of Pakistan, where shale gas exploration is in an initial stage and companies are relying on currently available datasets for the assessment of shale gas prospects. A workflow has been developed for the construction of 1D and 3D mechanical earth models for the Sembar Shale encountered at different wells (locations are shown in Figure 4.1a) in the Lower Indus Basin using drill cuttings, conventional logs (neutron, density, sonic, resistivity, photo-electric, gamma-ray) and post-stack seismic data (2D and 3D). The measured petrophysical and mechanical properties of the Sembar Shale in multiple wells of the study area enhance the reliability of estimated properties at data-poor locations. Knowledge of the spatial distribution of mechanical properties of the Sembar Shale in the study area helps to select the prospective zones for shale gas exploitation.

4.2.2 Literature Survey

Fundamental petrophysical properties of shale are burial depth, thickness, volume, mineralogy, porosity, permeability, fluid saturation, and total organic carbon (TOC) (Crain, 2016). These properties are necessary for reserve estimation and completion quality assessment ("fracability") of shale gas reservoirs (Al-Kharraa et al., 2015; Crain, 2016; Akono and Kabir, 2016). Two main types of porosity exist in most shales: matrix and fracture porosity (Wang and Reed, 2009). The matrix porosity may consist of mineral matrix or organic matter, and fracture porosity may be due to natural fractures or induced fractures (Wang and Reed, 2009). Additional types of porosity (interparticle and intraparticle, kerogen pores) with ultra-low permeability and different gas types (adsorbed or absorbed) introduce uncertainty in the estimation of volume of minerals and kerogen, and fluid saturations using conventional log-based techniques (Franquet et al., 2012; Sone and Zoback, 2013; Crain,

2016; Kennedy et al., 2016). The fluid saturations and quantity of organic material in shale gas reservoirs are estimated based on electrical resistivity logs, and these logs are affected by multiple factors: type of log (Induction or lateral), thermal maturity, total organic carbon, cation exchange capacity, formation water salinity, and temperature. Induction devices are sensitive to the horizontal resistivity of the formation, while the lateral-log is sensitive to both horizontal and vertical resistivity. Due to the vertically transverse nature of shale, the vertical resistivity is higher than the horizontal, though it is difficult to resolve vertical and horizontal components from routine log measurements (Miller, 2010). In shale gas reservoirs, the resistivity will increase only if the shale has sufficient thermal maturity to generate hydrocarbons. There are some North American gas producing shales where the resistivity is low due to the presence of conductive minerals (e.g., pyrite, graphite) (Anderson et al., 2008; Rezaee, 2015). The resistivity of pyrite varies with the frequency of the logging tool. The laterologs measure resistivity at less than 100 Hz and induction logs at 20 kHz, hence the laterolog tool measures higher resistivity than the induction tool for the same concentration of pyrite (Crain, 2016). It is challenging to define a global trend for conventional logs in shale gas reservoirs, so log-based estimation of petrophysical properties are typically calibrated with laboratory-based measurements.

Shale gas reservoirs are mostly exploited using hydraulic fracturing either in vertical wells or horizontal drilling and subsequent multistage fracturing to achieve economic production rates (Soliman et al., 2012). Both of these stages are affected by elastic properties (Young's modulus and Poisson's ratio), brittleness, stress regime and density of natural fractures (Plumb et al., 2000; Soliman et al., 2012; Sone and Zoback, 2013; Perez, 2014). Elastic properties of shale are related to brittleness which depends on the quantity of brittle minerals (quartz, carbonates) and total organic carbon content (Jarvie et al., 2007; Rickman et al. 2008; Wang and Gale, 2009; Sone and Zoback, 2013; Cui et al., 2017). Elastic properties are also sensitive to in-situ stresses and the density of natural fractures, so these properties play an indirect but significant role in defining the preferred horizontal well orientation and hydraulic fracturing pressure (Soliman et al., 2012). Horsrud (2001) and Lashkaripour and Dusseault (1993) found the dependency of elastic properties of shale on primary wave sonic velocity and this dependency can be better understood through the study of velocity-porosity relations. Cross plots between elastic properties (Young's modulus, Poisson's ratio) along with TOC and mineralogy can predict the brittleness of a shale (Rickman et al., 2008). The brittleness is further integrated with in-situ stresses, natural

fractures density, and fracability index to identify the intervals in a shale gas reservoir, which are favourable for hydraulic fracturing (Jin et al., 2014; Bai, 2016; Yuan et al., 2017).

Seismic surveys are a helpful tool for getting an assessment of lateral variations in petrophysical and mechanical properties of shale gas reservoirs. The reliability of seismic-based elastic properties and pore pressure is directly linked to the accuracy of seismic velocities (Holt et al., 2005; Chopra and Huffman, 2006; Das and Chatterjee, 2018). As such, it is essential to use a technique that can preserve the in-situ velocity information accurately. The seismic interval velocities are obtained either using root mean square (RMS) stacking velocities (used during seismic processing to stack the seismic traces) or well-seismic ties. The well-seismic tie technique produces less scattered interval velocity distributions (vertical and horizontal) as compared to the use of RMS stacking velocity (Dutta, 2002). Although the seismic velocities are of low frequency compared to sonic log velocities, a correlation between seismic data and synthetic seismograms (based on sonic-density logs and extracted low-frequency wavelet) helps to adjust the seismic velocities at well locations and to establish a velocity-time relation (Soleymani and Riahi, 2012). The velocity-time relation (found at well location) is utilized to extract seismic velocities at all shot points of seismic sections and to construct a velocity cube. The velocity cube of primary seismic waves (Vp) is used to estimate shear wave velocities using empirical (generally linear) correlations between Vp and Vs established using well log data, and to extract elastic properties and pore pressures using relevant equations (Bowers, 2001; Soleymani and Riahi, 2012).

Seismic attributes (e.g., ant-tracking) provide a quick way to visualize the trends of faults/macro-fractures (resolution in the range of 500m to 1000m), which are hard to see or most times not visible on a conventional seismic profile. Ant-tracking (also called an artificial intelligence technique) was developed based on the notion of ant colony systems to determine discontinuities such as faults/macro-fractures in 3D seismic data (Pedersen et al., 2002). This attribute uses the philosophy of swarm intelligence, which describes the cooperative behavior of social insects in discovering the shortest path between the nest and food by communicating via a chemical substance known as a pheromone. When searching for foods, ants use these pheromone trails to direct other colony members to the food they have found. Through this process, the ants find the most efficient path from the nest to the food. The shortest path is marked with more pheromones in the algorithm; ants are more likely to choose the shortest route, and so on. In the ant attribute algorithm, large numbers

of electronic “ants” are spread in the seismic volume allowing them to move along faults/macro-fractures and emitting “pheromones.” Surfaces that are strongly marked with pheromones are deemed likely to be associated with faults/fractures (Randen et al., 2001; Fehmers and Hocker, 2003; Cox and Seitz, 2007; Khair et al., 2012).

The inversion of seismic data transforms the seismic reflection data into an acoustic impedance, which is linked to elastic properties (Russell, 2004; Gogoi and Chatterjee, 2019). Several seismic inversion techniques (deterministic and stochastic) have been introduced for both pre and post-stack seismic data, and the applicability of a particular method depends on the objective of the study. Stochastic or geostatistical inversion techniques (e.g., backpropagation (BP), genetic inversion (GI), multilayer linear calculator (MLC), particle swarm optimization (PSO)) utilized neural nets (NN) for training the input data according to a target (Robinson, 2001; Liu, 2017;Yasin et al., 2020). These techniques derive lateral resolution from seismic data and vertical resolution from well log data, which enhances the effectiveness of these techniques for reservoir characterization (Robinson, 2001). The NN-based methods extract the non-linear relationships between input and output data and are less sensitive to noise in the data. In BP, the data is fed forward through the network, and the network training is done by back propagating the error. GI is a non-linear multitrace seismic inversion algorithm, which combines the neural network and genetic algorithm. The MLC inversion technique is composed of multiple linear calculators and domain gates, capable of dividing a complicated function into simple linear ones with the domain gate controlling the output weight of each layer. The PSO consists of particles that have multiple dimensions, and the algorithm searches and updates each particle and has the ability of convergence; in other words, to find the global optimum of the problem (Parsopoulos and Vrahatis, 2004). The theoretical details of MLC+PSO and GI are given in Appendices 4-A and 4-B, respectively.

4.3 Geological Settings of Study Area and Stresses Orientation

The Lower Indus Basin (LIB), covering nearly 137,500 km^2, is located in southeastern Pakistan. The geological setting of the Lower Indus Basin is linked to the Greater Indus Basin through two significant events: the rifting and break-up of Gondwana that occurred in the Jurassic period, and the separation of East Gondwana (India-Antarctica-Australia) from the West Gondwana (Africa-South America) that happened in the Cretaceous period (Ahmad and Ahmad, 1991; Kazmi and Abbasi, 2008). These events

controlled the geological structures and sedimentation processes of the Indus Basin. Uplifting, tilting and strike-slip faulting were dominant in the Indus Basin from Mid to Late Cretaceous. Horst and graben structures also developed during the Mid-Cretaceous due to the separation of Indian Plate from Madagascar. In the Tertiary period, the Indian Plate collided with the Eurasian Plate, a process that continues currently. This ongoing event controls the development of major geological structures (thrusts and highs) in all parts (Upper, Middle, and Lower) of the Indus Basin (Kazmi and Abbasi, 2008).

A sedimentary succession 8500 m in thickness exists in the Lower Indus Basin, ranging from Precambrian to recent in age. During the Cambrian period, clastics were deposited in a hot and dry climate. No sediments of the Ordovician to the Carboniferous are present, while in the Permian period the area was glaciated and a fluvioglacial environment prevailed all over the Indus Basin. Subsequently, the climatic conditions became warmer, and continental to shallow marine environments prevailed in the Indus Basin, resulting in tremendous sedimentological diversity in the form of clastic and non-clastic sediments (Kadri, 1995). From the Triassic to Early Jurassic periods, carbonate deposition was dominant. Rapid facies changes occurred during the Early Cretaceous period, due to rifting and drifting of the Indian plate, and the Sembar Formation (the focus of this study) was deposited. During subsequent (Tertiary period) collision of the Indian and Eurasian plates, the Upper Indus Basin (i.e., the northern part of the Indus Basin) was uplifted and the Lower Indus Basin remained under marine conditions. Consequently, marine deposits are found at shallow depths in the Lower Indus Basin (Ahmad and Ahmad, 1991; Kadri, 1995).

The study area is located in the northwest of the Lower Indus Basin (LIB) and is bounded by two local highs (Mari-Kandhkot and Jacobabad) as shown in Figure 4.1b. The generalized stratigraphy based on drilled wells (Y, M, R, K-1, K-2, and X) used in this study is shown in Figure 4.2b, and wells locations are given in Figure 4.1a. The sedimentary sequences encountered in different wells of the study area are correlated along the polygon (line connects studied wells as shown in Figure 4.1a) based on gamma-ray and mud log data to construct a subsurface cross-section, as given in Figure 4.2a. This cross-section shows that a thick sequence of Sembar Formation exists in the study area. The Sembar Formation (shale and sandy shale) is deeper in the north-east compared to the south-west of the study area. It is overlaid by the Goru Formation, which is further divided into Upper and Lower Goru. The Lower Goru contains multiple strata of medium to coarse-grained sandstone and is a gas-producing reservoir in the study area. The contact between Sembar and underlying

Chiltan Formation (limestone) is unconformable and easily recognizable due to a sudden change from clastic to non-clastic (Kadri, 1995).

Previous core-based studies have shown that dominant minerals in shaly intervals of the Sembar Formation are quartz and clays (chlorite, illite, kaolinite) with minor quantities of dolomite, feldspar, and pyrite (Ahmad et al., 2012; Farooqui, 2014). The Sembar Shale is more siliceous in the study area compared to the western and eastern side, and mineral assemblages are detrital quartz and feldspar plus a mixture of detrital and authigenic clays. The source of organic matter in the Sembar Shale is marine algae and was deposited in an anoxic depositional environment (Ahmad et al., 2012; Farooqui, 2014).

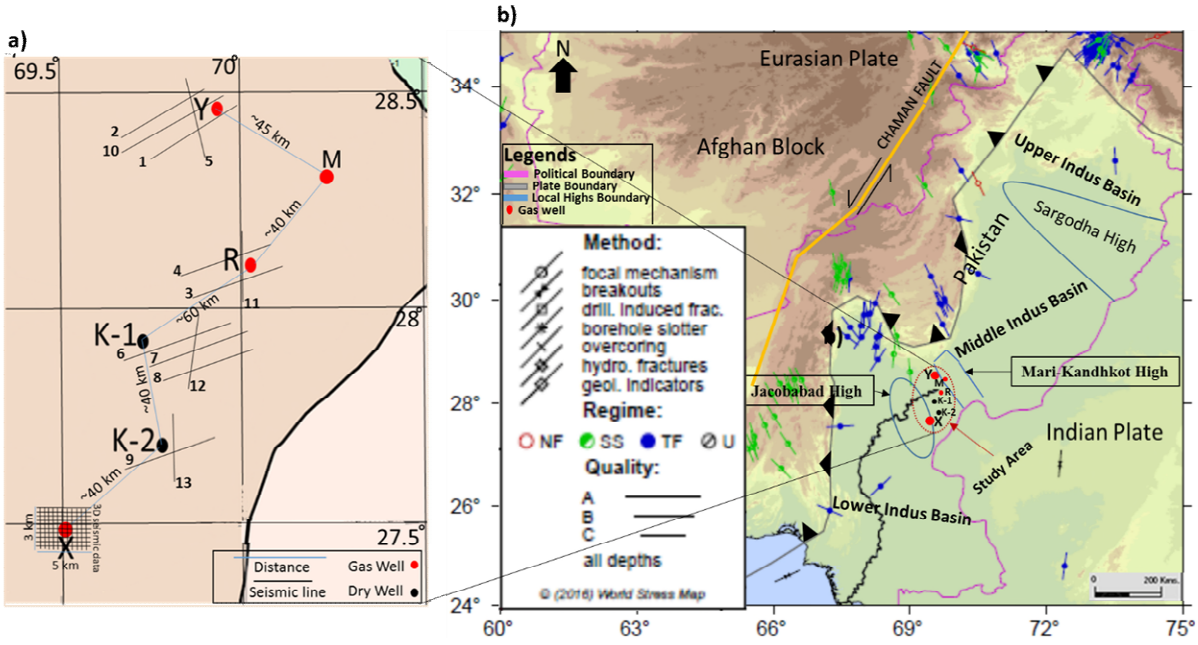

Figure 4.1 a) Location of wells (Y, M, R, K-1, K-2 and X) and seismic lines used in this study. Numbers were arbitrarily assigned to these seismic lines by the authors to facilitate discussion; the numbers do not correlate to the actual titles assigned to these lines by seismic surveying companies. The light grey line segments connecting the wells trace the path of the subsurface cross-section shown in Figure 2. **b)** World Stress Map is showing the orientation of maximum horizontal in-situ stresses in and around the Indian Plate (after Heidbach et al., 2016). The locations of wells X and Y (the subject of focused investigation in this work) have been added to this map.

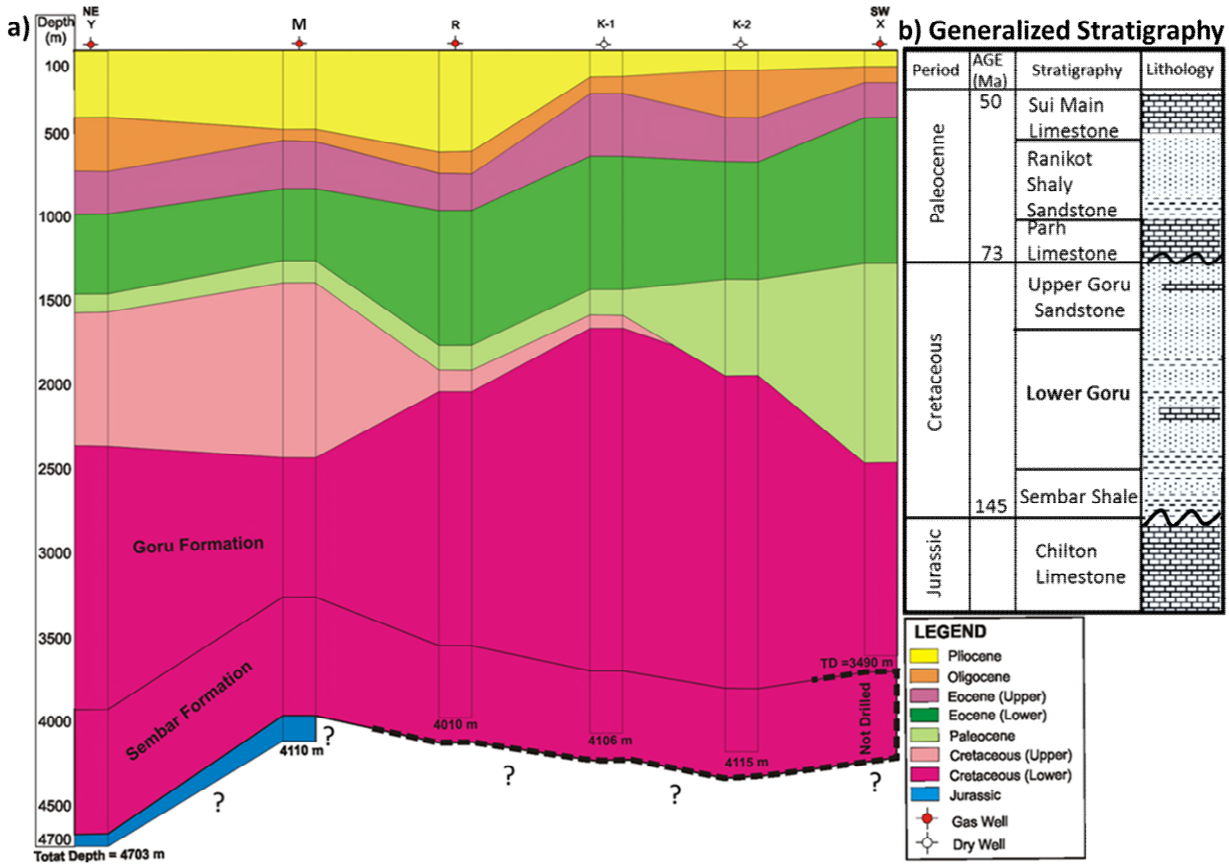

Figure 4.2 a) Subsurface correlation of wells in the study area (see Figure 4.1a for well locations) to delineate the structure of the Sembar Formation. Dashed lines are used to denote the top and base of the Sembar Formation for well-X, and the base of the Sembar for wells R through X, to reflect some uncertainty in these surfaces because they were interpreted solely from seismic data (these wells did not penetrate Jurassic-age formations). **b)** Generalized stratigraphy of the study area (after Raza et al., 1990).

The present-day strike-slip movement of the Indian plate with respect to the Afghan block may also play a role in controlling surface and subsurface geological structures in the Lower Indus Basin (Kazmi and Abbasi, 2008; Zoback, 2014). Based on a recent earthquake (Mw 7.7) in the study area, strike-slip faults are deemed to be active at depths of approximately 10 km, which suggests a present-day strike-slip stress regime in the study area (Lisa and Jan, 2015), although a previous study by Verma et al. (1980) concluded the existence of both strike-slip and normal faulting in the study area. Based on the world stress map (Figure 4.1b), the maximum horizontal in-situ stresses seem to be oriented in the northeast-southwest direction in the Lower Indus Basin. This is also supported by a borehole breakout analysis conducted for well-X in this study, as shown in Figure 4.3 (the location of well-X is shown in Figures 4.1a and 4.1b).

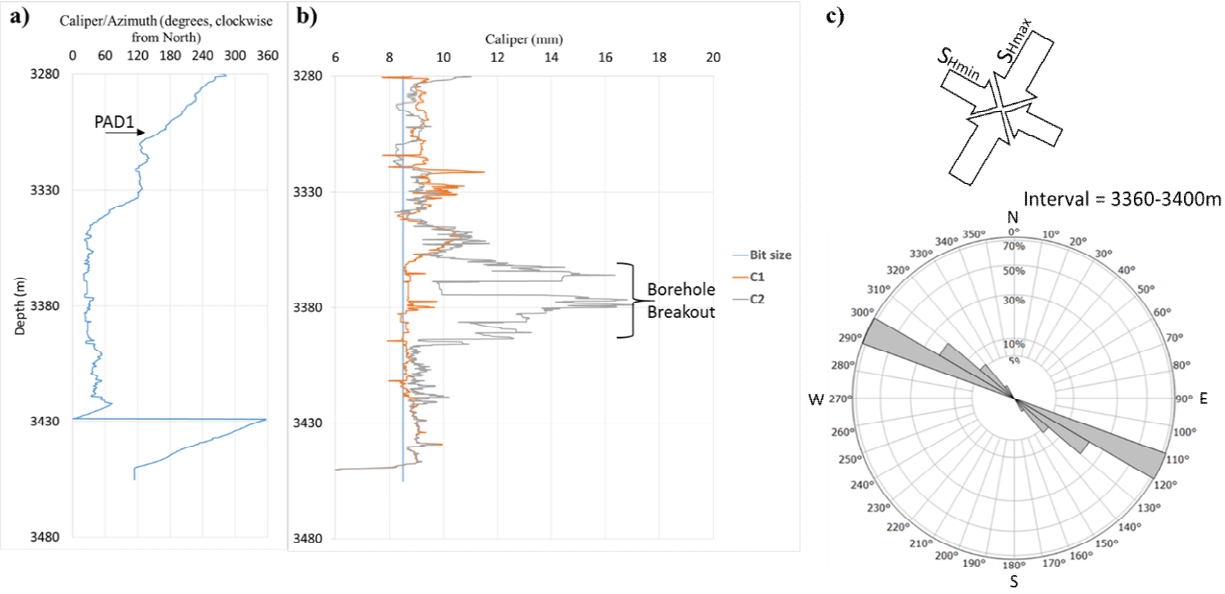

Figure 4.3 Borehole breakout analysis result for well-X. **(a)** Caliper Pad1 azimuth, **(b)** calipers C1 and C2 and drill bit diameter (bit size). **(c)** Rosette plot showing the orientations of borehole breakout over the interval from 3380 to 3400 m depth, along with the orientations of maximum and minimum horizontal stresses (S_{Hmax} and S_{Hmin}, respectively) interpreted by these authors (see Figure 4.1(a & b) for well location).

4.4 Methodology

4.4.1 Data Collection/Selection

This study utilized the data (as summarized in Table4.1) of a gas-producing well (well-Y) drilled in the Lower Indus Basin, Pakistan to calculate petrophysical and geomechanical properties of the Sembar Shale. Well cuttings collected at different intervals of the Sembar Formation in well-Y were used for mineralogical analysis. A shaly sandstone interval (4470-4498 m) of Sembar Formation is a proven gas reservoir, which produced 4.28 MMSCFD (million standard cubic feet per day) (0.00012 bcm/day) of gas at a wellhead flowing pressure of 770 Psi (5.3 MPa) on 32/64" choke. The interval (4415-4470 m) above the gas-producing reservoir was selected for this study due to its potential as a shale gas reservoir. The laboratory-based elastic properties, measured pore pressure (DST test) and hydraulic fracture data (mini-frac test) in the studied interval were extracted from published and unpublished reports (Farooq et al., 2009; Siddiqui et al., 2014; Usmani and Kamal, 2017; Soroush et al., 2018). The measured parameters (pore pressure and minimum horizontal stress) in the studied interval were also utilized to correct the log-based estimation. Data from seismic lines (three dip lines and one strike line) acquired near well-Y were obtained

and used to construct seismic velocity-based mechanical properties maps in the vicinity of this well, which provided the basis for the development of regional maps. The seismic and log data of other wells as given in Table-1 were used to study the spatial distribution of mechanical properties in the study area.

Table 4.1 Summary of available data

<table>
<tr><th rowspan="2">Well</th><th rowspan="2">Formation</th><th rowspan="2">Depth from Ground Level (m)</th><th rowspan="2">Minera logy</th><th colspan="7">Petrophysical logs</th><th colspan="4">Geomechanical Data</th><th>Post stack Seismic Data</th></tr>
<tr><th>HCGR</th><th>DENS</th><th>NPHI</th><th>LLD</th><th>Sonic</th><th>PEF</th><th>Well cuttings</th><th>DST</th><th>Well cores</th><th>Mini-frac Data</th><th rowspan="2">2D Seismic post stacks (stacking velocities and two-way seismic time)</th></tr>
<tr><td></td><td></td><td></td><td></td><td></td><td></td><td></td><td></td><td>P</td><td>S</td><td></td><td></td><td></td><td></td><td></td><td></td></tr>
<tr><td>Y</td><td rowspan="3">Sembar</td><td>Top = 4046
Bottom = 4680
Studied interval = 4415-4470
Gas Producing Interval = 4470-4498</td><td>XRD test</td><td>✓</td><td>✓</td><td>✓</td><td>✓</td><td>✓</td><td>*</td><td>✓</td><td>✓</td><td>✓</td><td>☒</td><td>✓</td></tr>
<tr><td>M, R,K-1 and K-2</td><td>Given in Figure 2</td><td>☒</td><td colspan="4">✓</td><td colspan="4">☒</td><td colspan="4">2D Seismic stacks</td></tr>
<tr><td>X</td><td>Given in Figure 2</td><td colspan="12">☒</td><td>3D Seismic cube</td></tr>
<tr><td></td><td colspan="16">XRD = X-ray powder diffration test, HCGR = Computed Gamma Ray, DENS = Bulk Density, NPHI = Neutron Porosity, LLD = Lateral Log Deep, Sonic (P = Primary and S = Shear), PEF = Photoelectric Absorption Factor, DST = Drill stem test, *S-sonic is available for a specific interval (4046 m - 4071 m)</td></tr>
</table>

4.4.2 Mineralogy of Sembar Shale

The cuttings samples at five depths within the studied interval were selected and analyzed for mineralogy; four were analyzed at the Mineralogy Laboratory of School of Geosciences, China University of Petroleum (Qingdao, China), and one was submitted to the Saskatchewan Research Council's Geoanalytics Laboratory for analysis. XRD (X-ray powder diffraction) and QEMSCAN (Quantitative Evaluation of Minerals by Scanning electron microscopy) techniques were utilized to determine mineralogies of the shale cuttings. The identified minerals were quartz, illite, kaolinite, dolomite, pyrite, albite and magnetite. The weight percentage of each mineral was converted to a volume percentage

using grain density and porosity (measured from the core) using the equation 4.1, and the results are shown in Figure 4.4b (lab-based data points):

$$Vol\% = W_{dry}\% * (1 - \phi_t) * \rho_g/\rho_{min} \quad 4.1$$

Where $Vol\%$ = volume percent, $W_{dry}\%$ = dry "weight" (mass) in percent, ϕ_t = total porosity from core, ρ_g = rock grain density, ρ_{min} = mineral grain density

Gamma-ray (GR) log interpretation is shown in Figure 4.4a (two tracks at the left). The shale baseline was set at 75 API, as per Al-Kharraa et al. (2015). The volume of shale (V_shale) was obtained by calculating the gamma-ray index (IGR), as follows:

$$IGR = (GR_{log} - GR_{min})/(GR_{max} - GR_{min}) \quad 4.2$$

Using maximum (GR_{max}) and minimum (GR_{min}) gamma-ray values of 100 API and 10 API, respectively, V_shale is equivalent to IGR (Al-Kharraa et al., 2015). [Note: Equation 4.2 is used again later in this paper, to evaluate the volume of clay (Vcl). This is based on Vernik (2016), who claims that Vcl is equal to IGR for illite-rich shales, when calculated using values of 230 API and 30 API for GR_{max} and GR_{min}, respectively. The volume of clay obtained in this manner is shown later in section 4.5.2, and was found to agree with the amount of clay (i.e., illite) obtained from a laboratory test.]

The bulk mineralogies of the shale zones were estimated using Schlumberger Techlog's Mineral Solver Package (Elan) using a combination of logs (density, resistivity, neutron, sonic, gamma-ray, photoelectric effect (PEF)) and presumed dominant minerals (quartz, illite, kaolinite, dolomite, pyrite). These minerals were selected based on the results of XRD analyses. Minor minerals were omitted from this analysis, as was kerogen (or total organic carbon), which was determined to be present in low quantities (as discussed later), and which is also known to have a negative impact on log-based mineralogy algorithms (Khan, 2016). Several iterations of the Mineral Solver Package were run in which the following parameters were varied within prescribed limits: mineral endpoints (specific value of the log reading for each mineral), maximum volume based on XRD data, uncertainty factors (fitting parameters), and sonic and neutron porosity model types. The final results after these iterations are shown in Figure 4.4c (right-most tracks).

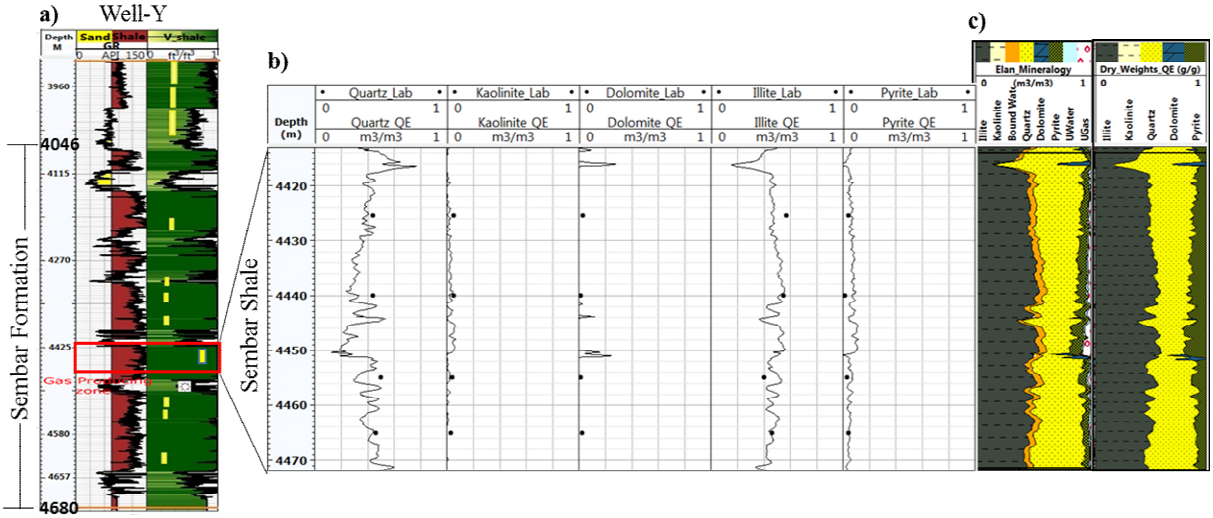

Figure 4.4 Log and core data pertaining to lithology and mineralogy of the Sembar Formation at well-Y. **a**) shows the GR log along with the volume of shale (V-shale) for the entire Sembar Formation. The red rectangle identifies the studied shale interval (4415-4470 m) above the gas-producing zone (4470-4498 m), **b**) a comparison of lab-based (data points) and log-based (continuous curves) mineralogy in the studied interval (Sembar Shale) of the Sembar Formation is shown, **c**) shows the results of Elan mineralogy package in volume (m3/m3) and weight (g/g) fraction.

4.4.3 Total Organic Carbon (TOC)

There are several techniques (Schmoker, Carbolog, sonic-resistivity log-based (Dlog_R)) in the literature for estimation of TOC using well logs (Schmoker and Hester, 1983; Bessereau et al., 1991; Vernik and Landis, 1996; Lewis et al., 2004; Passey et al., 2010). The DLog_R technique, which is based on the apparent difference between resistivity and sonic-porosity, may not be suitable in the presence of pyrite because pyrite is highly conductive and resistivity logs show lower values even in organic-rich (mature kerogen) intervals when pyrite is present (Passey et al., 2010); however, the lateral log (which was used in this work) is less affected by the pyrite than the induction log, due to its lower frequency (Clavier et al., 1976). Similarly, Jiang et al. (2018) established that Schmoker's density-based technique overestimates the TOC in pyrite-rich Eagle Ford Shale. All these techniques have their advantages and disadvantages, and the choice of method depends on their correlation with laboratory-based TOC values. The Dlog_R and Schmoker methods were employed in this study to estimate the TOC. The equations for these methods are given in Appendix 4-C. The average of TOC (vol%) based on DLog-R and Schmoker techniques were found to be comparable with measured TOC (vol%) in the studied interval of the Sembar Formation; hence this average was used in this work. A kerogen density of 1.4 g/cc

and a conversion factor of 0.8 (unitless) were used for weight to volume conversion of TOC (Crain and Holgate, 2014).

4.4.4 Porosity

Different combinations of logs (neutron-density, density-sonic and neutron-sonic) were tested to establish a workflow for porosity estimation. The combination of logs was finalized based on two criteria: 1) comparison against published porosities (5-7 %) of Ahmed et al. (2012) for the Sembar Shale in surrounding wells of the study area, 2) running a porosity-dependent rock-physics model using different porosity curves (obtained using different combinations of logs), and comparing calculated compressional wave velocities against measured compressional sonic log results. The total porosity obtained from the combination of neutron and sonic logs, as explained in equations 4.3 to 4.5, was deemed suitable based on the aforenoted criteria. The details of the rock-physics model (a modified version of the Xu and White (1995) model, as described by Sohail and Hawkes (2020)) are not given here in order to avoid further lengtheningof this manuscript. The total corrected porosity ($PHIT_{corrected} = \ effective\ porosity$) was in the range of 1-10% (average 6%), which is close to the published porosity values of Ahmed et al. (2012).

$$\phi_{effective\_sonic} = \phi_{sonic} - V_{TOC}\phi_{TOC} - V_{cl}\phi_{clay} \quad 4.3$$

$$\phi_{effective\_neutron} = NPHI - V_{TOC}\phi_{TOC} - V_{cl}\phi_{clay} \quad 4.4$$

$$PHIT_{corrected} = \phi_{effective} = \frac{\phi_{effective_{neutron}} + \phi_{effective_{sonic}}}{2} \quad 4.5$$

Where $\phi_{sonic}$is total porosity from the sonic log ($PHIT_{sonic} = \phi_{sonic} = \frac{DT - DT_m}{DT_{fl} - DT_m}$), V_{cl} and ϕ_{clay} are volume and porosity of clay respectively, and ϕ_{clay} is calculated at the maximum value of the GR log in the studied interval, NPHI is porosity from the neutron log, ϕ_{TOC} is 0.53 for sonic log and 0.65 for neutron log-based porosity (Crain and Holgate, 2014).

4.4.5 Fluid Saturation

There are various log-based models (Indonesian, Dual Water, Simandaux) for determining water saturation (S_w) in conventional sandstone reservoirs. These models tend to overestimate S_w due to high conductive clay contents in sandy shales and shales (Kadkhodaie and Rezaee, 2016). In conventional reservoirs, the current flows only through

formation water. In shale gas reservoirs, the current has more paths in the form of interconnected clays accompanied by formation water (Rezaee, 2015). The modified Simandaux model, as given in equation 4.6, is designed explicitly for shale gas reservoirs and was used for the estimation of water saturation in the studied interval.

$$\frac{1}{R_t} = \left(\frac{\Phi_t^m S_w^n}{aR_w(1-V_{cl})}\right) + \left(\frac{V_{cl}S_w}{R_{sh}}\right) \quad 4.6$$

Where R_t is resistivity in ohm·m from a deep resistivity log (LLD), S_w and R_w are water saturation and resistivity (0.03 ohm·m), R_{sh} is average resistivity in a 100% shale/clay interval, m & n (=1.8) are cementation and saturation exponents for shaly sandstone/sandy shale intervals, respectively, and a (=1) is a tortuosity factor for these same lithologies (Entyre, 1993).

4.4.6 Shear Wave Velocity Estimation

Shear wave velocities (Vs) (in addition to compressional wave velocities and bulk densities) are required to calculate dynamic elastic properties, yet shear wave velocities were not logged in the studied interval of well-Y. Different mathematical models to estimate Vs are available for shaly sandstone gas reservoirs, but some amendments are necessary before using these for shale gas reservoirs (Xu & White, 1995). A modified mathematical model for Vs estimation in shale gas reservoir was developed after incorporating the shale properties (porosity, fluid saturation, pore types, aspect ratio, and mineralogy) in the model of Xu & White (1995). The results were compared against measured Vs data in the upper interval of the Sembar Formation (4046-4170 m) in well-Y, and the entire Sembar Formation in a nearby well. The error was found to be 1% to 5% (average 3%) in both wells, hence the estimated Vs values were deemed appropriate for use in the Sembar Shale interval of well-Y. The detailed workflow used for Vs is reported in Sohail and Hawkes (2020).

4.4.7 Dynamic Elastic Properties

The dynamic elastic properties (Young's modulus and Poisson's ratio) of rocks can be calculated from bulk densities and velocities, as given in equations 4.7 and 4.8:

$$E_{dyn} = \frac{\rho_b V_s^2(3V_p^2 - 4V_s^2)}{V_p^2 - V_s^2} \quad 4.7$$

$$\nu_{dyn} = \frac{V_p^2 - 2V_s^2}{2(V_p^2 - V_s^2)} \quad 4.8$$

Where $E_{dyn}$and ν_{dyn} are dynamic Young's modulus and Poisson's ratio respectively, ρ_b is bulk density, and V_p and V_s are compressional and shear waves sonic velocities, respectively.

Based on the published core-based study on the Sembar Shale in nearby wells by Souroush et al. (2018), the static Young's modulus was assumed to be 15% less than dynamic Young's modulus, and static Poisson's ratio was assumed to equal the dynamic Poisson's ratio.

4.4.8 Pore Pressure

Traditional methods for estimating pore pressure utilize resistivity, density, or sonic logs (e.g., Eaton's method (1972)). These may lead to erroneous results due to the involvement of multiple factors in the development of high pressures (e.g., unloading, compaction disequilibrium, and fluid expansion mechanism) (Bowers, 1995; Bowers, 2001; Passey et al., 2010; Green et al., 2017). Due to the high pore pressure in the studied interval of well-Y, a very small mud weight window was available to drill and run the drill stem test (DST). This also created challenges for the estimation of pore pressure. In the absence of sonic velocities in shallow formations, it was not possible to establish a normal compaction trend, so the equivalent depth method was not an option (Bowers, 2001). The velocity-effective stress relation, as given in equation 4.9, has successfully been applied in the U.S Gulf Coast, the Gulf of Mexico, and Central North Sea (Bowers, 1995), hence it was used for pore pressure estimation in Sembar Shale of well-Y. The values of constants V_o, A and B were optimized through iteration to get a match between estimated and measured pore pressure in well-Y. For other wells (near well-X) the pore pressure gradient in the Sembar Shale was extracted from literature data (e.g., Souroush et al., 2018). The pore pressure gradient near well-X varies from 0.013 to 0.015 MPa/m (average 0.014 MPa/m).

$$P_p = S_v - 0.0069((V_p - V_o)/A)^{1/B} \quad 4.9$$

Where V_p is measured primary wave sonic velocity in m/s, V_o is primary wave velocity at zero effective stress in m/s, S_v and Pp are vertical stress and pore pressure in MPa, respectively, A and B are constants. For the studied interval, values of 11, 0.65, and 1585

m/s for A, B and V_o, respectively, were found to provide the best match between estimated and measured pore pressure (from a drillstem test) in well-Y (with ~3% error).

4.4.9 In-Situ Stresses

The principal in-situ stresses at any point in a flat-lying sedimentary sequence are defined by the magnitudes of the vertical, maximum horizontal and minimum horizontal stresses, and the orientations of these horizontal stresses. The magnitude of vertical stress (S_v) for well-Y was determined using bulk density log data as input for equation 4.10. Given that bulk density was not logged for well-Y over the interval from 0 to 2500m, density logs from nearby wells (within a radius of 10 km) were used to generate an averaged representation of bulk density for the shallower formations existing through this interval.

$$S_v = 10^{-6} \int_{z=0}^{z=TVD} g * \rho_b \, dz \qquad 4.10$$

Where S_v is vertical stress in MPa, z is depth in meters (m), g is gravitational acceleration (9.81 m/s^2), ρ_b is bulk density in kg/m^3.

The magnitudes of maximum and minimum horizontal stresses, assuming uniaxial tectonic strain and isotropic elastic properties, were calculated using the equations 4.11 and 4.12, respectively (Jaeger and Cook, 1979; Thiercelin and Plumb, 1994; Ito et al., 1999; Rutqvist et al., 2000, Waters et al., 2011).

$$S_{Hmax} = \frac{\nu}{1-\nu}\sigma_v + \frac{1-2\nu}{1-\nu}\alpha p_p + \frac{1}{1-\nu^2}E\varepsilon_{Hmax} \qquad 4.11$$

Where S_{Hmax} is maximum horizontal stress in MPa, ν is static Poisson's ratio (unitless), α is Biot's coefficient (assumed to be 1), p_p is pore pressure, E is static Young's modulus in MPa, ε_{Hmax} is the present-day, elastic component of horizontal tectonic strain in the direction of maximum horizontal stress (unitless), and $\frac{1}{1-\nu^2}E\varepsilon_{Hmax}$ represents the tectonic stress due to ε_{Hmax}. Similarly,

$$S_{Hmin} = \frac{\nu}{1-\nu}S_v + \frac{1-2\nu}{1-\nu}\alpha p_p + \frac{\nu}{1-\nu^2}E\varepsilon_{Hmax} \qquad 4.12$$

Where S_{Hmin} is minimum horizontal stress in MPa, $\frac{\nu}{1-\nu^2} E \varepsilon_{Hmax}$ represents the component of tectonic stress induced in the minimum horizontal stress direction due to the Poisson effect.

Biot's coefficient was estimated to be approximately 0.6 to 0.7 for clay-rich intervals of the Sembar Shale. This value was obtained using log-derived estimates of static bulk modulus (Kb) and literature-derived values for illite and quartz particles (Kgrain), based on the relation α = 1- Kb/Kgrain as presented by Nur and Byerlee (1971).

The maximum horizontal strain (Ɛ_Hmax) was obtained by manipulating equation 4.12 to solve for Ɛ_Hmax, for two scenarios where estimated values for all other parameters in this equation were available. For both of these scenarios, the minimum horizontal stress magnitude had been estimated using the instantaneous shut-in pressure from a mini-frac test; one conducted at approximately 3400 m depth near well-X, and another at 4428 m in well-Y. Static Young's modulus and Poisson's ratio values were available from a prior laboratory-based core testing program for the well near well-X, and were estimated from wireline logs for well-Y. Measured pore pressures at these two locations were extracted from literature. The tectonic strain was found to be 0.0050 at well-Y and 0.0056 at well-X when using a value of 0.6 for Biot's coefficient, and 0.0046 at well-Y and 0.0049 at well-X when using a value of 0.7 for Biot's coefficient. It was assumed that the Ɛ_Hmax values obtained at these two specific depths were constant over the entire depth interval studied throughout the study area. Continuous profiles of S_Hmax and S_Hmin were thus generated across the Sembar Shale interval in the studied wells using log-derived static Young's modulus and Poisson's ratio. During the calculation of these stress profiles, no discernable difference was observed when comparing the horizontal stress profiles generated with α = 0.6 against those generated with α = 0.7; hence the latter profiles (using average value of Ɛ_Hmax = 0.0050) were used moving forward in this work.

The orientation of horizontal stresses was assessed through borehole breakout analysis. This analysis was conducted in well-X where 4-arm caliper log data were available; the results of this analysis were presented previously, in Figure 4.3. For lack of additional data, this orientation was assumed to be representative of the entire study area.

4.4.10 Brittleness Index

Brittleness index is a dimensionless ratio ranging from 0 (pure ductile behaviour) to 1 (pure brittle behaviour). Although brittleness is fundamentally related to the amount of strain that occurs in a medium prior to fracture, it is often characterized using more readily available properties that are deemed to correlate to brittleness. In this work, BI was evaluated using a number of methods. The methods used are presented below, and the relative merits of each are discussed in section 4.6.

Brittleness index (BI) was first evaluated based on mineralogy, following the framework used by Wang & Gale (2009) and Zhang et al. (2017), as follows:

$$BI_{mineralogy} = \frac{Qz+Dol+Pyrite}{Qz+Dol+Pyrite+Kaol+Illite+TOC} \quad 4.13$$

Where Qz (quartz), Dol (dolomite), Pyrite, Kaol (kaolinite), Illite and TOC (total organic carbon) are expressed as weight fractions.

The studied interval contains three brittle minerals; quartz, dolomite, and pyrite, so equation 4.13 was developed based on Sembar Shale mineralogy. The inclusion of pyrite and dolomite as brittle minerals in equation 4.13 has recently been demonstrated as appropriate and useful by Zhang et al. (2017) for the Longmaxi Shale in China. The TOC in the denominator has a negligible impact on the BI of the studied interval, likely due to the low (2-4 %) TOC values for this interval. The mineralogy-based BI was calculated using both weight and volumetric fractions of minerals, because of a lack of consistent use of one versus the other in the literature (Zoback and Kohli, 2019; Sone and Zoback, 2013). A minor difference was observed, due to the low quantity of relatively dense pyrite. Although the inclusion of density and porosity for the conversion of weight to the volume fraction of minerals impacted the brittleness index calculation, this issue did not significantly affect the assessment of brittle and ductile zones in the Sembar Shale.

Brittleness indices were also calculated based on dynamic elastic properties, based on the framework presented by Grieser & Bray (2007) and Rickman et al. (2008), as follows:

$$BI\_YME = \frac{E - E_{min}}{E_{max} - E_{min}} \quad 4.14$$

$$BI\_PR = \frac{\nu - \nu_{max}}{\nu_{min} - \nu_{max}} \quad 4.15$$

$$BRIT_{average} = (BI_E + BI_\nu)/2 \quad 4.16$$

Where E is Young's modulus (referred to as YME in the software used for this work) in GPa, ν is Poisson's ratio (PR), E_{max} and E_{min} are the maximum (68 GPa) and minimum (30 GPa) Young's moduli, and ν_{max} and ν_{min} are the maximum (0.3) and minimum (0.2) Poisson's ratios observed in the studied interval of Sembar Shale. BRIT_average is average brittleness index based on elastic properties, which records the mean effect of Young's modulus and Poisson's ratio because these two parameters correlate to brittleness in opposite ways (e.g., high E and low ν typically characterizes a brittle rock). The maximum and minimum values of Young's modulus (80 and 10 GPa respectively) and Poisson's ratio (0.15 and 0.4) recommended by Rickman et al. (2008) for Barnett Shale, did not work effectively for Sembar Shale to normalize the data in the range of 0 to 1.

The effective thickness of brittle zones was calculated using a threshold of BRIT_average > 0.5 and BI_Minerals_vol > 0.5 (initial threshold set by the author for testing purposes). The identified brittle zones were also assessed with reference to two established criteria (E = 50 GPa and ν = 0.25 by Rickman et al. (2008) for North American Shales; E = 30 GPa and ν = 0.25 by Zhang et al. (2017) for Longmaxi Shale, China) (details are given in section 4.6).

4.4.11 Seismic Data Interpretation

The sonic and bulk density logs and check shot data (time-depth relation or TDR) of well-Y, as well as seismic line SL_1 (near well-Y), were loaded into the Petrel software for the construction of a synthetic seismogram. The aligned sonic velocity (*Vp*) and bulk density (ρ_b) log curves were refined and multiplied to obtain acoustic impedance (*AI*) as given in equation 4.17. From acoustic impedance, the reflection coefficient (*RC*) for each reflecting interface was computed using equation 4.18 (with layer-1 representing the deepest layer, and layer numbers incrementing upwards through the stratigraphic section). The software enabled the use of either a Ricker wavelet or a wavelet from the original seismic line for the convolution of reflection time series, in order to generate a synthetic trace. Based on iterative trials that ultimately yielded the best comparison between the seismic and synthetic seismogram, a Ricker wavelet with fixed parameters (128-millisecond sample lengths, two-millisecond sample rate, and 25 Hz frequency) was selected to generate the synthetic trace

for this data set. All available quality control parameters (e.g., Datum correction, sonic data calibration, drift correction, correlation of seismic traces) were utilized during the construction of the synthetic seismogram. The optional parameter (Backus averaging) was handled separately for upscaling the input logs to a given seismic frequency. The Backus (1962) average computation was based on the description made by Mavko et al. (2003) for transverse isotropic (TI) media and results are shown later in section 4.4.12, and an explanation is given in Appendix 4-C.

$$AI = \rho_b * Vp \quad (4.17)$$

$$RC = \frac{(A.I)_{layer-1} - (A.I)_{layer-2}}{(A.I)_{layer-1} + (A.I)_{layer-2}} \quad (4.18)$$

A minor amount of time-stretching and squeezing was applied to align the seismic and synthetic seismogram reflectors. The final position of reflectors closely matched the depths of the respective horizons (e.g., Sembar Formation top), as shown in Figure 4.5.

The seismic lines shown in Figure 4.6a were acquired near well-Y, as shown on the base map given in Figure 4.6b. No vertical shift was applied to these seismic lines because they were tied at crossing points for the Sembar top and bottom. The other formation tops were also identified on the seismic lines, as shown in Figures 4.7a to 4.7d, using the synthetic seismogram and stratigraphic column for the study area. Two faults were identified on two dip lines (SL_1 and SL_10) and may have a minor impact on computed velocities. The impacts of these faults on computed velocities were considered negligible due to their absence on other seismic lines near wells M, R, K-1, K-2 and X in the study area.

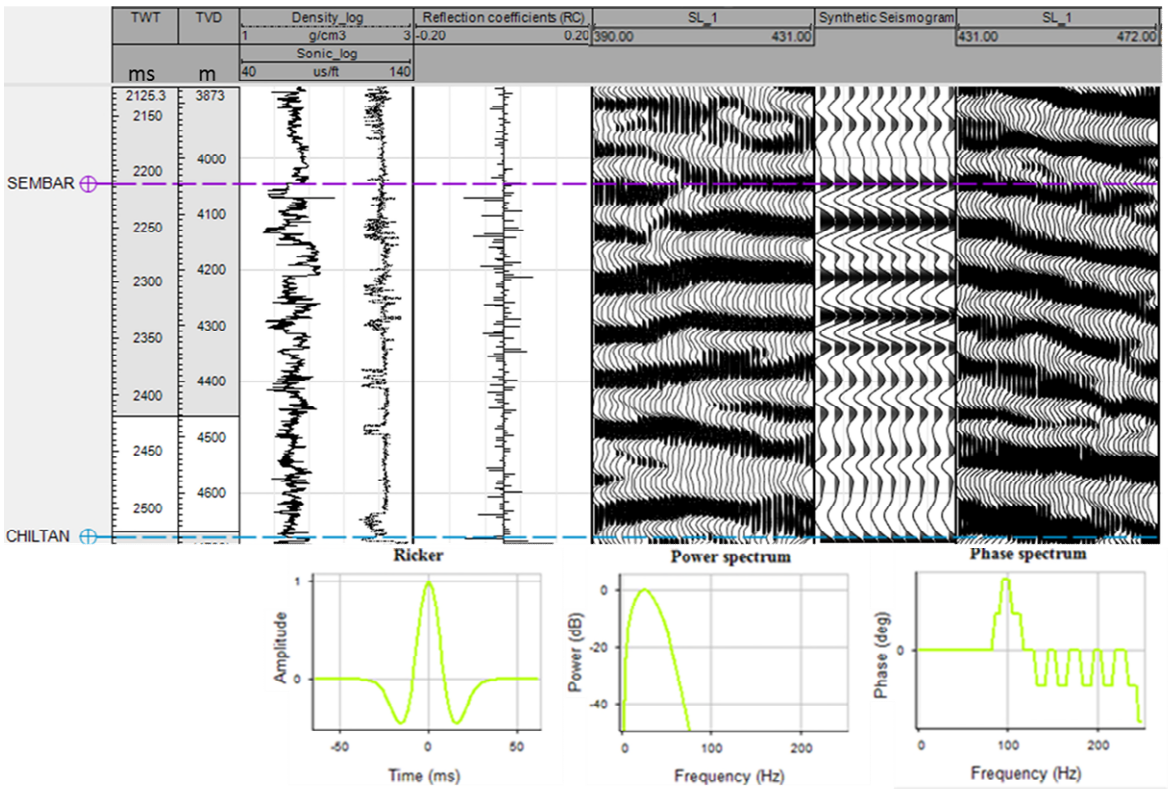

Figure 4.5 Synthetic seismogram for well-Y, showing (left to right): TWT (two-way time) in ms, TVD (true vertical depth) in m, sonic transit time and bulk density from logs (in µs/ft and g/cm^3, respectively), RC (reflection coefficient), traces from a portion of seismic line SL_1 adjacent to well-Y, synthetic seismogram for well-Y, and additional traces from seismic line SL_1. At the bottom, the plots of the source wavelet (Time-Amplitude, Frequency-Power, Frequency-Phase) are shown.

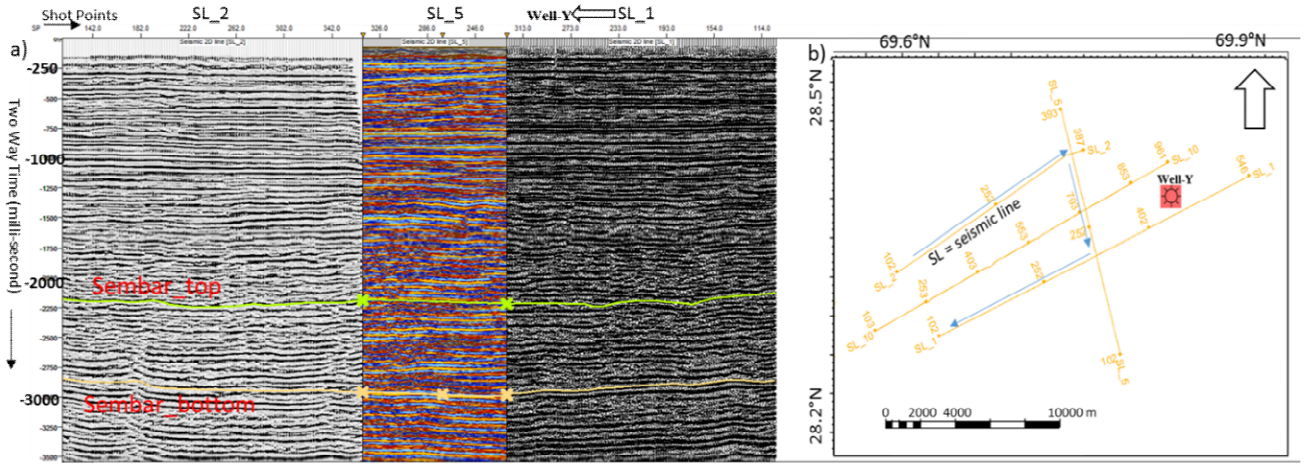

Figure 4.6 a) Tie-in of seismic line segments as identified by the blue arrows in part b), **b)** Base-map of study area showing seismic lines and well location. A polygon on the base-map (blue color) was constructed for tying the seismic lines at crossing points and transferring the seismic horizons from synthetic to seismic lines.

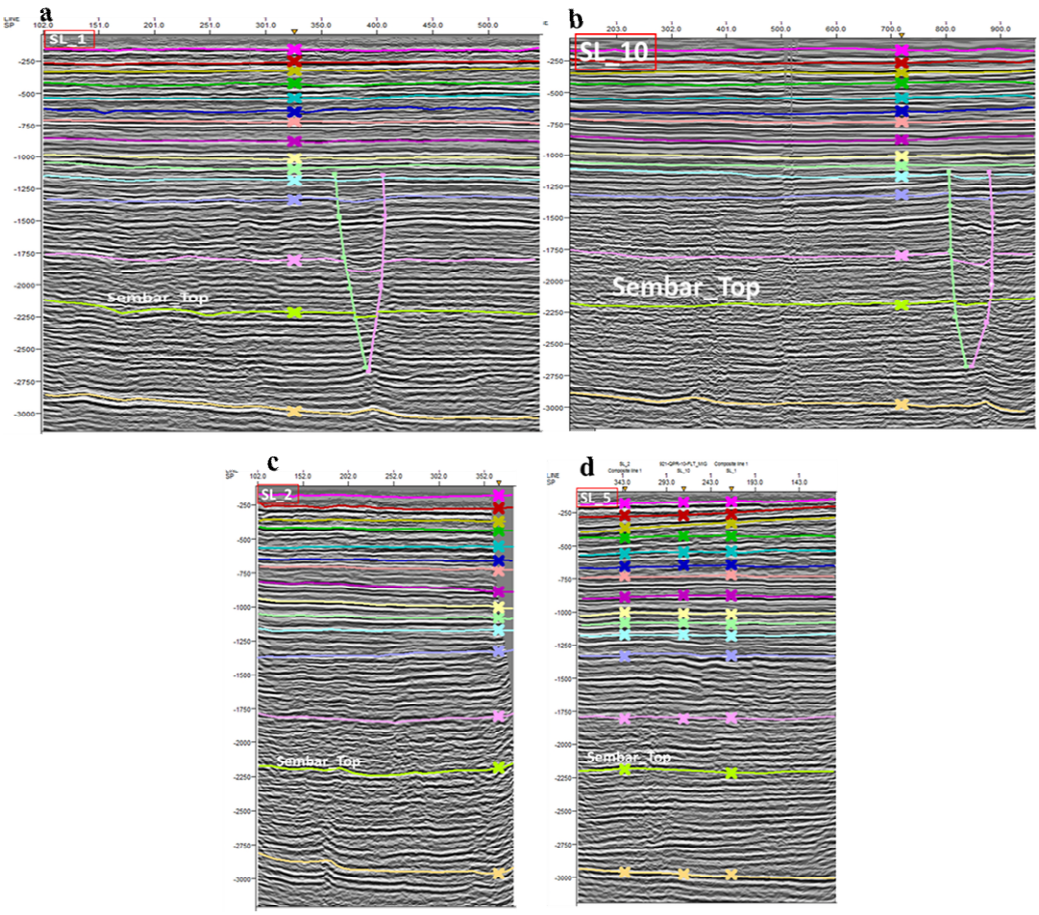

Figure 4.7 Interpreted seismic lines SL_1(**a**), SL_10 (**b**), SL_2 (**c**), and SL_5 (**d**), where colored sub-horizontal lines represent geological formation tops and sub-vertical lines on a and b represent normal faults.

4.4.12 Velocity Model

The calibrated interval velocities and two-way travel-times (TWT) obtained from the seismic-well tie (input data for seismic-well tie is shown in Figure 4.8a) were plotted separately to establish a trend line within the Sembar Formation, as shown in Figure 4.8b. The velocity function (equation 4.19) was fitted to the velocity-time plot using the least square method, and the constant values of Vo and K were extracted for the Sembar interval.

$$V_{int.P} = V_o + KT \qquad 4.19$$

Where $V_{int,P}$ is interval velocity of primary waves, T is two-way travel time, V_o is the velocity at the seismic horizon top, K is slope of the trend line.

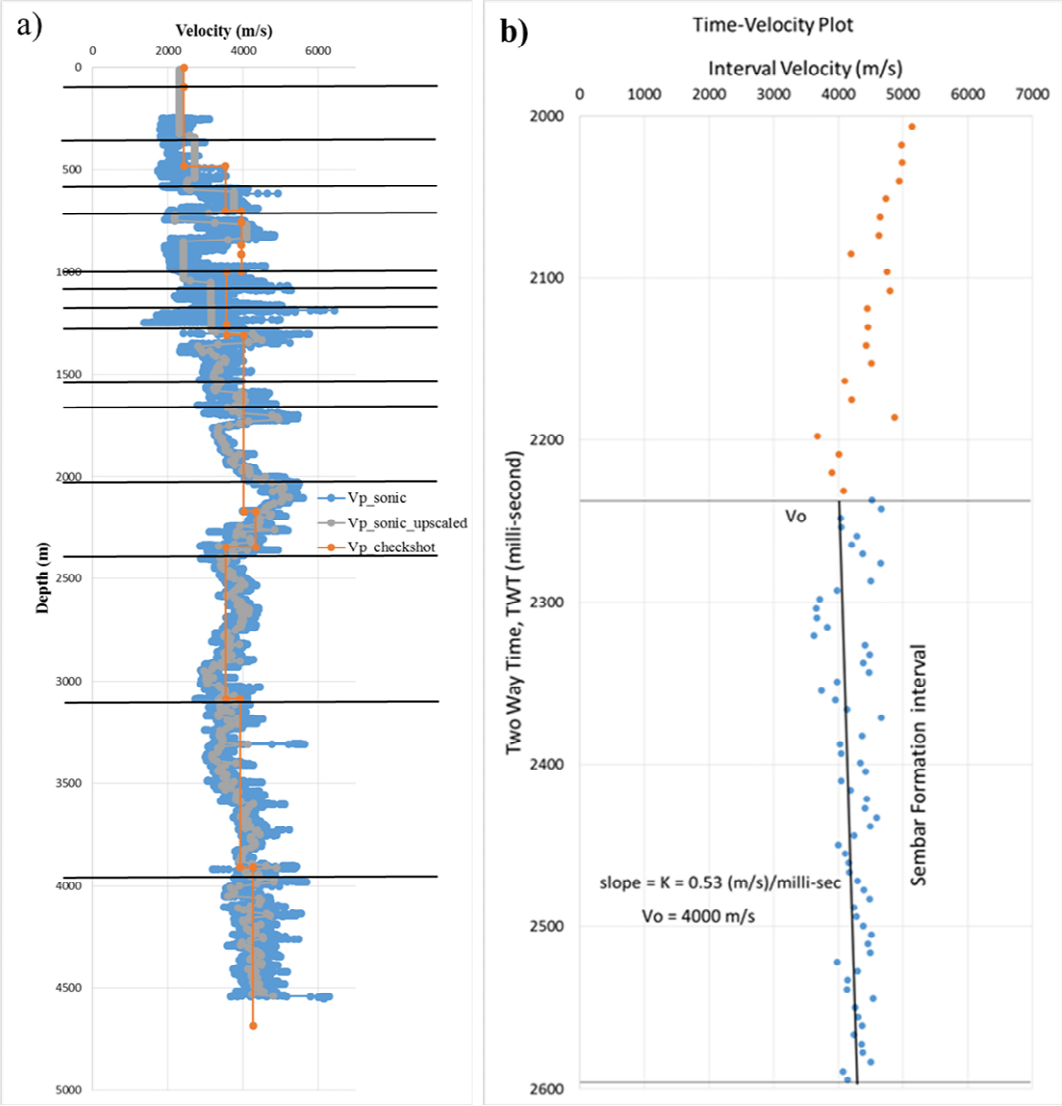

Figure 4.8 a) Shows the recorded sonic log (Vp_sonic) and upscaled_sonic (upscaled using Backus averaging), and check shot data extracted from offset well (within 10 km radius). The solid horizontal lines show formation tops. **b)** Calibrated interval-velocity versus two-way time (TWT) plot for the Sembar Formation encountered in well-Y. The trend line was established using least square method.

The calibrated velocity curve was also correlated with curves generated at three different shot points on the seismic lines using equation 4.20 (Dix, 1955), where stacking velocities (V_{st}) were available.

$$V_i = \sqrt{\frac{V_{st\_n}^2 T_n - V_{st_{n-1}}^2 T_{n-1}}{T_n - T_{n-1}}} \qquad 4.20$$

Where n represents the layer number, V_{st} & T_n are the stacking velocity and vertical two-way travel time (TWT), respectively, for the top of the nth layer.

It can be observed in Figure 4.9 the interval velocity curves compare favorably to the calibrated interval velocity for the Sembar Formation in well-Y, although interval velocities for other horizons show some differences against well velocities which may results from deviations for the assumptions underlying equation 4.20 (e.g., layered media and hyperbolic moveout) (Soleymani and Riahi, 2012).The breaks in these curves correlate strongly with known changes in lithology occurring at several formation tops in areas unaffected by faulting; in the faulted zone, there are additional breaks which are attributed to offset of the lithological layers.

The velocity-time function (equation 4.19) was employed at Sembar seismic horizons (top and bottom), and the values of Vo and K, and TWT surface maps of the top and bottom of the Sembar were inserted into the Petrel software to generate an interval velocity grid (Vp grid). The interval-velocity grid of the Sembar Formation was converted to a pore pressure grid using the log-based function (equation 4.9) described in section 4.4.8. The velocity and pore-pressure grids surrounding the well-Y were mapped using the GRFS (Gaussian random function simulation) algorithm (as shown in section 4.5.3).

The seismic two-way travel time contour maps for each seismic horizon (or layer) were converted to a depth map using the average velocity. The average velocity at the top of each horizon was calculated using equation 4.21.

$$V_{avg\_i} = \frac{\sum_{i=1}^{N} V_i \Delta T_{0i}}{\sum_{i=1}^{N} \Delta T_{0i}} \qquad 4.21$$

Where N is the total number of layers, V_i is the interval velocity in the ith layer, and ΔT_{0i} is the difference between zero-offset travel times at the top and bottom of the ith layer.

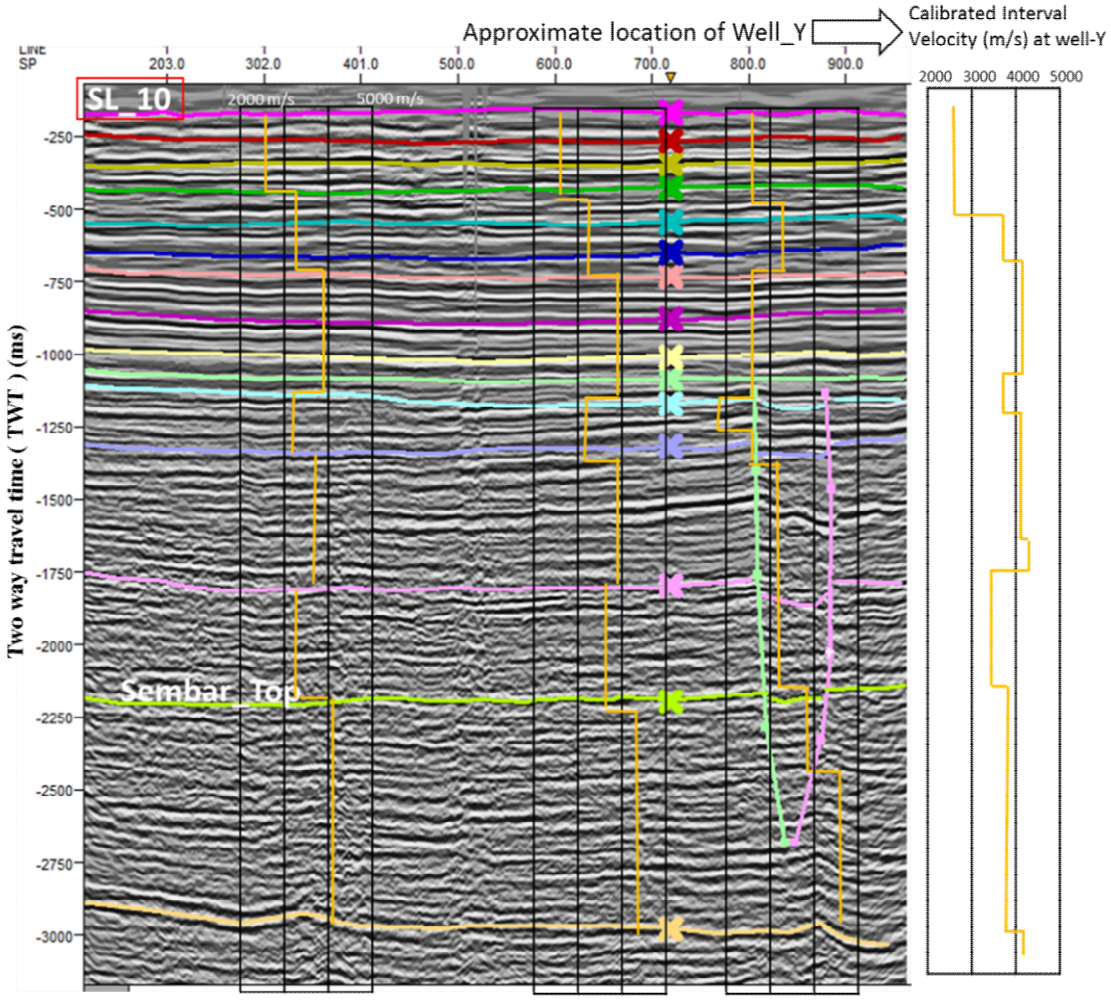

Figure 4.9 Interval velocity curves (gold color) obtained at selected shot points on the seismic line (SL_10) using the Dix equation (equation 4.19) and stacking velocities. The track on the right shows the calibrated interval velocity curve obtained from the well-seismic tie.

The synthetic seismogram of well-X is shown in Figure 4.10; the prominent reflectors on seismic lines at the bottom of the log curves show the top of the Sembar Formation, which was not logged in this well. Based on Figure 4.10 (which helps to identify shallow horizons above the Sembar Formation) and the well correlation profile (as given in Figure 4.2), the Sembar top was identified on 3D seismic data at the location of well-X. An estimated bottom of the Sembar Shale is also shown on seismic lines (Figures 4.10 and 4.11), based on the fact that this surface was encountered in offset wells within a 10 km radius at roughly 2400 ms. A similar procedure, as described above, was also followed for other wells mentioned in Table-1. The details of seismic horizon picking and velocity modeling of other wells are not included here for the sake of brevity.

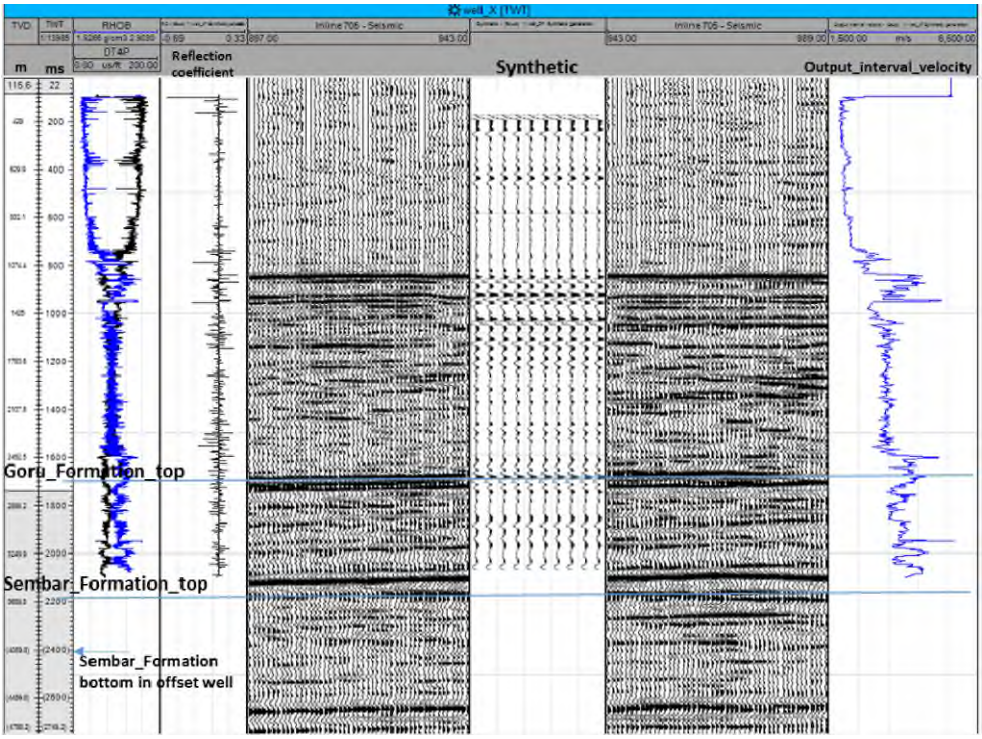

Figure 4.10 Construction of synthetic seismogram for well-X using density (RHOB) and sonic (DTP) logs and picking of expected Sembar Formation_top (~2200 ms) and bottom (~2400 ms) based on drilling report and regional geology of the study area.

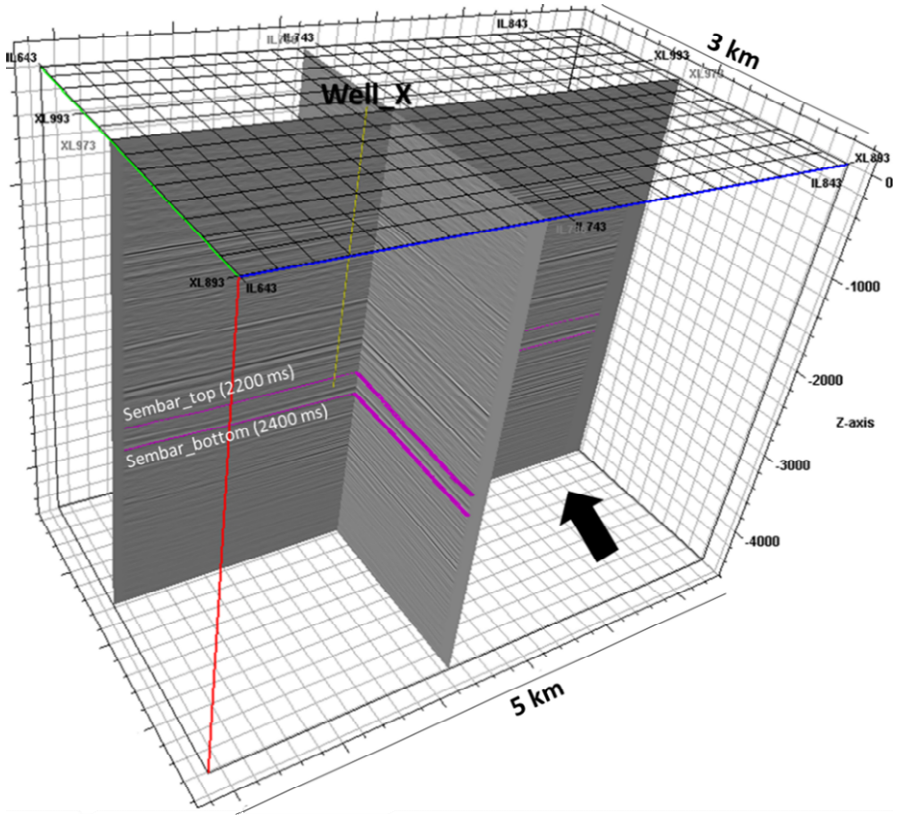

Figure 4.11 Picking of Sembar top and bottom on 3D seismic data at the location of well-X.

The Vp-contour map (at regional scale including studied wells) was converted to a shear wave velocity (Vs) map using a log-based Vp-Vs relationship (equation 4.22), which was established at well-Y, and similar relationships were also established at other wells in the study area. Both seismic interval velocities (Vp and Vs) and constant average-density corresponding to the Sembar Shale interval (obtained at multiple wells) were employed in equations 4.7 and 4.8 to calculate dynamic elastic properties (Young's modulus and Poisson's ratio) at each shot point. The seismic-velocity-based pore pressure and static elastic properties were employed in equations 4.10 and 4.11 to determine the minimum and maximum horizontal stresses, respectively, at each shot point of the seismic lines.

$$V_{s\_estimated} = 0.68\, V_{p\_log} - 497 \qquad 4.22$$

Where $V_{s\_estimated}$ is the estimated velocity of shear waves based on the rock physics model by Sohail and Hawkes (2020), V_{p_log} is measured compressional wave velocity in m/s.

4.4.13 Seismic Attribute Analysis

The 3D seismic data near well-X was also analyzed using the ant-tracking attribute to assess the presence and orientation of macro-fractures within the Sembar Formation. The 3D seismic data (Figure 4.12a) was conditioned through structural smoothing and variance attributes (Figure 4.12b) to enhance the visibility of the geometrical characteristics of seismic reflectors (Brouwer and Huck, 2011). After conditioning the seismic data, the ant-tracking attribute was run to delineate the tracks, as shown in Figures 4.12c. Most of the tracks are oriented in the northeast to the southwest direction (as highlighted by the dash-lines on Figure 4.12d), which is consistent with the orientation of maximum horizontal stresses observed in Figure 4.3 (borehole breakout analysis). Further investigations could be conducted if additional data (e.g., image logs, cores) are obtained to confirm the presence and characteristics of macro-fracture networks in the Sembar Shale.

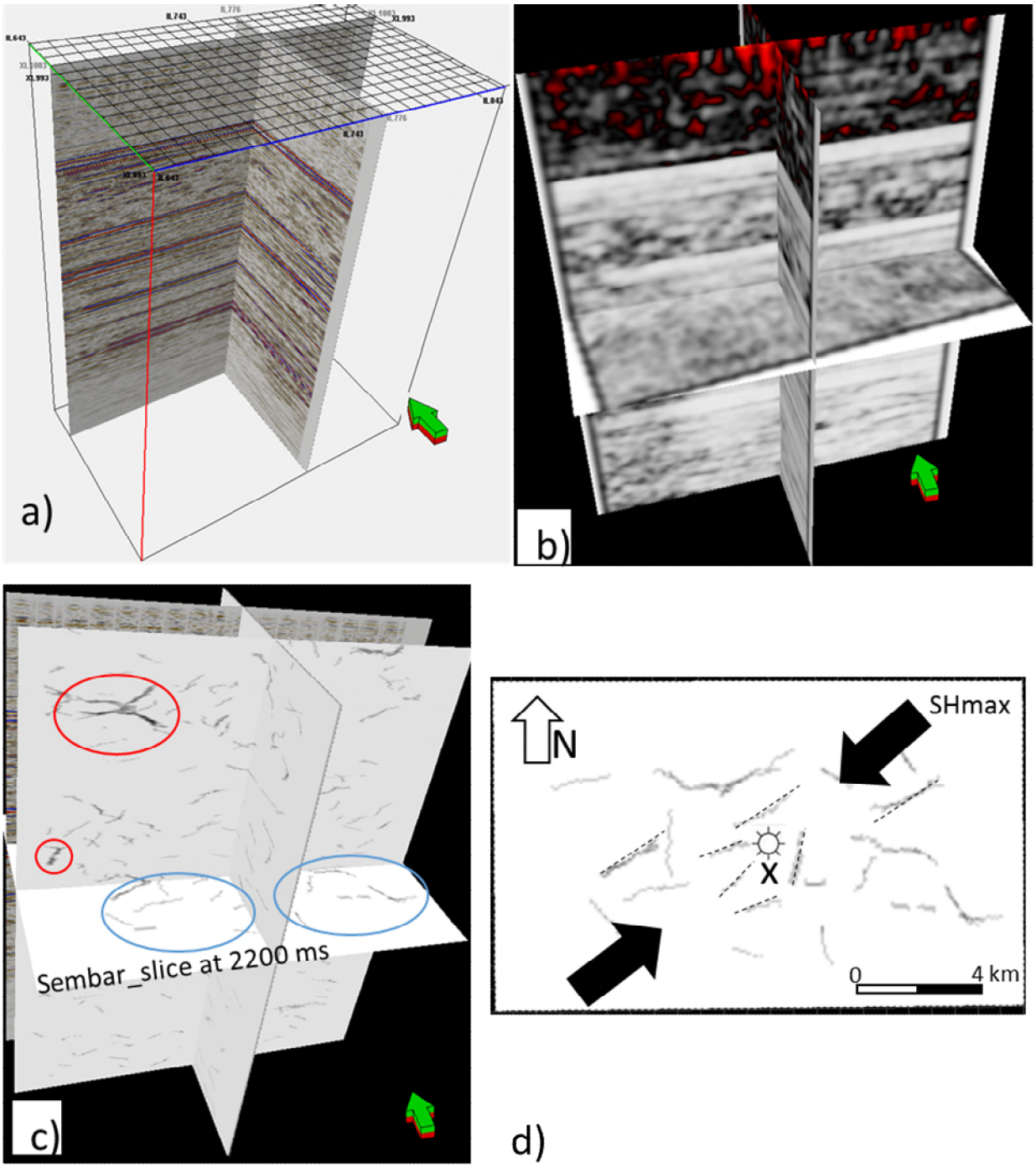

Figure 4.12 a) Original 3D seismic data with selected seismic lines (1003 cross line and 776 inline), **b)** Vertical and horizontal stacks after applying the structural smoothing and variance (3D Edge enhancement) attributes. **c)** Final stacks after running the ant-tracking attributes and slicing at the Sembar Formation horizon (at ~2200ms). The red-circles show faults/macro-fractures above from the Sembar and blue show macro-fractures at the top of Sembar Formation. **d)** Dashed lines show probable macro-fractures on the Sembar slice, which are predominantly oriented NE-SW.

4.4.14 Seismic Inversion

Four neural network-based seismic inversion techniques (BP, GI, MLC, PSO) were tested in this work using commercial software. The results of these inversions are shown in Figures 4.13a, 4.13b and 4.13c. The seismic attributes, velocities and densities (compressional and shear velocities and their relationship with densities using Gardner's equation (Gardner et al., 1974)) were used as an input layer, and these same attributes from logs for well-X were set as the output layer. Gardner's equation was available as an optional tool in the software to better understand velocity-density relationships based on known geological facies. The software was allowed to activate it in zones with known geological facies, where the estimated/measured data are poor or missing. It was demonstrated in a separate study on Lower Goru Shale (Du et al., 2019) that activating this option improves the final results of seismic facies analysis. For seismic inversion the dependancy on Gardner's equation was minimal, and in most of studied intervals the algorithm was trained based on measured data and known geological facies. The velocities and density of the Sembar Formation in well-X were obtained after studying other wells in the study area (where this formation was logged) and also learning the trends in Lower Goru Shales (which are considered equivalent to Sembar Shales) in well-X. The data was trained until maximizing the correlation coefficient between original and synthetic acoustic impedance, as shown in Figure 4.13d. The combination of MLC and PSO was found to provide the best agreement between the original and inverted acoustic impedance log.

The BP has a single structure which allows the network to converge to a local minimum and results in strong randomness, i.e., the results are inconsistent every time. The genetic algorithm in GI does not have a real global optimization, and often converges to the local minimum and has strong randomness (Dandan and Qiaodeng, 2002). The optimization problems are generally divided into local optimal and global optimal. Local optimal refers to finding the minimum value in a finite region of the function value space. The global optimum is to find the minimum value problem in the whole region of the function value space. The MLC+PSO strategy establishes a nonlinear relationship between AI and seismic waveform and calculates appropriate weights to predict AI effectively.

The elastic properties estimated using seismic velocities and bulk density were set as input parameters, and elastic properties at well-X were set as output parameters to rerun the inversion module to invert 3D seismic data into an elastic properties cube. The software inherently established relationships between input and output parameters to reduce the error between measured and estimated elastic properties. The same procedure was followed to

invert 2D seismic stacks near well-Y. The inverted elastic property trends (from seismic data) near wells X and Y were compared to regional trends in the study area.

The medium to high range of acoustic impedance, as highlighted by dashed white-colored-rectangles on the inverted seismic stacks (Figure 4.13), is identified as the Sembar Shale interval within the Sembar Formation. A facies analysis based on seismic reflection data and well logs for some offset wells near well-X, conducted by by Ahmad et al., (2004), Du et al., (2019) and Ashraf et al., (2019), also confirmed the depth/seismic-time of Sembar Formation in the study area, although these authors were studying the characteristics of Lower Goru Formation, which overlies the Sembar Formation.

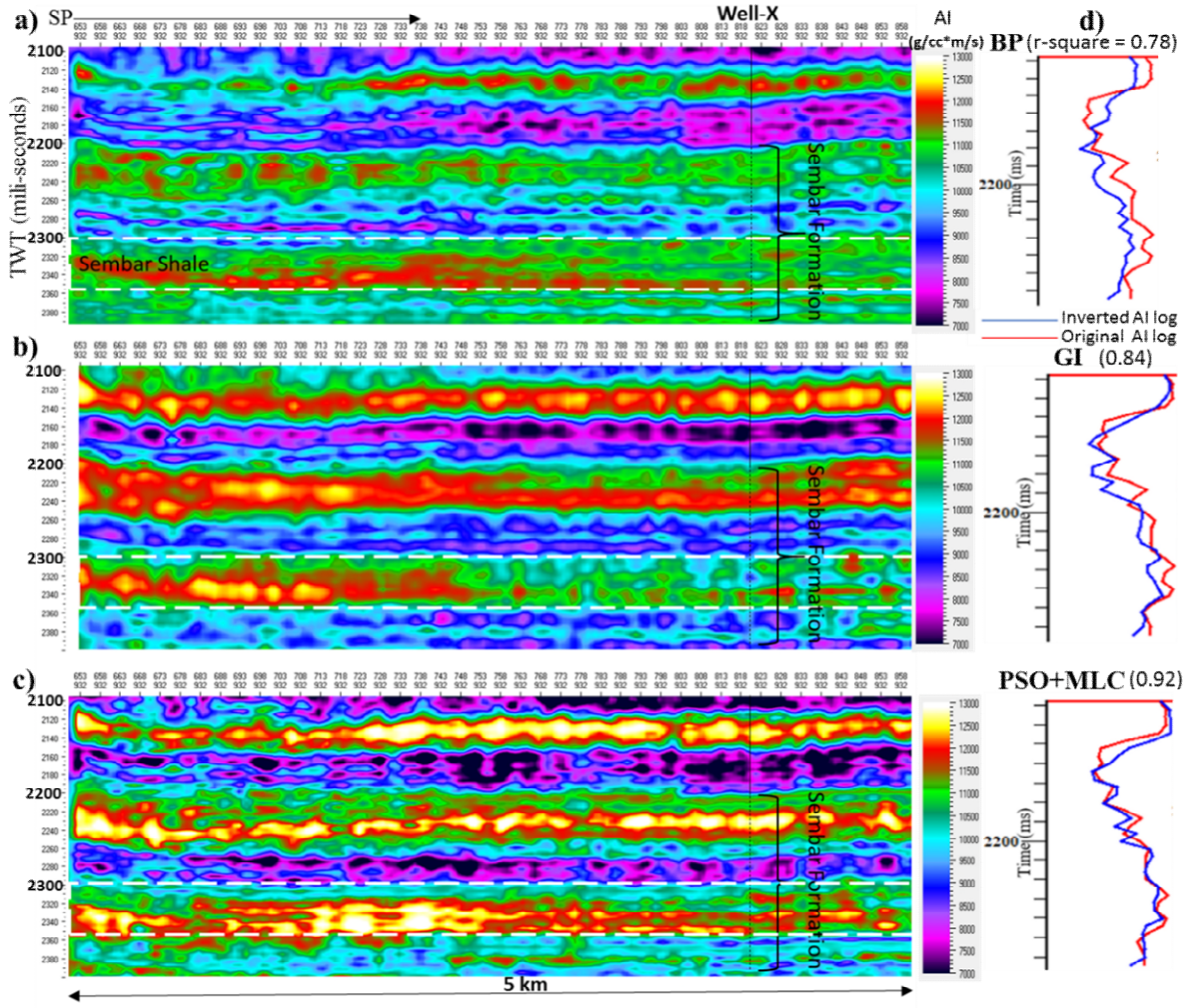

Figure 4.13 Inverted acoustic impedance (AI) stack using **a)** BP, **b)** GI. **c)** MLC+PSO, **d)** Comparison of original (red color) and inverted (blue color) acoustic impedance curves. The red curves were extracted from the relevant inverted seismic stack at well-X. The dashed rectangle (white color) on inverted stacks highlights the shale interval (2300-2350 ms) in the Sembar Formation, which is associated with medium to high AI.

4.5 Results

4.5.1 Petrophysical Characterization

The gamma-ray log for well-Y (shown in track-2 of Figure 4.14) shows a general trend of increasing upward through much of the Sembar Shale (4430-4468 m), overlain by a zone of relatively constant gamma-ray readings which ends sharply at the top of this interval (4418 m). The volume of clay calculated from the gamma-ray log generally increases upward from 0.4 to 0.6 between 4430 m and 4468 m, and ranges between 0.4 and 0.5 from 4430 m to 4418 m. These log-based results suggest a fining upward trend, which is consistent with Nazeer et al. (2016) who found that the Sembar Formation contains sequences of various prograde and retrograde (mixed coarsening and fining) cycles which pass from shallow marine facies near the base of the interval to basinal facies near the top. As discussed in the methodology section (see Figure 4.4), the predominant minerals over the interval of interest are clay and quartz, with pyrite and dolomite existing in minor quantities. As shown in tracks 4 and 6 of Figure 4.14, the TOC and porosity range from 2% to 4% (volumetric) and 0.05 to 0.1 (fraction), respectively. As shown in track 5, log-based water saturations are slightly higher than 0.2 (fraction) through much of the interval, with local highs in the range of 0.7 to 0.8 occurring in some of the sandier intervals. These petrophysical properties were used as inputs for the calculation of Vp using the modified rock-physics model of Xu and White (1995). The favorable comparison between calculated Vp (Vp_RP) and measured Vp (Vp_log), as shown in track 7, supports the validity of these log-based petrophysical properties, and the rock physics model. This, by association, yields increased confidence in the estimated Vs values (see Vs_RP in track 8) that were calculated using these same inputs and rock physics model.

4.5.2 Log-based Geomechanical Characterization

The lithostratigraphy interpreted through petrophysical characterization was used to build the mechanical stratigraphy for the study interval. This interval was subdivided into grain-supported facies and clay-supported facies according to the volume fraction of clays, as shown in track-2 of Figure 4.15. The clay-supported facies are defined as those with Vcl > 40%, and grain-supported facies are those with Vcl < 40%. The threshold value of 40% was proposed as a transitional point based on microstructures, mechanical and flow properties by Zoback and Kohli (2019). The results show that the upper half of the study

interval is predominated by thick clay-supported units, whereas the lower half consists of interbedded clay and grain-supported units, with the latter becoming more prevalent near the base of the interval.

The dynamic Young's modulus (track-3 of Figure 4.15) varies between 35 GPa and 40 GPa through most of the study interval, with one distinct interval of slightly lower values (~30 GPa) from 4445m to 4451 m. The dynamic Poisson's ratio generally varies between 0.2 and 0.3, with no obvious correlation to grain or clay-supported facies. Poisson's ratio shows a more variable character than Young's modulus, though the overall range of variation (0.2 to 0.3) is modest. It should also be noted that Poisson's ratio is strongly sensitive to the Vp/Vs ratio, and Vs was estimated in this work. Bulk modulus (K_b) was also calculated using the relation $K_b = E/[3(1-2\nu)]$, though the results are not shown in Figure 4.15 for the sake of simplicity

Most of the published relationships for the brittleness index (BI) are based on weight fractions of brittle minerals. It is suggested that a volume fraction-based approach might be more appropriate; hence both approaches were used in this work. It can be observed in Figure 4.15 (tracks 7 and 8) that these approaches yield slightly different results due to the increased influence of the relatively dense pyrite in the weight fraction-based approach. The general character of tracks 7 and 8 is similar, though the BI values for the volume fraction-based model (track 8) are slightly lower than the weight fraction-based values (track 7) in most of the shaley intervals. Track 12 shows a binary classification of brittle and ductile units, based on a threshold value of BI = 0.5 applied to track 8.

Brittleness indices based on log-derived elastic properties are shown in tracks 9 (Young's modulus-based), 10 (Poisson's ratio-based) and 11 (average). One of the perceived benefits of these indices is the fact that they implicitly account for various factors beyond mineralogy; e.g., grain size, cementation and effective stress (Holt et al., 2011; Yang et al., 2013; Wasantha and Ranjith, 2014; Luan et al., 2014). The general character of the BI profile based on average elastic properties (track 11) is generally similar to the mineralogy-based profiles, though the contrast between shaley and sandy intervals is more pronounced. Track 12 shows a binary classification of brittle and ductile units, based on a threshold value of BI = 0.5 applied to track 11.

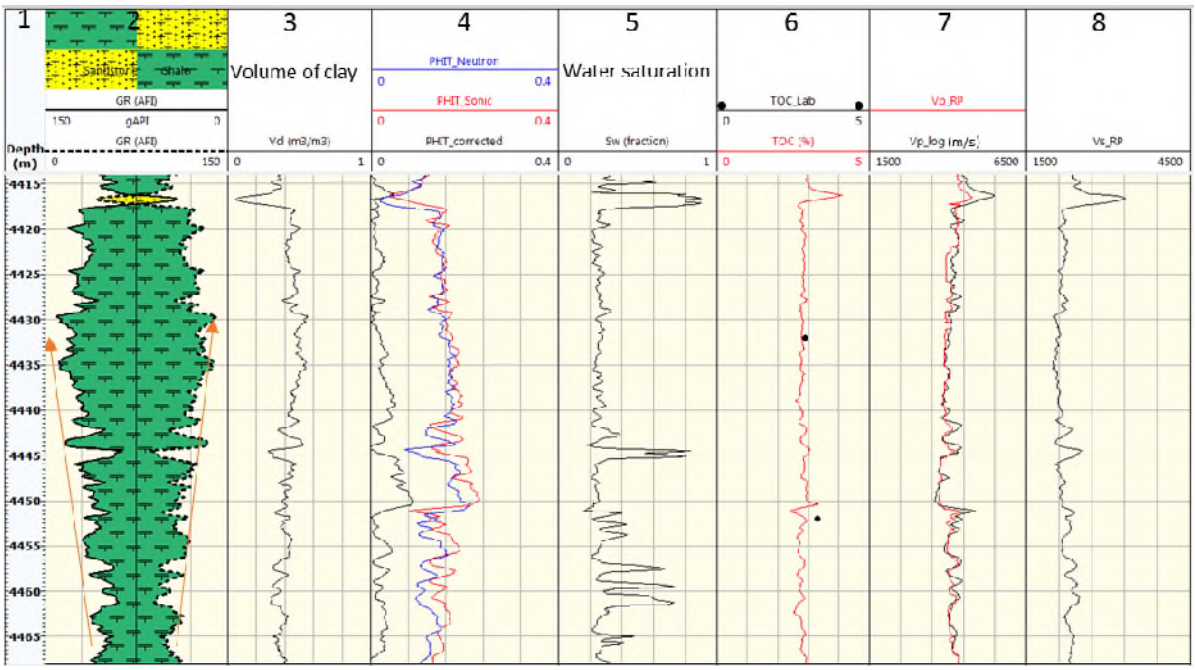

Figure 4.14 Log data and interpreted petrophysical properties for the Sembar Shale interval in well-Y. Track-1 shows depth, track-2 shows GR_log plotted in inverted and standard form for interpretation (using a baseline of 75API) (arrows show the interval with the fining upward trend), track 3 shows volume of clay, track-4 shows total porosity (PHIT) using neutron and sonic log-derived porosities, track-5 shows water saturation (Sw), track 6 shows total organic carbon (TOC) from laboratory (black-dots) and logs (red curves), track-7 shows measured (black) and estimated (rock-physics-based-model) compressional wave velocity (Vp), and track-8 shows estimated shear wave velocity calculated using a rock-physics model (Vs_RP).

The estimated pore pressure curve, as shown in track-5 of Figure 4.15, was calibrated with measured pore pressure at one point (shown by the dark-blue dot), as discussed in section 4.4.8. The principal in-situ stress magnitudes calculated for the study interval are shown in track-6 of Figure 4.15. The minimum horizontal stress was calibrated using data from a mini-frac test at 4428 m depth (unpublished well report). These results suggest that the Sembar Shale interval in well-Y falls in a present-day strike-slip stress regime ($S_{Hmax} > S_v > S_{Hmin}$). In some intervals, the difference between maximum horizontal stress and vertical stress becomes small, which seems to be due to relatively high pore pressure and/or relatively low Young's modulus. This, coupled with the observation of some normal faults on some seismic lines near well-Y, suggests that the stress regime for the study area ranges from a strike-slip regime to transitional (strike-slip / normal) regime.

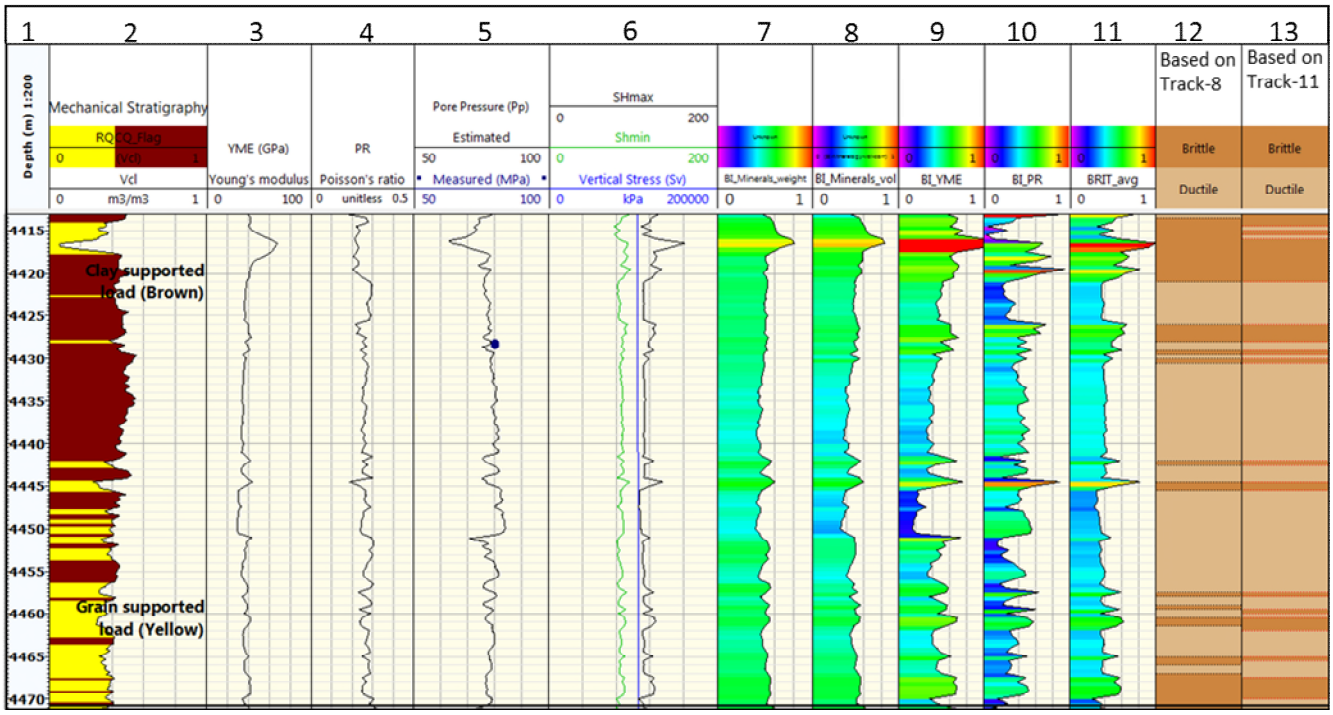

Figure 4.15 Interpreted mechanical properties for the Sembar Shale interval in well-Y. Track-1 for depth, track-2 shows mechanical stratigraphy based on volume of clay (Vcl), track-3 shows dynamic Young's modulus (YME), track-4 shows dynamic Poisson's ratio (PR), track-5 shows estimated (black curve) and measured (dark blue dot) pore pressure in MPa, track-6 shows S_{Hmax} for maximum horizontal stress; S_{Hmin} for minimum horizontal stress; S_v for vertical stress, track-7 shows brittleness index (BI) based on minerals weights, track-8 shows brittleness index (BI) based on minerals volume, track-9 shows BI based on YME (BI_YME), track-10 shows BI based on PR (BI_PR), track-11 shows an average of tracks- 9 and 10 (BRIT_average), track-12 shows the brittle and ductile intervals based on a BI threshold of 0.5 applied to track-8, and track-13 shows the brittle and ductile intervals based on a BI threshold of 0.5 applied to track-11.

4.5.3 Seismic-Well-based Geomechanical Characterization

Interval velocities of the Sembar Formation extracted from seismic stacks near well-Y were used to estimate pore pressures. Both velocity and pore-pressure cubes were generated using the GRFS algorithm, which confirms that the GRFS honors well data and seismic data. A detailed description of this algorithm is beyond the scope of this paper but can be found in Schlumberger Petrel Manual (2019). The time/depth slices of interval velocity and pore-pressure for the Sembar Formation were extracted from the cube of whole well-Y, as shown in Figures 4.16a and 4.16b, respectively. Similarly, depth slices specific to the Sembar Shale interval are shown in Figures 4.16c and 4.16d, respectively. The high pore-pressure zones are associated with low velocities, which is consistent with the observations at well-Y. These results are consistent with the published pore pressure gradient for the Sembar Formation in the study area (Farooq et al., 2009). A similar approach was

adopted for other wells in the study area for the estimation of pore pressures at individual well location, and then these estimations were utilized to construct a regional scale map of pore pressure.

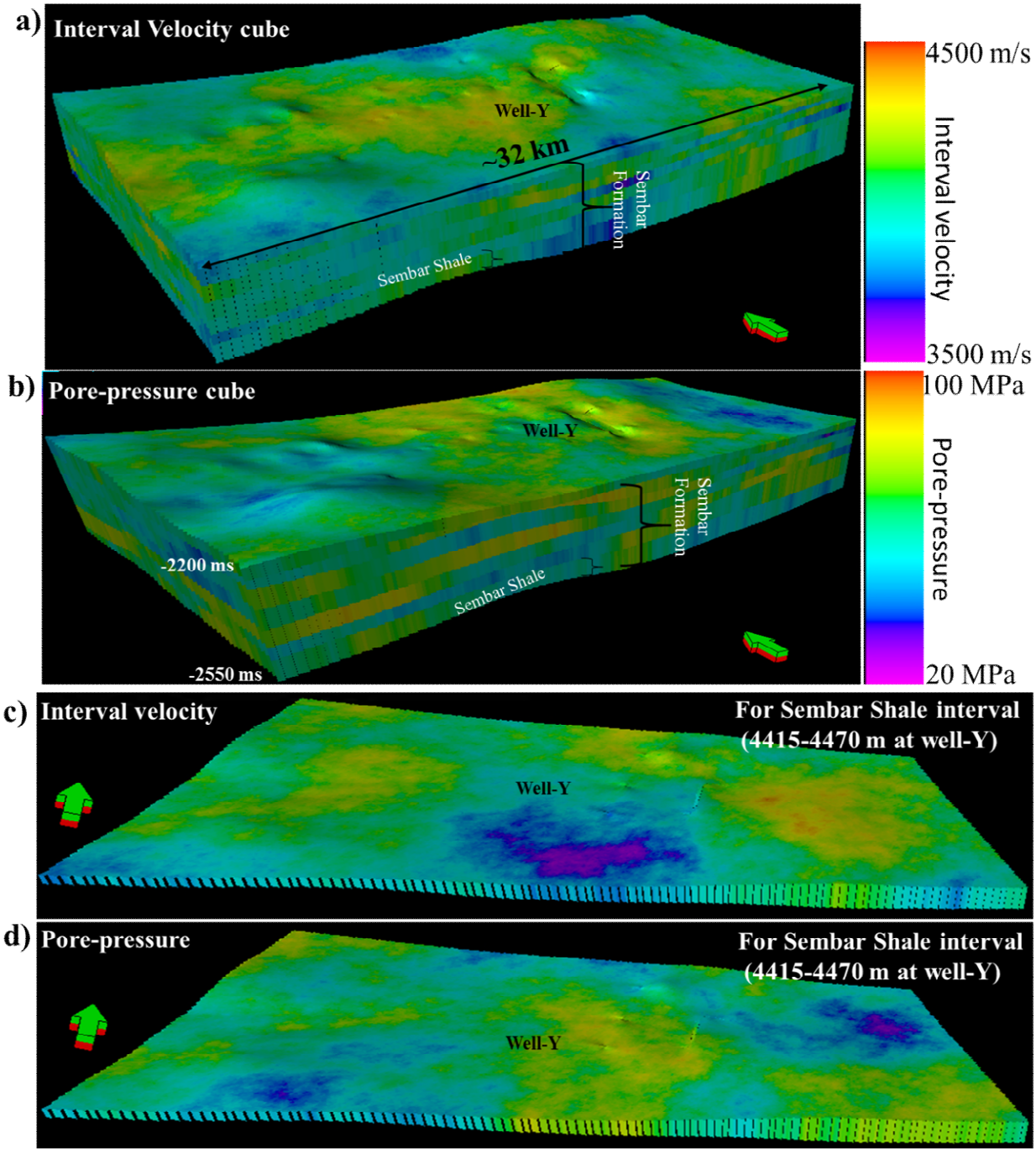

Figure 4.16 Shows cubes and depth slices of seismic interval velocities (**a** – Sembar Formation; **c** – Sembar Shale) and pore pressure (**b** – Sembar Formation; **d** – Sembar Shale) in the vicinity of well-Y, developed using the Gaussian random function simulation (GRFS) algorithm (developed by Schlumberger). The arrow denotes north in each figure.

Contour maps of seismic two-way travel time and depth (constructed using average velocities at the top of Sembar Formation, evaluated using equation 4.21) are shown in

Figures 4.17a and 4.17b, respectively. The depth map is consistent with the depth of the Sembar Formation where it was encountered in the studied wells. The velocity distribution maps, as shown in Figure 4.18, show zones of high average velocities near well-Y compared to well-X. Figure 4.18 (Pp map) shows pore pressure distribution at the regional scale, based on the pore pressure gradient interpreted at each well (calibrated with seismic data). This figure shows comparatively high pore pressure zones near well-Y compared to well-X. The inverted seismic stacks of elastic properties for the entire Sembar Formation near wells X and Y, as shown in Figures 4.19a (for well-Y) and 4.19c (for well-X), show that Young's modulus and Poisson's ratio of Sembar Shale are comparable with regional trends (Figure 4.19b). Dynamic Young's modulus is relatively high in the north-northeast of the study area (near wells M and Y) compared to the southeast (near well-X). Poisson's ratio is higher in northeast compared to the southeast of the study area, as illustrated in Figure 4.19b. The regional trend in Poisson's ratio is different from the trend observed for Young's modulus. BRIT_avg is lower in the northwest compared to the southeast portion of the study area.

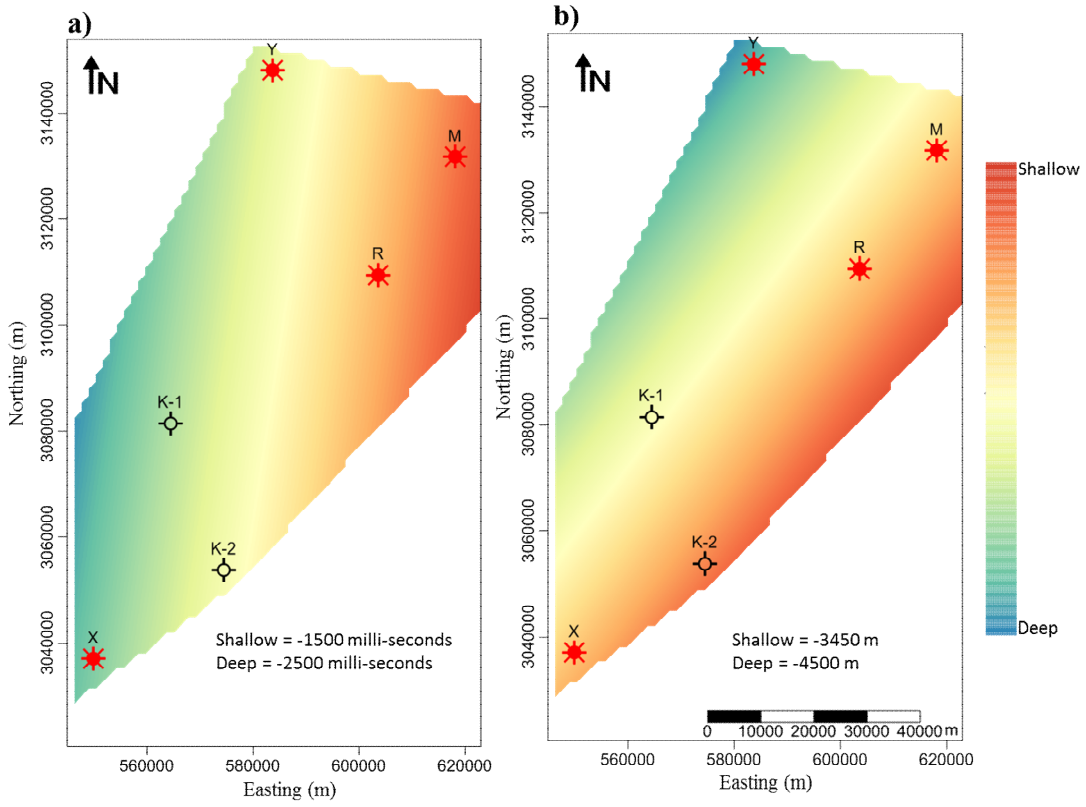

Figure 4.17 Contour maps of two-way travel time **(a)** and depth **(b)** for the Sembar Formation top, overlayed by well locations. The negative sign with contour values is used to denote depth below the surface. The reference datum is WGS84, and the study area is located in UTM zone 42N.

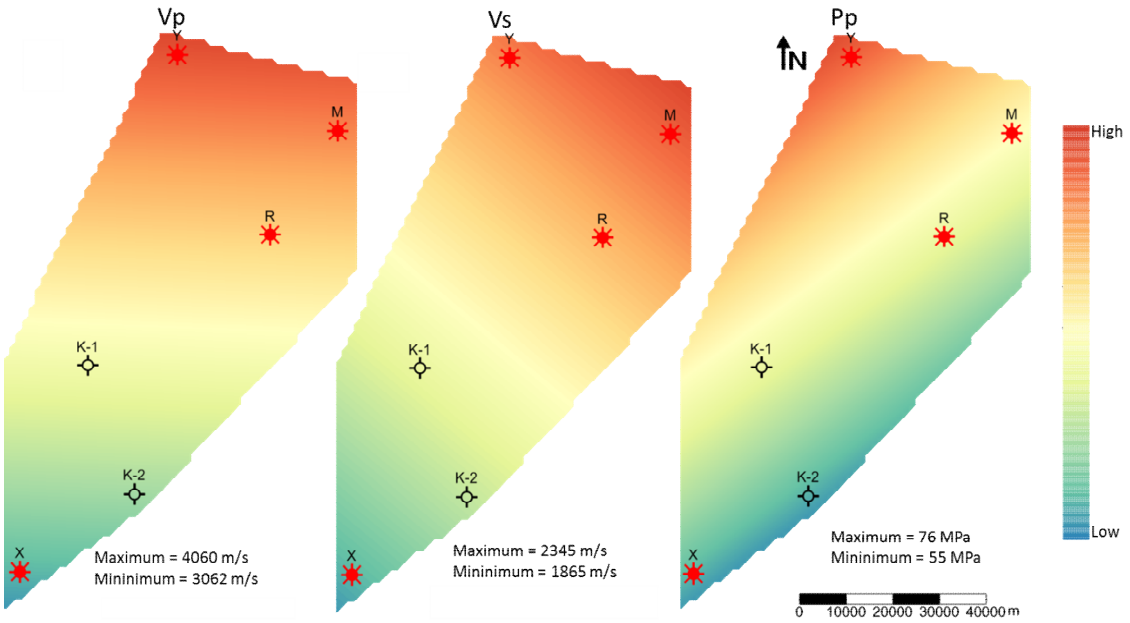

Figure 4.18 Average compressional and shear wave velocities (Vp and Vs), and pore pressure (Pp) maps for the Sembar Formation in the study area.

The inverted elastic properties cube generated using robust inversion techniques (e.g., MLC+PSO), as shown in Figure 4.20, enhances the resolution of elastic properties in the area surrounding well-X. Figure 4.20 shows that Young's modulus and Poisson's ratio in the Sembar Shale interval vary spatially between 35 GPa to 40 GPa and 0.24 to 0.28 in the Sembar Formation, respectively. These ranges are generally consistent with the 2D inverted seismic stacks shown in Figure 4.19c.

The stresses and pore-pressure gradients extracted from the data for wells X and Y, as given in Table 4.2, are consistent with the gradients published by different researchers in the study area. The stress gradients for well-Y were assigned to wells M and R, which are relatively close to well-Y and have similar Sembar Formation thicknesses at slightly shallower depths. For similar reasons, the stress gradients for well-X were assigned to wells K-1 and K-2. Figure 4.21 shows the stress magnitudes calculated from the stress gradients assigned to the aforenoted six wells, and the depth of the Sembar Formation (Figure 4.18b). These contour maps show that stress magnitudes increase from southeast to northwest, which is consistent with the higher horizontal stress gradients and the greater depths in the northwest. These stress maps also show a strike-slip stress regime throughout the study area. Vertical slices showing inverted horizontal stresses from the 3D seismic data at well-X are given in Appendix 4-D.

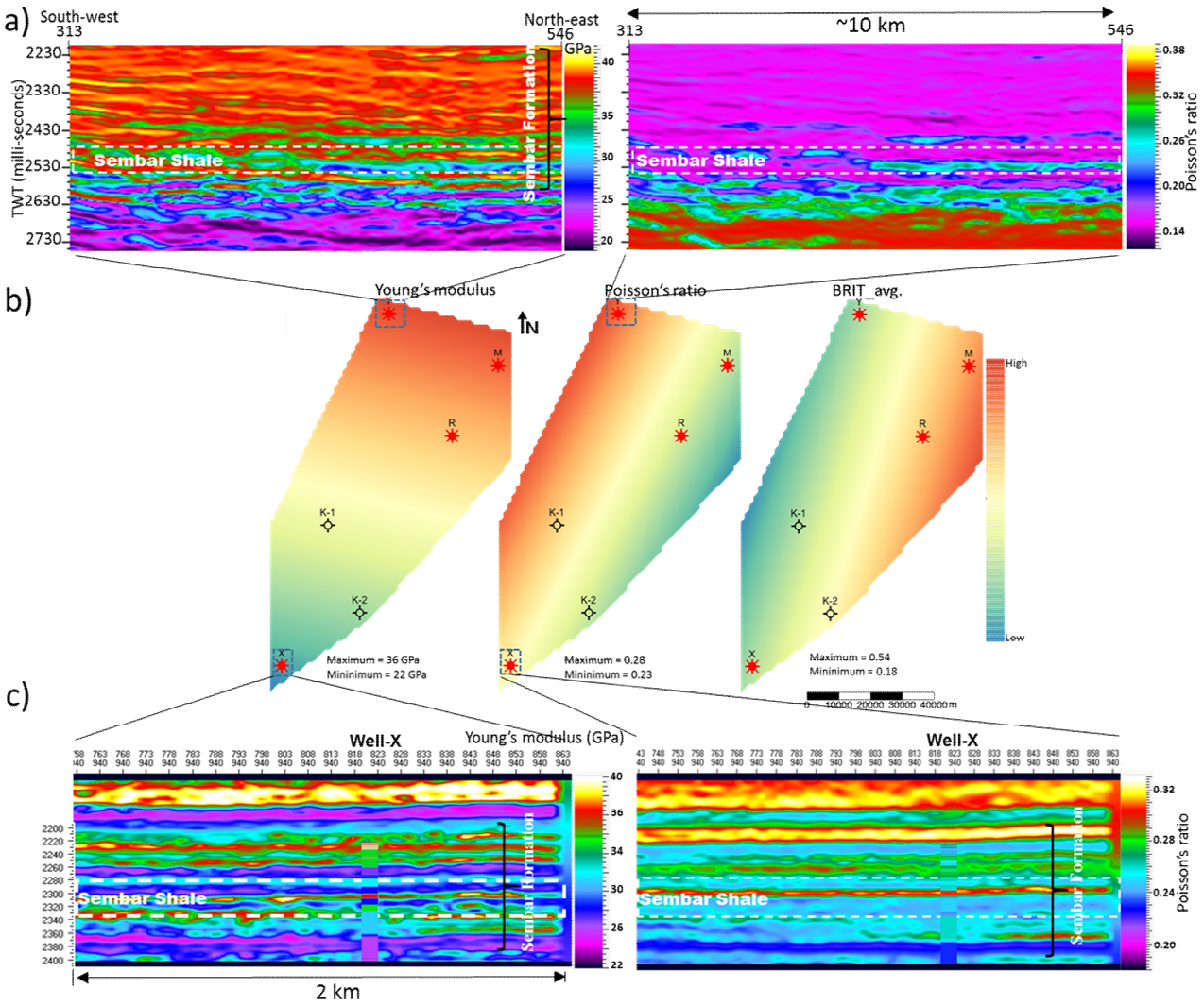

Figure 4.19 a) Inverted seismic stacks of Young's modulus and Poisson's ratio near well-Y for the entire Sembar Formation (2230 ms to 2550 ms); the white-color rectangle delineates the Sembar Shale interval, **b)** Contour maps of average Young's modulus, Poisson's ratio and elastic properties-based average brittleness index (BRIT_avg) for the Sembar Shale interval based on well and seismic data, **c)** Inverted seismic stacks at well-X for the entire Sembar Formation (2200 ms to 2400 ms) and Sembar Shale (2300 ms to 2340 ms).

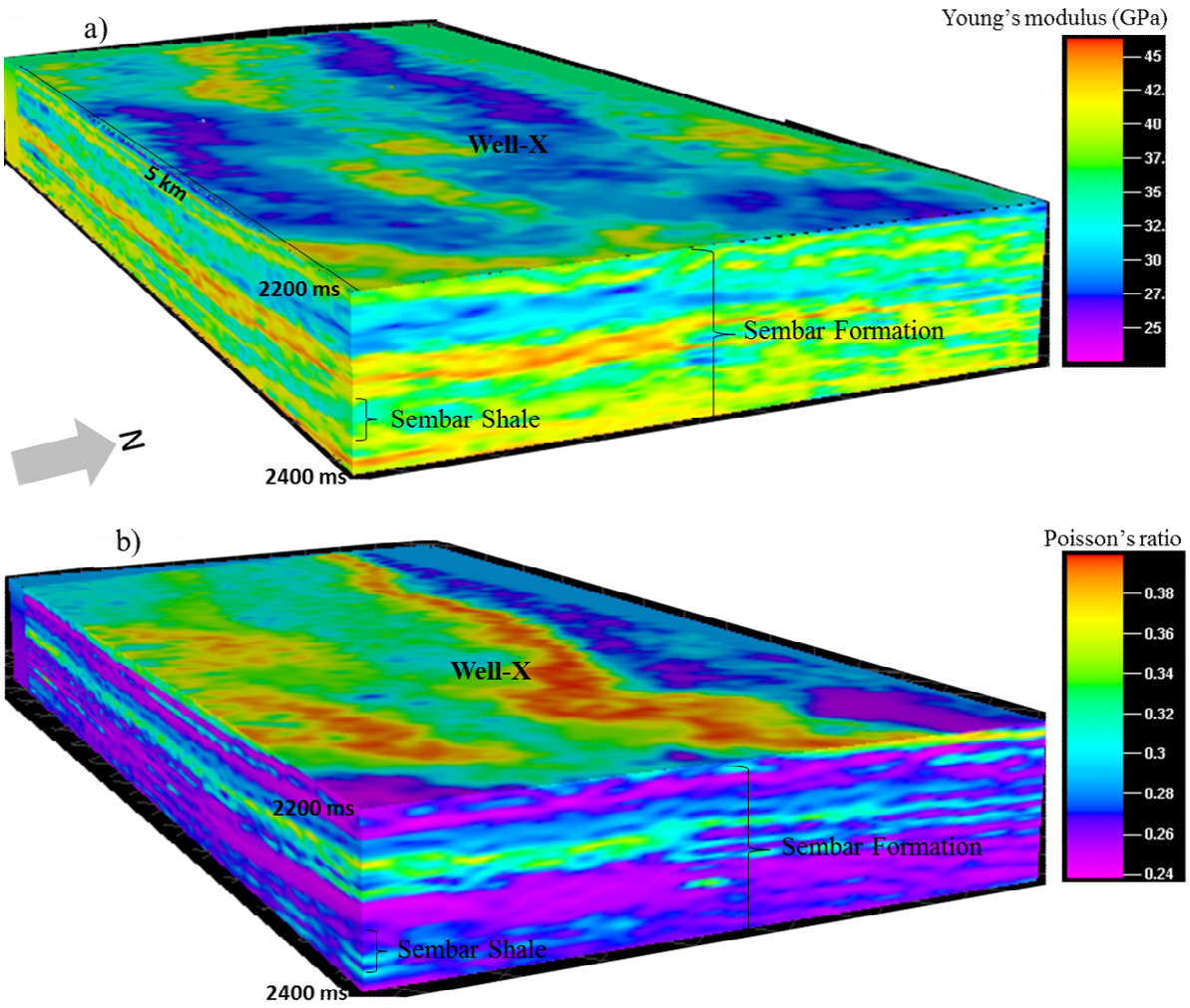

Figure 4.20 Inverted seismic cubes of (a) Young's modulus and (b) Poisson's ratio around well-X for the Sembar Formation.

Table 4.2 Stress and pore-pressure gradients for wells Y and X

Gradient	Well-Y	Well-X
S_{Hmax} (MPa/m)	0.026	0.024
S_{Hmin} (MPa/m)	0.020	0.018
S_v (MPa/m)	0.023	0.023
Pore-pressur (MPa/m)	0.017	0.014

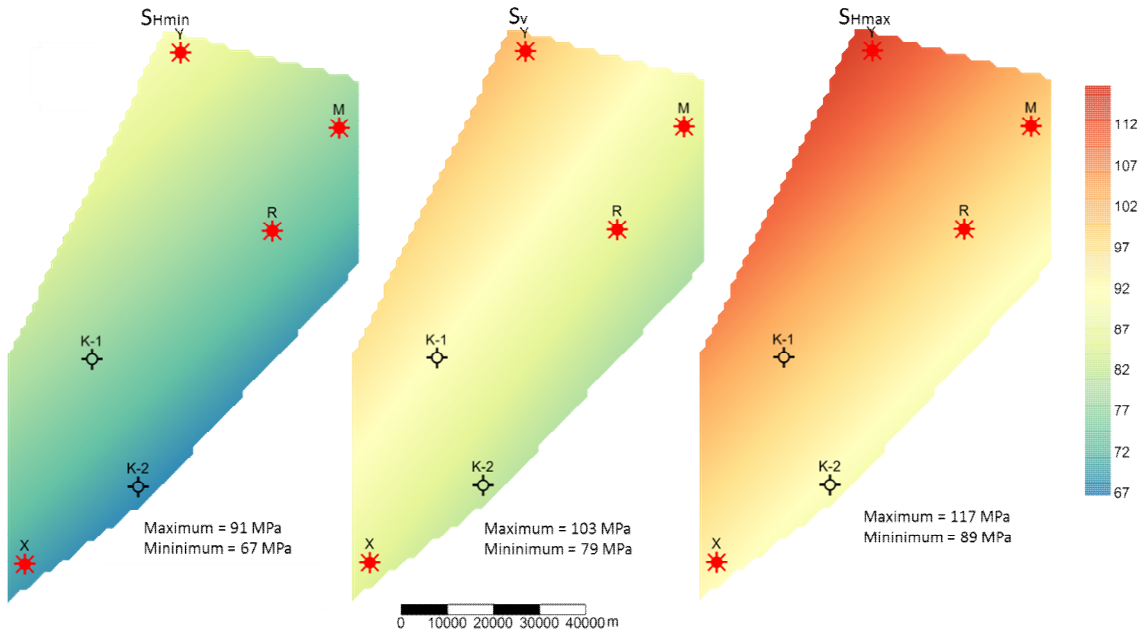

Figure 4.21 Contour maps of average minimum and maximum horizontal stresses (S_{Hmin} and S_{Hmax}, respectively), and vertical stress (S_v) for the entire Sembar Shale interval in the study area.

4.6 Discussion

The Sembar Formation interval of the study area is in a relatively undisturbed zone where generally monoclinal strata rest on the crystalline basement (Indian shield). There was no major fault activity or deformation related to the basement structure observed in the studied seismic lines, although some normal faults with minimum throw were interpreted on 2D seismic lines near well-Y, and the overlying strata of Middle Cretaceous to recent age seem to be disturbed due to the collision of the Indian and Eurasian plates in the Eocene epoch. Due to the lack of structural complexity in the Sembar Formation in the study area, the generated seismic velocity maps are deemed appropriate for representing spatial variations in geomechanical properties interpreted from these velocities.

A shale gas reservoir should fulfill the following criteria: suitable thickness (>100m), organically rich and mature with free gas (TOC>2%, R0>0.55%, Kerogen type-II or III), good porosity (>5%), high quantity of quartz (>40%) and low clay volume (<30%), high values of Young's modulus with low Poisson's ratio, high brittleness index for hydraulic fracturing, and known stresses magnitudes and orientations to allow appropriate placement, orientation and completion design for horizontal wells (Sondergeld et al., 2010; Dembicki and Madren, 2014). Although shale itself is a good seal, the presence of additional shale layers above the shale gas reservoir diminishes the chance of leakage or migration of

hydrocarbons from the shale gas reservoir (Dembicki and Madren, 2014). All of these parameters, and their interrelation, play a crucial role in screening a shale gas reservoir at a local and regional scale. Following is an assessment of the Sembar Shale as a prospective shale gas reservoir, based on the aforenoted criteria.

Theoretically, the density of shale should decrease with increasing TOC. This, in turn, should reduce sonic velocities and dynamic elastic properties. This expectation is consistent with data for shales of the Cooper Basin, Australia, which showed a significant effect on dynamic elastic properties for TOC > 1% (Iqbal et al., 2018). However, in most of the North American Shales (particularly Marcellus Shale), TOC values less than 6% does not have any significant impact on sonic velocities and elastic properties (Wang and Carr, 2012). Further, a laboratory-based study on synthetic shales by Altowairqi et al. (2015) demonstrated a minimal impact on ultrasonic velocities and static elastic properties for TOC values in the range of 2% to 4%. The latter studies are consistent with the results of this research, in which it was found that Sembar Shale TOC values range from 2% to 4% (average 3%) but have a limited impact on Vp (see Figure 4.22a). As such, TOC values in the Sembar Shale may be sufficient to warrant consideration for shale gas production. Velocity-based maps will not assist in mapping the lateral distribution of TOC.

A detailed mineralogy analysis using drill cuttings of Sembar Shale provides support for mineralogical interpretations using log data. The intervals of Sembar Shale where clay is higher (40% or more) than brittle minerals may be classified as ductile, based on results published for shales elsewhere (Jarvie et al., 2007; Wang and Gale, 2009). By analogy, it seems reasonable to suggest that intervals with brittle mineral (quartz, dolomite and pyrite) content greater than 40% may exhibit brittle behavior, though this is not clearly supported from literature at present.

Cuttings-based mineralogical data were only available for well-Y in the study area. This is a significant limitation because prior work has suggested that mineralogy can vary significantly in the Sembar Formation throughout the Lower Indus Basin (Nazeer et al., 2016; Ahmad et al., 2012). As such, a broadly applicable mineralogy-based study of brittleness, which is recommended as a future task, will require cuttings and/or core samples from several wells. Due to the unavailability of such samples and data at present, the use of elastic properties to estimate brittleness was pursued in this study.

The BRIT_average (elastic properties-based average brittleness index) implicitly accounts for matrix and cement mineralogy, fabric and mechanical behavior of different types of clays (Ikari et al., 2009). Given that the TOC values are generally low and have limited impact on velocities (hence mechanical properties and brittleness index; see Figure 22a), and BRIT_avg were investigated in this work as a function of the sum of clay and kerogen/TOC (i.e., the soft components of shale, following the approach used by Sone and Zoback (2013)). As shown in Figure 4.22b, Vp and BRIT_avg decrease with the increasing volume fraction of soft-components. Similarly, the plots of Young's modulus (YME) and Poisson's ratio (PR) with soft-components show a decrease in YME and an increase of PR with increase of soft components, as shown in Figures 4.22c and 4.22d.

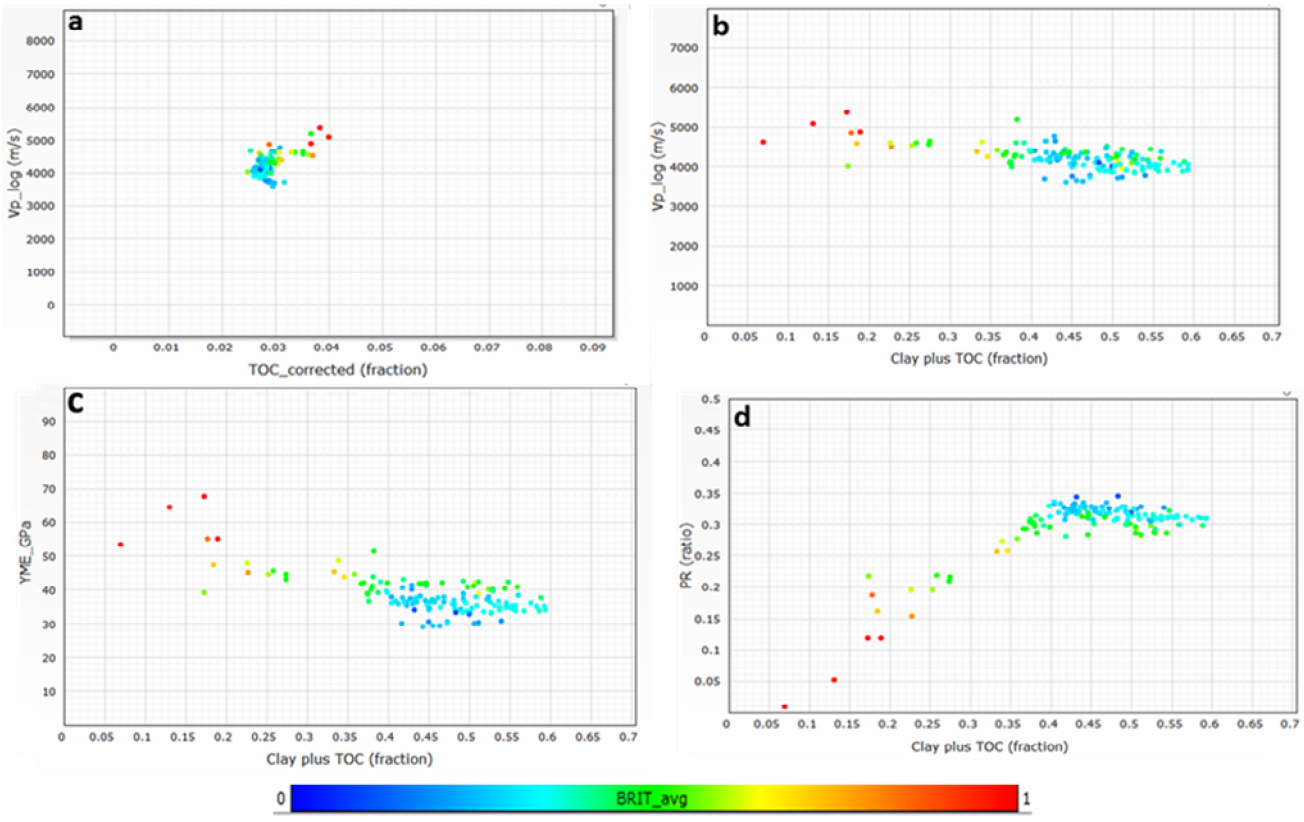

Figure 4.22 Log data and log-derived properties used for brittleness analysis of well-Y. Cross plots of compressional wave velocity (Vp) with **(a)** corrected TOC and **(b)** total volume fraction of clay and TOC color-coded with BRIT_avg. Cross plots of (**c)** YME (Young's modulus), and **(d)** PR (Poisson's ratio) with total volume fraction of clay and TOC color-coded with BRIT_avg.

Figure 4.23 shows a cross plot of YME and Poisson's ratio with thresholds of 50 GPa and 0.25, as recommended by Rickman et al. (2008), to classify rocks based on brittleness. Based on these thresholds, a limited number of data points plot as brittle (i.e., top left corner,

YME > 50 GPa and PR < 0.25). A majority of the data points fall in the ductile regime (YME < 50 GPa and PR > 0.25), with the balance falling in the lower-left transitional quadrant (YME < 50 GPa, PR < 0.25). Using a brittleness threshold based BRIT_avg > 0.5, a more appropriate YME threshold would fall in the 35 to 40 GPa range. This seems more consistent with the YME threshold value of 30 GPa suggested by Zhang et al. (2017), based on research conducted on shales of the Longmaxi Formation in China.

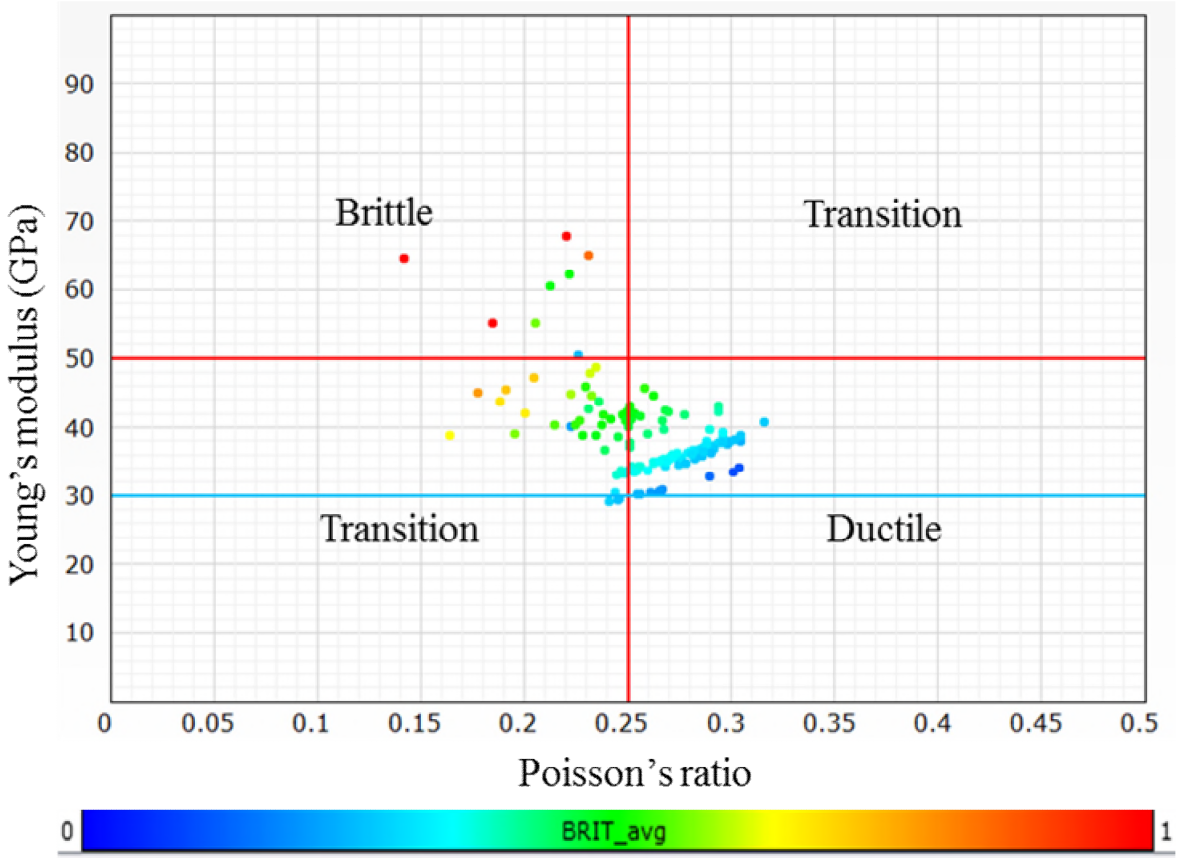

Figure 4.23 Cross plot between YME (Young's modulus) and Poisson's ratio (PR) overlaid with the average brittleness index (BRIT_avg). Red lines are brittleness classification thresholds recommended by Rickman et al. (2008), and the blue line is a modified YME threshold suggested by Zhang et al. (2017).

Though much focus has previously been placed on the impact of Young's modulus on hydraulic fracturing based on brittleness (e.g., Smith and Montgomery, 2015; Rickman et al., 2008), it is also important to note that a lower Young's modulus is actually beneficial for facilitating fracture opening (i.e., larger fracture apertures) after a fracture has developed (e.g., Hiyama et al., 2013; Nasehi and Mortazavi, 2013). As such, the fact that the Sembar Shale has Young's moduli at the low end of the brittleness threshold suggests that it might possess a favorable compromise between fracability and aperture development.

Zones with Young's modulus > 30GPa and Poisson's ratio < 0.25 predominantly exist in the northeastern part of the study area (towards well-M), as shown in Figure 4.19b. Although Poisson's ratio near well-X is about 0.25, the low Young's modulus (<25GPa) suggests that this area is a less brittle zone. Detailed mapping of well-X using 3D seismic data enhances the resolution of elastic properties, as shown in Figure 4.20. The Sembar Formation cube at well-X shows that relatively high Young's modulus (>30GPa) and low Poisson's ratio (<0.25) for Sembar Shale interval exists to the surroundings of well-X, and can be considered favorable for hydraulic fracturing. It is observed that the regional trend may not represent the real trends of brittleness-index due to the low density of seismic lines and well data and the heterogeneity of shale. Therefore, the use of suggested seismic inversion techniques (e.g., MLC+PSO) for the interpretation of individual wells along with 3D seismic data can provide better results.

The macro-fractures, identified in Figure 4.12d for Sembar Shale, are mostly oriented in northeast-southwest, sub-parallel to the maximum horizontal stress direction. As such, given the predominant strike-slip stress regime in the study area with maximum horizontal stress oriented northeast-southwest, drilling horizontal wells in the minimum horizontal stress direction (i.e., northwest-southeast) would be favourable both for the intersection of natural fractures and for the creation of hydraulic fractures that are oriented normal to the well axis (i.e., transverse fractures). These hydraulic fractures would be expected to have a simpler (more planar) geometry in intervals where S_{Hmax} significantly exceeds S_v, but perhaps more complicated in intervals where S_{Hmax} is similar in magnitude to S_v.

The results of this study provide guidance for selecting the placement (depth) of horizontal wells in the Sembar Shale. For example, because the sandier, more brittle intervals of the Sembar Shale have horizontal stresses slightly greater than the more shaley intervals (see Figure 4.15), it might be advantageous to place the horizontal wells within one of the thicker sandy intervals. This would increase the potential for initiating a brittle fracture near the well perforations and should result in fracture pressures that are sufficient to allow these fractures to continue propagating vertically when reaching the interface with shaley intervals (because of the lower stresses in the latter).

For horizontal wells drilled in the study area, the in-situ stress, pore pressures and mechanical properties interpreted in this work could be used to select appropriate drilling

mud densities that mitigate the potential for excessive hole enlargement or drilling-induced tensile fractures. Such analysis, however, is beyond the scope of this paper.

This study relies on available conventional petrophysical logs and post-stack seismic data, and conventional laboratory testing is absent due to the unavailability of standard core samples for the Sembar Shale. Although some data extracted from literature (porosity and static elastic properties) had been measured on core samples from wells near the study area, there is still a need to extract core samples from Sembar Shale in our study area and run laboratory testing for these properties. The study also relies on a limited dataset for in-situ stress measurements (specifically, minimum horizontal stress), hence the calculated horizontal stress profiles should be regarded as approximate estimates. The acquisition of new core-testing data and stress measurements will enable future revision and improvement of the mechanical earth models presented in this paper. Regardless, the author suggests that the current work is sufficient to identify suitable zones in the study area for future shale gas exploration, and rough estimates of the properties of these zones.

4.7 Conclusion

A workflow has been developed and used for a petrophysical and geomechanical characterization of Sembar Shale in Lower Indus Basin of Pakistan using well logs and post-stack seismic data of a single well. This workflow then applied to other wells of the study area. It is useful because these are the only data types available in this early stage of shale gas exploration in the Lower Indus Basin. The petrophysical properties (e.g., mineralogy, TOC, porosity and fluid saturation) were extracted from well logs, which compared favourably with values from literature (for porosity and fluid saturation) and laboratory testing of drill cuttings (for mineralogy and TOC). The pore pressure and minimum horizontal stresses were calibrated to available measurements at well-Y and literature data at other wells, hence increasing their credibility.

The following results obtained at the well-scale suggest that the Sembar Shale is favorable for development: high gas saturation, good porosity (up to 10%), moderate quantity of thermally mature organic matter (2% - 4% TOC), a number of brittle intervals separated by thicker intervals that fall slightly below the brittle-ductile threshold, and a strike-slip stress regime (with a maximum horizontal stress orientation sub-parallel to the orientations of macro-fractures observed in the seismic-based analysis). The brittleness

assessment for the well-scale analysis was based on independently-calculated mineralogy and elastic property-based indices, both of which provided consistent results. At the scale of the study area, robust statistical techniques were used to invert seismic stacks and develop a 3D mechanical earth model. This model shows a trend of increasing shale brittleness towards the northeastern portion of the study area, hence suggesting that this area might be most prospective for initial shale gas development. The brittleness index used for the 3D mechanical earth model was based solely on elastic properties, given the lack of available data to characterize variations in mineralogy throughout the study area.

A sensitivity analysis of the results (as given in Appendix 4-E) provides the error window for estimated mechanical properties. Further, a sensitivity analysis measures the propagation of error in sonic velocities to mechanical properties, which can be used as criteria for the application of the proposed workflow globally. Errors of roughly 10% in the velocities interpreted in this work would results in error up to 20% for elastic properties and horizontal stress magnitudes.

4.7.1 Recommendation

The models presented in this study are developed based on interpretation of available seismic and well data, and integrated with measured elastic properties and mini-frac test data for a single well. These models should be updated when additional datasets (e.g., image logs, dipole shear sonic, micro-seismic data, core sampling and testing) are available, ideally from several wells located throughout the study area, and calibrated more thoroughly once additional pore pressure and stress magnitude measurements have been obtained. Further, the various brittleness indices estimated based on mineralogy and elastic properties should be compared and evaluated more critically, once direct measurements of brittleness have been conducted on core samples which have been preserved at their native moisture content.

Acknowledgment

The authors would like to thank the Directorate General of Petroleum Concessions (DGPC), Pakistan, for providing the seismic and well log data for research and publication purposes and University of Saskatchewan, Canada for providing the computing facility to complete this work. Schlumberger Canada's office is also deeply acknowledged for their support with

software applications. University of Engineering and Technology, Lahore and Higher Education Commission of Pakistan are acknowledged for FDP scholarship.

References

Ahmad, N., Javed, M., Kashif, S., Mehmood, N., & Arif, F. (2012). *Shale gas potential of Lower Cretaceous Sembar Formation in Middle and Lower Indus sub-basins, Pakistan.* Search and Discovery, Retrieved May 7, 2018, from http://www.searchanddiscovery.com/abstracts/pdf/2012/90138papg/abstracts/ndx_ahmad04.pdf

Ahmed N, Fink P, Sturrock S, Mahmood T, Ibrahim M. (2004). *Sequence stratigraphy as predictive tool in Lower Goru Fairway, Lower and Middle Indus Platform, Pakistan*. PAPG Annual Technical Conference, Pakistan. Retrieved June 7, 2019, from https://www.researchgate.net/profile/Nadeem_Ahmad35/publication/327791105

Ahmad, R., & Ahmad, J. (1991). Petroleum Geology and Prospects of Sukkur Rift Zone, Pakistan with Special Reference to Jaisalmer Cambay and Bombay High Basins of India. *Pakistan Journal of Hydrocarbon Research,3(2),* 33-41.

Akono, A., & Kabir, P. (2016). Nano-Scale Characterization of Organic-Rich Shale via Indentation Methods. *New Frontiers in Oil and Gas Exploration,* 209-233. doi:10.1007/978-3-319-40124-9_6

Al-Kharraa, H., Al-Ameer, A., Al-Qahtani, F., Al-Sultan, A., Al-Abbad, M., & Al-Obaid, O. (2015, April). *Integration of Petrophysical and Geomechanical Properties for Enhanced Fracture Design.* SPE Saudi Arabia Section Annual Technical Symposium and Exhibition. doi:10.2118/178032-MS.

Altowairqi, Y., Rezaee, R., Evans, B., & Urosevic, M. (2015). Shale Elastic Property Relationships as a Function of Total Organic Carbon Content using Synthetic Samples. *Journal of Petroleum Science and Engineering, 133,* 392-400. doi:10.1016/j.petrol.2015.06.028.

Anderson, Barbara, Barber, Thomas, Martin, Taherian, Jim. (2008, January). *Identifying Potential Gas-Producing Shales From Large Dielectric Permittivities Measured By Induction Quadrature Signals.* Society of Petrophysicist and Well logging Analysts. Retrieved January 7, 2018, from https://www.onepetro.org/conference-paper/SPWLA-2008-HHHH .

Ashraf, U., Zhu, P., Yasin, Q., Anees, A., Imraz, M., Mangi, H. N., & Shakeel, S. (2019). Classification of reservoir facies using well log and 3D seismic attributes for prospect evaluation and field development: A case study of Sawan gas field, Pakistan. *Journal of Petroleum Science and Engineering, 175,* 338–351. doi: 10.1016/j.petrol.2018.12.060.

Backus, G. E. (1962). Long-wave elastic anisotropy produced by horizontal layering. *Journal of Geophysical Research, 67(11),* 4427–4440. doi: 10.1029/jz067i011p04427.

Bai, M. (2016). Why are brittleness and fracability not equivalent in designing hydraulic fracturing in tight shale gas reservoirs. *Petroleum, 2(1),* 1-19. doi: 10.1016/j.petlm.2016.01.001

Bessereau, G., Carpentier, B., & Huc, A. (1991, May). *Wireline Logging And Source Rocks - Estimation Of Organic Carbon Content By The Carbolbg Method*. Society of Petrophysicist and Well logging Analysts Retrieved June 05, 2016, from https://www.onepetro.org/journal-paper/SPWLA-1991-v32n3a9.

Bowers, G. L. (1995). Pore Pressure Estimation From Velocity Data: Accounting for Overpressure Mechanisms Besides Undercompaction. *SPE Drilling & Completion,10*(02), 89-95. doi:10.2118/27488-pa

Bowers, G. L. (2001 May). *Determining an Appropriate Pore-Pressure Estimation Strategy.* Offshore Technology Conference. doi:10.4043/13042-MS.

Brouwer, F., & Huck, A. (2011). An Integrated Workflow to Optimize Discontinuity Attributes for the Imaging of Faults, Retrieved March 7, 2019, from http://static.dgbes.com/images/PDF/browhuck.pdf

Clavier, C., Heim, A., & Scala, C. (1976, January). *Effect Of Pyrite On Resistivity And Other Logging Measurements*. Society of Petrophysicists and Well-Log Analysts.

Chopra, S., & Huffman, A. R. (2006). Velocity determination for pore-pressure prediction. *The Leading Edge,25(12),* 1502-1515. doi:10.1190/1.2405336.

Cox, T., and Seitz, K., (2007, May). *Ant Tracking Seismic Volumes for Automated Fault Interpretation.* CSPG/CSPE GeoConvention, Calgary, Alberta, Canada.

Crain, E. R. (2016). *Petrophysical Handbook.* Retrieved from https://spec2000.net/

Crain, E. R, and Holgate, D., (2014 April). *A 12-step program to reduce uncertainty in kerogen-rich reservoirs*: FOCUS, GeoConvention, 1-11.

Cui, A., Wust, R., & Nassichuk, B. (2017). *A Comparison study of existing and new mineralogical, (geo)mechanical, and petrophysical brittleness indices of Alberta Montney and their applicability for optimizing well stimulations*. GeoConvention, Calgary, Canada.

Daber, R., Aqrawi, A., (2011). *Petrel 2010 : interpreter's guide to seismic attributes*. Schlumberger, Housten, USA.

Danadan, F., & Qiaodeng, H. (2002). An improved genetic algorithm and its application in parameter inversion in anisotropic media. *Geophysical Prospecting for Petroleum*, *41*, 293–298. http://gpp.geophysics.cn/EN/

Das, B., & Chatterjee, R. (2018). Mapping of pore pressure, in-situ stress and brittleness in unconventional shale reservoir of Krishna-Godavari basin. *Journal of Natural Gas Science and Engineering*, *50*, 74–89. doi: 10.1016/j.jngse.2017.10.021

Dembicki, H., & Madren, J. D. (2014). Lessons learned from the Floyd shale play. *Journal of Unconventional Oil and Gas Resources,7*, 1-10. doi:10.1016/j.juogr.2014.03.001.

Dix, C. H. (1955). Seismic Velocities From Surface Measurements. *Geophysics, 20(1),* 68–86. doi: 10.1190/1.1438126.

Du, Q., Yasin, Q., Ismail, A., & Sohail, G. M. (2019). Combining classification and regression for improving shear wave velocity estimation from well logs data. *Journal of Petroleum Science and Engineering, 182*, 106260. doi: 10.1016/j.petrol.2019.106260.

Dutta, N. C. (2002). Geopressure prediction using seismic data: Current status and the road ahead. *Geophysics,67*(6), 2012-2041. doi:10.1190/1.1527101.

Eaton, B. A. (1972). Graphical method predicts geopressures worldwide. *World Oil 7 (76)*: 100-104.

Entyre, L. M. (1993, January). *Comparative Performance Of A Dual Water Model Equation In Laminar Shaly Sands.* Society of Petrophysicists and Well-Log Analysts.

Eshkalak, M. O., Mohaghegh, S. D., & Esmaili, S. (2014). Geomechanical Properties of Unconventional Shale Reservoirs. *Journal of Petroleum Engineering,* 1-10. doi:10.1155/2014/961641

Farooq, L., Iqbal, M. U., & Zolalemin, S. A. (2009). *Successful Testing of Extreme HP-HT Well in Pakistan*:. International Petroleum Technology Conference. doi:10.2523/13899-MS.

Farooqui, M. (2014). *Geochemical Characteristics and Depositional Environment of Lower Cretaceous Sembar Formation, Western Sulaiman Foldbelt, Pakistan.* Retrieved from https://gsa.confex.com/gsa/2014AM/finalprogram/abstract_245155.htm

Fehmers, G.C., and Hocker C.F. (2003). Fast structural interpretation with structure-oriented filtering. *Geophysics, 68,* 4; 1286-1293.

Franquet, J. A., Bratovich, M. W., & Glass, R. D. (2012, January). *State-of-the-Art Openhole Shale Gas Logging.* Society of Petroleum Engineers. doi:10.2118/160862-MS.

Gardner, G. H. F., Gardner, L. W., & Gregory, A. R. (1974). Formation Velocity And Density—The Diagnostic Basics For Stratigraphic Traps. *Geophysics*, *39*(6), 770–780. doi: 10.1190/1.1440465.

Gogoi, T., Chatterjee, R., 2019. Estimation of petrophysical parameters using seismic inversion and neural network modeling in Upper Assam basin, India. *Geoscience Frontiers*. https://doi.org/10.1016/j.gsf.2018.07.002

Green , S., Hillier, C., Dunphy, R., & Thurston, D. (2017). *Using traditional methods to predict pore pressure in Devonian Black Shale Basins of North East British Columbia*. GeoConvention, Calgary, Canada.

Grieser, W. V., & Bray, J. M. (2007, April). *Identification of Production Potential in Unconventional Reservoirs*. Production and Operations Symposium. doi:10.2118/106623-MS.

Heidbach, Oliver; Rajabi, Mojtaba; Reiter, Karsten; Ziegler, Moritz; (2016): *World Stress Map Database* Release 2016. GFZ. Data Services. doi.org/10.5880/WSM.2016.001

Hiyama,M.,Shimizu,H.,Ito,T.,Tamagawa,T.,Tezuka,K. (2013, June). *Distinct Element Analysis for hydraulic fracturing in shale - effect of brittleness on the fracture propagation.* 47th US RockMechanics/Geomechanics Symposium, American Rock Mechanics Association.

Holt, R. M., Nes, O., & Fjaer, E. (2005). In-situ stress dependence of wave velocities in reservoir and overburden rocks. *The Leading Edge,24(12),* 1268-1274. doi:10.1190/1.2149650.

Holt, R., Fjaer, E., Nes, O.M., Alassi, H.T., (2011, June). *A Shaly Look at Brittleness,* 45th US Rock Mechanics/Geomechanics Symposium,. American Rock Mechanics Association.

Horsrud, P. (2001). Estimating Mechanical Properties of Shale From Empirical Correlations. *SPE Drilling & Completion, 16(02),* 68-73. doi:10.2118/56017-pa.

Ikari, M. J., Saffer, D. M., & Marone, C. (2009). Frictional and hydrologic properties of clay-rich fault gouge. *Journal of Geophysical Research,114(B5).* doi:10.1029/2008jb006089.

Iqbal, O., Ahmad, M., & Kadir, A. A. (2018). Effective evaluation of shale gas reservoirs by means of an integrated approach to petrophysics and geomechanics for the optimization of hydraulic fracturing: A case study of the Permian Roseneath and Murteree Shale Gas reservoirs, Cooper Basin, Australia. *Journal of Natural Gas Science and Engineering,58,* 34-58. doi:10.1016/j.jngse.2018.07.017

Ito, T., Evans, K., Kawai, K., & Hayashi, K. (1999). Hydraulic fracture reopening pressure and the estimation of maximum horizontal stress. *International Journal of Rock Mechanics and Mining Sciences,36*(6), 811-826. doi:10.1016/s0148-9062(99)00053-4.

Jaeger, J. C., & Cook, N. W. G. (1979). Fundamentals of Rock Mechanics New York: Chapman & Hall.

Jarvie, D. M., Hill, R. J., Ruble, T. E., & Pollastro, R. M. (2007). Unconventional shale-gas systems: The Mississippian Barnett Shale of north-central Texas as one model for thermogenic shale-gas assessment. *AAPG Bulletin,91(4),* 475-499. doi:10.1306/12190606068.

Jiang, S., Mokhtari, M., Borrok, D., & Lee, J. (2018). Improving the Total Organic Carbon Estimation of the Eagle Ford Shale with Density Logs by Considering the Effect of Pyrite. *Minerals,8(4),* 154. doi:10.3390/min8040154.

Jin, X., Shah, S. N., Roegiers, J.-C., & Zhang, B. (2014). *Fracability Evaluation in Shale Reservoirs - An Integrated Petrophysics and Geomechanics* Approach. SPE Hydraulic Fracturing Technology Conference. doi: 10.2118/168589-ms.

Kadkhodaie, A., & Rezaee, R. (2016). A new correlation for water saturation calculation in gas shale reservoirs based on compensation of kerogen-clay conductivity. *Journal of Petroleum Science and Engineering,146,* 932-939. doi:10.1016/j.petrol.2016.08.004.

Kadri, I. B. (1995). *Petroleum Geology of Pakistan* Karachi, Pakistan: Pakistan Petroleum Ltd.

Kazmi, A. H., & Abbasi, I. A. (2008). *Stratigraphy & historical geology of Pakistan.* Peshawar: Dept. & National Centre of Excellence in Geology.

Kennedy, R., Luo X. L., and Kussakra, V. (2016). The Unconventional Basins and Plays-North America, the Rest of the World and Emerging Basins, In: Ahmed U. and Nathan M, D.,(eds.), *Unconventional Oil and Gas Resources: Exploitation and Development,* Baker Hughes, Canada.

Khair, H. A., Cooke, D., Becke, G., King, R., Hand, M., Tingay, M., & Holford, S. (2012, May). *Subsurface Mapping of natural fracture networks; a major challenge to be solved. case study from the shale intervals in the Cooper Basin, South Australia.* 37th Workshop on Gethermeal Reservoir Engineering, Stanford University. Retrieved from https://pangea.stanford.edu/ERE/pdf/IGAstandard/SGW/2012/Khair.pdf

Khan, J. Q. (2016). *Unconventional shale gas reservoir characterization and modelling of the Permian Roseneath and Murteree shales in the Cooper Basin, Australia,* PhD Thesis. James Cook University, Australia, Retrieved from https://researchonline.jcu.edu.au/46477/.

Lashkaripour, G. R., & Dusseault, M. D. (1993, October). *A statistical study of shale properties: Relationships among principal shale properties.* Conference on Probabilistic Methods in Geotechnical Engineering, Balkema.

Lewis, R., Ingraham, D., Pearcy, M., Williamson, J., Sawyer, W., & Frantz, J. (2004, September). *New Evaluation Techniques for Gas Shale Reservoirs.* In Reservoir Symposium Schlumberger. Retrieved November 2018, from http://large.stanford.edu/courses/2010/ph240/alnoaimi2/docs/Pickens%20Shale%20Gas.pdf.

Lisa, M., & Jan, Q. (2015, January). *Awaran, Pakistan, Earthquake of Mw 7.7 in Makran,* Proceedings of Pakistan Academy of Sciences, Retrieved February, 2018, from http://paspk.org/wp-content/uploads/proceedings/52, No.2/86052059Awaran.pdf

Liu, Y., (2017, April) *Applications of Machine Learning for Seismic Quatitative Interpretation,* GeoConvention Canada.

Luan, X., B. Di, J. Wei, X. Li, K. Qian, J. Xie, P. Ding. (2014, October). *Laboratory Measurements of brittleness anisotropy in synthetic shale with different cementation.*

Proceedings of the 2014 Annual Meeting. Denver, Society of Exploration Geophysicists. 3005–3009.

Mavko, G, Mukerji, T, and Dvorkin, J., (2003). *The Rock Physics Handbook*: Tools for Seismic Analysis of Porous Media. Cambridge University Press, New York.

Miller M. (2010) Gas Shale Evaluation Techniques Things to Think About. A Report, Retrieved from http://www.ogs.ou.edu/MEETINGS/Presentations/Shales2010/Miller.pdf

Nasehi, M. J., & Mortazavi, A. (2013). Effects of in-situ stress regime and intact rock strength parameters on the hydraulic fracturing. *Journal of Petroleum Science and Engineering*, *108*, 211–221. doi: 10.1016/j.petrol.2013.04.001

Nazeer, A., Abbasi, S. A., & Solangi, S. H. (2016). Sedimentary facies interpretation of Gamma Ray (GR) log as basic well logs in Central and Lower Indus Basin of Pakistan. *Geodesy and Geodynamics*,*7*(6), 432-443. doi:10.1016/j.geog.2016.06.006.

Nur, A., & Byerlee, J. D. (1971). An exact effective stress law for elastic deformation of rock with fluids. *Journal of Geophysical Research*, 76(26), 6414–6419. http://doi: 10.1029/jb076i026p06414

Parsopoulos, K., & Vrahatis, M. (2004). On the Computation of All Global Minimizers Through Particle Swarm Optimization. *IEEE Transactions on Evolutionary Computation*,*8*(3), 211-224. doi:10.1109/tevc.2004.826076.

Passey, Q. R., Bohacs, K., Esch, W. L., Klimentidis, R., & Sinha, S. (2010, January). *From Oil-Prone Source Rock to Gas-Producing Shale Reservoir - Geologic and Petrophysical Characterization of Unconventional Shale Gas Reservoirs*. Society of Petroleum Engineers. doi:10.2118/131350-MS.

Pedersen, S.I., Randen, T., Sonneland, L. & Steen, O. (2002, September). *Automatic fault extraction usingartificial ants.* 72nd Annual International Meeting of the Society of Exploration Geophysicists.

Perez, R. (2014, June). Seismic Brittleness Index Volume Estimation from Well Logs. AAPG Annual Convention and Exhibition, Houston, Texas. Retrieved March 17, 2017, from http://www.searchanddiscovery.com/pdfz/documents/2014/80381perez/ndx_perez.pdf.htm

Plumb, R., Edwards, S., Pidcock, G., Lee, D., & Stacey, B. (2000, January). *The Mechanical Earth Model Concept and Its Application to High-Risk Well Construction Projects*. Society of Petroleum Engineers. doi:10.2118/59128-MS.

Randen, T., Perdensen, S., Sonneland, L., (2001, September). *Automatic Extraction of Fault Surfaces fromThree-Dimensional Seismic Data.* Annual Meeting., Society of Exploration Geophysicist.

Rezaee, R. (2015). *Fundamentals of Gas Shale Reservoirs*. Hoboken: John Wiley & Sons.

Raza, H. A., S. M. Ali, and R. Ahmed, (1990), Petroleum geology of Kirthar sub-basin and part of Kutch basin. *Pakistan Journal of Hydrocarbon Research, 2 (1)*, 29–74.

Rickman, R., Mullen, M. J., Petre, J. E., Grieser, W. V., & Kundert, D. (2008, January). *A Practical Use of Shale Petrophysics for Stimulation Design Optimization: All Shale Plays Are Not Clones of the Barnett Shale*. Society of Petroleum Engineers. doi:10.2118/115258-MS.

Rickman, R., Mullen, M. J., Petre, J. E., Grieser, W. V., & Kundert, D. (2008, January). *A Practical Use of Shale Petrophysics for Stimulation Design Optimization: All Shale Plays Are Not Clones of the Barnett Shale.* Society of Petroleum Engineers. doi:10.2118/115258-MS.

Robinson, G. (2001, January). Stochastic Seismic Inversion Applied to Reservoir Characterization. Retrieved from https://csegrecorder.com/articles/view/stochastic-seismic-inversion-applied-to-reservoir-characterization

Russell, B., 2004. The application of multivariate statistics and neural networks to the prediction of reservoir parameters using seismic attributes, *Ph.D. Thesis*. University of Calgary.

Rutqvist, J., Tsang, C., & Stephansson, O. (2000). Uncertainty in the maximum principal stress estimated from hydraulic fracturing measurements due to the presence of the induced fracture. *International Journal of Rock Mechanics and Mining Sciences,37*(1-2), 107-120. doi:10.1016/s1365-1609(99)00097-0.

Schmoker, J.W. and Hester, T.C., 1983, Organic Carbon in Bakken Formation, United States Portion of Williston Basin, *AAPG Bulletin, 67*,12, 2165-2174.

Siddiqui, A. A., Khan, M. W., Khan, M. N., Kamaletdinov, B., & Palekar, A. H. (2014). *Integration of Geomechanics Along with Application of New Fracturing Technique Results in Production Increment Above Expectations*. PAPG/SPE Pakistan Section Annual Technical Conference. doi:10.2118/174713-MS.

Smith, M., Montgomery, C. (2015). Hydraulic Fracturing. Boca Raton: CRC Press, https://doi.org/10.1201/b16287

Sohail, G. M., & Hawkes, C. D. (2020). An evaluation of empirical and rock physics models to estimate shear wave velocity in a potential shale gas reservoir using wireline logs. *Journal of Petroleum Science and Engineering, 186* 106666. doi: 10.1016/j.petrol.2020.106666.

Soleymani, H., & Riahi, M. (2012). Velocity based pore pressure prediction—A case study at one of the Iranian southwest oil fields. *Journal of Petroleum Science and Engineering,94-95*, 40-46. doi:10.1016/j.petrol.2012.06.024

Soliman, M., Daal, J., & East, L. (2012). Fracturing unconventional formations to enhance productivity. *Journal of Natural Gas Science and Engineering,8*, 52-67. doi:10.1016/j.jngse.2012.01.007.

Sondergeld, C., Newsham, K., Comisky, J., Rice, M., & Rai, C. (2010, October). *Petrophysical Considerations in Evaluating and Producing Shale Gas Resources.* Proceedings of SPE Unconventional Gas Conference. doi: 10.2523/131768-ms

Sone, H., & Zoback, M. D. (2013). Mechanical properties of shale-gas reservoir rocks — Part 2: Ductile creep, brittle strength, and their relation to the elastic modulus. *Geophysics, 78(5)*. doi:10.1190/geo2013-0051.1

Soroush, H., Ginty, W., Pan, C., Ferguson, W., Bere, A., Farid, U., Hussain, Z., (2018, August). *Geomechanics-Based Hydraulic Fracturing Modelling for Tight Gas Carbonates: Case Study of Naushahro Feroz Field in Pakistan.* American Rock Mechanics Association.

Thiercelin, M. J., & Plumb, R. A. (1994). Core based predictions of lithologic stress contrasts in east Texas formations. *Journal of SPE Formation Evaluation, 9(14),* 251–258.

Usmani, M. M., & Kamal, S. (2017, November). *A Holistic Approach to Drill First Deep Horizontal Well with Multistage Fracking in Tight Carbonate Reservoir - A Case Study of Lower Indus Basin in Pakistan.* Society of Petroleum Engineers. doi:10.2118/188593-MS

Veeken, P. C., Priezzhev, I. I., Shmaryan, L. E., Shteyn, Y. I., Barkov, A. Y., & Ampilov, Y. P. (2009). Nonlinear multitrace genetic inversion applied on seismic data across the Shtokman field, offshore northern Russia. *Geophysics*, *74*(6). doi: 10.1190/1.3223314

Verma, R., Mukhopadhyay, M., & Bhanja, A. (1980). Seismotectonics of the Hindukush and Baluchistan arc. *Tectonophysics,66*(4), 301-322. doi:10.1016/0040-1951 (80) 90247-4.

Vernik, L. (2016). *Seismic Petrophysics in Quantitative Interpretation.* S.l.: Society of Exploration Geophysicists.

Vernik, L., & Landis, C. (1996). Elastic Anisotropy of Source Rocks: Implications for Hydrocarbon Generation and Primary Migration. *AAPG Bulletin,80*. doi:10.1306/64ed8836-1724-11d7-8645000102c1865d.

Wang, F. P., & Gale, J. F. (2009). Screening Criteria for Shale-Gas Systems. GCAGS 59th Annual Meeting, Shreveport, Louisiana. Retrieved 2016, from http://www.searchanddiscovery.com/abstracts/html/2009/gcags/abstracts/wang.htm

Wang, G., & Carr, T. R. (2012). Marcellus Shale Lithofacies Prediction by Multiclass Neural Network Classification in the Appalachian Basin. *Mathematical Geosciences, 44(8),* 975–1004. doi: 10.1007/s11004-012-9421-6.

Wang, F. P., & Reed, R. M. (2009). *Pore Networks and Fluid Flow in Gas Shales*. SPE Annual Technical Conference and Exhibition. doi:10.2118/124253-MS.

Wasantha, P. L. P., & Ranjith, P. G. (2014). Water-weakening Behavior of Hawkesbury Sandstone in Brittle Regime. *Engineering Geology*, *178,* 91-101. doi:10.1016/j.enggeo.2014.05.015.

Waters, G., Lewis, R., & Bently, D. (2011). The effect of mechanical properties anisotropy in the generation of hydraulic fractures in organic shales. In Proceedings of SPE ATCE. Denver, 30 Oct–2 Nov, SPE 146776.

Xu, S, and White, R. E. (1995). A New Velocity Model for Clays and Mixtures: *Geophysical Prospecting, 43*, 91-118.

Yang, Y., Sone, H., Hows, A., Zoback, M.D. (2013, June). Comparison of Brittleness Indices in Organic-rich Shale Formations. 47th US Rock Mechanics/Geomechanics Symposium, American Rock Mechanics Association.

Yasin, Q., Sohail, G. M., Ding, Y., Ismail, A., & Du, Q. (2020). Estimation of Petrophysical Parameters from Seismic Inversion by Combining Particle Swarm Optimization and Multilayer Linear Calculator. *Natural Resources Research*. http://doi: 10.1007/s11053-020-09641-3

Yuan, J., Zhou, J., Liu, S., Feng, Y., Deng, J., Xie, Q., & Lu, Z. (2017). An Improved Fracability-Evaluation Method for Shale Reservoirs Based on New Fracture Toughness-Prediction Models. *SPE Journal*. doi: 10.2118/185963-pa

Zhang, C., Dong, D., Wang, Y., & Guan, Q. (2017). Brittleness evaluation of the Upper Ordovician Wufeng–Lower Silurian Longmaxi shale in Southern Sichuan Basin, China. *Energy Exploration & Exploitation*,*35*(4), 430-443. doi:10.1177/0144598716687929.

Zoback, M., & Kohli, A. (2019). *Unconventional Reservoir Geomechanics: Shale Gas, Tight Oil, and Induced Seismicity*. Cambridge: Cambridge University Press. doi:10.1017/9781316091869

Zoback, M. D. (2014). *Reservoir Geomechanics*. New York, Cambridge University Press

Appendix 4-A: Theory of Multi-layer Linear Calculator (MLC) and Particle Swarm Optimization (PSO) (Yasin et al., 2020)

Figure 4-A shows the detail of workflow for MLC+PSO inversion. A function in one dimension can be divided into several linear segments, whereas a two-dimensional function can be divided into a number of facets with MLC. Based on the approximation of linear segmentation, the nonlinear inversion problem is converted to estimate the weights of several linear calculators. Suppose that A^* is a set of elastic properties (e.g., acoustic impedance) calculated at relevant well location, and B is the collection of seismic records (seismic waveform). The two parameters are connected by the projection operator Ω as given below.

$$A^* = \Omega(B)$$

The relationship between two variables is injective and nonlinear. An optimum response function could be found,

$$\phi(B) = \sum_{i=1}^{m} (A_i(B) - A_i^*(B))^2$$

Where $\phi(B)$ is the objective function, m is the number of target; $A_i(B)$ is the value of the learning data, B, with a multi-layer linear calculator; $A_i^*(B)$ is the real corresponding value of the learning data.

In multi-layer linear calculator, the input sample (B) is weighted-stacked and added to bias b, as given below

$$A = f\left(\sum_{i=0}^{n} B_i w_i + b\right)$$

f is an activation function that represents the designed domain gates, and can be calculated with following formula:

$$f = \frac{1}{1 + \sum_{i=1}^{l} exp\left(-\sum_{i=0}^{n} B_i w_i + b\right)}$$

Where, l is the number of linear calculators.

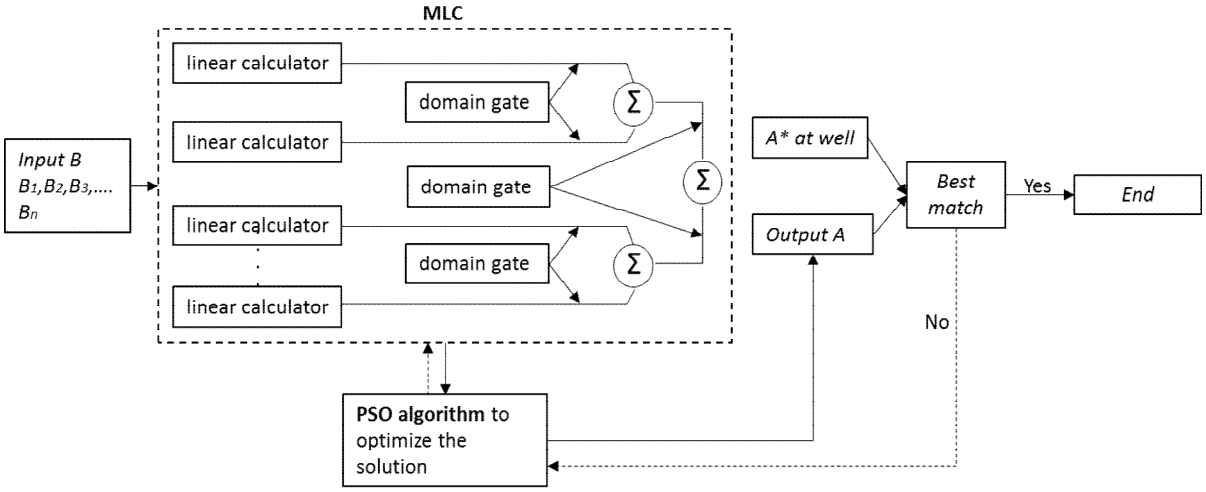

Figure 4-A MLC + PSO inversion workflow (after Yasin et al., 2020).

The weight of each multi-layer linear calculator inversion model, which includes the bias, is determined by the particle swarm optimization (PSO) algorithm (Parsopoulos and Vrahatis, 2004). PSO algorithm can search and updates each particle for convergence, in other words, to find the global optimum of the problem. The parameters for every particle at each moment are denoted as follow:

The particle location is represented by $\boldsymbol{X}_i^t = \left(\boldsymbol{X}_{i1}^t, \boldsymbol{X}_{i2}^t, \cdots, \boldsymbol{X}_{id}^t\right)^T, \boldsymbol{X}_{id}^t \in \left[\boldsymbol{L}_d, \boldsymbol{U}_d\right]$, where $\boldsymbol{U}_d$ and $\boldsymbol{L}_d$ are the upper and lower limits of search space, respectively. The velocity is $\boldsymbol{V}_i^t = \left(\boldsymbol{V}_{i1}^t, \boldsymbol{V}_{i2}^t, \cdots, \boldsymbol{V}_{id}^t\right)^T$ and $\boldsymbol{V}_{id}^t \in \left[\boldsymbol{V}_{\min,d}, \boldsymbol{V}_{\max,d}\right]$, where $\boldsymbol{V}_{max,d}$ and $\boldsymbol{V}_{min,d}$ denote the maximum velocity and minimum velocities, respectively. The ranges of parameters *i* and *d* are $1 \leq d \leq D$ and $1 \leq i \leq$ M, respectively, where D and M are for multiple dimensions and number of particles, respectively. The individual optimal position is labelled as $\boldsymbol{p}_i^t = \left(\boldsymbol{p}_{i1}^t, \boldsymbol{p}_{i2}^t, \cdots, \boldsymbol{p}_{iD}^t\right)^T$ and the global optimal positions $\boldsymbol{p}_g^t = \left(\boldsymbol{p}_{g1}^t, \boldsymbol{p}_{g2}^t, \cdots, \boldsymbol{p}_{gD}^t\right)^T$ are the respective positions of the particle swarm after the update of each iteration. The parameters at time t + 1 can be computed by following equations.

$$\boldsymbol{V}_{id}^{t+1} = \omega \boldsymbol{V}_{id}^t + c_1 r_1^t \cdot \left(\boldsymbol{p}_{id}^t - \boldsymbol{x}_{id}^t\right) + c_2 r_2^t \cdot \left(\boldsymbol{p}_{gd}^t - \boldsymbol{x}_{gd}^t\right)$$

$$\boldsymbol{X}_{id}^{t+1} = \boldsymbol{X}_{id}^t + \boldsymbol{V}_{id}^{t+1}$$

In the above formulas c_1 and c_2 are called learning factors. ω is the inertia weight which can balance the effects between global search and local search.

The parameter settings of the 3D seismic cube (nearby well-X) were taken as follows: the number of the linear calculator l=5, particle number=100, learning factors c1=c2=2, the inertia weight ω=1, lower limit L_d=-3, and upper limit U_d=3. The maximum velocityis V_{max}=0.08, the number of iterations is T_{max}=200, and the precision e=0.1. With a calculation precision of 92% and computation time of 5 minutes, these parameters are proved to be efficient for convergence.

Appendix 4-B: Genetic Inversion (GI)

In the genetic inversion (GI) technique, multilayer neural networks and genetic algorithms are combined in order to provide a robust and straightforward approach to seismic inversion. GI requires a single seismic cube (seismic amplitude or acoustic impedance) and a set of wells/single well with required petrophysical properties (e.g., velocities, acoustic impedance, elastic moduli, Poisson's ratio).

Initially, 50 weight combinations are chosen randomly, all of which are used in the first iteration of a neural network (as shown under "Population" in Figure 4-B). The output and input parameters (e.g., well log measurements) are compared to calculate an error function. As soon as the error is computed for each of the 50 input weight combinations, the process enters into the genetic part of the algorithm. During the learning/training phase of the neural network the genetic algorithm updates the weights for the neural network (instead of back-propagating the error, as usually done in back-propagation (BP) inversion) using the evolutionary approach (i.e., selection, cross-over and mutation). The GI workflow (as shown in Figure 4-B) generates a nonlinear multitrace operator through training of a seismic volume against well data. The multitrace operator is used to invert seismic data into desired well log response (e.g., acoustic log), producing the best fit to the well data (Veeken et al., 2009).

The genetic part of GI consists of three steps: 1) Selection — weight combinations with the smallest error are selected, 2) Cross-over — weight combinations exchange single weights from one combination to another (the number of exchanged weights can be singular or multiple), 3) Mutation — single weights are exchanged randomly from one weight combination to another, which ensures that the process does not converge to a local minimum. The mutation event occurs with a higher probability as soon as the error function starts to stabilize (i.e., reach a minimum) (Daber and Aqrawi, 2011).

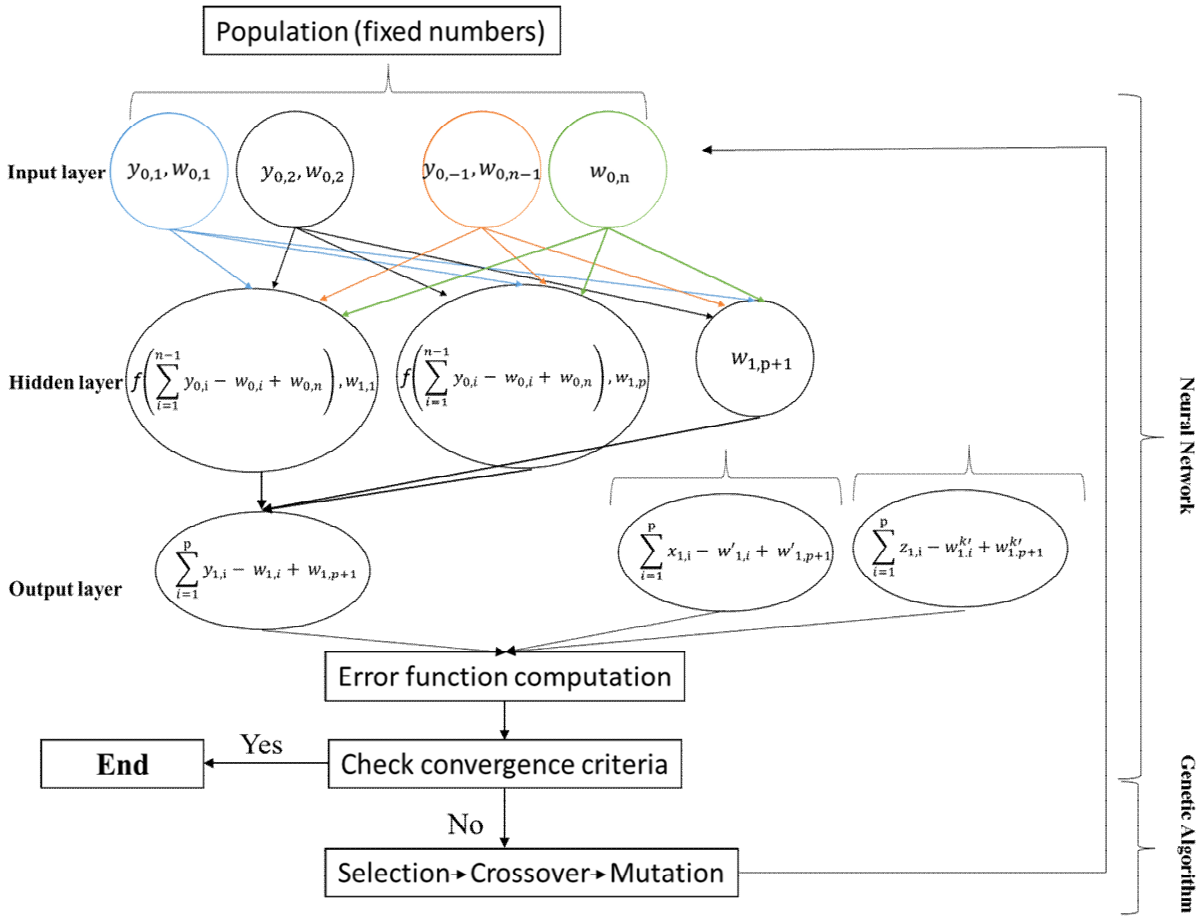

Where:

$Activation\ function\ (sigmoid\ function) = f(x) = 1/(1+e^{-x})$

Input/hidden layer relationship:

$$y_{hidden\_layer} = f\left[\sum_{i=1}^{n=1} y_{input,i}.w_{input,i} + w_{input,n}\right]$$

The bias of the input layer, and the one of the hidden layer are respectively represented by $W_{0,n}$ and $W_{0,p+1}$

Figure 4-B Genetic inversion workflow (after Daber and Aqrawi, 2011)

Appendix 4-C

4-C.1 Schmoker Technique (Schmoker and Hester, 1983):

The Schmoker equation looks at the dependency of bulk density on TOC (Schmoker and Hester, 1983). TOC by Modified Schmoker is calculated as follows:

$$Schmoker_A = \frac{1}{1 - \frac{1}{\rho_g}}$$

$$Schmoker_B = Schmoker_A - 1$$

$$TOC_{schmoker} = \frac{Schmoker_A}{\rho_b} - Schmoker_B$$

Where ρ_g is grain density (calculated in this work as a weighted average using log-based mineralogy and literature values of density for the mineral phases present); ρ_b is bulk density from log.

4-C.2 DeltaLogR Technique:

The Delta Log R technique was developed by Passey et al. (2010). It involves using an overlay between a porosity log and a resistivity log to capture the deviation from expected formation log response values due to the presence of organic matter.

$$\mathrm{TOC_{DLogR}} = \mathrm{DeltaLogR_{Sonic}} * 10^{(2.297 - (0.169 * \mathrm{LOM}))}$$

Where the parameters used in this calculation are obtained as follows:

$$\mathrm{DeltaLogR_{Sonic}} = \log\left(\frac{\mathrm{R_{LLD}}}{\mathrm{R_{LLD_{baseline}}}}\right) + 0.02 * \left(\mathrm{DT_{p-sonic}} - \mathrm{DT_{p-sonic\ baseline}}\right)$$

$\mathrm{R_{LLD_{baseline}}}$ (for both wells) $= 5$ ohm. m

$\mathrm{DT_{p-sonic\ baseline}}$(for both wells) $= 295\,\frac{\mu\mathrm{sec}}{\mathrm{m}}$

$$\mathrm{LOM} = 0.099 * \mathrm{x}^5 - 2.159 * \mathrm{x}^4 + 12.392 * \mathrm{x}^3 - 29.032 * \mathrm{x}^2 + 32.53 * \mathrm{x} - 3.034$$

Where LOM is Level of maturity, x = VR = Vitrinite reflectance value = 0.90 (from laboratory testing for both wells).

4-C.3 Backus averaging (performed in Techlog software) (Mavko et al., 2003)

Prior to use in the generation of a synthetic seismogram, velocity logs need to be upscaled. It is generally accepted that the best way to that is through Backus averaging, which involves the following steps:

1. Determine shear and bulk moduli from sonic and density logs.
2. For a selected seismic wavelength, calculate the arithmetic average of density and harmonic average of moduli (bulk and shear).
3. Reconstitute the velocities (e.g., computed Vp-upscaled using moduli and density obtained at step-2).

Appendix 4-D: Horizontal Stresses

Figure 4-D shows vertical profile of horizontal stresses based on inverted cubes of elastic properties and pore pressure at well-X, showing favourable comparison between well-X and seismic data.

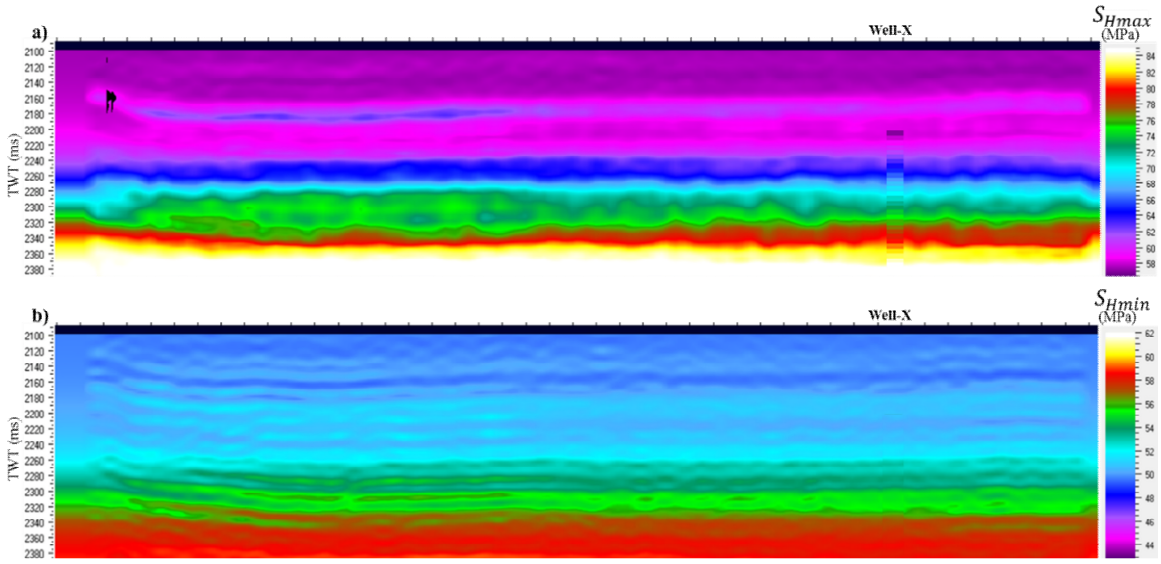

Figure 4-D Vertical profile of maximum (a) and minimum (b) horizontal stresses at well-X.

Appendix 4-E: Sensitivity Analysis

The mechanical properties estimated in this work are dependent on sonic velocity data, and any error in sonic velocities will propagate to mechanical properties (and, in turn, to calculated in-situ stresses). This is relevant in this work because shear wave velocities (Vs) were estimated rather than measured (except for the upper part of the Sembar Formation in well-Y). Also, although various methods (e.g., slowness time coherence) were used to reduce the error in interpreted compressional-wave velocities using the seismic data, some degree of error likely remains. As such, it seems reasonable to consider error in both velocities (Vp and Vs) and study the propagation of this error to mechanical properties and in-situ stresses.

The results of this sensitivity (error propagation) analysis are shown in Table 4-E, and Figures 4-E.1 and 4-E.2. The following equation was used to calculate percent error of each property:

$$\%\ Error = \left(\frac{estimated - measured}{measured}\right) * 100$$

Figure 4-E.1 shows that an error of 10% in Vp and Vs will introduce roughly 20% error in dynamic Young's modulus (E_dyn), and lesser errors (<16%) in calculated stresses. The error between estimated and recorded velocities in the upper interval of Sembar Formation (4046-4071 m) in well-Y is actually around 5%, which means the error in mechanical properties should be around 10%. This is deemed acceptable by the authors, for regional study based on an incomplete dataset.

Figure 4-E.2 shows another scenario, in which the value of Vp at depth 4071 m (as shown in Table 4-E) was kept constant and error was introduced in Vs only. The resulted curves for mechanical properties are similar to Figure 4-E.1, except Poisson's ratio shows sensitivity to errors in Vs (similar percent errors to Young's modulus for Vs errors in the ±20% range), and errors in calculated stresses are slightly larger (but still less than or similar to the error in Young's modulus).

Table 4-E: Calculation of errors in mechanical properties and in-situ stresses for hypothetical errors in velocities. These illustrative calculations were made based on log measurements from a depth of 4071 m in well-Y, where both compressional and shear wave velocities were logged.

At Depth 4071 m of well-Y			Introduce error in Velocities			New mechanical properties				% Error in new mechanical properties			
measured values			Reduced by %	Vp	Vs	E_dyn	Pois.	SHmin	SHmax	E_dyn	Pois.	SHmin	SHmax
Vp	4178	m/s	-5	3969	1981	28	0.3	74	148	-9	0	-5	-7
Vs	2085	m/s	-10	3760	1876	25	0.3	71	137	-19	0	-9	-14
E_dyn.	31	GPa	-15	3551	1772	23	0.3	67	126	-27	0	-14	-21
Pois.	0.33	unitless	-20	3342	1668	20	0.3	64	116	-36	0	-18	-28
SHmin	78	GPa	-25	3134	1564	18	0.3	61	106	-43	0	-22	-33
SHmax	160	GPa	-30	2925	1459	15	0.3	58	98	-51	0	-26	-39
			-35	2716	1355	13	0.3	55	89	-58	0	-30	-44
			-40	2507	1251	11	0.3	52	82	-64	0	-33	-49
			-45	2298	1147	9	0.3	50	75	-70	0	-36	-53
			-50	2089	1042	8	0.3	48	68	-75	0	-39	-57
			Increased by %	**Vp**	**Vs**								
			5	4387	2189	34	0.3	83	173	11	0	6	8
			10	4596	2293	38	0.3	87	186	22	0	12	16
Data for Figure E1			15	4805	2398	41	0.3	92	200	33	0	18	25
			20	5014	2502	45	0.3	97	214	45	0	24	34
			25	5223	2606	49	0.3	102	229	57	0	30	43
			30	5431	2710	53	0.3	107	245	70	0	37	53
			35	5640	2815	57	0.3	112	261	83	0	44	63
			40	5849	2919	61	0.3	118	278	97	0	51	74
			45	6058	3023	65	0.3	124	295	111	0	59	85
			50	6267	3127	70	0.3	130	314	126	0	66	96
			Reduced Vs by %	**Vp_const.**	**Vs**								
			-5	4178	1981	29	0.4	74	148	-8	6	-5	-8
			-10	4178	1876	26	0.4	70	136	-17	12	-11	-15
			-15	4178	1772	23	0.4	65	124	-25	17	-17	-23
			-20	4178	1668	21	0.4	60	112	-33	21	-24	-30
			-25	4178	1564	19	0.4	54	100	-40	25	-31	-37
			-30	4178	1459	16	0.4	49	89	-47	29	-38	-45
			-35	4178	1355	14	0.4	43	78	-54	32	-45	-52
			-40	4178	1251	12	0.5	38	67	-61	35	-52	-58
			-45	4178	1147	10	0.5	32	57	-67	37	-59	-64
			-50	4178	1042	9	0.5	27	48	-73	40	-65	-70
Data for Figure E2			**Increased Vs by %**	**Vp_const.**	**Vs**								
			5	4178	2189	34	0.3	82	172	8	-7	4	7
			10	4178	2293	36	0.3	85	183	16	-15	8	15
			15	4178	2398	39	0.3	86	194	24	-24	10	21
			20	4178	2502	41	0.2	87	205	32	-34	11	28
			25	4178	2606	43	0.2	87	215	38	-46	11	34
			30	4178	2710	45	0.1	85	223	44	-59	9	39
			35	4178	2815	46	0.1	82	231	48	-75	5	44
			40	4178	2919	47	0.0	77	237	50	-93	-2	48
			45	4178	3023	47	0.0	71	242	50	-115	-10	51
			50	4178	3127	45	-0.1	62	246	46	-141	-21	54

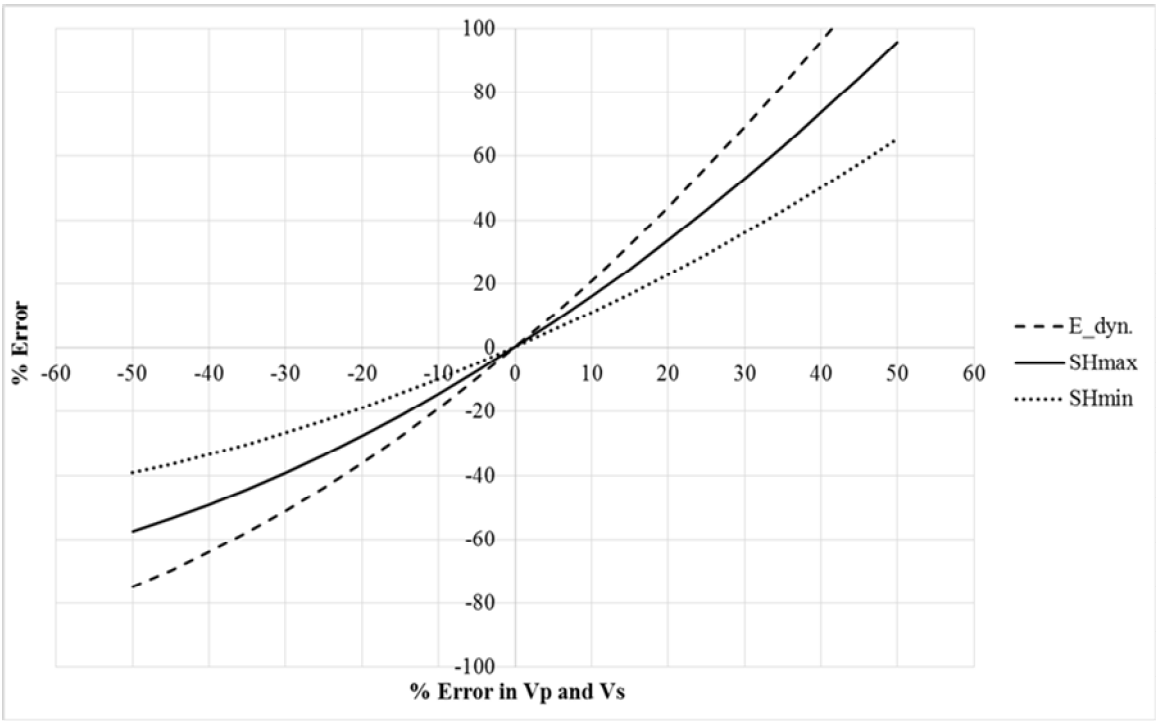

Figure 4-E.1 Calculated errors in dynamic Young's modulus and calculated in-situ stresses as a function of errors in Vp and Vs. (Note that Poisson's ratio is not affected by the velocity errors considered in this scenario, because Vp/Vs ratio was constant).

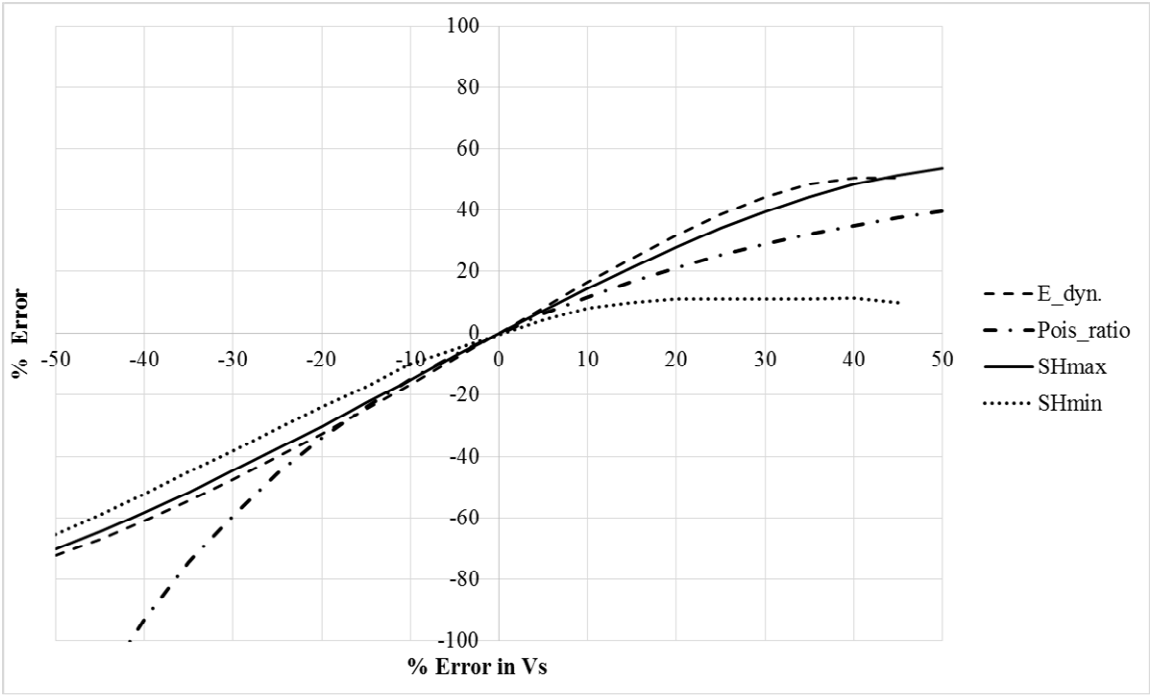

Figure 4-E.2 A comparison of percentage errors in mechanical properties due to error in Vs only (assuming Vp constant for a specific depth).

Chapter - 5 Microindentation Testing for Shale: Development of a Testing Methodology and Application to the Sembar Formation

This chapter will be submitted as a research paper to the 11th Asian Rock Mechanics Symposium, Challenges and Opportunities in Rock Mechanics - an ISRM Regional Symposium, 2021, Beijing China.

Contribution of the Ph.D. candidate

Ghulam Mohyuddin Sohail carried out the evaluation presented in this chapter, with technical review feedback provided by Dr. Christopher Hawkes during weekly meetings. Mr. Sohail wrote the manuscript with review feedback provided by Dr. Hawkes.

Contribution of this chapter to the overall study

This study developed/improved the methodology to determine the microhardness of shale cuttings. This study covers the measurement of microhardness which can be utilized to explore its relationship to macro-scale Young's modulus through testing of core samples and developing theoretical rock-physics models.

5.1 Abstract

Rock mechanical properties such as Young's modulus, hardness and brittleness have significant impacts on the effectiveness of hydraulic fracturing operations in shale gas reservoir development. Ideally, these properties can be measured on core samples. Unfortunately, in many cases, core samples are unavailable, and drill cuttings are the only available samples for testing. The objective of this study was to investigate techniques for estimating mechanical properties using drill cuttings. Drill cuttings for the Sembar Formation, a prospective shale gas reservoir in the Lower Indus Basin of Pakistan, were used as the basis for this work because core samples were not available for this formation. An existing microindentation testing technique was used. New and improved methods of implementing this technique that were developed in this work include: embedding multiple cuttings into an epoxy puck to facilitate sample preparation, mineralogical analysis, and testing of a large number of sampling points; progressive re-saturation to restore cuttings to representative moisture conditions; selection of optimal indentation force; and brittleness assessment based on indentation morphology. Limitations of this testing method are discussed, and recommendations for future research are given.

5.2 Introduction

5.2.1 Background

Young's modulus impacts the hydraulic fracture aperture during hydraulic fracturing (Smith and Montgomery, 2015); microhardness controls the proppant embedment, thus affecting the ultimate fracture conductivity (Alramahi and Sundberg, 2012); and brittleness is the material property of fracturing with little plastic deformation forming a substantial number of cracks (Zhang et al., 2016). Macroscopic properties of rock, such as Young's modulus, are generally obtained through laboratory testing (e.g., uniaxial compression test) using core samples 25 mm in diameter or greater, with length/diameter ratios of at least 2. Microindentation testing is a technique that shows some potential for mechanical property characterization, in cases where no core samples are available.

5.2.2 Microindentation Testing Methods

Microindentation testing is a quick and economical technique to determine the microhardness of materials. In general, the materials tested using this technique are metals, although the effectiveness of this testing method for rocks has been under investigation for some time. There are five widely used microindentation tests; Vickers (or modified Vickers), Berkovich, Knoop, Buchholz, and Micro-IHRD. The Vickers hardness test is believed to be more accurate under low loads (e.g., 1 to 10 N), and has been used for a wide variety of metals and rocks (Fan et al., 2019; Broitman, 2017; Mason et al., 2014; Bokko and Ulm, 2008; Dorner, 2002; Schneider et al., 1999). No examples showing the use of other types of microindentation tests on rocks have been found in the literature. As such, the Vickers hardness test (using a Mitutoyo MVK-H1 Microhardness Tester) was selected for this research.

5.2.3 Microindentation Testing of Shales

Shales are generally composed of silicates (quartz, feldspar, mica, chlorite), carbonates (limestone, dolomite), diagenetic pyrite, and different clay minerals, and can be quite heterogeneous at the micro-scale (Verba et al., 2016). The organic matter (kerogen or bitumen) is also a critical component of shale, and its volume fraction can be quite variable. The mineralogy of shale is a dominant factor that controls the variability of elastic properties and hardness at both the micro and macro scales (Kumar et al., 2015; Yoon et al., 2015: Goral et al., 2018; Manjunath and Jha, 2019). The Young's modulus of a shale which is predominantly silica (e.g., quartz, a monophasic material) can be similar at the micro and macro scales, whereas a shale which is dominated by clays (multiphase nature) can vary significantly depending on the volume of sample tested (Oliveira et al., 2014; Auvray et al., 2017; Han et al., 2018).

Standard microindentation testing procedures are designed for metals (ductile materials with a smooth surface), so special attention regarding sample preparation is required when this test is performed on rocks such as shales, which may possess rough surfaces and/or cracks which may be natural or developed during sample preparation. Some researchers (Boulenouar et al., 2017; Veytskin et al., 2017) suggested that for indentation on rocks, the sample surfaces should be polished and tested carefully to avoid the formation of cracks, and natural cracks (if present) should also be avoided. These authors were focusing

on nano-indentation, where cracks formation during indentation may be avoided, which may not be valid for microindentation. Fan et al. (2019) observed it is inevitable to control the cracks events during micro indentations on Longmaxi Shale (siliceous) provided that samples were polished carefully and no natural cracks existed. The cracking characteristics of shale under the microindentation loading can be used as a tool to assess brittleness (Fan et al., 2019).

In previously published studies on several shales from the USA (Michael et al., 2016) and the Longmaxi Formation shale of China (Han et al., 2018; Han et al., 2015) for microhardness, microhardness values of 1 GPa (for siliceous shale) and 3 GPa (for mixed grain shale) were found to be associated with static Young's moduli of 20 GPa and 30 GPa, respectively. Though the relationship between microhardness and Young's modulus show considerable scatter for each individual dataset (i.e., clay-rich USA shales; clay-poor Longmaxi shale), the collective dataset suggests that there might be a linear trend may prevail for the collective dataset, as shown in Figure 5.1. If such a trend could be established with confidence, it would enable the estimation of Young's modulus based on microindentation measurements conducted on shale cuttings.

5.2.4 Objectives

The long-term objective of the author's broader research program is to determine the relationship between microhardness measured on shale cuttings, and macro-scale mechanical properties such as Young's modulus. This will require a sample set that includes both core samples (for compression testing) and cuttings (for microhardness testing), for a number of shale formations, in addition to testing methods that obtain representative and reliable results. At the time of this research, neither an appropriate sample set nor a well-defined testing methodology were available. As such, the specific objective of the work reported here was to investigate and improve experimental techniques for determining microhardness on shale cuttings, using cuttings samples available for the Sembar Shale. A secondary objective was to assess methods to characterize brittleness using microindentation tests.

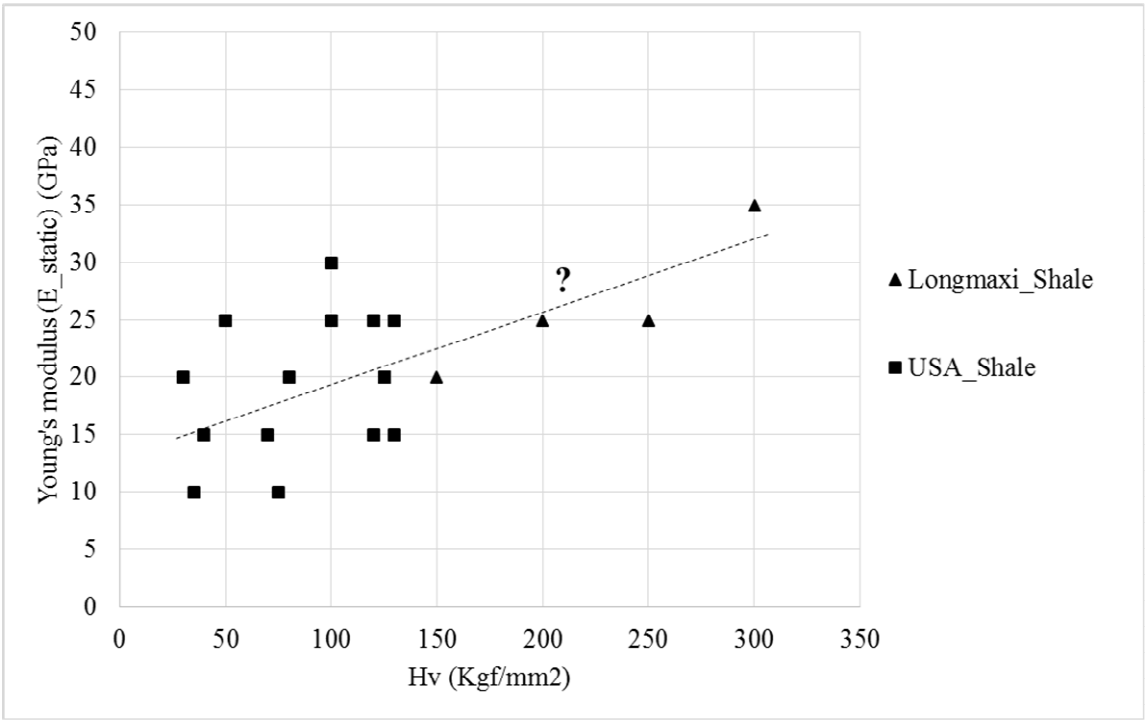

Figure 5.1 Plot of static Young's modulus (E_static) versus Vickers microhardness (Hv) for various shales from the USA (Data Source: Michael et al., 2016) and shale samples from the Longmaxi Formation, China (Data Sources: Han et al., 2018; Han et al., 2015). A regression line is shown with the "?" symbol added to denote the tentative/uncertain nature of this correlation.

5.3 Materials and Methods

5.3.1 Materials

Shales of the Sembar Formation ("Sembar Shale") were deposited in a marine shelf environment in the Early Cretaceous Period. It serves as a source rock for a number of gas-producing sandstone reservoirs in the Middle and Lower Indus Basins of Pakistan (Haider et al., 2012). The drill cuttings of Sembar Shale were retrieved from an already drilled well-Y (Lower Indus Basin, Pakistan) at a depth of ~3950 m. The Sembar Shale in well-Y has been identified as the source rock for a gas-producing sandstone reservoir (Lower Goru Sands) and is an ideal candidate for shale gas exploration (Haider et al., 2012). Previous core-based studies have shown that dominant minerals in shaly intervals of the Sembar Formation are quartz (40-50%) and clays (30-40%) with minor quantities (10-15%) of dolomite, feldspar, and pyrite (Ahmad et al., 2012).

5.3.2 Methods

5.3.2.1 Experiment apparatus and testing scheme

The Microhardness Tester (Mitutoyo MVK-H1) was used to determine microhardness (Hv) according to the ASTM standard (ASTM, 2017). It consists of a loading frame, diamond indenter, 40X lens, sample holding device and displacement sensors. The pyramid indenter (square base and an angle of 136 degrees between opposite faces), with a hardness of 100 GPa, as shown in Figure 5.2, is subjected to a load of 1N to 10 N (newton). The full load is usually applied for 10 to 15 seconds. The two diagonals of the indentation left in the surface of the material after removal of the load are measured using a microscope. A metal block with known hardness (Hv = 150) was available for calibration, and before the start of each session, the indenter was calibrated. The test scheme is illustrated in Figure 5.3a, which shows a minimum distance of $2.5d_v$ should be maintained between two indents. An appropriate size of the sample is required to perform an optimum number of tests. In summary, the operator chooses load (F_gf), creates an indentation, and measures the diagonal length of indent (d_v) using a microscope, then Hv is displayed by the apparatus, as calculated using equation 5.2.

$$Hv = \frac{F_{gf}}{A_s} \tag{5.1}$$

Where F_{gf} is test force in grams-force, A_s is surface area of indentation in μm² = $d_v^2/2\sin\frac{\alpha}{2}$, d_v is mean Vickers indentation diagonal length in micrometer (μm) = $\frac{d1+d2}{2}$, α is face angle of the diamond indenter (136^0).

After substituting known parameters for the Mitutoyo MVK-H1 in equation 5.1, the final form as given in equation 5.2 is used by the machine to calculate Hv in gf/μm². In this work, the results are converted from gf/μm² to GPa .

$$H_v = \frac{F_{gf}}{d_v^2} \times 1854.4 \tag{5.2}$$

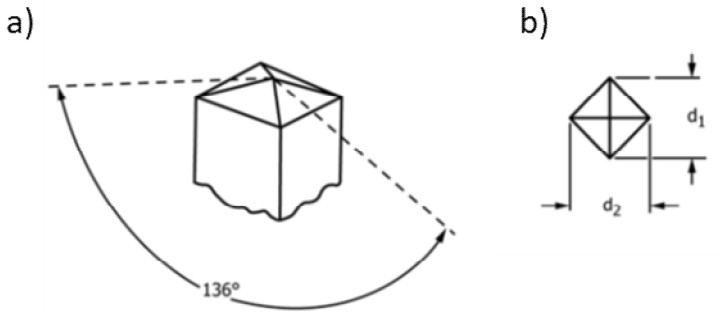

Figure 5.2 a) Geometry of Vickers Indenter with face angle of 136°. b) Plan view of an indent created by the Vickers Indenter, showing diagonal lengths d_1 and d_2 (ASTM, 2017).

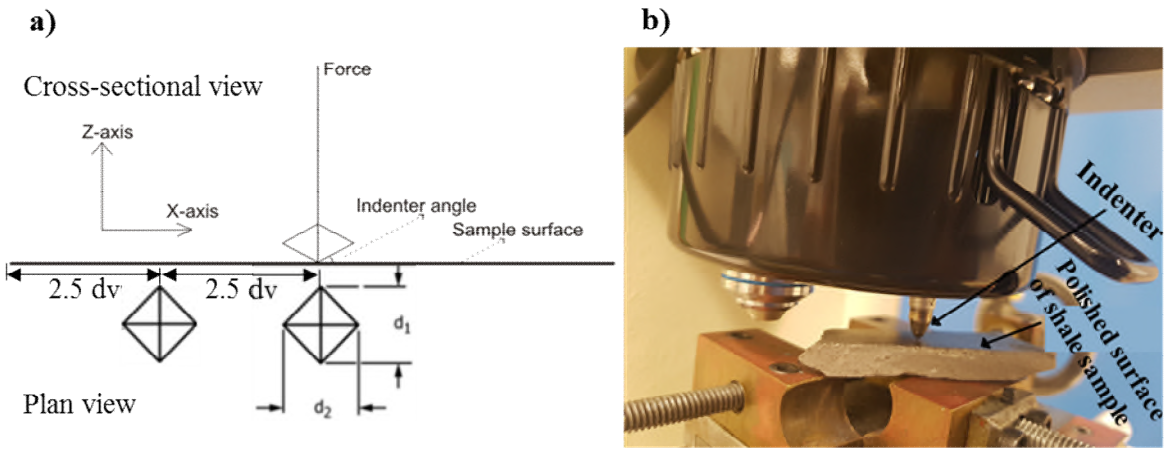

Figure 5.3 a) Cross-sectional and plan views of Vickers Indentation test scheme shows the minimum spacing between two indents (ASTM, 2017). **b)** Indenter and polished shale sample.

5.3.2.2 Sample preparation

The well cuttings of Sembar Shale were collected and examined. The samples were tested as received; they had not been preserved for moisture content. The cuttings ranges in size from fine powder to roughly 2 mm in width. In order to obtain a subset of the cuttings that were sufficiently large for micro indentation testing, cuttings in the range of 1 mm to 2 mm diameter were separated from a bulk sample using a sieve shaker apparatus. From this 1-2 mm subset, cuttings were then randomly selected for testing with the goal of obtaining a representative sample set including all types of cuttings (siliceous, calcareous, argillaceous and mixed). The siliceous cuttings were generally random in shape, and the argillaceous cuttings were tabular. Additionally, a 500 g sample of cuttings was delivered to the

Saskatchewan Research Council (SRC) Geoanalytics Laboratory for x-ray diffraction (XRD) analysis for bulk mineralogy (details of XRD are given in Appendix 5-A).

A pilot experiment was conducted on several individual cuttings using microhardness tester. It was found that cuttings moved during the tests, because it was not possible to hold these small, weak and irregular shaped cuttings in place with the available sample. To overcome this problem, a disc was prepared in the SRC Geoanalytics Laboratory, in which cuttings were embedded into epoxy, as shown in Figure 5.4. The tabular shaped cuttings (e.g., argillaceous) were observed to settle into the puck in a horizontal orientation due to gravitational effects. Once the epoxy had set, one end was polished using a lapping wheel (as per standard techniques for preparing polished thin sections). The polished surface was then analyzed using the Quantitative Evaluation of Materials by Scanning Electron Microscopy (QEMSCAN) technique (see Appendix 5-A for details).

Five types of epoxy resin-hardener blends were in use at SRC Geoanalytical Laboratory over the time interval where the puck was made. The specific blend used was not specified. However, none of their blends heat up beyond 40 to 60°C during curing, hence the cuttings properties should not have been affected by thermal processes. Similarly, the viscosity of the blends used is relatively high (in the 400 to 900 centipoise range), hence the epoxy blend should not have penetrated into shale cuttings during the relatively short cure time (approximately 4 hours). The small air-filled bubbles observed in Figure 5.4 would not have formed if the epoxy blend had a viscosity sufficiently low to penetrate the pores in the cuttings.

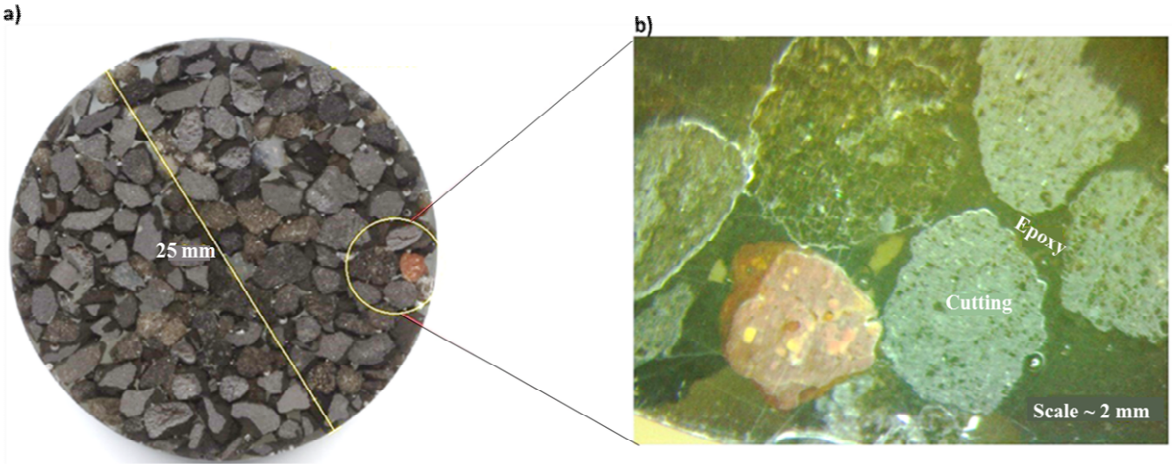

Figure 5.4 a) Epoxy disc containing Sembar Shale drill cuttings, created for microindentation testing, **b)** Enlarged view of the zone circled on the disc.

5.3.2.3 Axial load - magnitude

The equipment used could perform indentations at axial forces ranging from 1 N to 10 N. In the preliminary stages of this work, tests were run using various forces in order to identify an appropriate value. The results obtained after performing several tests at different forces on mixed clay-sand cuttings (the most abundant type of cutting lithology) are shown in Figure 5.5. The idents at low loads (3N) yielded relatively high and scattered hardness values . The indents made at high load (10N) yielded lower and less scattered hardness values, but the sizes of resulting indents were generally high (diagonal lengths of approximately 200 µm) which made it challenging to conduct a large number of tests in the limited available surface area. The indents obtained at intermediate loads (5 N) yielded hardness values similar to (slightly larger than) the results obtained at 10 N loads, and with less scatter. The indentation sizes at 5 N load (diagonal lengths of approximately 100 µm) were small enough to allow a large number of tests per sample, yet large enough to span multiple clay particles (nano to micrometer size) and silt sized quartz inclusion (of ~ 10^{-3} m size) in the clay-sand cuttings (Ulm et al., 2007).

Fan et al. (2019) observed negligible impact of load on microhardness while testing the Longmaxi Shale, for loads of 10N, 20N and 40N. However, other researchers (Bokko et al., 2010; Hu et al., 2017) obtained results similar to those presented here, in the sense that microhardness measurements were affected by load. As such, it is suggested that a standard load should be adopted broadly, in order to facilitate comparison of results obtained by different researchers. In the work presented here, a load of 5 N was used for all subsequent indentation tests.

For all of the Sembar Shale tests reported here, the axial load was applied in an orientation normal to bedding. Fan et al. (2019) observed similar results in microindentation tests conducted on surfaces normal and parallel to bedding in the Longmaxi Shale. However, given the anisotropic fabric generally present in shales, it seems reasonable to expect that tests conducted normal and parallel to bedding would usually yield different results (lower hardness parallel to bedding); hence testing of microhardness anisotropy is suggested as a topic of future investigation.

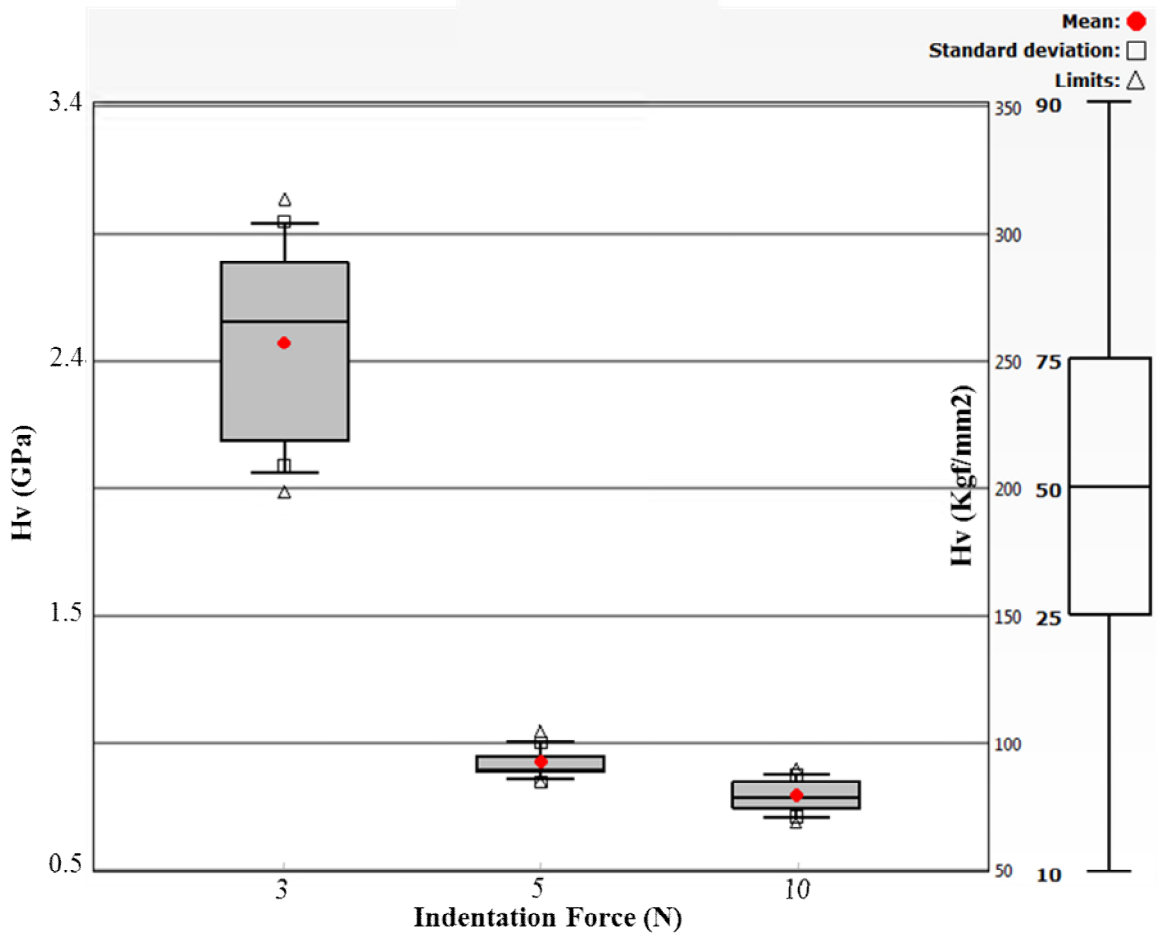

Figure 5.5 Box plots of Hv at different axial loads (pilot experiment on clay-sand mixed cuttings.

5.3.2.4 Testing sequence

In order to capture an averaged representation of shale cutting properties while conducting microindentation tests that probe an area roughly 100 µm by 100 µm, it is important to conduct a large number of tests. However, the number of tests is constrained by the amount of surface area available for testing, the need to ensure adequate spacing between successive tests, the desire to run a number of testing sequences on each cutting at different moisture conditions, and the fact that manual data entry is required for each microindentation. In this work, approximately 100 microindentation tests were run on each type of drill cutting (e.g., siliceous, calcareous, argillaceous and clay-sand mixed) during each testing sequence. These microindentations were spread uniformly across the different cuttings in the epoxy puck, and each microindentation was cataloged based on the cutting's identification number, and a unique (sequential) number that was assigned to each indentation in any given cutting.

In addition to measuring microhardness for each indentation test, observations were recorded regarding the shape, edge fragmentation and indentation contact face to support assessments of sample brittleness.

5.3.2.5 Assessment of sample moisture effects

Previous investigations have shown that the mechanical properties of clay-rich rocks are sensitive to moisture content (Cherblanc et al., 2016; Hawkins and McConnell, 1992). Thus, shales should ideally be tested at moisture conditions representative of in-situ conditions. The Sembar Shale cuttings obtained for this work had been exposed to ambient conditions for an extended period of time prior to testing, and hence were presumed to be relatively dry compared to in-situ conditions. In order to avoid sample damage (e.g., cracking) which can occur in dry samples of clay-rich rocks when immersed in water, the cuttings disc was progressively resaturated, and tested at different moisture conditions to assess the impact of saturation on microhardness. The sample disc was first exposed to a relative humidity (RH) of 60% for roughly one month to achieve a relatively low water saturation (representative of ambient "air dry" conditions in the laboratory), then a microindentation testing sequence was conducted. Next, in a manner similar to the work presented by Pham et al. (2005), the samples were placed on a plaform in the upper part of an airtight desiccator in which constant relative humidity (RH) was imposed using a saline solution (filling the lower part of the dessicator). The apparatus used for this, including a RoHS RH-USB sensor, is shown in Figure 5.6. Different alkaline solutions were selected to impose RH values of 80% and 90% at ambient temperature (~20 °C), as described in Table 5.1. The mass of the sample disc was recorded periodically. Figure 5.7 shows a plot of measured masses and RH values versus time.

An indentation testing sequence was conducted when sample mass had stabilized at 80% RH after 215 days. When exposed to 90% RH, sample mass increased relatively quickly for one month, the the rate of increase began to taper off. After more than one year at 90% RH, however, sample mass had not reached a constant value. Due to time contraints, it was not possible to wait longer, so the sample was subjected to an additional microindentation testing sequence at 650 days. It is suggested that the upper surface of the cuttings in the epoxy disc had equilibrated with the 90% atmosphere in the dessicator, and the gradual increase in mass was occurring as moisture diffused into the lower parts of the cuttings. Given that microhardness testing was conducted on the upper surface, it is assumed here that

the results obtained at 650 days are representative of micro-hardess at a 90% RH condition. When exposed to 100% RH, sample mass increased relatively quickly for few days (675 to 680 days) and then seems to taper off at 687 days before it was merged into distilled water, as shown in Figure 5.7.

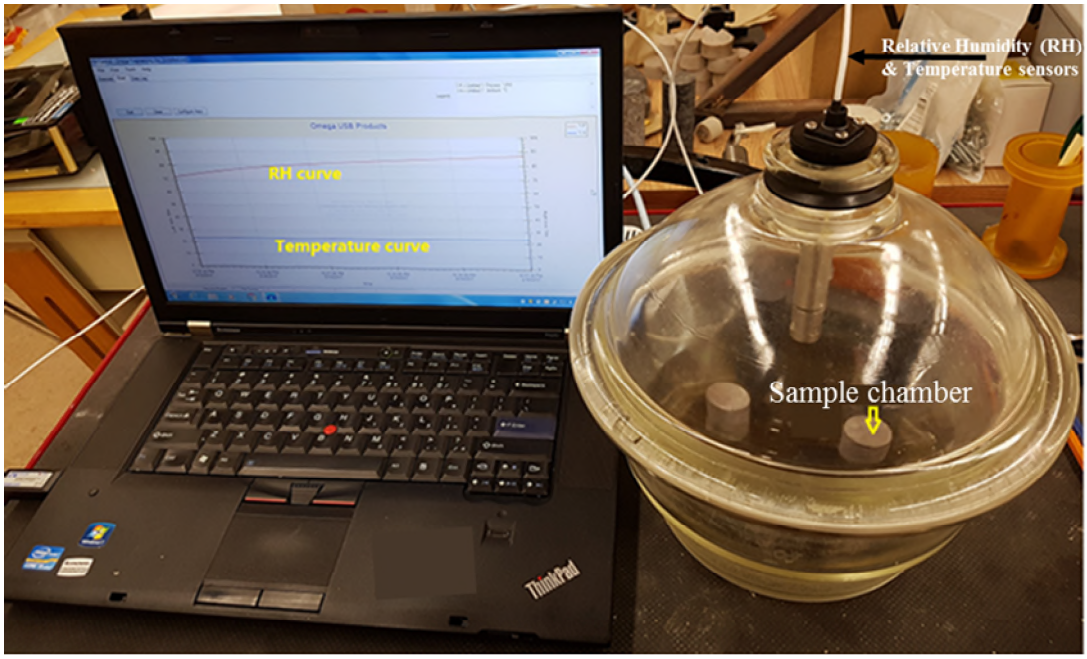

Figure 5.6 Setup for saturation of shale samples (modified after Pham et al., 2005).

Table 5.1 Quantity of chemicals used to achieve different Relative Humidity (RH) values.

Chemicals	%RH at 20 °C	Solubility (g/l) 20 °C	Volume (Liter (l))	Total quantity (g)
Na_2CO_3	90	215	1	215
NaCL	80	360	1	360

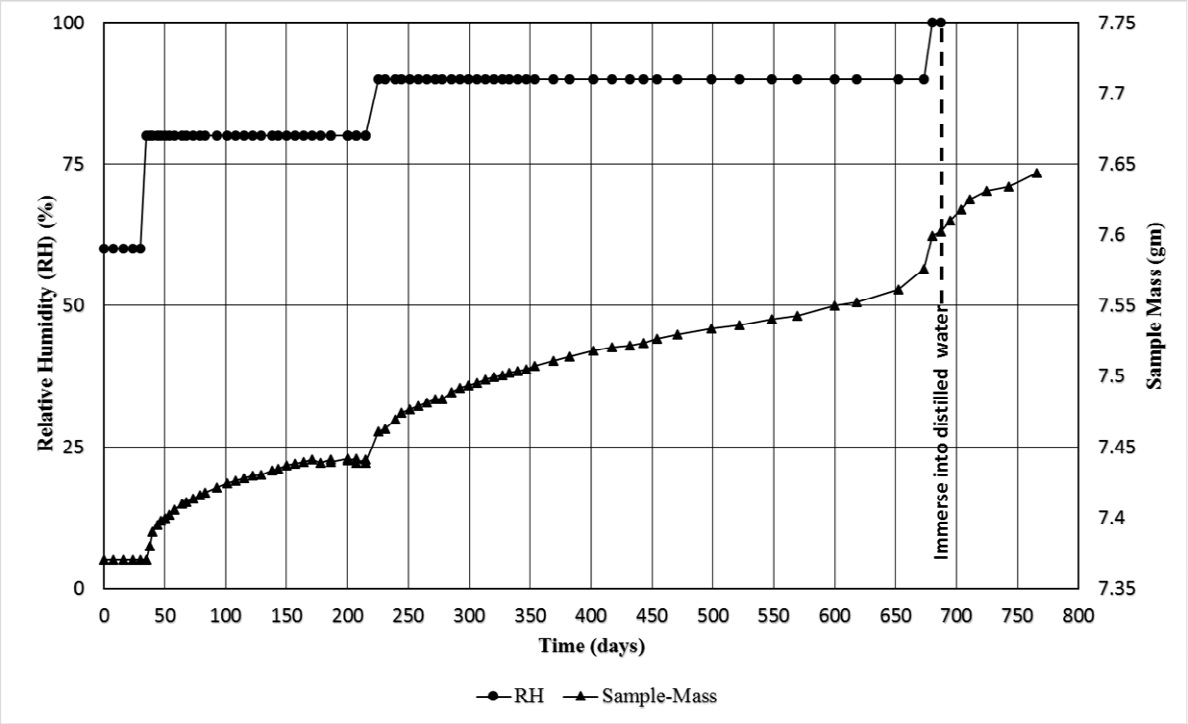

Figure 5.7 Plot of relative humidity (RH) and Sample mass versus time for drill cuttings of Sembar Shale.

5.4 Results

5.4.1 Mineralogy

The results of the XRD analysis on the bulk sample, which are shown in Figure 5.8, indicate that the Sembar Shale is siliceous (quartz dominant). Localized mineralogy results based on QEMSCAN analysis are shown in Figure 5.9. These results suggest the Sembar Shale cuttings can be sorted into four broad categories as follows: siliceous (quartz dominant), argillaceous (clay dominant), calcareous (calcite dominant) and mixed clay-sand.

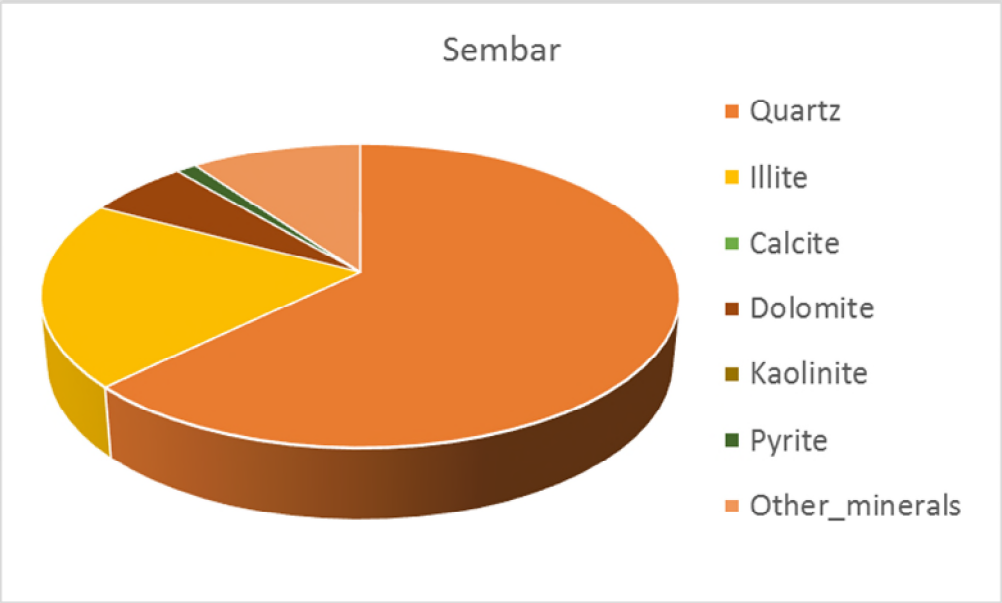

Figure 5.8 Pie chart of mineralogies determined by bulk XRD analysis for the Sembar Shale.

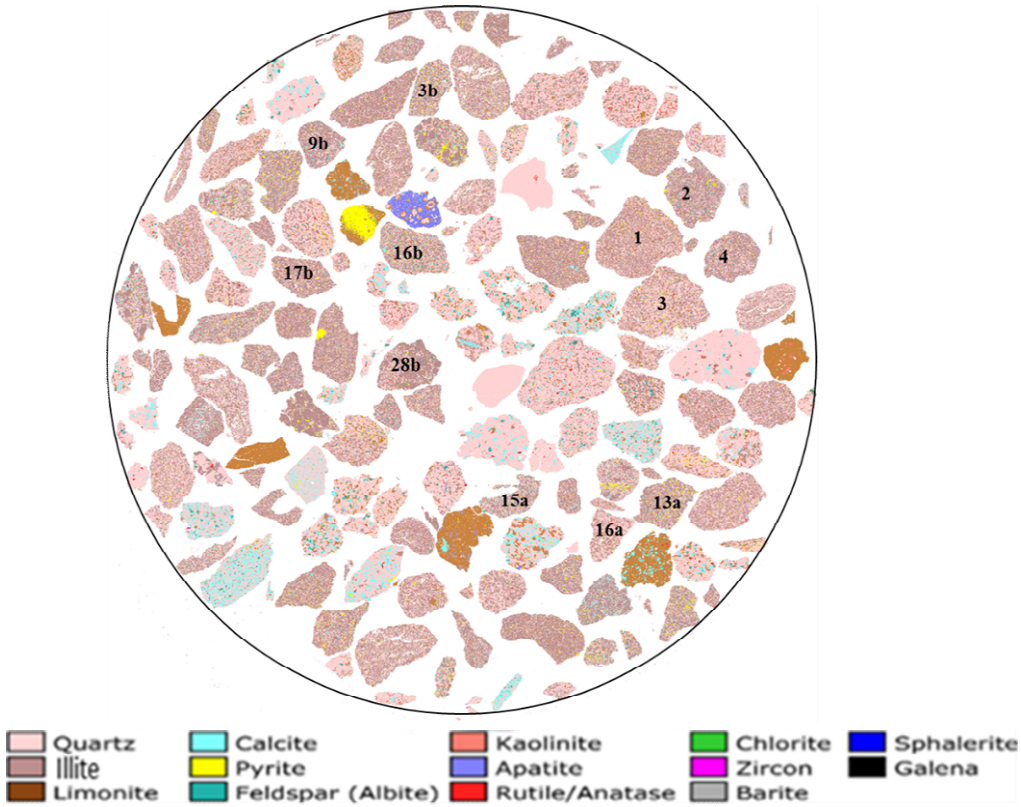

Figure 5.9 Mineralogy of Sembar Shale cuttings based on QEMSCAN analysis of the disc shown in Figure 5.4a. Each cutting was allotted a specific identification number (ID); examples of a few IDs are shown here.

5.4.2 Vickers Microhardness (Hv)

Box plots summarizing the results of Hv measurements for eight selected mixed clay-sand cuttings of Sembar Shale (at RH = 60%) are shown in Figure 5.10. The minimum and maximum mean Hv values for these cuttings are approximately 0.9 GPa and 3.9 GPa, respectively. Based on a tentative regression line fit to the literature data plotted in Figure 5.1, these results suggest static Young's modulus values of 20 to 35 GPa for mixed clay-sand cuttings.

Box plots summarizing Hv results for three clay-sand grains at different RH values are shown in Figure 5.11. These cuttings were chosen because data quality was good for the measurements conducted on them (i.e., the microindentations had regular shapes and well-defined edges), and because clay-bearing cuttings were expected to be most sensitive to moisture. The results for these cuttings show that mean Hv decreased by about 50% as RH was increased from 60% to 80%. Mean Hv decreased by 25% for cutting #1 as RH increased from 80% to 90%, whereas the reduction in mean Hv with this RH change was smaller for cuttings # 2 and 4 (8% and 21%, respectively). For all three cuttings, the change in mean Hv was small as RH was increased from 90% to 100% (3%, 2%, and 1.98% for cuttings #1, 2 and 4, respectively).

The minimum and maximum mean values of microhardness for siliceous cuttings were approximately 2.5 GPa and 11 GPa, respectively, and for calcareous cuttings were approximately 2 GPa and 9 GPa. Microhardness testing results for these cuttings are not shown here due to the predominance of mixed clay-sand cuttings in the Sembar Formation, although these data were recorded and may be used for future research.

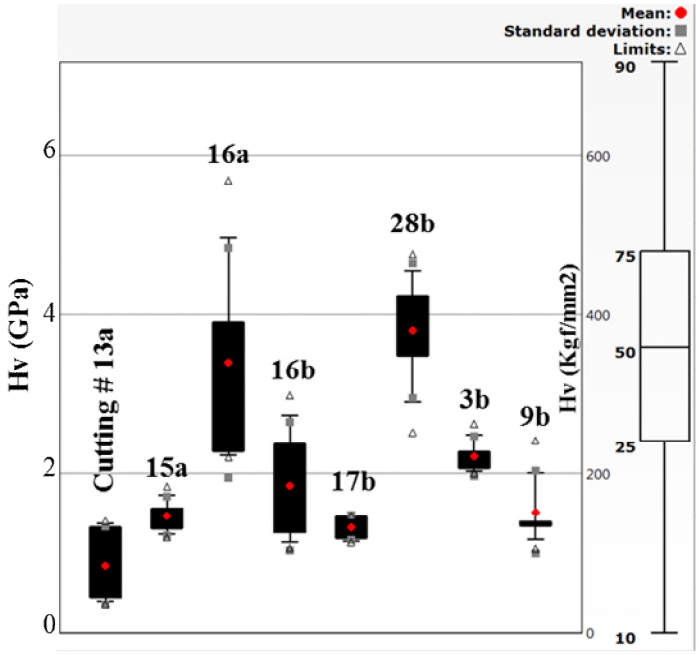

Figure 5.10 Box plots summarising the distribution of Vickers microhardness (Hv) values measured on eight selected Sembar Shale cuttings, measured at RH = 60%. All of the cuttings shown here had a mixed clay-sand mineralogy.

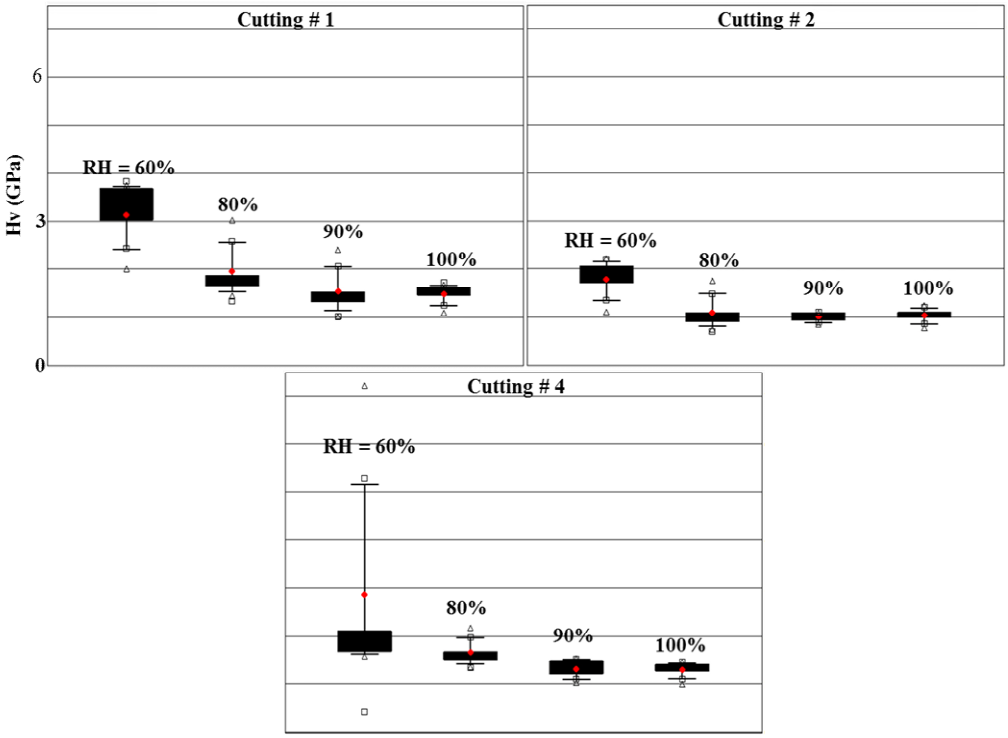

Figure 5.11 Box plots of Vickers microhardness (Hv) for selected Sembar Shale drill cuttings at RH of 60%, 80%, 90% and 100%. Each box represents a different cutting of mixed type (i.e., a mixture of clay and quartz); the cuttings numbers are shown in Figure 5.9. Data for these cuttings are given in Appendix 5-B.

5.4.3 Microindentation Morphology and Assessment of Brittleness

Assuming that sample preparation and microindentation test procedures are conducted in a consistent manner for all tests, the morphology of each microindent can be used as an indicator of the constitutive behaviour of the sample tested. For example, the stress concentration induced by the microindenter should induce an elastic-plastic response (and uniform microindentation shape) for relatively ductile materials (e.g., clay-rich shale), and an elastic-brittle response for stiffer material such as quartz grains.

Figure 5.12(a) shows the microindentation created during a test on a quartz-rich zone of one cutting. The morphology of this feature suggests that the stress concentration beneath the tip of microindenter created a brittle fracture, resulting in the detachment of a chip. A relatively high Hv value of 13 GPa was calculated for this test, based on the diagonal length of the chip. Figure 5.12(c) shows the microindentation created during a test on a different quartz-rich zone. In this case, cracks were observed to have propagated outside of the area where the microindenter contacted the sample surface. The geometry of the depression created where the microindenter made contact with the sample was highly irregular; hence no value was calculated for Hv.

Figure 5.12(b) shows the microindentation created during a test on a clay-rich zone of one cutting. The deformation in this case was clearly ductile in nature, as the shape of the microindent is a close match to the shape of the microindenter. An Hv value of 7 GPa was calculated for this feature.

Figure 5.12(d) shows the microindentation created during a test on a calcite-rich zone of one cutting. The deformation in this case was mixed in nature. It was ductile directly beneath the tip of the microindenter, resulting in a shape that closely matched the microindenter. However, chips – indicative of brittle failure, developed around the edges of the indent. An Hv value of 4 GPa was calculated for this feature, using a diagonal length that neglects to presence of the chips. It is interesting to note that this more brittle response (compared to Figure 5.12(b)) corresponded to a lower hardness value, which is not consistent with the general expectation that stiffer rocks tend to be harder and more brittle (Kias et al., 2015). This could be due, in part, to increased hardness in the zone tested in Figure 5.12(b) due to the presence of microcrystalline quartz (as imaged for several cuttings in the QEMSCAN analysis).

Some researchers (Copur et al., 2003; Hucka and Das, 1974) have derived relationships between microhardness and brittleness index. The difficulty stemming from hardness measurement in cases where indent morphology is variable (as demonstrated in this work) suggests that these relationships might be inappropriate. It is suggested that this is an area that requires further investigation. Methods that quantify the dimensions of brittle fractures resulting during microindentation might prove useful in this regard. Further, it is suggested that microindentation testers which continuously record load and displacement during each test might prove useful (e.g., see Fan et al., 2019).

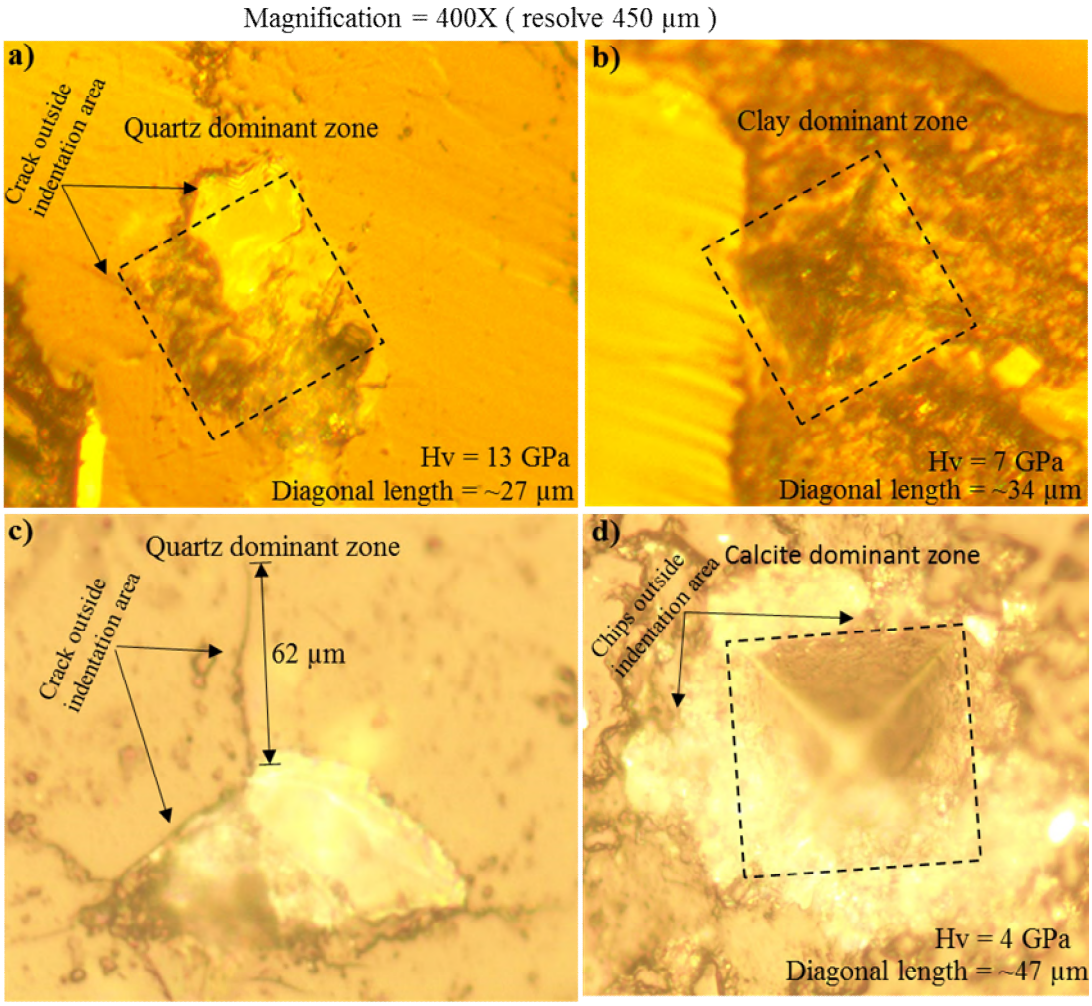

Figure 5.12 Microscopic images of indentation impressions. a) the pyramid indent was not developed properly and microhardness recorded based on maximum area disturbed due to indentation, b) the pyramid indent was developed properly without any cracks or chips, c) indent was not developed may be due to cracks, d) indent seems good but with chips at the boundary of the indent.

5.5 Discussion

The microhardness results obtained in this work were highly variable, both within individual cuttings samples (in some cases) and when comparing cuttings samples of different lithologies. It is suggested that the improvements in testing methodology developed in this work enable the collection of reliable micro-scale measurements, and that future work to provide a framework for integration of these results to enable estimation of macro-scale properties is worth pursuing. Such work could include statistical analysis of test results (as required to obtain average values that account for spatial variability and anisotropy), micro-scale numerical modeling, and/or adaptation of existing rock physics models that account for micro-scale fabric

Microhardness testing produces results that range from elastoplastic to elastic-brittle depending on the lithology of the rock tested. It is still under debate whether microhardness should be correlated directly and specifically to Young's modulus. Previous studies on clay-dominated North American shales have established that the elastic properties are dependant on microstructures and anisotropy, and this dependency reduces with the increase of quartz and decrease of clay (Zoback and Kohli, 2019). Fan et al. (2019) ran indentation tests on Longmaxi Shale of Jiaoshiba region, southwest China, with 20% clay (volume), and observed that the mechanical anisotropy was very weak due to two reasons, first a small number of fabrics covered in tested area and second the elastic anisotropy of these fabrics is linked to the oriented clay deposition and intrinsic anisotropy of clay itself.

Clay minerals are the primary source of mechanical weakness and anisotropy in sandy shale/shale due to its intrinsic anisotropy and tendency to align in the bedding plane during deposition and diagenesis (Sayers, 1994; Zoback and Kohli, 2019). At the micro-scale, the clays form local preferred orientations that appear to flow around clastic grains (Curtis et al., 2012). It seems that the quantity/distribution of clay in studied shales may play a pivotal role in defining the strength of the material, and it may be the common base for studying the microhardness and Young's modulus. It is suggested here that theoretical rock-physics models of clay-sand mixing could be developed to strengthen this hypothesis, and (as mentioned above) to provide a framework for integrating large numbers of microindentation test results in such a way that macro-scopic properties can be estimated, even in anisotropic materials. More information on the potential use of rock physics models is given in the following section.

5.6 Conclusions and Recommendations

This paper proposes improvements for the experimental methodology used to characterize rock cuttings using microindentaton tests, and illustrate this methodology for the Sembar Shale. The Vickers microhardness tester can be used effectively for determining the microhardness (Hv) of shale cuttings if the following tasks are completed carefully: embed the cuttings in epoxy, to facilitate the preparation of a smooth (polished) surface and secure sample-holding during testing; conduct mineralogical analyses on the cuttings to provide context for the interpretation of microindentation test results; establish an appropriate axial load (5 N was found effective in this work) through pilot experiments then use this load consistently; establish the effects of sample moisture on test results and – if significant – run the testing program at this condition (80% relative humidity was found to yield results similar to those at saturated conditions, while mitigating the risk of sample damage associated with immersion of clay-rich rocks in water).

It is suggested that the experimental methodology could be improved through following amendments: use of advanced indentation equipment which can measure continuous load and displacement during indentation; run tests on core samples (for macro-scale mechanical properties) and cuttings (for micro-scale properties) of multiple shales, to enable investigation of general relationships between these parameters; testing at greater axial loads (> 10N) to more broadly and fully assess a standard load; investigation of anisotropy in microhardness testing of shale by performing tests on surfaces perpendicular and parallel to bedding. For tests parallel to bedding, the disc used in this study could be cut into slices along planes normal to its axis, following the conclusion tests on the bedding-parallel surfaces described (and tested) in this work. Also, regardless of the orientation of the tested surface, it might be possible to significantly increase the number of tests re-polishing the surface then re-resting. For example, The sample could be re-polished up to 60 micrometers (as the depth of indents is in the range of 15 to 25 micrometers).

Rock physics models should be used to investigate the relationships between Young's modulus and microhardness. The known mineralogies could be mixed based on Hashin-Shtrikman (HS) theory (1963), and penny shaped randomly-oriented micro-cracks could be introduced based on Kuster and Toksoz (1974) and Budiansky and Oconnel (1976) theories. These theories provide upper and lower theoretical bounds for macro and micro

elastic properties, which could be utilized to compare against macro-scale measurements made on core samples.

References

ASTM. (2017). Test Methods for Vickers Hardness and Knoop Hardness of Metallic Materials. doi: 10.1520/e0092-17

Auvray, C., Lafrance, N., & Bartier, D. (2017). Elastic modulus of claystone evaluated by nano-/microindentation tests and meso-compression tests. *Journal of Rock Mechanics and Geotechnical Engineering, 9(1),* 84–91. doi: 10.1016/j.jrmge.2016.02.002

Alramahi, & Sundberg. (2012, January). Proppant Embedment And Conductivity of Hydraulic Fractures In Shales. Retrieved from https://www.onepetro.org/conference-paper/ARMA-2012-291

Bobko, C. P., Gathier, B., Ortega, J. A., Ulm, F.-J., Borges, L., & Abousleiman, Y. N. (2010). The nanogranular origin of friction and cohesion in shale-A strength homogenization approach to interpretation of nanoindentation results. *International Journal for Numerical and Analytical Methods in Geomechanics, 35(17),* 1854–1876. doi: 10.1002/nag.984.

Bobko, C., & Ulm, F.-J. (2008). The nano-mechanical morphology of shale. *Mechanics of Materials, 40(4-5),* 318–337. doi: 10.1016/j.mechmat.2007.09.006

Broitman, E. (2017) Tribol Lett, 65: 23. https://doi.org/10.1007/s11249-016-0805-5

Bobko, C., and Ulm, F.-J. (2008). The nano-mechanical morphology of shale. *Mechanics of Materials, 40(4-5),* 318-337.

Boulenouar, A., Mighani, S., Pourpak, H., Bernabé, Y., & Evans, B. (2017, August). *Mechanical Properties of Vaca Muerta Shales From Nano-Indentation Tests*. American Rock Mechanics Association.

Budiansky, B., & Oconnell, R. J. (1976). Elastic moduli of a cracked solid. *International Journal of Solids and Structures, 12*(2), 81–97. doi: 10.1016/0020-7683(76)90044-5

Copur, H., . Bilgin, N., Tuncdemir, H., & Balci, C. (2003). A set of indices based on indentation tests for assessment of rock cutting performance and rock properties. *Journal of The Southern African Institute of Mining and Metallurgy, 103*(9), 589-599.

Curtis, M. E., Sondergeld, C. H., Ambrose, R. J., & Rai, C. S. (2012). Microstructural investigation of gas shales in two and three dimensions using nanometer-scale resolution imaging. *AAPG Bulletin*, *96*(4), 665–677. doi: 10.1306/08151110188

Dorner Dorothée. (2002). *Indentation methods in experimental rock deformation.* Erscheinungsort nicht ermittelbar: Verlag nicht ermittelbar.

Fan, M., Jin, Y., Chen, M., & Geng, Z. (2019). Mechanical characterization of shale through instrumented indentation test. *Journal of Petroleum Science and Engineering*, *174*, 607–616. doi: 10.1016/j.petrol.2018.11.083

Goral, Deo, Mattson, & Huang. (2018, August). *Micro- and Macro-Scale Geomechanical Testing of Woodford Shale.* American Rock Mechanics Association, Retrieved from https://www.onepetro.org/conference-paper/ARMA-2018-1220

Haider, A. B., Aizad, T., Ayaz, A. S., and Shoukry, A. (2012, December). *A Comprehensive Shale Gas Exploitation Sequence for Pakistan and other Emerging Shale Plays*, Society of Petroleum Engineers (SPE) Annual Technical Conference, Islamabad, Pakistan.

Han, Q., Chen, P., & Ma, T. (2015). Influencing factor analysis of shale microindentation measurement. *Journal of Natural Gas Science and Engineering*, *27*, 641–650. doi: 10.1016/j.jngse.2015.09.010

Han Q, Qu Z, Ye Z. (2018). Research on the mechanical behaviour of shale based on multiscale analysis. *Royal Society. open science. 5: 181039.* http://dx.doi.org/10.1098/rsos.181039

Hashin, Z., & Shtrikman, S. (1963). A variational approach to the theory of the elastic behaviour of multiphase materials. *Journal of the Mechanics and Physics of Solids, 11(2),* 127-140. doi:10.1016/0022-5096(63)90060-7.

Hu, J., Sun, W., Jiang, Z., Zhang, W., Lu, J., Huo, W., … Zhang, P. (2017). Indentation size effect on hardness in the body-centered cubic coarse-grained and nanocrystalline tantalum. *Materials Science and Engineering: A, 686,* 19–25. doi: 10.1016/j.msea.2017.01.033.

Hucka, V., and Das, B. (1974). Brittleness determination of rocks by different methods. *International Journal of Rock Mechanics and Mining Sciences & Geomechanics, 11*, 389-392.

Kias, E., Maharidge, R., & Hurt, R. (2015). *Mechanical Versus Mineralogical Brittleness Indices Across Various Shale Plays.* SPE Annual Technical Conference and Exhibition. doi: 10.2118/174781-ms

Kumar, V., Sondergeld, C., & Rai, C. S. (2015). Effect of mineralogy and organic matter on mechanical properties of shale. *Interpretation,3(3).* doi:10.1190/int-2014-0238.1

Kuster, G.T, and Toksoz, M.N., 1974, Velocity and attenuation of seismic waves in two-phase media: *Geophysics, 39*, 587-618.

Manjunath, G., & Jha, B. (2019). Geomechanical characterization of gondwana shale across nano-micro-meso scales. *International Journal of Rock Mechanics and Mining Sciences,119*, 35-45. doi:10.1016/j.ijrmms.2019.04.003

Mason, J., Carloni, J., Baker, S., Zehnder, A., & Jordan, T. (2014, September). *Dependence of Micro-Mechanical Properties on Lithofacies: Indentation Experiments on Marcellus Shale.* Proceedings of the 2nd Unconventional Resources Technology Conference. doi: 10.15530/urtec-2014-1922919.

Michael A. Addis, Sanjeev Bordoloi, Javier A. Franquet, Patrick J. Hooyman, Robert S. Hurt, Julie E. Kowan, Abbas K. (2016). Role of Geomechanical Engineering in Unconventional Resources Developments, In: Ahmed U. and Nathan M, D.,(eds.),

Unconventional Oil and Gas Resources: Exploitation and Development, Baker Hughes, Canada, 280–290.

Oliveira, G., Costa, C., Teixeira, S., & Costa, M. (2014). The use of nano- and micro-instrumented indentation tests to evaluate viscoelastic behavior of poly(vinylidene fluoride) (PVDF). *Polymer Testing, 34*, 10–16. doi: 10.1016/j.polymertesting.2013.12.006

Pham, Q. T., Vales, F., Malinsky, L., Nguyen Minh, D., & Gharbi, H. (2005, January). Effect of desaturation-resaturation on mechanical behaviour of shale. *American Rock Mechanics Association*.

Sayers C.M. (1994). The elastic anisotropy of shales. *Journal of Geophysical Research*, 99 (B1), 767-774.

Smith, M. B., & Montgomery, C. T. (2015). *Hydraulic fracturing*. Boca Raton: CRC Press.

Schneider, J.-M., Bigerelle, M., Iost, A. (1999). Statistical analysis of the Vickers hardness,*Materials Science and Engineering A,* 262 (1-2), 256-263.

Ulm, F.-J., Vandamme, M., Bobko, C., Ortega, J. A., Tai, K., & Ortiz, C. (2007). Statistical Indentation Techniques for Hydrated Nanocomposites: Concrete, Bone, and Shale. *Journal of the American Ceramic Society*, *90*(9), 2677–2692. doi: 10.1111/j.1551-2916.2007.02012.x

Veytskin, Y. B., Tammina, V. K., Bobko, C. P., Hartley, P. G., Clennell, M. B., Dewhurst, D. N., & Dagastine, R. R. (2017). Micromechanical characterization of shales through nanoindentation and energy dispersive x-ray spectrometry. *Geomechanics for Energy and the Environment*, *9*, 21–35. doi: 10.1016/j.gete.2016.10.004

Verba, C., Crandall, D., & Moore, J. (2016). *Multiscale Shale Pore Characterization.* Proceedings of the 4th Unconventional Resources Technology Conference. doi: 10.15530/urtec-2016-2448192

Yoon, Dewers, Grigg, & Mozley. (2015, November). Multiscale Characterization of Physical, Chemical, and Mechanical Heterogeneity of Mudstones. Retrieved from https://www.onepetro.org/conference-paper/ARMA-2015-463

Zhang, D., Ranjith, P., & Perera, M. (2016). The brittleness indices used in rock mechanics and their application in shale hydraulic fracturing: A review. *Journal of Petroleum Science and Engineering*, *143*, 158–170. doi: 10.1016/j.petrol.2016.02.011.

Zoback, M., & Kohli, A. H. (2019). *Unconventional Reservoir Geomechanics. Shale Gas, Tight Oil, and Induced Seismicity*. Cambridge University Press.

Appendix 5-A: Analytical Methods Procedures (SRC Geoanalytics Laboratory)

5-A.1 X-ray Diffraction

The sample was irradiated with Cu Kα radiation (λ=1.54056 Å) in a Bruker D4 Endeavor X-ray diffractometer (XRD) operating at 1.6 kW power (40 kV accelerating potential and 40 mA current). The XRD is outfitted with a high-speed LynxEye silicon strip detector with fluorescence background suppression. The sample was measured from 3.5 to 70° 2θ with a 0.02° step size and 0.3 seconds dwell time with a 0.300° divergence slit. The raw diffraction data were processed using MDI Products Jade software for mineral identification and quantification. Minerals were identified based on the observed interatomic spacing of the crystal lattices present constrained by common mineral associations. All mineral abundances were calculated using whole-pattern fitting algorithms with peak intensities scaled with internally-consistent relative intensity ratios using patterns derived from the American Mineralogist Crystal Structure Database (AMCSD).

5-A.2 QEMSCAN

The QEMSCAN in the SRC Advanced Microanalysis Centre is built on an FEI Quanta 650 scanning electron microscope fitted with a field emission gun (10nm resolution) and dual Bruker XFlash 5030 energy dispersive spectrometers with a maximum throughput of 1.5Mcps.

QEMSCAN analyses are a collection of back-scattered electron images and semi-quantitative point chemical analyses. The grain images and EDS data are combined using

image analysis to calculate various parameters such as particle size distribution, mineral associations and liberation, modal abundances. Operating conditions were set to 25kV and 10nA beam current, measured in a Faraday cup at the sample surface. Data were collected in Field Stitched Analysis (FSA) mode with a nominal point spacing of either 3 or 20µm. Raw X-ray energy spectra were compared to a mineral composition database customized for this analysis.

Note: muscovite (as reported by the QEMSCAN results) is reported as illite in this work.

Appendix 5-B: Sample of data

The data collected for cutting # 1, 2 and 4 is shown as a sample in Table 5-B. Five indents were produced on each mixed clay-sand cutting at each RH stage.

Test No.	RH = 60%		80%		90%		100%	
	Vickers Hardness (Hv)							
Sample data for Cutting # 1								
	Kgf/mm2	GPa	Kgf/mm2	GPa	Kgf/mm2	GPa	Kgf/mm2	GPa
1	369	4	180	2	153	1	163	2
2	376	4	145	1	240	2	158	2
3	303	3	303	3	102	1	168	2
4	187	2	187	2	133	1	147	1
5	166	2	166	2	145	1	110	1
Sample data for Cutting # 2								
1	222	2	75	1	109	1	100	1
2	205	2	98	1	110	1	110	1
3	111	1	109	1	106	1	125	1
4	172	2	92	1	95	1	78	1
5	181	2	176	2	85	1	105	1
Sample data for Cutting # 4								
1	168	2	151	1	103	1	100	1
2	174	2	167	2	130	1	140	1
3	158	2	134	1	121	1	127	1
4	721	7	158	2	153	1	145	1
5	212	2	218	2	148	1	130	1

Chapter 6 – Conclusion

6.1 Summary of Results

This thesis had three primary objectives. The addressed in Chapter 2, evaluated the available geological, geochemical, petrophysical and geomechanical properties of source rocks of Pakistan based on comparison with gas-producing North American shales. The second , which was addressed in chapters 3 and 4, evaluated the relationships in literature for the estimation of Vs applied to sandy shale and shale of Lower Goru Formation and characterized the shale of Sembar Formation using well logs and post-stack seismic data. The third objective (addressed in Chapter 5) was to assess and improve techniques for estimating mechanical properties using drill cuttings.

In Chapter 2, results show that the geological and geochemical parameters of all the Pakistani shales reviewed in this work are promising regarding their shale gas potential. The shales of the Lower Goru and Sembar Formations seem most promisingin terms of their depositional environment, mineralogy, depth, thickness, quantity and quality of organic carbon, and porosity. However, more geochemical, petrophysical and geomechanical data/analysis are required before conclusions on economic production from these shales can be made with confidence.

In Chapter 3, results reveal that the estimation of shear wave velocity using Vp-based empirical (linear and polynomial) models and porosity-modulus-based simple rock physics models can be useful if the coefficients are adjusted based on available Vs data. However, these models cannot explain the mechanism of velocity variations in sandy shale and shale due to pore geometry (aspect ratio), consolidation and fluid saturations. Modifications are made to the effective medium inclusion model of Xu and White (1995) (e.g., use of effective porosity, adjust aspect ratios, use of Biot instead of Gassmann), which make it suitable for Vs estimation in gas-saturated sandy shale and shale of the Lower Goru Formation. The accurate prediction of Vs in LGF resulted in following two advantages: the validation of petrophysical properties (e.g., mineralogy, porosity, and saturation) which are helpful for assessing the shale gas potential of LGF, and the methodology developed in this chapter was useful for the Sembar Shale investigations presented in Chapter 4.

In Chapter 4, analysis of well-scale data identified several aspects of the Sembar Shale that make it favorable for development: high gas saturation, good porosity (up to 10%), moderate quality of organic matter (2-4%), multiple brittle intervals, and a strike-slip stress regime. At the scale of the study area, robust statistical techniques were used to invert seismic stacks and develop a 3D mechanical earth model. This model shows a trend of increasing shale brittleness towards the northeastern portion of the study area, hence suggesting that this area might be the preferred locationfor initial shale gas development providing that other properties (e.g., stress regime, pore pressure and stress gradients) are favorable. The workflow developed in this investigation may apply to other shales of the world where limited data are available.

In Chapter 5, based on microindentation results, the minimum and maximum values of microhardness for dry mixed grains are 0.9 GPa and 3.9 GPa, respectively, which based on literarture suggest the static Young's modulus values of 20 GPa to 35 GPa for mixed clay-sand cuttings. The results for saturated mixed clay-sand cuttings at different RH values show that mean Hv decreased by about 50% as RH was increased from 60% to 80%. Mean Hv decreased by 25% to 8% for mixed cuttings as RH increased from 80% to 90%, whereas, the change in mean Hv was 1% to 3% as RH was increased from 90% to 100%. The morphology of several indents on three types of zones show: the development of brittle fracture in quartz-rich cuttings, which may relate to the brittle nature of these cuttings; deformation created on clay-rich zones with a morphology that closely matches the geometry of the indenter, which may be due to the ductile nature of these cuttings; and deformation created on calcite rich zones which may relate to a mixed material behaviour (ductile under the tip of microindenter and brittle at the edges of the indents). The authors feel that more tests and analyses need to be performed to confirm the relationships of Young's modulus and brittleness with microhardness.

6.2 Research Contributions and Recommendations

The following are the specific research contributions of each study reported in this thesis (Chapters 2 through 5), and some recommendations for future research.

1. An overview of Pakistani shales was completed by comparison of Pakistani shales against well documented, gas-producing North American shales. Although this study was based on previously published data, the analogs for comparisons of two shales provided a

basis to explore the similarities and dissimilarities between Pakistani and North America shales. This study defined criteria to identify the most prospective shales for further study. This will save time and money, and can expedite shale gas exploration activities in Pakistan. Most of the Pakistani shales are lacking in measurements of petrophysical and elastic properties, which is a data gap that should be addressed in future research.

2. Comprehensive research for estimating Vs has been completed to select a suitable rock-physics model for a potential shale gas reservoir of Pakistan. This study will be useful for wells where no Vs data is available/recorded. It also provides geoscientists and engineers with an alternative rock physics workflow for the estimation of Vs in a shale gas reservoir (e.g., use of the Biot model rather than Gassmann's model for fluid substitution). The modified rock-physics model outperformed an existing rock-physics model, and it can be used globally in settings where the lithology of the shale formations are known. It is deemed to be the best option available at present for Pakistani shales and can be further evaluated once core samples are obtained and more Vs data have been obtained in well logging operations.

3. A mechanical earth model (MEM) of Sembar Shale was developed through the integration of petrophysical and mechanical properties using well logs and post-stack seismic data, which is a novel work in the Lower Indus Basin of Pakistan. Further, the workflow designed in this study for MEM resolved one of the significant issues in the Indus Basin of Pakistan (i.e., the lack of data for MEM development), which was a hurdle for companies to select a suitable area in the Indus Basin for shale gas exploration. The MEM model is flexible and can be refined when additional data (e.g., borehole image logs, drilling and testing of shale cores, dipole shear sonic logging, diagnostic fracture injection tests, and microseismic monitoring of hydraulic fracturing) become available.

4. A micro-scale study on Sembar Shales using drill cuttings was completed for assessing and improving the techniques for the estimation of microhardness and Young's modulus. The acquisition parameters designed for microindenation in this study for the Sembar Shale may save time and money for future research. At least this study highlights available resources from different disciplines for the study of micro-mechanical properties (e.g., microhardness, indentation modulus) of rocks, which provide a base to initiate a multidisciplinary study on shales to design new technologies for micromechanical characterization.

It is suggested that the experimental methodology could be improved through the following amendments: use of advanced indentation equipment which can measure continuous load and displacement during indentation; running tests on core samples (for macro-scale mechanical properties) and cuttings (for micro-scale properties) of multiple shales, to enable investigation of general relationships between these parameters; testing at greater axial loads (> 10 N) to more broadly and fully assess a standard load; investigation of anisotropy in microhardness testing of shale by performing tests on surfaces perpendicular and parallel to bedding. For tests parallel to bedding, the disc used in this study could be cut into slices along planes normal to its axis, following the conclusion tests on the bedding-parallel surfaces described (and tested) in this work.

Rock Physics models should be used to investigate the relationships between macro-scale Young's modulus and microhardness. Different theoretical models could be used to mix the known mineralogies and to introduce randomly oriented penny shaped cracks. These theoretical models could be utilized to compare macro and micro-scale measurements on core samples.